Contribution to the investigation of the chemical interaction between sodium and irradiated MOX fuel for the safety of Sodium-cooled Fast Reactors

Guilhem Kauric

Thèse de doctorat

NNT : 2020UPASF027

université PARIS-SACLAY

Contribution to the investigation of the chemical interaction between sodium and irradiated MOX fuel for the safety of Sodium-cooled Fast Reactors

Thèse de doctorat de l'université Paris-Saclay

École doctorale n° 571, Sciences chimiques : molécules, matériaux, instrumentation et biosystèmes (2MIB)
Spécialité de doctorat: Chimie
Unité de recherche : Université Paris-Saclay, CEA, Service de la Corrosion et du Comportement des Matériaux dans leur Environnement, 91191, Gif-sur-Yvette, France.
Référent : Faculté des sciences d'Orsay

Thèse présentée et soutenue en visioconférence totale, le 20 Novembre 2020, par

Guilhem KAURIC

Composition du Jury

Gianguido BALDINOZZI Directeur de recherche, Centrale Supelec, Université Paris-Saclay	Président
Alexander PISCH Chargé de recherche (HDR), SIMAP, Grenoble INP	Rapporteur & Examinateur
Olivier TOUGAIT Professeur, UCCS, Université de Lille	Rapporteur & Examinateur
Lionel DESGRANGES Ingénieur Chercheur, CEA Cadarache	Examinateur
Rudy KONINGS Professeur, JRC-Karlsruhe, European Commission	Examinateur
Christine GUÉNEAU Ingénieur Chercheur, CEA, Université Paris-Saclay	Directrice de thèse
Karin POPA Associated Professor, University of Iasi	Invité
Anna Louise SMITH Assistant Professor, Delft University of Technology	Invitée

Every great improvement has come after repeated failures. Virtually nothing comes out right the first time. Failures, repeated failures, are finger posts on the road to achievement. One fails forward toward success

Charles F. Kettering

Acknowledgments

Along these three years of PhD spent at a different place each year I met and worked with a lot of people that I would like to thank for their support.

Firstly, I would like to thank the jury members of my PhD defence: Dr. Pisch, Pr. Tougait, Pr. Baldinozzi, Dr. Desgranges, Pr. Konings, and my daily supervisors during the PhD Dr. Guéneau, Dr. Popa and Dr. Smith.

I would like to thank first Anna Smith as without you nothing would have been possible. Indeed, I discovered the research world with you during the internship I made in Delft. I loved working with you and you taught me how to behave and be a good scientist!

After the internship, you mentioned a PhD position opening and introduced me to Christine Guéneau. After the first meeting, I knew directly that you would be a person I will get along really well. This first feeling was right! All the discussions we had and the suggestions you made were extremely useful to me both on the working part but also on the personal viewpoint. So I would like to thank you for these three years that I spent fully focused on the topic!

Finally, the last place I went is the JRC-Karlsruhe. Karin you taught me how to work efficiently in a lab doing at least 10 tasks at the same time! It matched directly as we have the same concept of the lab work: run from an experiment to another one! You also taught me all the tips to work at the JRC! I will always remember your first reaction to my data: “You know your results bring more questions than answers!”

Rudy, you have always found some time to discuss the results, suggests new experiments to perform, taking care that I had everything I needed! So I would like to thank you for these amazing talks we had!

I would also like to thank the “chef de programme SFRAG” F. Serre and then F. Payot.

At the different places I met amazing people. The first person I am thinking of is Enrica. We were following each other from Paris to Delft and then back to Paris! You became more than a friend for me! I would say my big sister! I would also like to thank Elisa, Marco, Fahad, Koos, Sara, Jaèn, Fulvio and Laura for the great times we spent in Delft especially in the lab, on the beach volley court, at the bouldering gym, at Koepeltje, at BierFabrik’s, etc… Thanks to you, everyday was a new story with a lot of craziness!

I would also like to thank L. van Eijck who helped me performing neutron diffraction experiments at the PEARL reactor in TU Delft, Nicolas Clavier for the Raman measurements at ICSM and Enrica, Sara and the support team of the BM26 beamline, in particular Banerjee Dipanjan for the help received during the XAS experiments at the ESRF in Grenoble.

When I arrived in Karlsruhe, I felt directly home! This might be related to the amount of Kraüsen drank with you, especially Ema and Tommaso! When I arrived, I got directly adopted by the Italian group of JRC (I got well-trained in Delft)! I would like to thank you for the complaining coffee time, the nights spent at Vogelbraü or Stövchen, the basketball training or the climbing moments etc… Thank you Ema, Luana, Pauline, Tommaso B., Tommaso S., Concettina, Sara, Luca B, Luca L., Jone, Viktoria, Jessika, Lorenza, Laura M, Olaf, J-F aka Johnny and Petra.

I also wanted to thank the people I worked with at JRC, Cô, Herwin, Daniel, Antony, Jean-Yves, Oliver. It was a real pleasure to work with all of you and you always took the time to explain me how the machine was working and all the details! I was always bringing a lot of samples to analyse with the XRD and to do the accountancy so a second time thank you Cô, Daniel and Antony.

I would also like to thank Laura M. and T. Charpentier for their help with the NMR experiments and analyses and the INE group, especially Dr Vitova and A. Beck for the different measurements you performed on my samples at the KARA synchrotron.

Now the last place I went is the LM2T in Saclay. Everytime I was coming back for a short period or for the longer one at the end, I had the feeling I spent all the PhD there! Therefore, I would like to thank all the staff of the lab: Alain, Sylvie, Laure, Paul, Andrea, Christophe, Eric, Jean-Louis, Philippe, Laurent, Thierry, Stéphanie. I would also like to thank the "chef de labo" Stéphane Gossé and the "chef de Service" Fabrice Legendre and then Fanny Balbaud.

Finally, in Saclay I met also PhD students that were finishing, starting (even the same day as me) and maybe future PhD. I would like to thank all of you for the advices, the coffee times, the discussions… Thank you Eva, Luca S, Hector, Marie B, Mathieu, Xian, Alan, Clément.

I met a lot of new people during these different travels around Europe but now I would like to thank all the people I met before starting the PhD. For sure without you and your support from when we met to today where I am writing these words, things might have gone differently!

I will start with the Poh-lanta group. We met at High-school or later on for some of you! For sure without you guys life would have been different! Thank you Alex, Hugo, Richard, Laurent, Christian, Anna, Axelle, Martin, Marie-Alix, Marc, Laura, Matthieu.

I would like to thank Helene B. and Laure B., we shared the harsh times of prep classes together and kept contact, sharing the adventure of a life in Germany! So thank you for your support and the "short" sum up by audio!

Now I will go to people from Chimie Paris! We spent 3 amazing years all together and then split around the world but reading the messages and seeing each other as much as we could was really a way to escape from the routine! Thank you Stan, Natacha, André, Yacine, Yann, Béné, Tomas, Marion, Bastien, Cyrielle, Flavien, Marie L.P and Noémie.

I will end this part with the friends I met during my internship at CEIDRE. I will always remember the surprise you made all coming to Amsterdam without telling me and all the plans you made so that I got the surprise! Your messages in the good times but also the harsh ones were keeping me sane or at least less insane! I want to thank you for all the times we shared travelling to see each other! It was always amazing! Thank you, Audrey, Clem, Pierre, Coco, Benoît, Charlène, Léa, Willy!

Je voulais aussi remercier ma famille et surtout mes parents qui m'ont toujours soutenu et ont cru en moi et m'encourageant chaque jour me permettant ainsi de profiter au maximum des bons moments et de surmonter les épreuves qui m'ont forgées jusqu'à en arriver où j'en suis aujourd'hui ! UN GRAND MERCI !

These words are obviously not enough to express everything but as sum up THANK YOU!

Contents

List of Figures

List of Tables

Chapter 1:
Introduction and thesis outline

The context of the thesis, related to the interaction between sodium and irradiated fuel under severe accident conditions in Sodium-cooled Fast Reactors is first introduced. Then, the evolution of the fuel chemistry under operating conditions is presented to understand the fuel chemical state before the accident. Finally, the phenomenology of the main severe accident cases is shortly described with the open questions remaining on the irradiated fuel behaviour and its interaction with sodium.

1.1. Context

One of the major challenges of the 21st century is the management of a rising world population and energy needs, while reducing carbon dioxide emissions to mitigate the impact on climate change. In this context, nuclear energy can play a key role in the energy mix. Nowadays, in France, 77% of the produced energy comes from Nuclear Power Plants [1]. Nevertheless, the French nuclear fleet is getting old and will soon need to be renewed. One of the possibilities is to develop a Generation IV nuclear power plant design at industrial scale and adopting a closed fuel cycle. With this system some uranium resources would be saved and wastes reduced by burning plutonium and using ^{238}U as fissile element. Finally, transmutation of minor actinides would also be possible.

The Generation IV International forum (GIF) defined four main criteria for these systems, namely Sustainability, Economics, Safety and Reliability, and Proliferation Resistance and Physical Protection [2]. Six nuclear power plant designs satisfy these requirements: the Gas-cooled Fast Reactor, Lead-cooled Reactor, Molten Salt Reactor, Sodium-cooled Fast Reactor, Supercritical-Water-cooled Reactor, and Very-High-Temperature Reactor. Among these designs, the **Sodium-cooled Fast Reactor** (SFR) is one of the most advanced concept.

1.1.1 Sodium-cooled Fast Reactor (SFR)

Sodium cooled Fast Reactors that were operating or are under commissioning are reported in **table 1.1**. In France, R&D activities are still ongoing to develop a new SFR design using the feedback gained with Rapsodie, Phénix and Superphénix reactors.

Table 1.1: SFR nuclear power plants in the world (2012) [3]

Reactor (country)	Thermal Power (and electric) MW	First start	Final stop	Number of operating years
EBR-I (USA)(NaK)	1,4 (0,2)	1951	1963	12
BR-5/BR-10 (Russia)	8 (0)	1958	2002	44
DFR (UK) (NaK)	60 (15)	1959	1977	18
EBR-II (USA)	62,5 (20)	1961	1991	30
EFFBR (USA)	200 (61)	1963	1972	9
RAPSODIE (France)	40 (0)	1967	1983	16
BOR-60 (Russia)	55 (12)	1968		44
SEFOR (USA)	20 (0)	1969	1972	3
BN-350 (Kazakhstan)	750 (130)	1972	1999	27
PHÉNIX (France)	563 (250)	1973	2009	36
PFR (UK)	650 (250)	1974	1994	20
JOYO (Japan)	50-75/100 (0)	1977		35
KNK-II (Germany)	58 (20)	1977	1991	14
FFTF (USA)	400 (0)	1980	1993	13
BN-600 (Russia)	1470 (600)	1980		32
SUPERPHÉNIX (France)	3000 (1240)	1985	1997	12
FBTR (India)	40 (13)	1985		27
MONJU (Japan)	714 (280)	1994		18
CEFR (China)	65 (25)	2010		2
PFBR (India)	1250 (500)	Under commissioning		
BN-800 (Russia)	2100 (880)	Under commissioning		
Total				418

In SFRs (**figure 1.1**), sodium is the coolant and the heat transfer medium allowing high power density with low coolant volume fraction. As sodium is activated by neutrons and emits β and γ radiations, (^{24}Na has a half-life of nearly 15 hours), two circuits are used. A primary "pool" exchanges the produced heat by the core with a second sodium loop, used to heat water/steam or supercritical carbon dioxide.

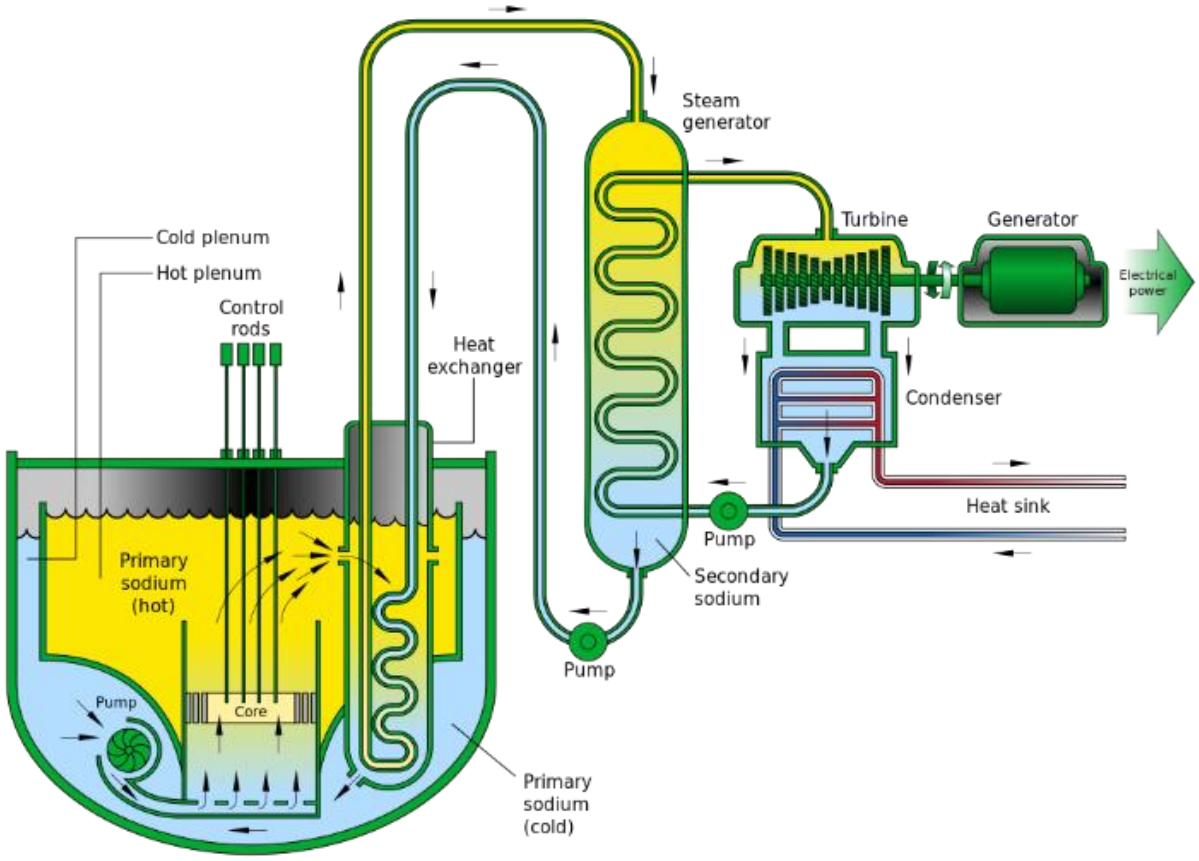

Figure 1.1: Sketch of the Sodium-cooled Fast Reactor design [2]

Among the different nuclear fuels considered for SFRs (oxides, carbides, nitrides and metals), $U_{1-x}Pu_xO_{2-y}$ homogeneous mixed oxide fuel (MOX) is currently the reference, with a plutonium content *"x"* higher than 0.2 and an oxygen stoichiometry "2-y" between 1.93 and 1.98.

The fuel pellets are introduced (**figure 1.2a**) in a stainless steel tube constituting the fuel pin. The core of the reactor, where the fission reactions take place, is made of numerous subassemblies, constituted of several fuel pins surrounded by Hexagonal Tube (HT), as presented in **figure 1.2b**.

a)

b)

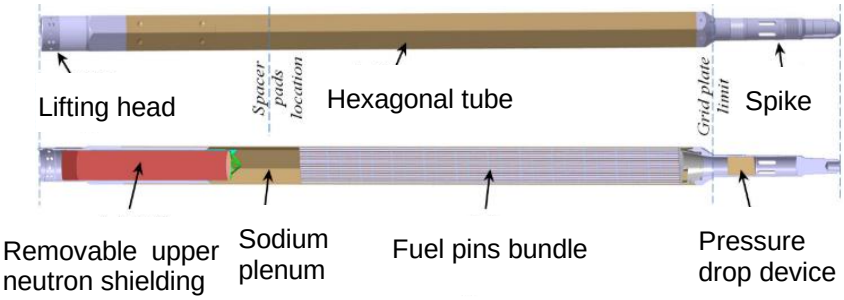

Figure 1.2: a) MOX fuel pellets [3] ; b) scheme of a fuel subassembly [4]

The use of sodium has several advantages:

- Its production is cheap [3].
- It has very advantageous thermal properties for cooling down the reactor with its high heat capacity and thermal conductivity. Moreover, in case of loss-of-flow with scram, the decay heat can be safely removed through natural convection [5].
- It remains in liquid state under operating conditions (core outlet temperature at 1 bar: 550°C) and there is a large safety margin for sodium vaporisation (~900°C at 1 bar) [3]. Thanks to this high operating temperature, a high efficiency coefficient in the energy production is obtained.
- It has a low neutron absorption cross-section and does not slow down neutrons.

However, some drawbacks exist with this technology mainly due to sodium chemical reactivity. Indeed, in case of contact between sodium and air or water, an energetic accident could occur causing a sodium fire and/or an explosive reaction forming NaOH and dihydrogen H_2.

1.1.2. Fuel behaviour under operating conditions

During irradiation, a neutron hits a fissile atom, splitting it into two new atoms called fission products and some additional neutrons that will produce other fissions and maintain the chain reaction as described in **figure 1.3**.

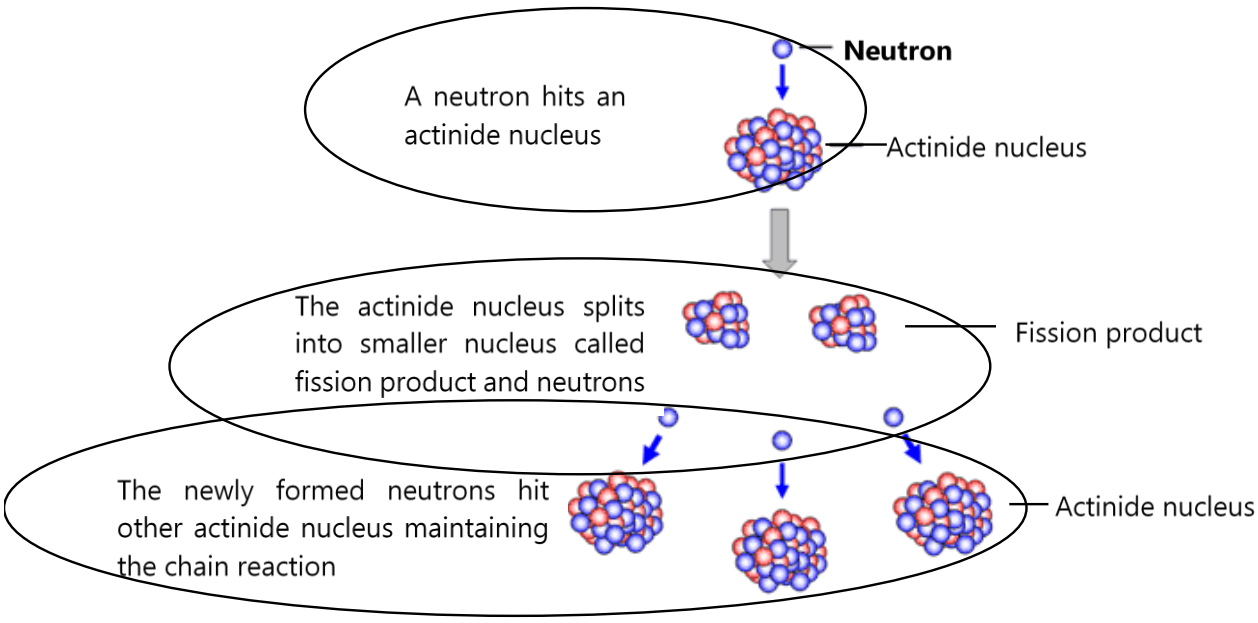

Figure 1.3: Principle of the chain reaction [6]

In **table 1.2**, typical fission product yields for an irradiated fuel in Phénix reactor (Pu/(U+Pu)∼0.2) are reported for a 10 at. % burnup. The burnup measures the fuel utilisation and represents the fraction of atoms from the fuel that underwent fission (percentage of fissions per initial metal atom).

For the fission of one heavy atom, two oxygen atoms are released inducing an increase in the oxygen potential of the fuel. Then, the chemical state of the fission products depends on the oxygen potential, temperature and plutonium concentration of the fuel.

Table 1.2: Elemental yields of fission products in a Phenix fuel pin at 10 at.% burnup [7]. Fission products are listed in alphabetical order.

Fission Product	Yields (%fission products per fission)	Fission Product	Yields (%fission products per fission)
Ag	1.3	Pd	13.8
Ba	6.8	Pm	1.2
Br	0.1	Pr	4.8
Cd	1	Rb	1.5
Ce	11.4	Rh	5.8
Cs	20.1	Ru	22.0
Eu	0.6	Sb	0.2
He	0.8	Sn	0.5
I	1.7	Sm	3.4
In	0.1	Sr	3.6
Kr	1.8	Tc	5.5
La	5.6	Te	3.5
Mo	21.3	Xe	23.6
Nb	0.2	Y	1.9
Nd	15.5	Zr	1.2

The numerous fission products found in the fuel have different physico-chemical properties. Kleykamp [8] proposed to gather the major ones in four classes:

- Fission gases and other volatile fission products: Kr, Xe, Br, I;
- Fission products forming metallic precipitates: Mo, Tc, Ru, Rh, Pd, Ag, Cd, In, Sn, Sb, Te;
- Fission products dissolved in the oxide fuel matrix: Ce, Nd, La, Gd, Y, Sr, Zr, Nb;
- Fission products forming secondary oxide precipitates: Rb, Cs, Ba, Zr, Nb, Mo, Te.

Therefore, fission products are found under gaseous form or/and in the fuel either dissolved in the fuel matrix or associated with other fission products in separate oxide or metallic secondary phases.

Under operating conditions, the fuel pellets are submitted to extreme thermal conditions. Indeed, as reported in **figure 1.4**, there is a very large temperature gradient (around 500 K/mm) between the pellet centre (~2000 K) and the pellet rim (~900 K). Due to this thermal gradient, mass transport of the fuel chemical elements occurs along the pellet radius. As shown in **figure 1.4**, one of the consequence is the hole formation in the pellet centre governed by a vaporisation/condensation phenomenon of uranium oxide gaseous species (mainly UO_3), as described by Guerin in the chapter 2.21 of the Comprehensive Nuclear Material [7]. This phenomenon leads to an increase of the plutonium content and a decrease of the oxygen stoichiometry in the centre of the pellet. On the contrary, the oxygen stoichiometry is higher in the pellet rim. Therefore, the plutonium, uranium and oxygen concentrations change along the pellet radius.

The fission products react differently depending on the local oxygen potential and temperature in the fuel pellet. As reported by Samuelsson *et al.* [9], the main secondary phases observed in the irradiated MOX fuels are:

- The so-called "*grey phase*" precipitates with the formula (Ba,Sr)(Zr,Mo,U,Pu)O_3 [8] [10];
- The metallic precipitates (Ru, Mo, Pd, Rh, Tc) also called Five Metals Precipitates;
- The (Pd,Te) rich precipitates.

As first reported by Tourasse *et al.* [11], due to the large thermal gradient in the fuel pellet, from a burnup of 7 at. %, mass transport of the volatile fission products towards the pellet periphery happens. It leads to the formation of the so called" Joint Oxyde-Gaine" (JOG), which is a layer between the pellet and the cladding enriched in volatile fission products. The main constituting elements are cesium, tellurium and iodine. However, palladium and Cs_2MoO_4, which have a high vapour pressure, are also found in this region, as reported by Guerin [7].

The JOG formation is a peculiarity of the MOX fuels irradiated in SFRs. However, the precise composition and structure of this JOG layer are still not well-known. Tourasse *et al.* [11] found using X-ray mapping that cesium and molybdenum are the main elements forming the JOG.

Later, thermodynamic calculations were performed by J-C Dumas [12] and Ball *et al.* [13]. The phases predicted to form in the JOG from these calculations were CsI in solid, liquid or gas state, Cs_2I_2(g), and Cs_2Te in solid and liquid forms. However, post irradiation experiments hardly showed the presence of these compounds in the JOG [7].

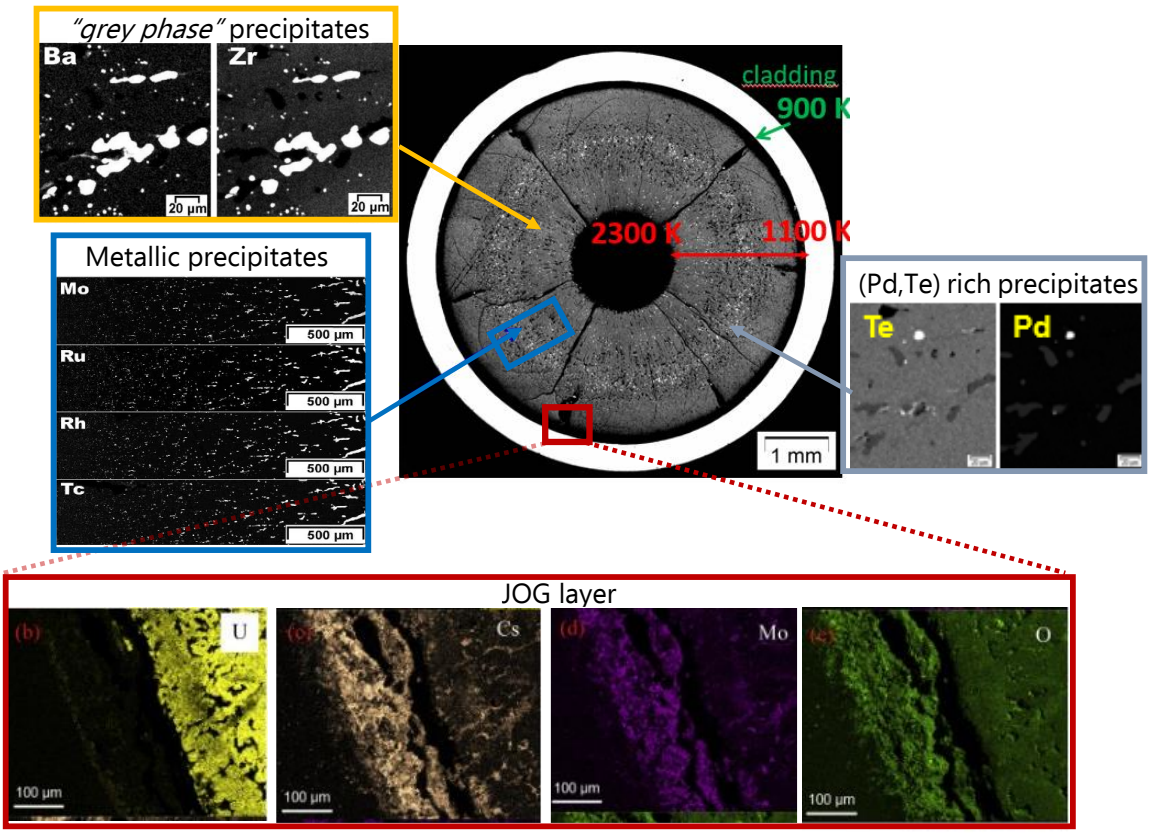

Figure 1.4: Micrograph of MOX fuel pellet irradiated at 13 at. % in the PHENIX reactor [14]. The X-ray mapping for the grey phase precipitates, metallic precipitates and (Pd,Te) precipitates are reported in Samuelsson *et al* [9]. BSE micrograph of the outer part of the pellet with qualitative EDS maps from the red dashed box taken from Cappia *et al.* [15].

In post irradiation examinations of high burnup fuels, Ba-O phases by Kleykamp [8] and $BaMoO_4$ compound by Castleman *et al.* [16] and Tête [17] were also found in the JOG.

Barium is not soluble in the fuel because of the large ionic radius of Ba^{2+} [18]. Therefore, it can react with the free oxygen released by the fission of uranium leading to the formation of Ba-O phases. Due to the high vapour pressure of BaO, this phase can also precipitate in the cold regions of the pellet near the JOG or in the "*grey phase*" [8].

Barrachin *et al* [19] reported that $BaMoO_4$ is the most stable barium compound under the normal temperature and oxygen potential conditions suggesting that the barium in the JOG should be under $BaMoO_4$ form. The formation of $BaMoO_4$ is also a result of the β decay of cesium in Cs_2MoO_4 as described by Tête [17]. However very recently, experiments on SIMFUELS (UO_2 samples doped with fission products simulating the irradiated fuel) performed by Geiger *et al* [20] have evidenced three different Mo/Ba ratios (1.2 ; 7 ; 8.4) in barium molybdates precipitates. Therefore, the interaction between barium, molybdenum and oxygen is much more complex than the thermodynamic estimations predicting the formation of $BaMoO_4$ as reported in the literature and described within the different analytical research programs PHEBUS FP, HI/VI, VEGA, VERCORS, etc [21].

In studies on corrosion of the steel cladding [8,17], other compounds have been reported to exist such as Cs_2TeO_3, $CrMoO_4$, $NiTeO_3$, barium oxitellurides or cesium-barium oxitelluride, forming in the gap between the blanket and the corroded steel cladding. Nevertheless, the mechanisms leading to their formation are not yet known.

Recently, the JOG composition has been reinvestigated by Cappia *et al.* [15] using EDS measurements. Cesium, molybdenum, tellurium, iodine and barium were found as major elements in the JOG, which is consistent with the previous studies. The Cs_2MoO_4 structure was identified by XRD for the first time and was reported as the main phase forming the JOG layer.

Finally, Samuelsson *et al.* [22] calculated the evolution of the JOG composition and thickness in irradiated MOX fuels as a function of burnup by coupling thermodynamic calculations with the fuel performance code GERMINAL. Both the TAF-ID [23] and TBASE databases were used for the thermodynamic calculations. From the calculations using the TAF-ID database, as all solution phases are described, a complex mixture of many different solid, liquid and gas phases is predicted to form.

Thus, the JOG chemistry is very complex and depends on the oxygen potential, temperature and burn-up. Up to now, only a few experimental quantitative results on the JOG composition are available and fission product compounds are mainly predicted by thermodynamic calculations.

In **figure 1.5**, a non-exhaustive summary of the main phases found in the JOG is proposed.

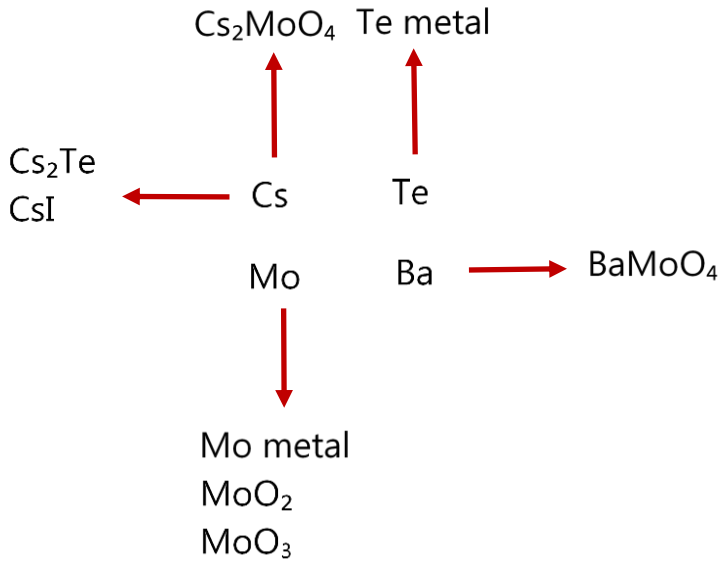

Figure 1.5: Summary of the main possible phases forming the JOG layer

1.1.3. Severe accident conditions

In this section, the phenomenology of severe accidents is introduced. From the different scenarii leading to a severe accident, the stages where a reaction between the irradiated fuel and sodium could occur are identified. Finally, the key chemical systems selected in this work to study the interaction between the irradiated fuel and sodium are listed.

1.1.3.1 Severe Accident scenarii

During a severe accident, the reactor fuel is damaged with a more or less extensive melting of the reactor core [24], which might lead to radioactive product release in the atmosphere. Even if this accident is highly unlikely happening, the impact on population and environment has to be assessed.

Two time scales can be defined in a severe accident [25]:

- The short term phase where the mechanical energy generation control is the key issue not to face a rupture of the confinement. The identification, control and understanding of the phenomena leading to mechanical energy release (void effect, recompaction, secondary phase recriticality) are the main issues under investigation.
- The long term phase where the relocation and cooling of the radioactive compounds formed after solidification are essential to lower the risks of recriticality and breach in the containment at the bottom part of the reactor.

Different initiating events might lead to a severe accident. The detailed scenarii together with every major event characteristic time in the three severe accident cases reported in the literature [25,26] are shown in **figure 1.7** (end of section 1.1.3.1):

- **UTOP**: Unprotected Transient Over Power

The initiating event is the inadvertent control rod withdrawal without backup control rod drop. The withdrawal of the control rod inserts reactivity in the reactor core leading to a linear power increase and partial fuel melting inside the fuel pins in the subassemblies. A cavity filled with molten fuel and fission gases forms. In case of clad failure, molten fuel ejection might happen [26].

- **TIB:** Total Instantaneous Inlet Blockage

In case of ingress of external material into the fuel pin bundle, a local blockage can occur. A part (or a whole) assembly is not cooled down anymore. Due to the very fast boiling of sodium (some seconds), the accident cannot be immediately detected and therefore the reactor is not shutdown. This leads to pin failure and possibly melting and degradation of the subassembly and propagation to other subassemblies.

- **ULOF**: Unprotected Loss of Flow

In the ULOF scenario, the heat removal from the primary coolant system is not high enough leading to a decrease of the sodium flow in the primary coolant system and a rise in the temperature inside the fuel pins [27].

All these scenarii may happen in a very short time however, four different steps can always be distinguished [25]:

- The "**Primary phase**" where the materials move predominantly in the axial direction. It begins with the degradation of the fuel pins and ends at the first break of hexagonal tubes (HT)
- The "**Transition phase**" where the hexagonal tubes melt or lose their mechanical integrity. Because of this loss of integrity, a transition occurs between the axial relocation and the radial propagation of the damaged materials.
- The "**Secondary phase**" in which large pools of molten materials are formed where re-criticality events can occur.
- The "**Post-Accidental cooling phase**" during which a large part of the core material inventory cools down on the core catcher.

Severe accidents generally induce a sharp rise in the pressure and the temperature in the cover gas space above the sodium pool of the primary coolant system leading to possible leakage of the primary coolant system which:

- creates a risk of sodium fire
- a possible transfer of fuel fission products and aerosols to the containment or to the cover gas circuit as described in **figure 1.6.**

Indeed, when the cladding is not tight anymore (either because of a breach or melting event), fission gases are released from the fuel pin. They leave the local accidental area and are either trapped in the sodium pool or mixed with sodium gas. In case of mixing with sodium gas, the gaseous mixture will recondense on the cold parts of the reactor [36] leading to an interaction between fission gases and sodium.

The radiological consequences have to be precisely assessed by determining the possible fission products and/or actinides compounds that can be transferred from the core to the primary cooling system.

Therefore, the nature, amount and composition of the phases (in gas, liquid and solid states) have to be known at each stage of a severe accident but also after the Post-Accidental cooling stage.

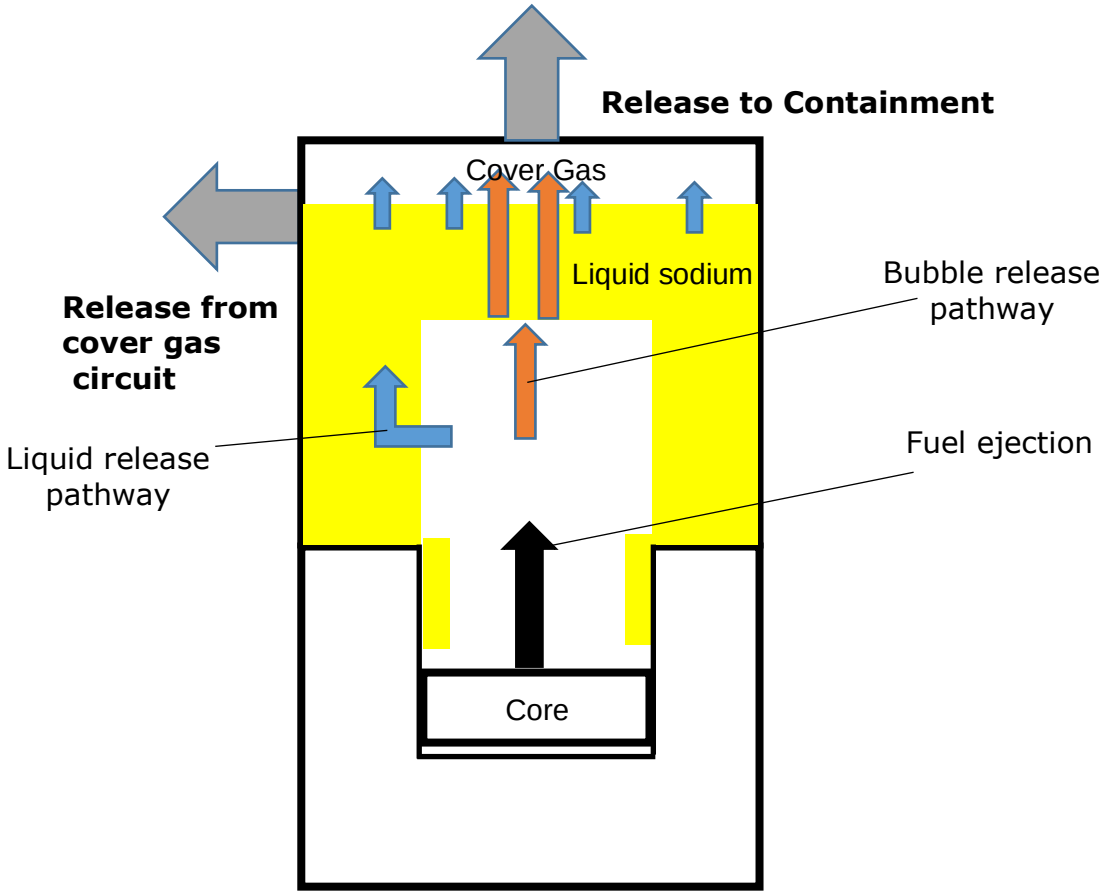

Figure 1.6: Aerosol transport and evaporation of liquid after severe accident leading to a leakage of the first barrier containment [28]

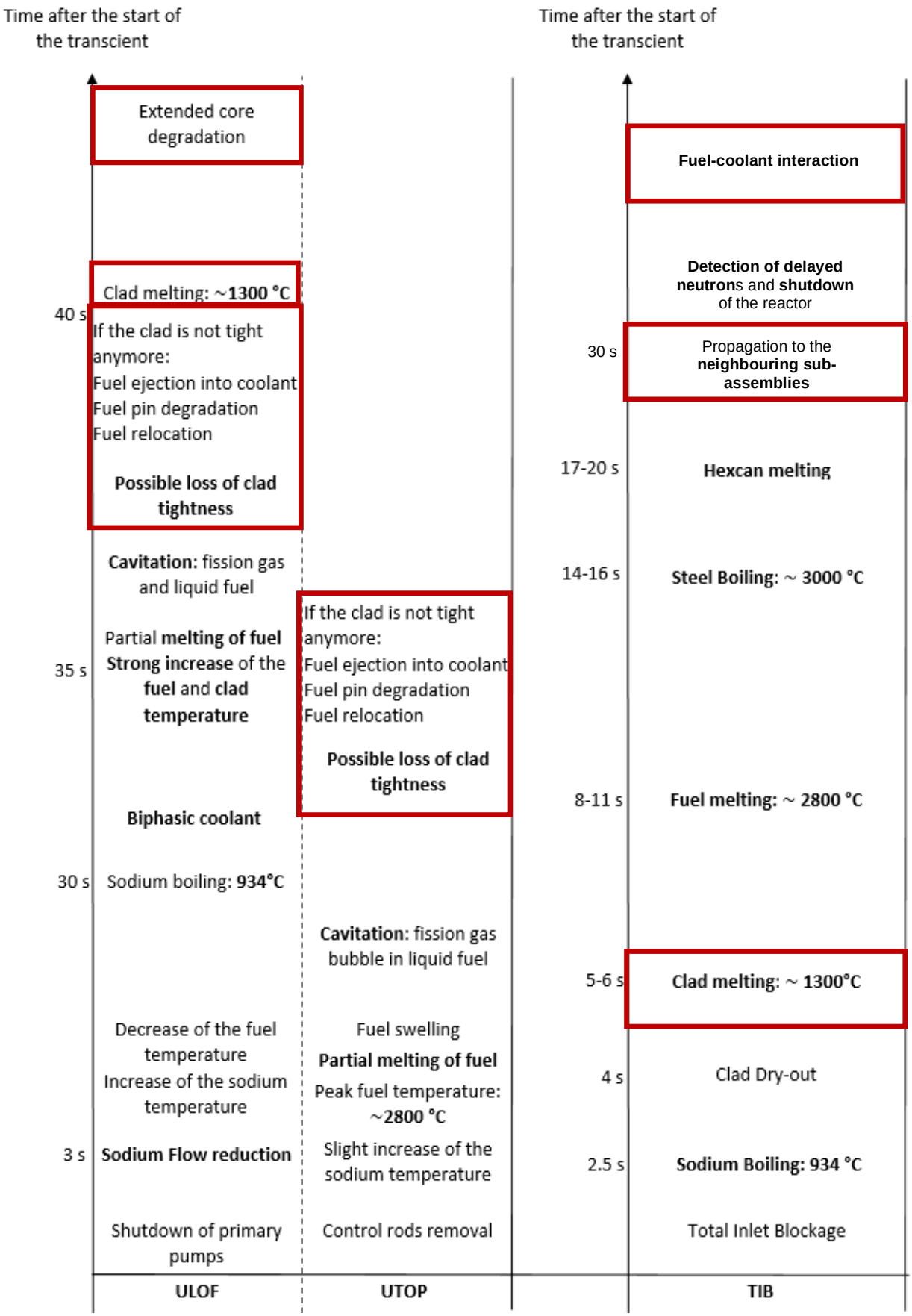

Figure 1.7: Description of the stages for the three types of severe accidents. The events leading to sodium/irradiated fuel interaction are highlighted in red [26] [29]

1.1.3.2 Fuel-sodium interaction in severe accidents

To model the evolution of the fuel pin under severe accidents, a mechanistic calculation code called SIMMER [30] and fast-running calculation tools [31–33] (compared with SIMMER) are developed. However, in this mechanistic approach, the chemistry of the fuel and the resulting interaction products with sodium, possibly formed, are not yet taken into account. To improve the models in these codes, a more accurate description of the phases forming at the different stages of the accident, is required.

In this section, the experimental campaigns CABRI and SCARABEE are shortly reviewed to identify the cases in which a reaction between the irradiated fuel and sodium could occur.

The conditions in which the fuel could interact with sodium are summarised in **table 1.3** and are discussed in the following section.

Table 1.3: Summary of the interaction conditions between irradiated fuel and sodium

Accident	Sodium		MOX		Volatile fission products	
	Chemical state	Temperature (K)	Chemical state	Temperature (K)	Chemical state	Localisation
ULOF-fuel ejection	Liquid/Gas	T~1200	Liquid	T>3100	Gas Liquid/solid	Cover gas plenum Cold parts reactor
UTOP-fuel ejection	Liquid	670>T>820	Liquid	T>3100	Gas	Cover gas plenum
					Liquid/solid	- Cold parts reactor - Liquid sodium
UTOP-fuel ejection- low enthalpy fuel	Liquid	670>T>820	Liquid/Solid	<3100	Gas	Cover gas plenum
					Liquid/solid	- Cold parts reactor - JOG compounds in liquid sodium
TIB-two pools-propagation to other subassemblies	Liquid/Gas	T>1200	Liquid	>3100	Gas Liquid/solid	Cover gas plenum Cold parts reactor

The CABRI experiments: ULOF and UTOP severe accident cases

To investigate experimentally the phenomenology of fuel materials degradation modes under severe accident conditions, extensive experimental campaigns were performed in the CABRI facility over the period 1973-2001. Many results were collected, especially during fuel transient and post-failure stages, as reported in the chapter 2.24 of the Comprehensive Nuclear Materials written by Papin in 2012 [26].

A short summary of the results on the interactions between sodium and irradiated fuel is presented hereafter to understand: (i) where the interaction takes place, (ii) which materials interact with sodium and (iii) the physico-chemical reaction conditions.

ULOF and UTOP scenarii are considered at the same time, as the main cause of the interaction between the fuel and the sodium comes from the fuel ejection into the primary sodium coolant system. In case of UTOP, this fuel ejection is due to cavity formation whereas in the ULOF case, it is due to sodium vaporisation near the cladding leading to a loss of tightness. For the interaction with sodium, the main difference is the temperature and chemical state of sodium (biphasic liquid-gas for ULOF, liquid for UTOP).

In both cases, fuel ejection might happen as reported in **figure 1.7.** The ejected fuel mostly under droplet form, interacts with liquid or biphasic sodium. Therefore, the interaction between high-temperature fuel droplets ejected from the fuel pin at $T>3100$ K and liquid sodium at $670<T<820$ K has to be investigated for UTOP [26]. In ULOF scenario, the difference comes from the biphasic state (liquid + gas) of the sodium.

This interaction leads to high temperature exchange between sodium and liquid fuel with sodium vaporisation, pressure increase and mechanical energy release. However, data on the resulting composition and structure of the formed phases are not available.

In severe accident studies, the thermodynamic quantity called "fuel enthalpy" corresponding to the pellet heat-up during an accident is often used. For low fuel enthalpy in case of UTOP scenario, the first part of the ejected fuel is the outer part of the pellet [26], enriched in fission products where the JOG layer is located. Therefore, the solid fuel is directly ejected in liquid sodium, as shown in **figure 1.8**. Therefore, the interaction between sodium, fission product compounds in the JOG layer and the solid fuel has to be investigated at temperatures under 1200 K where sodium is still liquid.

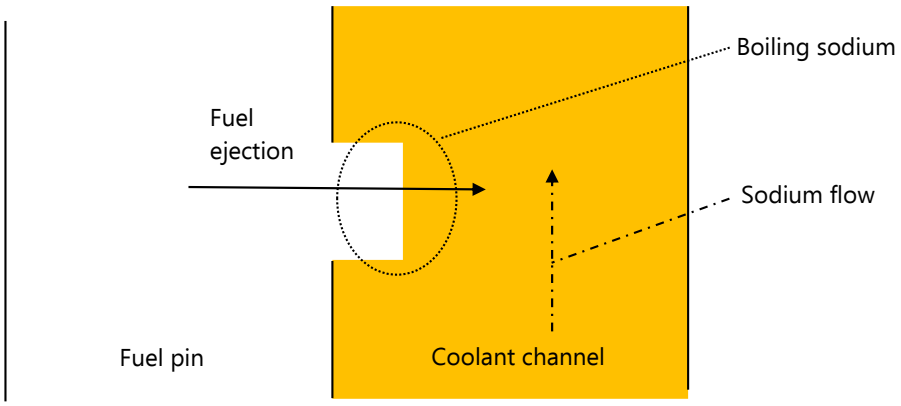

Figure 1.8: Schematic representation of fuel ejection from the fuel pin into the coolant channel.

SCARABEE program: TIB severe accident case

In the SCARABEE program (1983-1990) [34], experiments were performed to assess the phenomenology of a severe accident in case of a TIB scenario. When the cladding melts, the liquid steel drains downward the coolant channel, freezes and creates a steel blockage [35] (**figure 1.9)**. On top of this resolidified material, a liquid steel cladding pool forms that does not mix with the fuel. As the temperature is still increasing, the fuel starts to melt. Metallic fission products such as ruthenium for example, that were located in metallic precipitates in the fuel, relocate in the liquid steel pool. Finally, two pools form: one containing the cladding materials and the metallic fission products, the other one, the liquid MOX fuel. This is called the "two pools" phenomenon.

The liquid fuel pool is called "boiling pool" (**figure 1.9)** as fertile uranium that vaporizes is mixed in this pool. Steel droplets can also vaporise due to the high temperature. In this case an upper steel blockage occurs due to the relocation of partly molten material. Finally, the boiling pool containing liquid fuel will extend radially after the hexagonal tube melting and will react with sodium and other subassemblies.

As the cladding materials and the metallic fission products are unlikely reacting with sodium in severe accident conditions [35], they are not considered in the present study.

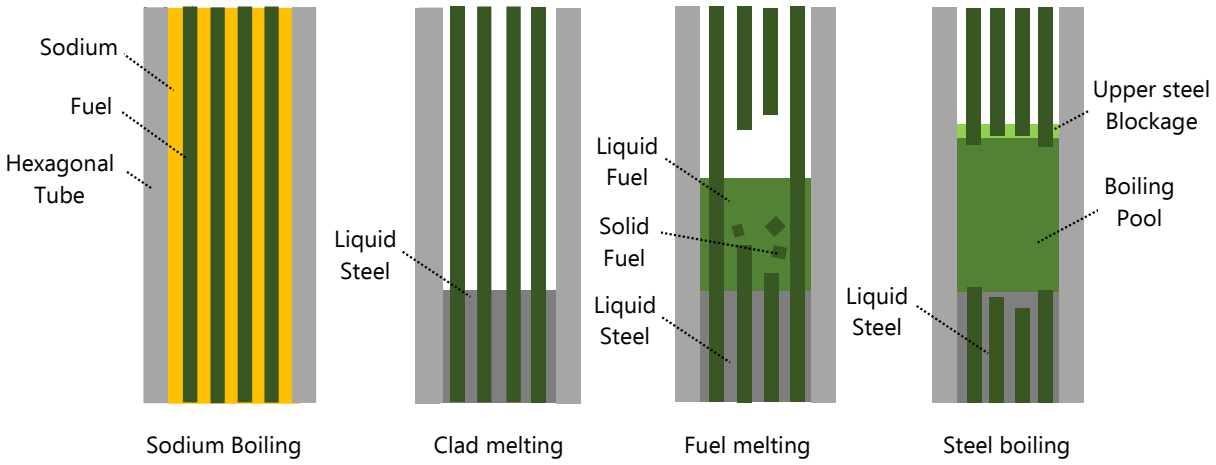

Figure 1.9: Evolution of a subassembly under a TIB scenario as described by Kayser *et al.* [34].

1.1.4. Conclusion

The chemistry of the irradiated MOX fuel under operating conditions has been described. The main phases are:

- the fuel matrix $(U,Pu,FPs)O_{2-x}$ with FPs: Ce, Nd, Gd, La ….
- the secondary fission product phases,mainly $(Ba,Sr)(Zr,Mo,U,Pu)O_3$,
- the Five Metals Particles (Mo, Ru, Pd, Rh, Tc) and (Pd,Te) rich precipitates;
- the JOG layer enriched in (Cs, I, Te, Mo, O) located in the pellet rim, mainly constituted of Cs_2MoO_4 but also of other phases still not yet well known.

The main scenarii of severe accidents have been shortly reviewed. The cases where the fuel would be in contact with the sodium are the following ones:

- Liquid oxide fuel at temperature>3100 K in contact with liquid and gas sodium at the vaporisation temperature of sodium or between 670 K and 820 K;
- Solid oxide fuel at T<3100 K in contact with liquid sodium between 670K and 820K

At lower temperature, the solid phases forming during the cooling stage of these molten materials have to be predicted for the management of the radioactive materials after the accident.

Among the fission products, the volatile ones (I, Cs, Te) are released in the cover gas or condensed on the cold parts of the vessel. Fission products forming secondary oxide phases (Ba, Sr, Mo) will generally stay in the fuel and possibly react with sodium. Metallic fission products and cladding will not be considered for this study as there is no interaction with sodium.

To conclude, the temperature and chemical composition of the systems that have to be studied to cover the different possible reactions in severe accident conditions are wide. Moreover, there is a need to predict the composition of the phases in both gas and liquid states at very high temperature and in solid state for the compounds forming at low temperature. Thus, the thermodynamic modelling of this system is required to describe such a large chemical system within a large composition and temperature range.

This computational tool shall bring more accurate physico-chemical input data on the materials involved in severe accident conditions. Moreover, this description could be further integrated in the SIMMER code to improve the modelling and prediction of the fuel pin degradation phenomena.

The TAF-ID (Thermodynamic Advanced Fuels – International Database) [23] developed in the frame of the TAF-ID joint project coordinated by the OECD/NEA allows the accurate description of the irradiated MOX fuel chemistry [9,22,23]. However, sodium is not yet implemented in the database. Thus, there is a need to extend the database with fuel-sodium systems.

1.2. Thesis outline

The aim of the thesis is to start the development of a thermodynamic database to perform calculations on the irradiated MOX fuel / sodium interaction.

Due to the large number of elements involved in the irradiated fuel, two chemical systems are selected:

- The Na-O-Pu-U system;
- The Ba-Cs-I-Mo-Na-Te-O system

To develop a thermodynamic modelling of these systems, CALPHAD (CALculation of Phase Diagram) is the most suitable method [36,37]. CALPHAD is a semi-empirical method that enables the development of a thermodynamic database containing the Gibbs energy functions of the gas, liquid and solid phases as a function of the temperature, composition and pressure. The equilibrium state of the system is then calculated by minimising the total Gibbs energy of the system, which is a linear combination of the Gibbs energies of the phases. To develop the database, adjustable parameters are optimised to fit the available experimental data (both phase diagram and thermodynamic properties). The principle is presented in **figure 1.10**.

The models are first developed for the binary, ternary and eventually quaternary sub-systems. The extrapolation from these sub-system models to higher order systems generally leads to accurate predictions. To feed the different models on binary and ternary sub-systems, experimental data on phase equilibria and thermodynamic data are needed.

The thermodynamic description is the first step in the study of the interactions under severe accident conditions but the reactions between the materials occur within a very short time. Thus, the system is probably in a non equilibrium state. Nevertheless, a good knowledge and modelling of the thermodynamic properties of such a complex chemical system is mandatory to get a better description of the chemical state of the irradiated fuel after interaction with sodium. In a second step, the kinetics of the different reactions should be further considered.

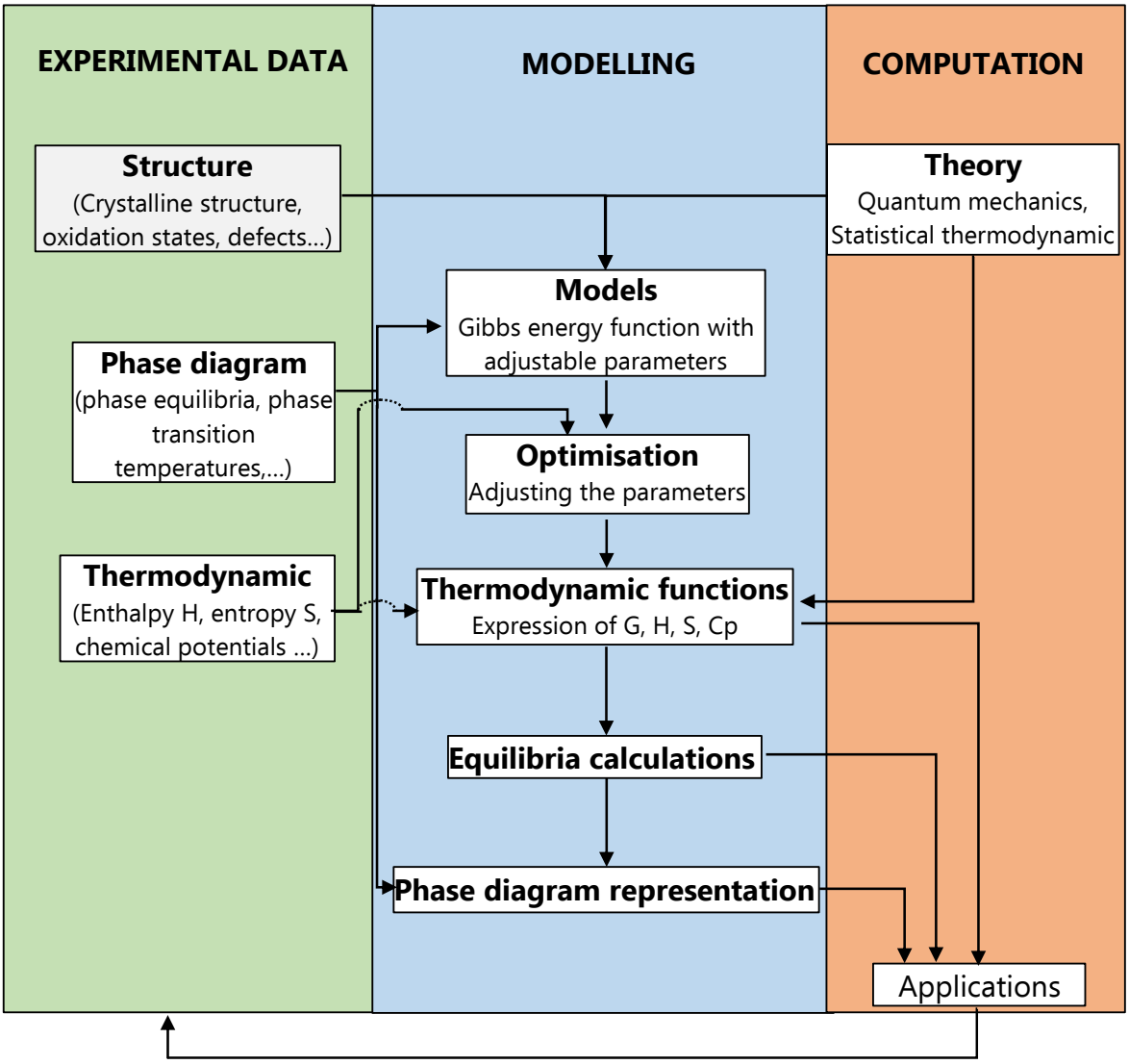

Figure 1.10: Principle of the Calphad method

In Chapter 2, a critical literature review of both the experimental data and thermodynamic models on the Na-O-Pu-U and Ba-Cs-I-Mo-Na-O-Te systems is reported. Thanks to this review, the missing experimental data and models are listed.

Then, the methodology adopted in the present work is described in Chapter 3.

In Chapter 4, the experimental results on the Na-O-Pu-U system are presented.

Then, the experimental investigations of the BaO-MoO_3-Na_2O and Cs_2O-MoO_3-Na_2O systems are reported in Chapters 5 and 6, respectively.

Finally, in Chapter 7, results on the CALPHAD modelling of sodium-fission product systems are presented.

To conclude, in Chapter 8, the experimental and modelling results obtained in this work are summarised. Their contribution to the better understanding of the chemical interaction between the irradiated MOX fuel and sodium occurring during a severe accident in SFRs is discussed together with the perspectives for further studies.

REFERENCES

[1] Le nucléaire en chiffres, EDF Fr. (2015). https://www.edf.fr/groupe-edf/espaces-dedies/l-energie-de-a-a-z/tout-sur-l-energie/produire-de-l-electricite/le-nucleaire-en-chiffres (accessed January 17, 2018).

[2] J.E. Kelly, Generation IV International Forum: A decade of progress through international cooperation, Prog. Nucl. Energy. 77 (2014) 240–246.

[3] J. GUIDEZ, B. BONIN, Réacteurs nucléaires à caloporteur sodium, CEA Saclay; Groupe Moniteur, 2014. https://hal-cea.archives-ouvertes.fr/cea-01152795 (accessed July 5, 2018).

[4] T. Beck, V. Blanc, J.-M. Escleine, D. Haubensack, M. Pelletier, M. Phelip, B. Perrin, C. Venard, Conceptual design of ASTRID fuel sub-assemblies, Nucl. Eng. Des. 315 (2017) 51–60.

[5] M. Sawada, H. Arikawa, N. Mizoo, Experiment and analysis on natural convection characteristics in the experimental fast reactor joyo, Nucl. Eng. Des. 120 (1990) 341–347.

[6] BBC - GCSE Bitesize: Nuclear fission. http://www.bbc.co.uk/schools/gcsebitesize/science/add_ocr_gateway/radiation/fissionrev2.shtml (accessed December 12, 2017).

[7] Y. Guerin, 2.21 - Fuel Performance of Fast Spectrum Oxide Fuel, in: Compr. Nucl. Mater., Elsevier, Oxford, 2012: pp. 547–578.

[8] H. Kleykamp, The chemical state of the fission products in oxide fuels, J. Nucl. Mater. 131 (1985) 221–246.

[9] K. Samuelsson, J.-C. Dumas, B. Sundman, J. Lamontagne, C. Guéneau, Simulation of the chemical state of high burnup $(U,Pu)O_2$ fuel in fast reactors based on thermodynamic calculations, J. Nucl. Mater. 532 (2020) 151969.

[10] H. Kleykamp, J.O. Paschoal, R. Pejsa, F. Thümmler, Composition and structure of fission product precipitates in irradiated oxide fuels: Correlation with phase studies in the Mo-Ru-Rh-Pd and BaO-UO_2-ZrO_2-MoO_2 Systems, J. Nucl. Mater. 130 (1985) 426–433.

[11] M. Tourasse, M. Boidron, B. Pasquet, Fission product behaviour in phenix fuel pins at high burnup, J. Nucl. Mater. 188 (1992) 49–57.

[12] J.-C. Dumas, Etude des conditions de formation du Joint-Oxyde-Gaine dans les combustibles oxydes mixtes des reacteurs à neutrons rapides, observations et proposition d'un modèle de comportement des produits de fission volatils, Institut national polytechnique de Grenoble, 1995.

[13] R.G.J Ball, W.G. Burns, J. Henshaw, M.A. Mignanelli, P.E. Potter, The chemical constitution of the fuel-clad gap in oxide fuel pins for nuclear reactors, J. Nucl. Mater. (1989) 191–204.

[14] J. Lamontagne, State-of-the-Art and Challenges for Post-Irradiation Examinations. In Proceedings of the Nuclear Materials Conference (NuMat 2014), Clearwater Beach, FL, October 27–30, 2014.

[15] F. Cappia, B.D. Miller, J.A. Aguiar, L. He, D.J. Murray, B.J. Frickey, J.D. Stanek, J.M. Harp, Electron microscopy characterization of fast reactor MOX Joint Oxyde-Gaine (JOG), J. Nucl. Mater. 531 (2020) 151964.

[16] A.W. Castleman Jr, I.N. Tang, R.A. Mackay, Fission Product Behavior In Sodium Systems., Brookhaven National Lab., Upton, NY, 1966.

[17] F. Tête, La réaction Cs_2MoO_4/ Na : Application à l'intéraction combustible / sodium lors d'une rupture de gaine à fort taux de combustion dans un RNR, Université de Provence, 1999.

[18] T.N. Pham Thi, Caractérisation et modélisation du comportement thermodynamique du combustible RNR-Na sous irradiation, 2014.
[19] M. Barrachin, D. Gavillet, R. Dubourg, A. De Bremaecker, Fuel and fission product behaviour in early phases of a severe accident. Part I: Experimental results of the PHEBUS FPT2 test, J. Nucl. Mater. 453 (2014) 340–354.
[20] E. Geiger, R. Bès, P. Martin, Y. Pontillon, P.L. Solari, M. Salome, Fission products behaviour in UO_2 submitted to nuclear severe accident conditions, J. Phys. Conf. Ser. 712 (n.d.).
[21] B.J. Lewis, R. Dickson, F.C. Iglesias, G. Ducros, T. Kudo, Overview of experimental programs on core melt progression and fission product release behaviour, J. Nucl. Mater. 380 (2008) 126–143.
[22] K. Samuelsson, J.-C. Dumas, B. Sundman, M. Lainet, An improved method to evaluate the "Joint Oxyde-Gaine" formation in $(U,Pu)O_2$ irradiated fuels using the GERMINAL V2 code coupled to Calphad thermodynamic computations, EPJ Nucl. Sci. Technol. 6 (2020) 47.
[23] NEA Nuclear Science Committee, Thermodynamics of Advanced Fuels - International Database (TAF-ID), https://www.oecd-nea.org/science/tafid/.
[24] IRSN, La gestion des accidents graves, (2018).
http://www.irsn.fr/FR/connaissances/Installations_nucleaires/Les-centrales-nucleaires/accidents-graves/Pages/sommaire.aspx#.WythBqczbb0.
[25] F. Bertrand, N. Marie, A. Bachrata, V. Brun-Magaud, J.B. Droin, X. Manchon, K. Herbreteau, B. Farges, B. Carluec, S. Poumerouly, D. Lemasson, Status of severe accident studies at the end of the conceptual design of ASTRID: Feedback on mitigation features, Nucl. Eng. Des. 326 (2018) 55–64.
[26] J. Papin, Behavior of Fast Reactor Fuel During Transient and Accident Conditions, in: Compr. Nucl. Mater., Elsevier, 2012: pp. 609–634.
[27] T. Suzuki, Y. Tobita, K. Kawada, H. Tagami, J. Sogabe, K. Matsuba, K. Ito, H. Ohshima, A preliminary evaluation of unprotected loss-of-flow accident for a prototype fast-breeder reactor, Nucl. Eng. Technol. 47 (2015) 240–252.
[28] IRSN presentation, Consultancy meeting on the preparation of the proposal of the CRP about Source term estimation for radioactivity release under severe accident scenario in SFRs IRSN point of view., (2014).
[29] A. Lazaro, M. Schikorr, K. Mikityuk, L. Ammirabile, G. Bandini, G. Darmet, D. Schmitt, Ph. Dufour, A. Tosello, E. Gallego, G. Jimenez, E. Bubelis, A. Ponomarev, R. Kruessmann, D. Struwe, M. Stempniewicz, Code assessment and modelling for Design Basis Accident analysis of the European Sodium Fast Reactor design. Part II: Optimised core and representative transients analysis, Nucl. Eng. Des. 277 (2014) 265–276.
[30] H. Yamano, S. Fujita, Y. Tobita, I. Sato, H. Niwa, Development of a three-dimensional CDA analysis code: SIMMER-IV and its first application to reactor case, Nucl. Eng. Des. 238 (2008) 66–73.
[31] N. Marie, A. Bachrata, J.M. Seiler, F. Barjot, A. Marrel, S. Gossé, F. Bertrand, A physical tool for severe accident mitigation studies, Nucl. Eng. Des. 309 (2016) 224–235.
[32] N. Marie, A. Marrel, J.M. Seiler, F. Bertrand, Physico-statistical approach to assess the core damage variability due to a total instantaneous blockage of SFR fuel sub-assembly, Nucl. Eng. Des. 297 (2016) 343–353.
[33] J.-B. Droin, N. Marie, A. Bachrata, F. Bertrand, E. Merle, J.-M. Seiler, Physical tool for Unprotected Loss Of Flow transient simulations in a Sodium Fast Reactor, Ann. Nucl. Energy. 106 (2017) 195–210.

[34] G. Kayser, J. Charpenel, C. Jamond, Summary of the SCARABEE-N Subassembly Melting and Propagation Tests with an Application to a Hypothetical Total Instantaneous Blockage in a Reactor, Nucl. Sci. Eng. 128 (1998) 144–185.
[35] H. Steiner, Fuel behaviour under severe accident conditions: Interpretation of PTE results from the CABRI test programme, J. Nucl. Mater. 188 (1992) 146–153.
[36] H.L. Lukas, S.G. Fries, B. Sundman, Computational thermodynamics: the CALPHAD method, Cambridge University Press, Cambridge ; New York, 2007.
[37] C. Guéneau, A. Chartier, L. Van Brutzel, 2.02 - Thermodynamic and Thermophysical Properties of the Actinide Oxides, in: R.J.M. Konings (Ed.), Compr. Nucl. Mater., Elsevier, Oxford, 2012: pp. 21–59.

CHAPTER 2: LITERATURE REVIEW

As mentioned in Chapter 1, during a severe accident, sodium and irradiated fuel could interact at different stages of the accident on a wide composition and temperature range. However, only data on the sodium / MOX fuel reaction under operating conditions are available in the literature and very limited information on the sodium / fission product interaction exist. In this chapter, these data are reviewed. Then, the state of the art on the phase diagram data and models of the chemical systems Na-O-Pu-U and Na-(Ba-Cs-I-Mo-O-Te) is presented.

In section 2.1, the structural and thermodynamic data of the ternary Na-O-U and Na-O-Pu, and quaternary Na-O-Pu-U systems are first reviewed. Then, the studies on the sodium / MOX fuel reaction under operating conditions are presented (section 2.2). In section 2.3, the possible reactions occurring in the Na-(Ba-Cs-I-Mo-O-Te) system are described. In section 2.4, the available Calphad models for the different systems are reviewed. Using the data reported in the literature review, the selected systems for experimental investigation in the present work are finally listed.

2.1. Structural and phase diagram study in the Na-O-Pu-U system

To understand the different phases, which could form in the quaternary system (Na-O-Pu-U), the ternary sub-systems (Na-O-U, Na-O-Pu) are first described. Finally, the phases existing in both ternary and quaternary systems are compared.

2.1.1. The Na-O-U ternary system

Three main studies made by Blackburn [1], Pillon [2] and Smith [3] on the Na-O-U phase diagram are available in the literature. The compounds investigated in these studies are reported in **figure 2.1** and their crystallographic data are summarised in **table 2.1**.

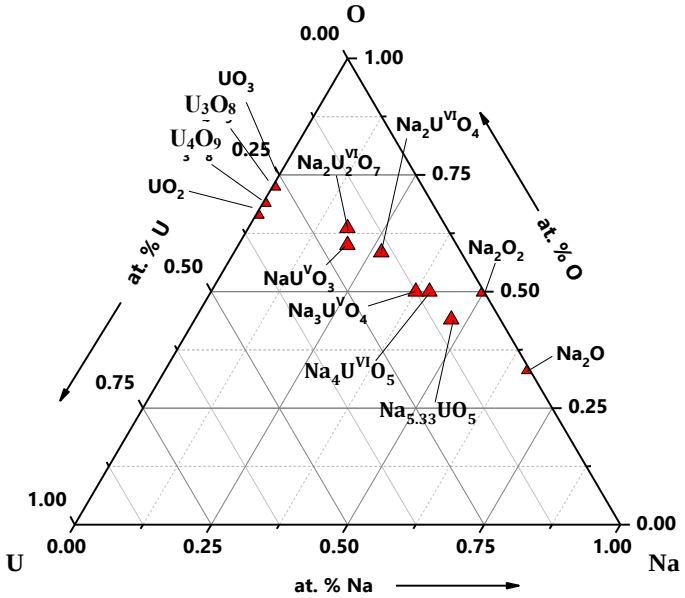

Figure 2.1: Sketch of the Na-O-U ternary phase diagram.

In 1974, the first study of the Na-O-U phase diagram was performed by Blackburn [1]. Sodium and oxygen pressures over the Na-O-U system were measured using mass spectrometry. Moreover, the samples after experiment were analysed by XRD. Using these results, Blackburn [1] proposed the first version of the Na-O-U phase diagram with the existence of five ternary compounds. The phase boundaries at 900 K and 1 bar (black dashed lines) are shown in **figure 2.2**. Three-phase equilibria between $U^{IV}O_2$-$NaU^{V}O_3$-$Na_3U^{V}O_4$ and $NaU^{V}O_3$-$Na_3U^{V}O_4$-$Na_4U^{VI}O_5$ were suggested by Blackburn [1].

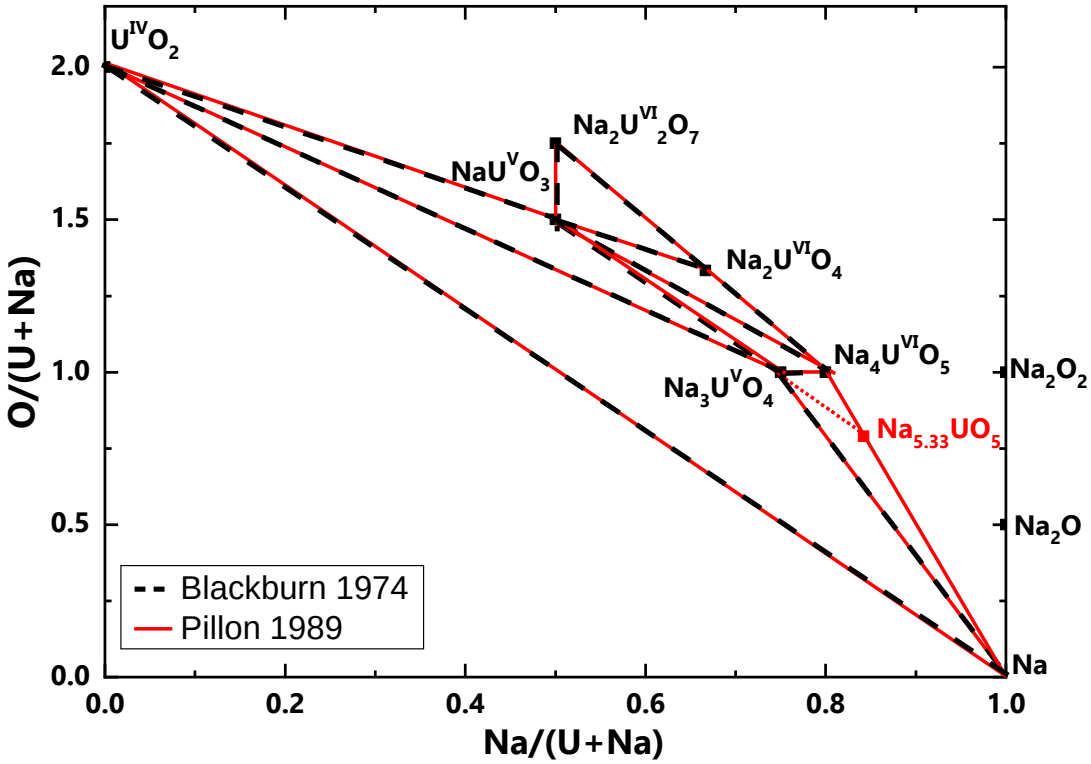

Figure 2.2: Na-O-U phase diagram at 900 K and 1 bar reported by Pillon [2] (red lines), and comparison with the phase boundaries between the ternary phase fields suggested by Backburn [1] (black dashed line).

Later, Pillon [2] extensively studied the Na-O-U phase diagram by solid state synthesis XRD, neutron diffraction and micro-calorimetry analyses. The author reported the same phase equilibria as Blackburn [1]. However, one additional phase $Na_{5.33}UO_5$ was observed in the investigation of the equilibrium between $Na_4U^{VI}O_5$ and Na. The compound exhibits an allotropic transition at ~573 K. Both phases have a tetragonal symmetry with cell parameters reported in **table 2.1.** Nevertheless, the author did not determine the space group of the compounds nor the phase equilibria involving this compound. Finally, the most probable phase equilibria involving the $Na_{5.33}UO_5$ phase were proposed by Pillon [2] (red lines) as reported in **figure 2.2**.

In this study, Pillon also reported the existence of a composition range for the $Na_3U^{V}O_4$ phase. It is represented in **figure 2.3** between the theoretical "Na_2UO_3" (the compound

does not exist) and $Na_4U^{VI}O_5$ along the O/(U+Na)=1 composition line. Nevertheless, the extent of the stability composition range of this phase was not determined.

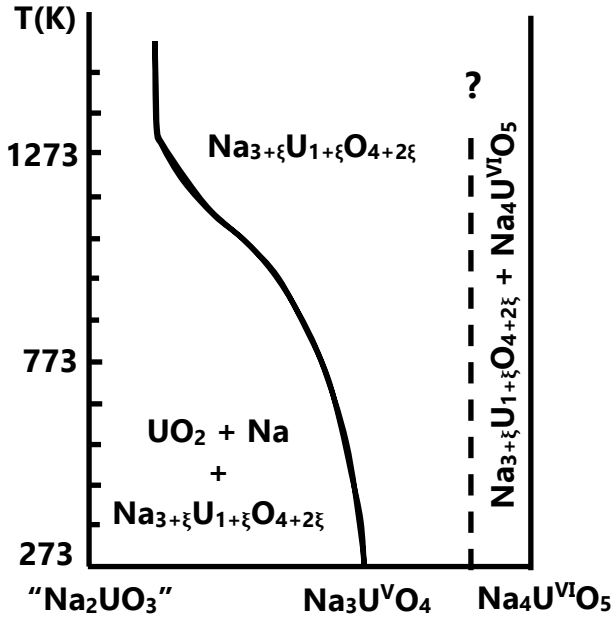

Figure 2.3: Na-O-U phase diagram section between the theoretical composition "Na_2UO_3" and $Na_4U^{VI}O_5$ along the O/(U+Na)=1 composition line [2]

More recently, the ternary system Na-O-U was re-investigated by Smith [3] using solid state synthesis and several techniques such as XRD, neutron diffraction, X-ray Absorption Spectroscopy, ^{23}Na NMR, Knudsen effusion mass loss (KEML) and Knudsen Effusion Mass Spectrometry (KEMS). The author found the same compounds as Blackburn [1], with oxidation states corresponding to the theoretical ones (see **figure 2.4**), as reported in Smith *et al.* [4]. However, the cubic compound formed with cell parameters close to those of $Na_3U^VO_4$ was analysed with HR-XANES to confirm the oxidation state of uranium. Instead of U^V expected from the theoretical formula, the author observed U^{VI} and finally attributed the phase synthesised in their work to the cubic metastable $Na_4U^{VI}O_5$ compound.

The other attempt to synthesise the $Na_3U^VO_4$ compound by Smith [3] lead to the formation of a monoclinic $Na_{3.16}U_{0.84}O_4$ compound with a mixed oxidation state of U^{VI}/U^V and cationic disorder on the uranium site due to sodium insertion highlighted in blue in **figure 2.4**. Therefore the compound has been attributed to $Na_3(U,Na)O_4$ [5]. These results give some insights on the solid solution structure reported by Pillon [2]. Nevertheless, the sodium solubility limit in the compound could not be determined and the $Na_3U^VO_4$ compound could not be synthesised as one single phase. Therefore, more experiments are needed to further assess this section of the phase diagram.

Thermodynamic data for all compounds were measured and are reported in the review by Smith *et al.* [6]. Only the data for $Na_3U^VO_4$ (O'Hare *et al.* [7]) were not measured on

a pure batch (containing 2±1.8 wt% of unreacted UO_2). The uranium oxidation state was not assessed in the work of O'Hare *et al.* [7], however, the sample composition was checked by five different methods. Therefore, as the chemical composition of the batch was precisely assessed, the thermodynamic data of $Na_3U^VO_4$ could be estimated and were used in the assessment of Smith *et al.* [6].

Finally, thermodynamic data have also been calculated by DFT (Density Functional Theory) [6]. Based on both experimental measurements and DFT calculations of the thermodynamic data in the Na-O-U system, a Calphad model was developed by Smith *et al.* [6] and is reported in **figure 2.4**. On the same figure the phase equilibria determined by Blackburn [1] are also reported. There is a good agreement between the calculated and experimental phase fields. Nevertheless, one difference can be noted. Blackburn [1], but also Pillon [2], suggested three-phase equilibria between $U^{IV}O_2$-NaU^VO_3-$Na_3U^VO_4$ and NaU^VO_3-$Na_3U^VO_4$-$Na_4U^{VI}O_5$ whereas the calculations of Smith *et al.* [6] predict three-phase equilibria between $U^{IV}O_2$-NaU^VO_3-$Na_4U^{VI}O_5$ and $U^{IV}O_2$-$Na_3U^VO_4$-$Na_4U^{VI}O_5$. These phase equilibria should be carefully investigated by performing long thermal treatments, quenching and XRD analyses to solve the discrepancy between the two phase diagrams. Moreover, the composition range around $Na_3U^VO_4$ has to be further investigated to improve the Na-O-U Calphad model if needed.

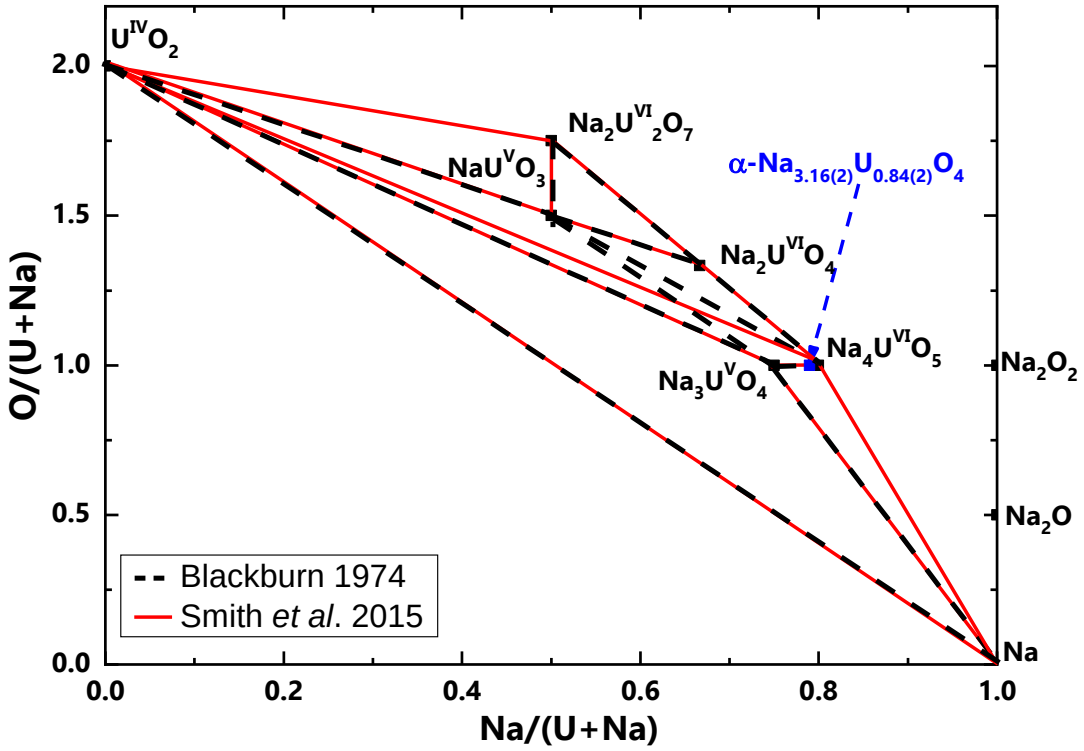

Figure 2.4: Calculated Na-O-U phase diagram at 900 K and 1 bar by Smith et al [6] (red line), and comparison with the phase equilibria suggested by Blackburn [1] (black dotted line).

To conclude, the structural and thermodynamic data of the phases in the Na-O-U system are well known, except for the $Na_3U^VO_4$ compound. Moreover, the structure and the composition range around this compound are not yet well characterised. The different studies reported in the literature on the Na-O-U phase diagram are in good agreement except for two phase equilibria where $Na_3U^VO_4$ is involved. In order to improve the Calphad model on the Na-O-U system, the synthesis of a pure batch of $Na_3U^VO_4$ is needed. Data on the uranium oxidation state and thermodynamic data of this compound would also be useful to assess the different phase equilibria involving $Na_3U^VO_4$. Nevertheless, the Na-O-U system is not further investigated in this work, as it appears from the literature review that synthesising a pure batch of $Na_3U^VO_4$ is extremely challenging.

Phase	Oxidation state U	Sym.	Z	Space group	a/Å	b/Å	c/ Å	β/°	Vol./ Å^3	T/K	Ref.
α-$Na_{5.33}UO_5$	4/5	Tetra.			5.26	5.26	12.57	90	348	RT	[2]
β -$Na_{5.33}UO_5$	4/5	Tetra.			5.86	5.86	5.49	90	189	923	[2]
NaU^VO_3	5	Ortho.	4	*Pbnm* (62)	5.7739[a]	5.9051[a]	8.2784[a]	90	282.26[a]	RT	[8]
					5.8321	5.9742	8.3699	90	291.87	0 (DFT)	[6]
m-$Na_3U^VO_4$	5	Cubic	1	*Fm*$\bar{3}$*m* (225)	4.77[b]	4.77[b]	4.77[b]	90	108.53	RT	[9]
α-$Na_{3.16(2)}U_{0.84(2)}O_4$	5/6	Mono.	2	*P2/c* (14)	5.892[c]	6.772[c]	5.916[c]	110.65[c]	220.83[c]	RT	[5]
α-$Na_3U^VO_4$	5	Mono.	2	*P2/c* (14)	5.937	6.845	5.978	110.54	227.3	0 (DFT)	[6]
β-$Na_{3+x}U_{1-x}O_4$	5/6	Cubic	8	*Fd*$\bar{3}$*m* (227)	9.589[c]	9.589[c]	9.589[c]	90	881.91[c]	RT	[5]
β-$Na_3U^VO_4$	5	Cubic	8	*Fd*$\bar{3}$*m* (227)	9.56[d]	9.56[d]	9.56[d]	90	873.7[d]	RT	[6]
α-$Na_2U^{VI}O_4$	6	Ortho.	2	*Pbam* (55)	9.7623[e]	5.7287[e]	3.4956[e]	90	195.496[e]	RT	[10]
					10.0103	5.7628	3.5236	90	203.352	0 (DFT)	[6]
β-$Na_2U^{VI}O_4$	6	Ortho.	4	*Pbca* (61)	5.8079[f]	5.9753[f]	11.7179[f]	90	406.650[f]	RT	[10]
					5.8598	6.0265	11.8836	90	419.514	0 (DFT)	[6]
m-$Na_4U^{VI}O_5$	6	Cubic	1	*Fm*$\bar{3}$*m* (225)	4.764[g]	4.764[g]	4.764[g]	90	108.12[g]	RT	[5]
$Na_4U^{VI}O_5$	6	Tetra.	2	*I4/m* (87)	7.5455(3)	7.5455(3)	4.6371(3)	90	261.78[h]	RT	[2]
					7.695	7.695	4.6325	90	275.42	0 (DFT)	[6]
α-$Na_2U^{VI}_2O_7$	6	Mono.	4	*P21/a* (14)	12.7617[i]	7.8384[i]	6.8962[i]	111.285[i]	642.78[i]	293	[11]
					13.1322	7.8815	6.9292	110.994	669.18	0 (DFT)	[6]
β-$Na_2U^{VI}_2O_7$	6	Mono.	4	*C2/m* (12)	12.933[j]	7.887[j]	6.9086[j]	110.816[j]	658.80[j]	773	[11]
					13.125	7.881	6.9291	110.967	669.33	0 (DFT)	[6]
γ-$Na_2U^{VI}_2O_7$	6	Trigonal.	3/2	*R*$\bar{3}$*m* (166)	3.987[k]	3.987[k]	18.491[k]	90	254.61[k]	1323	[5]

Standard uncertainties u are [a]u(a) = 0.00002 nm, u(b) = 0.00002 nm, u(c) = 0.00002 nm, u(Vol.) = 0.00001 nm^3
Standard uncertainties u are [b]u(a) = 0.002 nm, u(b) = 0.002 nm, u(c) = 0.002 nm, u(Vol.) = 0.0001 nm^3
Standard uncertainties u are [c]u(a) = 0.0002 nm, u(b) = 0.0002 nm, u(c) = 0.0002 nm, u(β) = 0.02, u(Vol.) = 0.00001 nm^3
Standard uncertainties u are [d]u(a) = 0.004 nm, u(b) = 0.004 nm, u(c) = 0.004 nm, u(Vol.) = 0.0001 nm^3
Standard uncertainties u are [e]u(a) = 0.00003 nm, u(b) = 0.00002 nm, u(c) = 0.00001 nm, u(Vol.) = 0.000011 nm^3
Standard uncertainties u are [f]u(a) = 0.00003 nm, u(b) = 0.00003 nm, u(c) = 0.00006 nm, u(Vol.) = 0.000034 nm^3
Standard uncertainties u are [g]u(a) = 0.0003 nm, u(b) = 0.0003 nm, u(c) = 0.0003 nm, u(Vol.) = 0.00001 nm^3
Standard uncertainties u are [h]u(a) = 0.00001 nm, u(b) = 0.00001 nm, u(c) = 0.00002 nm, u(Vol.) = 0.00001 nm^3
Standard uncertainties u are [i]u(a) = 0.000014 nm, u(b) = 0.000010 nm, u(c) = 0.00009 nm, u(β) = 0.009, u(Vol.) = 0.00010 nm^3
Standard uncertainties u are [j]u(a) = 0.0001 nm, u(b) = 0.0001 nm, u(c) = 0.00008 nm, u(β) = 0.010, u(Vol.) = 0.00013 nm^3
Standard uncertainties u are [k]u(a) = 0.0003 nm, u(b) = 0.0003 nm, u(c) = 0.0003 nm, u(Vol.) = 0.00001 nm^3

Table 2.1: Structural parameters of the sodium uranate phases [6]

2.1.2. The Na-O-Pu ternary system

In **figure 2.5**, the numerous compounds reported in the literature for Na-O-Pu system are shown. The available structural data for these compounds are reported in **table 2.2**

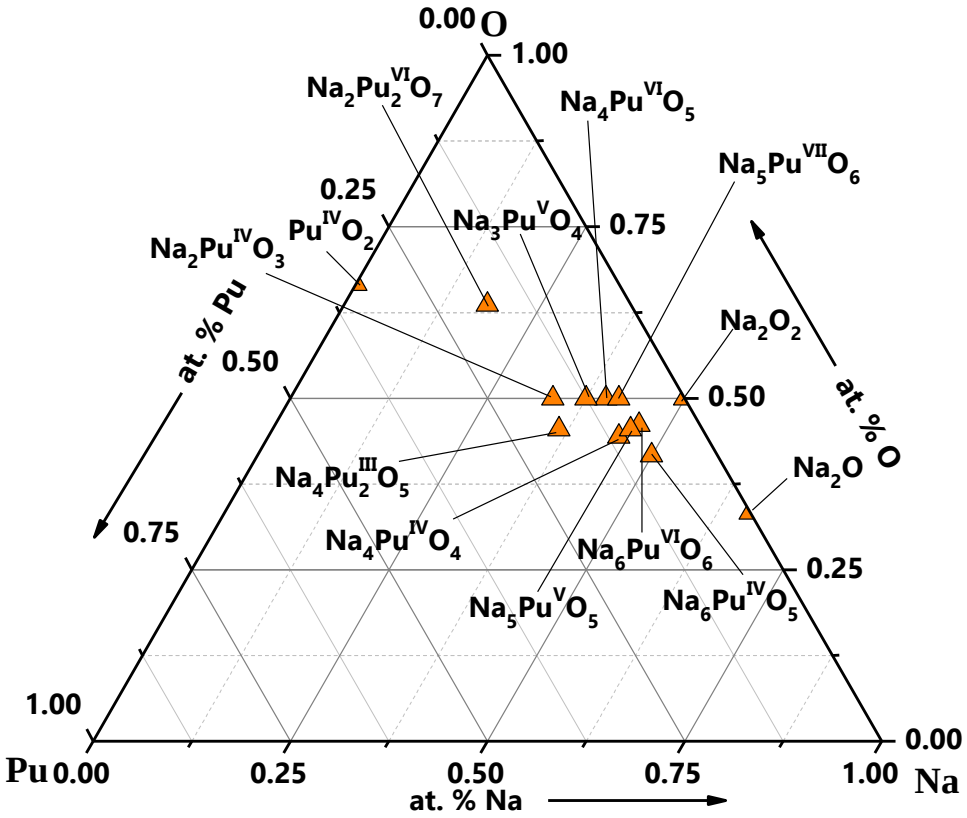

Figure 2.5: Sketch of the Na-O-Pu ternary phase diagram.

The first extensive study of the Na-O-Pu phase diagram was performed by Pillon [2]. The phase diagram was investigated by the same techniques used for the Na-O-U system. The author found the compounds $Na_4Pu^{III}_2O_5$, $Na_2Pu^{IV}O_3$, $Na_4Pu^{IV}O_4$, $Na_3Pu^{V}O_4$, $Na_4Pu^{VI}O_5$ and $Na_6Pu^{VI}O_6$. The different phase equilibria are reported in **figure 2.7** (black lines). However, no precise structural refinement was performed on the compounds.

As in the Na-O-U system, Pillon [2] reports a composition range for the $Na_3Pu^{V}O_4$ phase. However, contrary to the uranium system, no equilibrium with $Pu^{IV}O_2$ was obtained. The phase was observed in the section between $Na_2Pu^{IV}O_3$ and $Na_4Pu^{VI}O_5$ as shown in **figure 2.6**. However, the author did not investigate further the structure of the compounds and the phase boundary with $Na_4Pu^{VI}O_5$ was not determined.

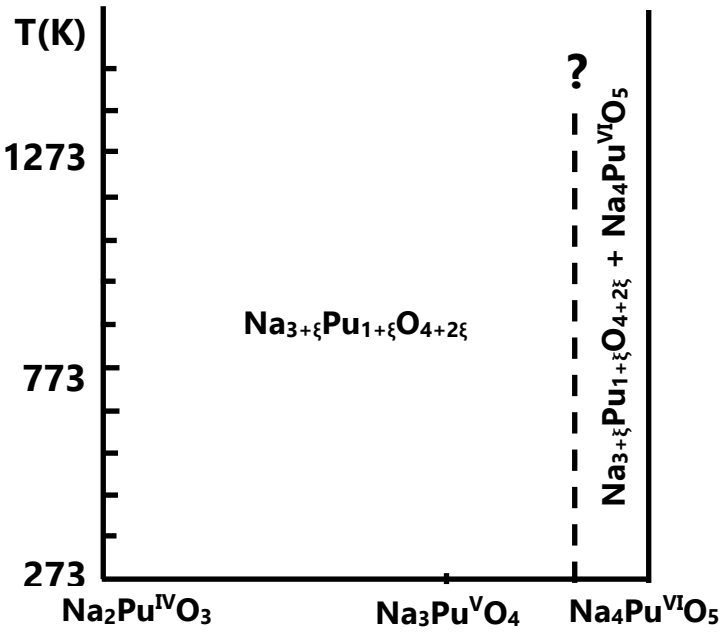

Figure 2.6: Pseudo binary phase diagram on the theoretical composition $Na_2Pu^{IV}O_3$ and $Na_4Pu^{VI}O_5$ representing the different phase fields evolution on the O/(U+Na)=1 line [2]

Pillon [2] proposed the first experimental Na-O-Pu phase diagram at 1073 K, reported in **figure 2.7**. An unknown phase (called "γ") was observed by XRD. Nevertheless, the composition and the structure of this "γ" phase were not determined by Pillon [2].

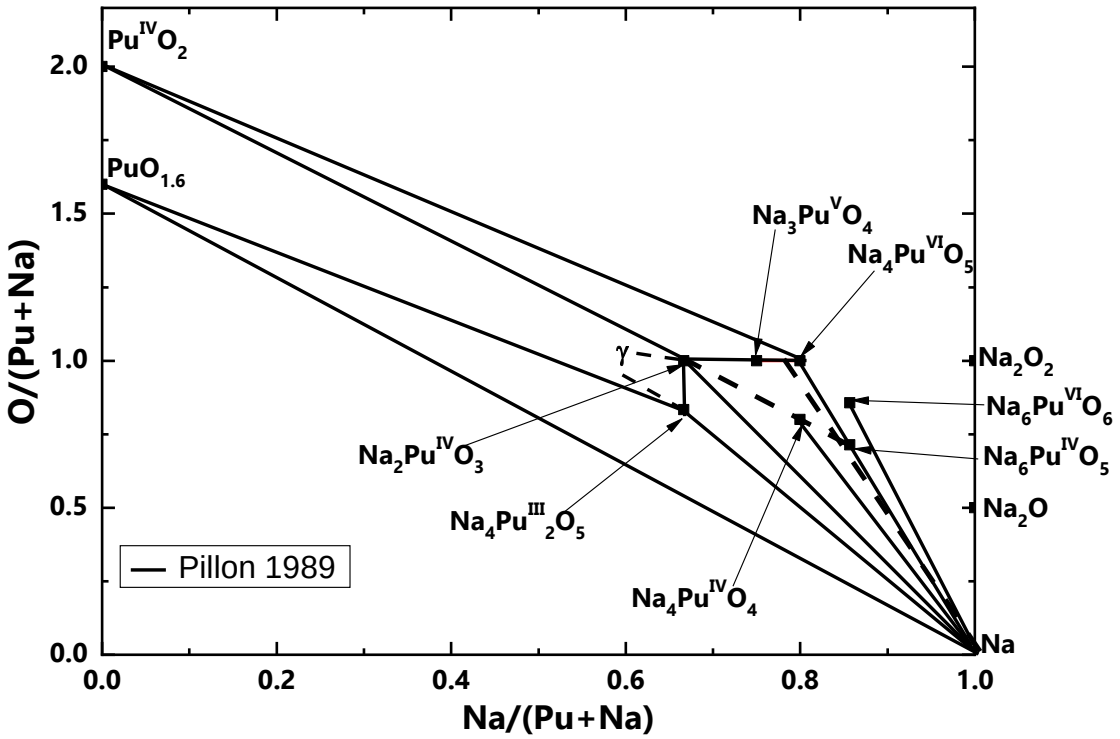

Figure 2.7: Ternary Na-O-Pu phase diagram at 1073 K obtained by Pillon in black line [2]

A peculiarity of the Na-O-Pu system is the existence of the $Na_2Pu^{IV}O_3$, $Na_3Pu^{V}O_4$ and $Na_4Pu^{VI}O_5$ compounds along the O/(Pu+Na) =1 composition line. Indeed, on a very narrow composition range, the plutonium can adopt the +IV, +V or +VI oxidation states whereas it is generally challenging to find stable solid plutonium compounds with an oxidation state over +IV. Moreover, on this section, a composition range for $Na_{3+\xi}Pu_{1+\xi}O_{4+2\xi}$ was also reported (see **figure 2.6**).

In addition, another specific feature of the Na-O-Pu phase diagram is the possibility to form stable compounds with a plutonium oxidation state under +IV such as $Na_4Pu^{III}_2O_5$ as reported by Pillon [2]. However, the structure of this compound was not reported.

To study the structure of the different compounds reported by Pillon [2], Bykov *et al.* [12], performed solid state synthesis experiments to form pure sodium plutonate phases and investigate their structure. The authors managed to synthesise the following compounds: $Na_2Pu^{IV}O_3$, $Na_5Pu^{V}O_5$, $Na_2Pu^{VI}_2O_7$, $Na_4Pu^{VI}O_5$, $Na_5Pu^{VII}O_6$. The structures of $Na_2Pu^{IV}O_3$ ($R\bar{3}m$), $Na_4Pu^{VI}O_5$ ($I4/m$) and $Na_5Pu^{VII}O_6$ ($C2/m$) were refined using XRD powder diffraction data. The $Na_5Pu^{V}O_5$ in the $C2/m$ space group was also studied by ab-initio calculations.

However, the compounds: $Na_4Pu^{III}_2O_5$, $Na_6Pu^{IV}O_5$, $Na_4Pu^{IV}O_4$, $Na_3Pu^{V}O_4$, $Na_6Pu^{VI}O_6$ reported by Pillon [2] could not be prepared by mixing Na_2O and PuO_2 in stoichiometric amounts and heating at 1000 K.

Finally, Smith [3] synthesised and studied the structure of $Na_2Pu^{IV}O_3$, $Na_3Pu^{V}O_4$, $Na_4Pu^{VI}O_5$ and $Na_5Pu^{VII}O_6$.

For the $Na_2Pu^{IV}O_3$ compound, the reflexions at low angle (~17°) on the XRD powder pattern were not well refined with the structure $R\bar{3}m$. The structure of the compound was then refined in the $C2/c$ space group using Na_2CeO_3 as starting structural model for the refinement.

Smith [3] managed to synthesise $Na_3Pu^{V}O_4$ using Na_2CO_3 as starting reagent. The structure was attributed to the orthorhombic symmetry in space group *Fmmm* (n°69) using $Na_3Np^{V}O_4$ as starting structure. The symmetry and the space group are different from the ones of $Na_3U^{V}O_4$, which is monoclinic. However, the oxidation state of the compound was not checked and no thermodynamic data were measured. For the same composition, Smith [3] also reported a disordered NaCl structure below 873 K, probably corresponding to a metastable phase.

$Na_4Pu^{VI}O_5$ was reported as tetragonal in space group $I4/m$. This compound was found isostructural to $Na_4U^{VI}O_5$. As Pu^{VI} has a lower ionic radius than U^{VI} in coordination 6, the oxygen atoms in axial direction are closer to the actinide atom in the plutonium compound and the cell parameters of $Na_4Pu^{VI}O_5$ are lower than those of $Na_4U^{VI}O_5$.

For the $Na_5Pu^{VII}O_6$, there is a good agreement between the structures reported by Bykov *et al.* [12] and Smith [3].

Finally, to determine the oxidation state of $Na_2Pu^{IV}O_3$, $Na_4Pu^{VI}O_5$ and $Na_5Pu^{VII}O_6$, XANES spectroscopy experiments at the Pu L_3-edge were performed by Smith *et al.* [4]. Plutonium was confirmed to be as Pu^{IV} in $Na_2Pu^{IV}O_3$ and Pu^{VI} in $Na_4Pu^{VI}O_5$. In $Na_5Pu^{VII}O_6$, plutonium was found as a mixture of Pu^{VI} and Pu^{VII}. Nevertheless, only a Pu^{IV} reference was used and the difference observed between the reported energies is small (0.8 eV between Pu^{IV} and Pu^{VI}). Therefore, the oxidation state of the plutonium atom in this compound needs to be precisely assessed with other techniques as discussed in Chapter 4.

Finally, Smith [3] proposed a Na-O-Pu phase diagram based on the phase equilibria in Na-O-U as presented in **figure 2.8** (red dotted lines). The phase diagram proposed by Pillon [2] was also reported for comparison. The phase equilibria from the two studies are very different. Therefore, a re-investigation of the Na-O-Pu phase diagram has to be performed.

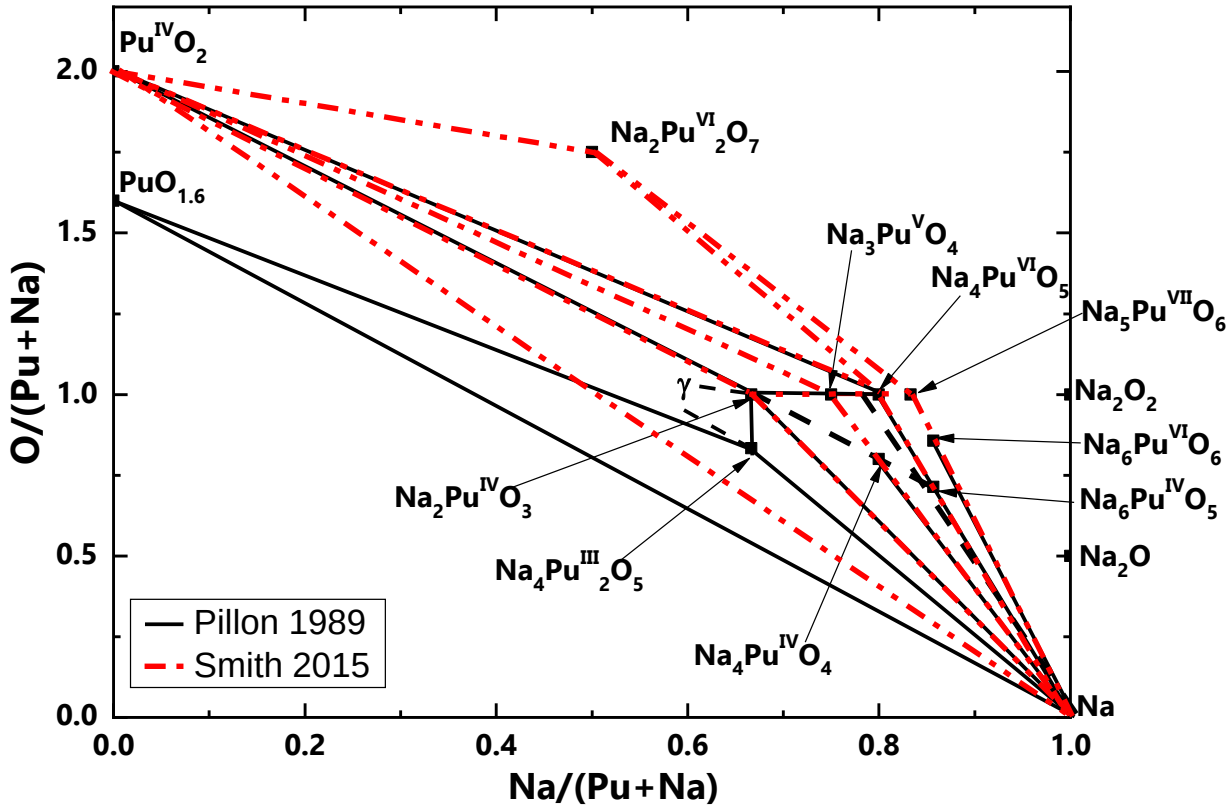

Figure 2.8: Ternary Na-O-Pu phase diagram at 800°C obtained by Pillon in black lines [2] and by Smith in red dotted lines [3].

Regarding the thermodynamic data available for this system, only the standard entropy ($S°_m(298K)$) and the Specific heat capacity ($C_p°_m(298K)$) for $Na_5Pu^{VII}O_6$ were reported by Smith on a batch containing impurities [3]. Thermodynamic data on other compounds have never been measured nor calculated.

Numerous compounds with various plutonium oxidation states have been reported in the Na-O-Pu system. However, the structure of only few compounds was characterised ($Na_2Pu^{IV}O_3$, $Na_5Pu^{V}O_5$, $Na_4Pu^{VI}O_5$, $Na_5Pu^{VII}O_6$,). Moreover, a discrepancy on the structure of $Na_2Pu^{IV}O_3$ has been raised. Therefore, a thorough study of the structural and thermodynamic properties of the Na-O-Pu compounds is needed.

Phase	Oxidation state Pu	Sym.	Z	Space group	a/Å	b/Å	c/Å	β/°	Vol./ Å^3	T/K	Ref.
$Na_4Pu^{III}_2O_5$	3	Cubic	-	-	4.8797(7)	4.8797(7)	4.8797(7)	-	-	-	[2]
$Na_2Pu^{IV}O_3$	4	Trigonal	3	*R*$\bar{3}$*m* (166)	3.440(2)	3.440(2)	16.603(8)	-	170.15	RT	[12]
$Na_2Pu^{IV}O_3$	4	Monoclinic	-	*C2/c* (15)	5.965(3)	10.313 (3)	11.772(3)	109.97(1)	680.56(1)	RT	[3]
α-$Na_4Pu^{IV}O_4$	4	Cubic	-	-	4.7903(7)	4.7903(7)	4.7903(7)	-	-	T<923K	[2]
β-$Na_4Pu^{IV}O_4$	4	Rhombo	-	-	6.795(3)	6.795(3)	6.795(3)	60.44(2)	-	-	[2]
γ-$Na_4Pu^{IV}O_4$	4	Cubic	-	-	4.797(3)	4.797(3)	4.797(3)	-	-	T>1173K	[2]
α-$Na_6Pu^{IV}O_5$	4	n.d	-	-	-	-	-	-	-	-	[2]
β-$Na_6Pu^{IV}O_5$	4	n.d	-	-	-	-	-	-	-	-	[2]
$Na_5Pu^{V}O_5$	5	Mono	2	*C2/m* (12)	10.9525(1)	4.6159(1)	6.4656(1)	71.3123(6)	314.304(7)	RT	[12]
α-$Na_3Pu^{V}O_4$	5	Ortho	-	*Fmmm* (69)	13.302(3)	9.634(3)	6.651(3)	-	852.3	RT	[3]
m-$Na_3Pu^{V}O_4$	5	Cubic	-	-	4.87(1)	4.87(1)	4.87(1)	-	-	T<873K	[13]
α-$Na_4Pu^{VI}O_5$	6	Cubic	-	-	4.718(5)	4.718(5)	4.718(5)	-	-	-	[14]
β-$Na_4Pu^{VI}O_5$	6	Tetra	2	*I4/m* (87)	7.519(2)	7.519(2)	4.619(1)	-	261.14	-	[12]
α-$Na_2Pu^{VI}_2O_7$	6	Mono	-	-	-	-	-	-	-	-	[12]
$Na_6Pu^{VI}O_6$	6	Hexagonal	-	R$\bar{3}$?	5.76	5.76	15.9	-	-	-	[14]
$Na_5Pu^{VII}O_6$	7	Mono	2	*C2/m* (12)	5.816(8)	9.98(1)	5.747(8)	110.76(6)	313.78(1)	RT	[12]

n.d: not determined

Table 2.2: Structural parameters of the sodium plutonate phases

2.1.3. The Na-O-Pu-U system

In this section, the phase diagram data on the Na-O-Pu-U system are first reviewed. Then, the data collected on the MO_2-Na_3MO_4-Na region with M=(U,Pu) at low temperature (800 K to 1050 K) are presented.

2.1.3.1 The Na-O-Pu-U phase diagram

A single extensive study on the Na-O-Pu-U phase diagram was performed by Pillon [2] with a Pu/(U+Pu) ratio of 0.28 for the starting $(U,Pu)O_2$ reagent. The same techniques as for the ternaries were used and the phase diagram determined at 1073 K is presented in **figure 2.9**.

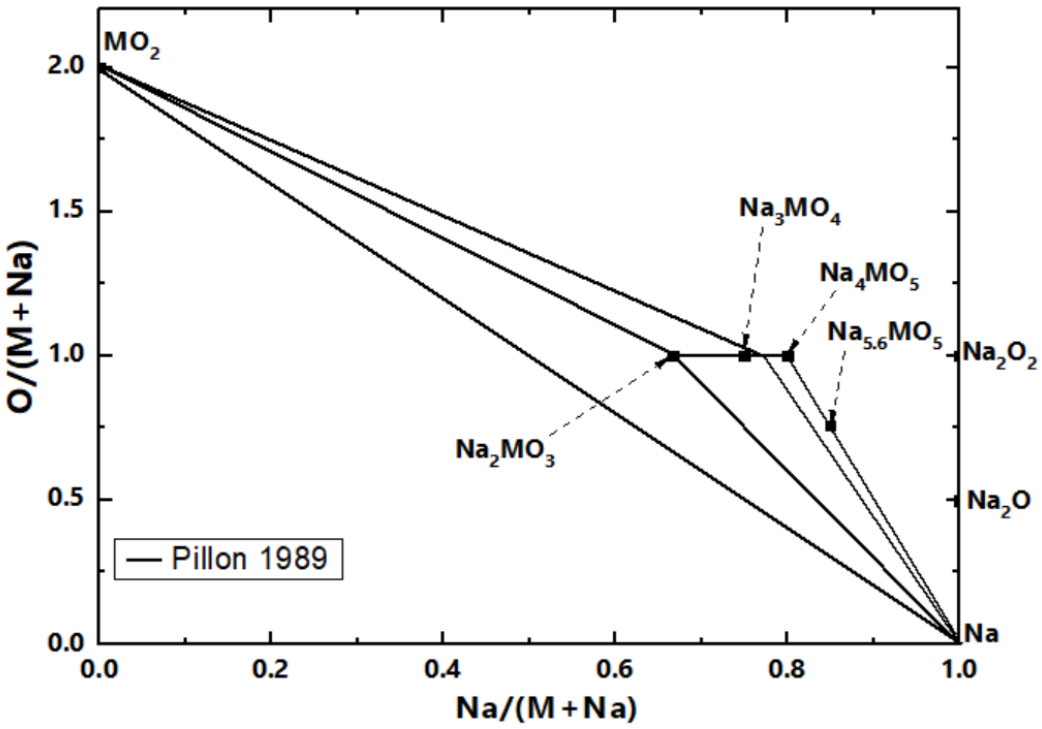

Figure 2.9: Na-M-O phase diagram at 1073 K with M=(U,Pu) reported by Pillon [2]

Pillon [2] identified four different sodium urano-plutonate phases Na_2MO_3, Na_3MO_4, Na_4MO_5 and $Na_{5.6}MO_5$. When a mixture of phases was obtained, the Pu/(U+Pu) ratio for all the sodium urano-plutonate phases was considered as equal to the one of the starting MO_2 reagent.

The Na_2MO_3 phase was found by Pillon [2] with a cubic symmetry and a lattice parameter a= 4.795(3) Å. The endmember only exists in the Na-O-Pu system where

two structures (trigonal and monoclinic) were proposed for $Na_2Pu^{IV}O_3$. Thus, the Na_2MO_3 phase reported by Pillon [2] has a different structure from the one of $Na_2Pu^{IV}O_3$. Nevertheless, no other characterisation or precise structural analysis were performed on this quaternary phase.

The data obtained on Na_3MO_4 phase are presented in the next section together with other studies.

The Na_4MO_5 was found by Pillon [2] as tetragonal crystallising in the *I4/m* space group, isostructural to the endmembers $Na_4U^{VI}O_5$ and $Na_4Pu^{VI}O_5$. As reported in **table 2.3**, the cell parameters of the three phases are close. This suggests the existence of a solid solution $Na_4(U^{VI},Pu^{VI})O_5$, which should be further investigated as a function of the Pu/(U+Pu) ratio.

Table 2.3: Structural data on the $Na_4U^{VI}O_5$, Na_4MO_5 and $Na_4Pu^{VI}O_5$.

Phase	Sym.	Space group	a/ Å	c/ Å	Ref
$Na_4U^{VI}O_5$	Tetra.	*I4/m*	7.5455(3)	4.6371(3)	[2]
Na_4MO_5			7.547(1)	4.632(1)	[2]
$Na_4Pu^{VI}O_5$			7.519(2)	4.619 (1)	[12]

Finally, Pillon [2] investigated the reaction between Na_4MO_5 and metallic sodium at 600, 800 and 1000°C and observed an insertion of sodium in the structure leading to the chemical formula $Na_{5.6}MO_5$. However, the structure was not determined.

2.1.3.2 The Na_3MO_4-MO_2-Na section

Before the extensive study of Pillon [2], Blackburn [1], Housseau *et al.* [15], Adamson *et al.* [16] and Mignanelli *et al.* [13,17] investigated the Na_3MO_4-MO_2-Na section. In fact, the Na_3MO_4 phase is expected to be the main product of the reaction between the MOX fuel and sodium in case of the formation of a breach in the fuel cladding under operating conditions.

The section of the Na-O-Pu-U phase diagram in the temperature range 800 K to 1050 K reported by Mignanelli *et al.* [13,17] is presented in **figure 2.10**.

The thermal properties of the Na_3MO_4 phase were extensively studied. Indeed, this phase was found to have a lower density and thermal conductivity than the MOX fuel [3]. Therefore, the formation of such phase would be an issue as it could cause fuel swelling and temperature increase in the fuel [13].

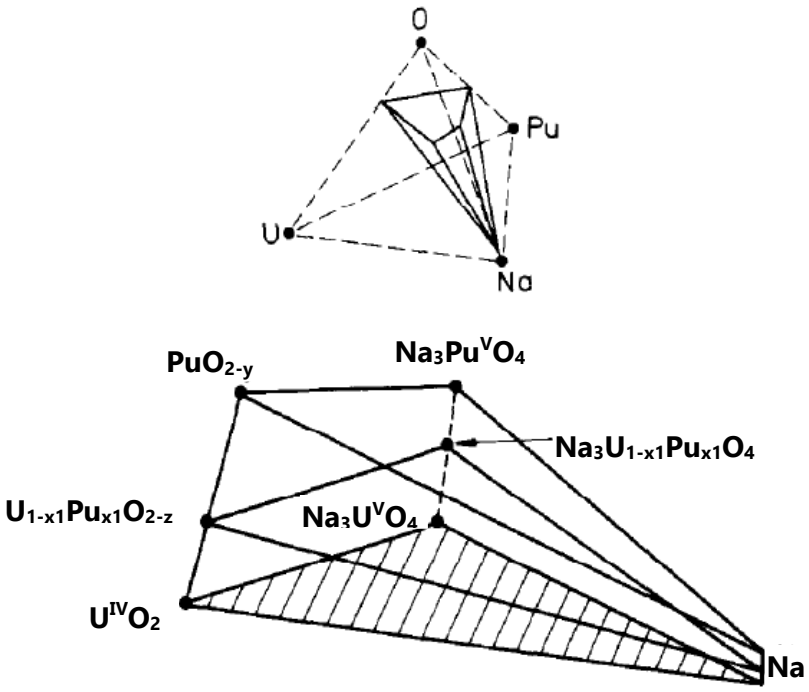

Figure 2.10: Sections of Na-O-Pu-U system of interest for the sodium / MOX reaction reported by Mignanelli *et al.* [13,17]

Thanks to the studies of Blackburn [1], Housseau *et al.* [15], Adamson *et al.* [16] and Mignanelli *et al.* [13,17], structural investigations of Na_3MO_4 were performed using XRD analysis. The authors found out that the Na_3MO_4 structure was face-centered cubic with a lattice parameter a = 4.77 Å for mixed oxides with Pu/(U+Pu) < 0.3. For higher ratios, a tetragonal form appears with *a* =4.77 Å *c*= 4.88 Å for Pu/(U+Pu)=0.3 and *a* =4.79 Å *c*= 4.925 Å for Pu/(U+Pu)=0.76. Nevertheless, no other structural characterisation was performed.

In the re-investigation of the Na-O-Pu-U phase diagram performed by Pillon [2] with Pu/(U+Pu)=0.28, the Na_3MO_4 was found cubic with a lattice parameter slightly higher than the one reported in the previous studies: *a* = 4.7805(5) Å. Moreover, a metastable phase called "m-Na_3MO_4", isostructural with $Na_3Pu^VO_4$ was observed. This phase was found as rhombohedric with lattice parameters: *a* = 6.757(2) Å and α = 60°25(2)'. However, as reported in section 2.1.2, in the recent works of Bykov *et al.* [12] and Smith [3], $Na_3Pu^VO_4$ was refined with an orthorhombic symmetry, in space group *Fmmm* (n°69). As the quaternary compound is reported to be isostructural to $Na_3Pu^VO_4$, it might be refined with the orthorhombic symmetry and not the rhombohedral one. Therefore, the Na_3MO_4 phase should be synthesised with different values of Pu/(U+Pu) and the structure should be refined with the Rietveld method.

Finally, Pillon [2] studied in details the section along the O/(Pu+Na) =1 composition line. As described in the earlier work of Adamson *et al.* [16] and Mignanelli *et al.* [13,17] on Na_3MO_4 the equilibrium between the three phases Na, Na_3MO_4 and MO_2 has been observed as shown in **figure 2.11**. However, while increasing the sodium content or the temperature, a one single phase compound is formed. Above 1073 K, this cubic phase $Na_{3+\xi}\ M_{1+\xi}\ O_{4+2\xi}$ extends from Na_2MO_3 to a composition close to Na_4MO_5. However, the phase boundaries were not determined by Pillon [2]. When the temperature decreases, the extent of the composition range of the $Na_{3+\xi}\ M_{1+\xi}\ O_{4+2\xi}$ phase decreases and a three phase equilibrium between sodium, MOX fuel and the urano-plutonate Na_3MO_4 is found.

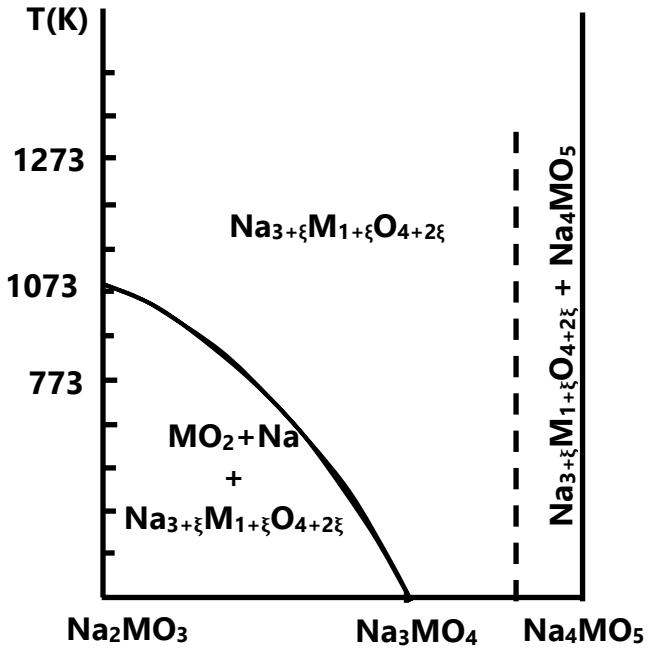

Figure 2.11: Pseudo-binary diagram between Na_2MO_3 and Na_4MO_5 reported by Pillon [2]

The study performed by Pillon [2] gives a new insight on the quaternary phase diagram compared to the work of Mignanelli *et al.* [17] (**figure 2.10**).

In **figure 2.12**, the composition range of $Na_{3+\xi}M_{1+\xi}O_{4+2\xi}$ has been added and the extent of the Na-MO_2-Na_3MO_4 phase field has been reduced to take into account the latest results obtained by Pillon [2]. Finally, the phase diagram representation has been extended up to the Na_4MO_5 phase to include the phase diagram data reported by Pillon [2] (**figure 2.9)**.

However, uncertainties are remaining on the structure, composition range and oxidation state of uranium and plutonium in the $Na_{3+\xi}\ M_{1+\xi}\ O_{4+2\xi}$ phase.

The phase equilibria at high Na/(M+Na) ratio are also still unclear. Moreover, surprisingly, the Na_2MO_3 phase, which was reported by Pillon [2] as a cubic stable phase does not appear on the phase diagram. Instead, either a three phase equilibria between Na-MO_2-$Na_{3+\xi}M_{1+\xi}O_{4+2\xi}$ or a single phase $Na_{3+\xi}M_{1+\xi}O_{4+2\xi}$ has been observed as reported in **figure 2.11**.

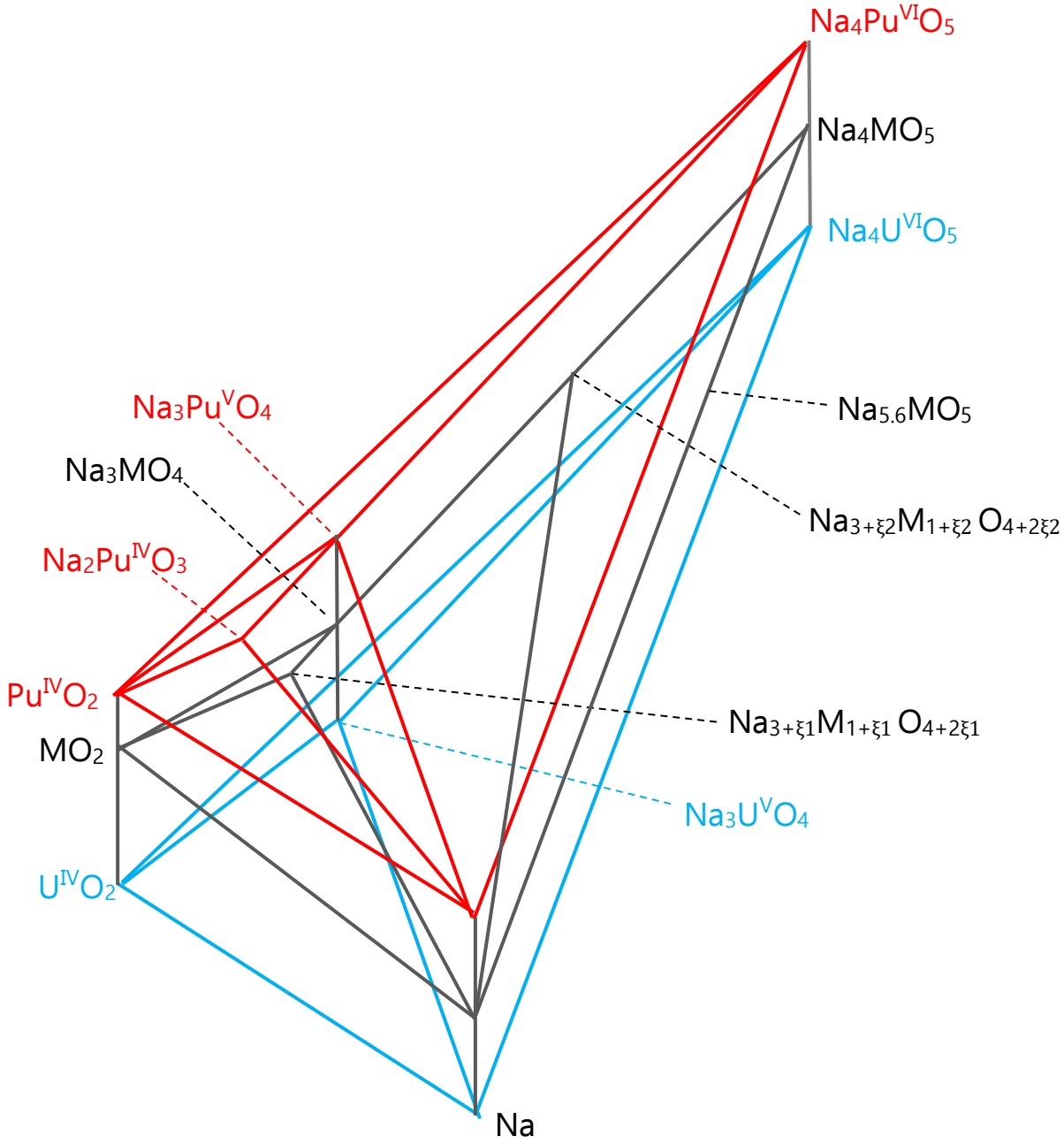

Figure 2.12: Representation of Na-O-Pu-U phase diagram sections for T<1073 K. The Na-O-U, Na-O-Pu and Na-O-Pu-U systems are respectively in blue, red and black. The Na-MO_2-$Na_{3+\xi1}M_{1+\xi1}O_{4+2\xi1}$ phase field is represented with dashed lines. The extend of the solid solution $Na_{3+\xi}M_{1+\xi}O_{4+2\xi}$ is represented by ξ1, ξ2 on the phase diagram.

Finally, Kleykamp [18] characterised a fuel pellet irradiated in the Siloé reactor where an artificial failure was performed. At ~900 K, the temperature range of the fuel pellet rim region [19], the Na_3MO_4 phase was observed as main phase forming. However, two other sodium urano-plutonate phases were reported to form: $Na_2M_2O_7$ and $NaMO_3$. No structural data were precisely reported in the study of Kleykamp [18]. However, for the $Na_2M_2O_7$ composition, both uranium and plutonium ternary compounds were reported to exist whereas for the $NaMO_3$, only the uranium compound exists. Thus, these two phases, which are not reported in the phase diagram of Pillon [2] would be interesting to study experimentally.

2.1.4. Conclusion

The structural data on the $Na_xM_yO_z$ phases are listed in **table 2.4** and compared to the data reported for the endmembers.

The Na_3MO_4 phase was extensively studied and its structural evolution with the Pu/(U+Pu) ratio was determined. For other phases, only few data are available. Moreover, the phases in the Na-M-O system are not isostructural to the end members except for Na_4MO_5 as reported in **table 2.4**.

Table 2.4: Structural data on the Na-M-O phases and endmembers reported by Pillon [2].

Composition	Uranium End member	Ref	$Na_xM_yO_z$	Ref	Plutonium End member	Ref
Na_2MO_3	-	-	Cubic	[2]	Trigonal	[12]
					Monoclinic	[3]
$NaMO_3$	Orthorhombic	[8]	?	[18]	-	-
Na_3MO_4	Cubic (metastable)	[6]	Cubic Pu/(U+Pu)<0.3	[13,17]	Cubic	[12]
	-	-	Tetragonal Pu/(U+Pu) ≥ 0.3	[13,17]	-	-
	Monoclinic	[3]	Orthorhombic (metastable)	[2]	Orthorhombic	[3]
$Na_{3+\varepsilon}M_{1+\varepsilon}O_{4+2\varepsilon}$	Monoclinic	[5]	Cubic	[2]	Rhombohedral	[2]
$Na_2M_2O_7$	Monoclinic	[11]	?	[18]	Monoclinic	[12]
Na_4MO_5	Tetragonal	[2]	Tetragonal	[2]	Tetragonal	[12]
	Cubic (metastable)	[3]	-	-	Cubic	[14]
$Na_{4+x}MO_5$	$Na_{5.33}UO_5$ Tetragonal	[2]	$Na_{5.6}MO_5$?	[2]	$Na_5Pu^{V}O_5$ Monoclinic	[12]
					$Na_6Pu^{IV}O_5$?	[2]

The Na-O-Pu-U phase diagram presents some similarities with the Na-O-U system:

- The $Na_{5.6}MO_5$ phase exhibiting a mixed actinide oxidation state between +IV and +V as $Na_{5.33}UO_5$ in the ternary system;.
- A composition range for the $Na_{3+x}M_{1+\varepsilon}O_{4+2\varepsilon}$ phase in both systems, which extent increases with the temperature;
- The existence of the three phase equilibrium Na-MO_2-$Na_{3+x}M_{1+\varepsilon}O_{4+2\varepsilon}$.

However, the insertion of plutonium induces the following important changes:

- Na_2MO_3 can form while Na_2UO_3 does not exist. However, the reported structure is different from the one of $Na_2Pu^{IV}O_3$;
- The insertion of plutonium stabilises the cubic phase of Na_3MO_4 while this cubic structure is metastable for the uranium end member;
- A metastable phase isostructural with Na_3PuO_4 exists;
- The solid solution $Na_{3+\varepsilon}M_{1+\varepsilon}O_{4+2\varepsilon}$ has a wider composition range than $Na_{3+\varepsilon}U_{1+\varepsilon}O_{4+2\varepsilon}$.

From these observations, the Na-O-U system can be used as a first approximation of the quaternary Na-O-Pu-U phase diagram. However, structural changes were reported for a Pu/(U+Pu) ratio of 0.28.

Therefore, the structure of the sodium urano plutonate phases has to be systematically studied as a function of the plutonium content in the MOX reagent. Thanks to these studies, the determination of the mutual solubilities of plutonium and uranium in these phases, not known yet, would be possible. Moreover, other compounds were reported in the ternary systems, which were not studied by Pillon. These phases would also be interesting to study, as for example, $NaMO_3$ and Na_2MO_4. Indeed, for these phases, the uranium endmembers $NaU^{V}O_3$ and $Na_2U^{VI}O_4$ exist while the plutonium end members "$NaPuO_3$" and "Na_2PuO_4" are not stable.

2.2. Sodium-MOX fuel chemical interaction under operating conditions

As mentioned in the previous section the formation of Na_3MO_4 has been extensively studied as this phase was reported to be the main product of the sodium/MOX fuel reaction under operating conditions.

From the experimental investigations of Blackburn [1] and Housseau *et al.* [15] and the calculations of Adamson *et al.* [16], and Mignanelli and Potter [13,17], the interaction between sodium and MOX fuel under operating conditions (temperature and oxygen potential) leads to the formation of the cubic Na_3MO_4 phase [17] according to the following reaction:

$$3(y-z)\,Na(l, O\ dissolved) + (2+y)\,U_{1-x_3}Pu_{x_3}O_{2-z}(cr) \rightarrow (y-z)\,Na_3U_{1-x_2}Pu_{x_2}O_4(cr) + (2+z)\,U_{1-x_1}Pu_{x_1}O_{2-y}(cr) \quad (1)$$

(with y>z) [16]

As a consequence, the formation of the Na_3MO_4 induces the decrease of the oxygen stoichiometry of the MOX fuel: y>z.

As summarised in the work of Tête [20], the formation of the sodium urano-plutonate phase is mainly influenced by the amount of available oxygen in the MOX fuel, given by its equilibrium oxygen potential, $\overline{\boldsymbol{\Delta G_{O_2}}}$. This thermodynamic data depends also on the O/(U+Pu) ratio of the fuel and the temperature in the reactor core.

The oxygen potential is defined by:

$$\overline{\Delta G_{O_2}} = RTln(\frac{P_{O_2}}{P^\circ_{O_2}})$$

where P_{O_2} is the oxygen partial pressure over the oxide and $P^\circ_{O_2}$ the standard oxygen partial pressure.

Adamson *et al.* [16] and Mignanelli and Potter [13,17] finally showed that the equilibrium oxygen potential for the formation of the mixed oxide Na_3MO_4 was similar to the one of the ternary Na_3UO_4 under operating conditions leading to an analogy between the Na-O-U and Na-O-Pu-U systems.

Many data were reported in the literature reviews by Tête [20] and Smith [3] on the threshold values of O/(U+Pu) ratio of the fuel for the formation of Na_3MO_4 at low plutonium content (Pu/(U+Pu) = 0.2), under operating conditions (~ 900 K). Moreover, in post-irradiation analysis of defected fuel pin, Kleykamp [18] observed the formation of $NaMO_3$ in the hot parts of the pellet whereas Na_3MO_4 was reported to form in the

"cold" parts. He justified it by the non-stability of Na_3MO_4 at high temperature, which is supported by the analogy with Na_3UO_4 only stable up to 1323 K. Therefore, at high temperature, the $NaMO_3$ phase is likely forming instead of Na_3MO_4.

Moreover, as mentioned in chapter 1, due to the high temperature gradient in the fuel pellet, the plutonium redistribution occurs leading to a plutonium enrichment in the centre of the pellet [21]. According to Bober *et al.* [21], it could reach a Pu/(U+Pu) ratio of 0.36 compared to the initial value of 0.2. Therefore, the sodium urano plutonate phases, which could form for high plutonium content in the fuel, have to be investigated.

Conclusion

Under operating conditions, the conditions for the formation of the mixed oxide Na_3MO_4 were found to be close to those for Na_3UO_4. Therefore, taking the data on the UO_2 fuel / sodium reaction to describe the MOX fuel / sodium interaction is a reasonable approach to understand the different mechanisms that might occur with the MOX fuel in these conditions. However, in case of a severe accident, the conditions are very different from the operating ones.

Indeed, as mentioned in Chapter 1, the interaction is occurring:

- at a very high temperature of the fuel (solid or liquid) and sodium (liquid or/and gas);

- with an important heat transfer between the fuel and the sodium;

- within a very short reaction time.

No experimental data on the chemical interaction are available in these extreme conditions. The approach is then to start developing a thermodynamic model on the Na-O-Pu-U system in order to perform calculations in the very wide range of composition and temperature.

The review of the experimental data on the Na-O-Pu-U system showed that numerous sodium urano plutonate phases exist. However, numerous data are still missing. Therefore, to fill this gap, the investigation of these compounds for high plutonium content is needed with thorough structural and thermodynamic study to determine the plutonium solubility in these phases.

In the next section, the data reported in the literature on the interaction between sodium and key fission products are presented.

2.3. Sodium-fission products reaction

In Chapter 1, the Ba-Cs-I-Mo-O-Te system was identified as the key fission product system to study under severe accident conditions.

During a severe accident, depending on their volatility, some fission products can be released from the fuel. Based on the data collected in CABRI and SCARABEE campaigns and the models on the fission products release, Balard and Carluec estimated the source reactor term [22]. **Table 2.5** presents data on the fraction of the fission products that are released during an accident.

For each fission product, the release factor versus time is expressed as:

$$F = 1 - e^{-kt} \text{ [22]}$$

where: k (min^{-1}) is the release constant and t (min.) is the time.

Table 2.5: Fraction of fission products released after a severe accident estimated by Balard and Carluec [22].

Fission Product	Release Fraction			
	1800°C	2100°C	2500°C	2800°C
Cs	0.57	1.0	1.0	1.0
I	0.57	1.0	1.0	1.0
Te	$1.9.10^{-2}$	$2.6.10^{-2}$	$7.2.10^{-2}$	1.0
Ba	-	-	$1.3.10^{-3}$	$2.1.10^{-2}$
Mo	$2.3.10^{-3}$	$2.6.10^{-3}$	$3.0.10^{-3}$	$3.3.10^{-3}$

As shown in **table 2.5**, a large amount of cesium and iodine are released from the fuel (57 % at 1800°C and 100 % at T>2100°C) in case of a severe accident. However, below 2100°C, the volatile fission products are not totally released. Therefore, an interaction between these fission products, sodium and the irradiated MOX fuel containing secondary fission product precipitates could happen. Therefore, an interaction between sodium and cesium and/or iodine dissolved in the fuel has to be considered below 2100°C.

Moreover, after their complete release from the fuel at very high temperature, cesium and iodine shall condense on the cold parts of the reactor where they could react with sodium that evaporated.

As described in **table 2.5**, tellurium is also very volatile and predicted to be fully released at 2800°C.

Other semi-volatile fission products, such as barium and molybdenum will be distributed both in the irradiated fuel as secondary phases (solid and liquid at high temperature) and in the gas phase at very high temperature. Thus, a reaction could occur between sodium and these elements located both in the secondary phases or in the gas phase.

In the following sections, the data on the interaction between sodium and each fission product are reviewed.

2.3.1. Iodine / sodium interaction

As reported in Chapter 1, iodine is expected to be mainly associated with cesium forming the CsI compound. However, this compound has never been observed experimentally in the irradiated MOX fuel. Silver iodide, AgI was also observed in the JOG by Cano *et al.* [23]. Moreover, under normal operating conditions, the presence of I_2 is very unlikely because iodine preferentially reacts with cesium and silver.

Castleman *et al.* [24] studied the interaction between CsI and sodium by mixing CsI with a large amount of liquid sodium in the temperature range 485-748°C. The authors observed the formation of NaI and a low release of cesium and iodine. Indeed, with such a large quantity of sodium, iodine reacts first with sodium forming the NaI compound. Although, CsI and AgI are thermodynamically more stable than NaI, the thermodynamic equilibrium takes a long time to be reached (see **figure 2.16c** in section 2.3.2.1.).

NaI has a low vapour pressure therefore very little NaI shall be released from the sodium coolant [25]. However, in case of a sodium fire at high temperature, the NaI compound decomposes and molecular iodine I_2 is likely forming [26]. In this case, one needs to consider the different reactions that might happen. Nevertheless, as reported by Herrantz *et al.* [26] the chemistry of iodine in these conditions is much simpler than in the light water reactor, where water is used as coolant.

Therefore, at the early stages of a severe accident, the sodium coolant acts as a safety barrier against iodine release, trapped under NaI form. Later on, some molecular iodine could be released but in less large concentration than in LWR reactors.

The systems I-Na and I-Na-O would be interesting to study because iodine is very volatile and has a high activity coefficient. However, handling iodine is very difficult so this system will not be studied experimentally in the present work.

2.3.2. Cesium / sodium interaction

As reported in Chapter 1 and in section 2.2.1, in the irradiated fuel, cesium can be found in the CsI compound. This compound is not stable in case of an ingress of sodium, thus elemental cesium can be formed. When released in sodium, cesium shall form a homogeneous liquid phase with sodium, as the binary compounds are only existing at very low temperature (see **figure 2.16a** in section 2.3.2). Therefore, the retention of cesium by the primary sodium coolant is likely very high [27].

However, cesium is also found in Cs_2Te, Cs_2UO_4 and/or Cs-Te-Ba oxide compounds [23] (see Chapter 1). Nevertheless, the interaction between these compounds and sodium has not been studied yet.

Finally, cesium is also reported as Cs_2MoO_4 in the outer part of the fuel pellet (chapter 1). As it is the main phase in the JOG layer, the chemical reactions with sodium were investigated in case of a breach in the cladding under operating conditions.

Kleykamp *et al.* [18] analysed a defected fuel pin from Siloé experiment. The authors observed that the gap between the fuel pellet and the cladding was filled with sodium molybdates. The author proposed the following reaction: $Na + Cs_2MoO_4 = Cs + Na_2MoO_4$ [18].

Tête [20] investigated the reaction between Cs_2MoO_4 and Na using Differential Scanning Calorimetry (DSC) and SEM analysis to characterise the compounds forming in samples with different ($Na : Cs_2MoO_4$) ratio (1:1, 2:1, 4:1). The author did not observe the Na_2MoO_4 compound and therefore disregarded the assumption made by Kleykamp *et al.* [18]. Nevertheless, a reaction between sodium and Cs_2MoO_4 was observed between 700-800 K but the compound could not be identified. Therefore, the mechanism of this interaction has to be re-investigated.

While studying the phase equilibria in the Na_2MoO_4-Cs_2MoO_4-Zn_2MoO_4 system, Zolotova *et al.* [28] very recently reported the existence of the $Cs_3Na(MoO_4)_2$ compound in the Cs-Mo-Na-O system. Finally, Smith *et al.* [29,30], using her newly measured thermodynamic data for $Cs_3Na(MoO_4)_2$, showed by thermodynamic calculations that this phase could be formed under operating conditions (temperature and oxygen potential). Therefore, this quaternary compound could possibly form as the result of the interaction between Cs_2MoO_4 and Na_2MoO_4 (ratio 3:1). Moreover, this assumption could explain the disappearance of Cs_2MoO_4 without observing the formation of Na_2MoO_4.

Finally, a second quaternary compound, $CsNaMo_3O_{10}$, was observed by Förster *et al.* [31]. Only the space group and cell parameters were reported. However, no structural refinement of the atomic positions was performed. Therefore, the study of the structure and thermodynamic properties of this compound is needed.

To conclude, a thorough re-examination of the sodium-cesium molybdates interaction should be performed. Moreover, phase diagram and thermodynamic data on the Cs-Mo-Na-O system would be useful to develop a thermodynamic model for this system and predict the phases forming.

2.3.3. Molybdenum / sodium interaction

Molybdenum can be found in the irradiated MOX fuel under numerous forms: metallic Mo (combined with Ru, Pd, Tc …), MoO_2, MoO_3 or combined with other fission products in oxide phases: Cs_2MoO_4, $BaMoO_3$, $BaMoO_4$.

Metallic molybdenum is one of the main compound of the white metallic precipitates. This metal is not soluble into sodium and no interaction with sodium is expected [27].

When oxidised or associated with other elements, molybdenum is likely reacting with sodium. To study the interaction of sodium with the phases located in the JOG, Tête [20] analysed the outer part of a fuel pellet coming from a fuel pin where a breach appeared after irradiation in the Siloe reactor. Using X-ray microanalyse, the author observed zones where Na, Mo and O elements were associated. Even if, these experiments were performed under operating conditions, this confirms that an interaction between liquid sodium and molybdenum oxide phases can happen.

The chemical systems including molybdenum are quite complex because of the speciation of molybdenum and the numerous compounds that can form with other fission products. Therefore, the Na-FP-Mo-O systems are important to study.

2.3.4. Tellurium / sodium interaction

Tellurium is mainly found in its metallic state in the irradiated fuel or as Cs_2Te in the JOG as reported in Chapter 1. Several Na-Te compounds were reported in the phase diagram study of Pelton and Petric [32]: Na_2Te, NaTe or $NaTe_3$. Therefore, a strong interaction is expected between sodium and tellurium in case of an accident.

Finally, tellurium can also be found in $BaTeO_3$ or Cs_2TeO_3 compounds (see Chapter 1) as reported by Kleykamp [33]. However, no interaction studies with sodium were performed.

In the analysis of the interaction of the JOG phases with liquid sodium, Tête [20] observed the disappearance of tellurium in the whole pellet except near the centre. Indeed, sodium "washes out" the irradiated fuel of tellurium, mainly found in the sodium coolant system. In case of an accident, tellurium is more likely found as Na_2Te, Na_2TeO_3 or Na_2TeO_4 according to the thermodynamic calculations of Lindemer *et al.* [34]. Finally, a comprehensive study of the Na-O-Te system is needed for the safety of the reactor and to understand the mechanisms of the binary and ternary compounds formation.

2.3.5. Barium / sodium interaction

As mentioned in Chapter 1, barium is found in:

- the perovskite phase: $(Ba, Sr, Cs)(Zr, Mo, U, Pu)O_3$ in the fuel;
- Ba-Mo-O oxides in the JOG, more likely $BaMoO_4$;
- Ba-O phases;

In post irradiation examinations of a fuel pellet, Tête [20] observed regions where Ba, Mo, O elements were associated. Therefore, in case of contact with sodium, an interaction between Ba-Mo-O phases and sodium could occur. However, no study was performed on this possible interaction.

To fill this gap, the study of the Ba-Mo-Na-O system is needed. In this system, the $Ba_2NaMoO_{5.5}$ quaternary compound was reported by Sabatier *et al.* [35].

Therefore, $Ba_2NaMoO_{5.5}$ could potentially form as the product of the reaction between barium molybdate, barium oxide and sodium as reported in equation (1) and (2):

(1) $BaMoO_{4\,(s)} + BaO_{(s)} + Na_{(l)} + \frac{1}{2} O_{2\,(g)} = Ba_2NaMoO_{5.5\,(s)}$

(2) $BaMoO_{3\,(s)} + BaO_{(s)} + Na_{(l)} + \frac{3}{2} O_{2\,(g)} = Ba_2NaMoO_{5.5\,(s)}$

In order to know if this phase can form and if the two mechanisms are valid, the enthalpy of formation and standard entropy of the pure compound have to be measured. These data are also needed to develop the thermodynamic model of the quaternary system Ba-Mo-Na-O.

2.3.6. Conclusion

Many studies on the irradiated fuel composition and the different secondary phases forming under irradiation were reported. However, only few data were collected on the interaction between these phases and sodium under operating conditions and none under severe accident conditions. Indeed, after reaction with liquid sodium, characterisations of the products are difficult to perform.

Table 2.6 presents a summary of the data reported in the literature and the systems that should be studied in case of a severe accident.

Table 2.6: Summary of the data on the interaction between the fission products and sodium. (with +++ high amount and + low amount).

Fission products	Phases in the irradiated fuel before the accident	Phases after the accident and interaction with sodium	Phases in the fuel after the accident	Systems	Author
Cs	Cs_2UO_4, Cs_2MoO_4, CsI, Cs_2Te, Cs_2TeO_3	Mainly in gaseous state, Cs soluble in sodium, possible interaction between Cs compounds and sodium	+	Cs-Mo-Na-O	Kleykamp [33] Kleykamp *et al.* [18] Castleman *et al.* [24] Tête [20] Grabaskas *et al* [27] Smith *et al.* [29,30]
Ba	Ba-Mo-O compounds, $BaTeO_3$	Oxide phases in the whole pellet	+++	Ba-Mo-Na-O	Kleykamp [33] Tête [20]
Mo	Mo, MoO_2, MoO_3, FP-Mo-O	Oxide phases, Na-Mo-O phases	++	Mo-Na-O FP-Mo-Na-O	Kleykamp [33] Grabaskas *et al* [27] Tête [20]
Te	Te, $BaTeO_3$, Cs_2TeO_3, Ba-Cs-Te-O	Na_2Te, Na_2TeO_3, Na_2TeO_4	No	Na-O-Te, Ba-Cs-Na-O-Te	Kleykamp [33] Lindemer *et al.* [34] Grabaskas *et al* [27]
I	CsI, AgI	NaI	No	I-Na	Castleman et al. [24] Herrantz *et al.* [26]

At very high temperature, volatile fission products should be instantly transferred to the sodium pool or the gas cover via the gas phase. Other fission products like molybdenum and/or barium, shall stay in the fuel after the accident.

The experimental investigation of the interaction between these fission products compounds with sodium at very high temperature is quite challenging.

Thus, the approach proposed in the present work is to develop a thermodynamic database on these systems using the Calphad method. The review of the existing models is presented in the following section.

2.4. Thermodynamic modelling with the Calphad method

The system under study is quite complex due to the large number of chemical elements involved: Na-(Ba-Cs-I-Mo-Te)-(Pu-U)-O. In this frame, Calphad is the most suitable method to develop a thermodynamic modelling on such complex system. With this a computational tool, it will be possible to analyse the chemical interaction between the fission products, the MOX fuel and sodium during the different stages of a severe accident.

Since 2013, the Thermodynamic Advanced Fuels – International Database project (www.oecd-nea.org/science/taf-id/) was initiated within the TAF-ID joint project at the OECD/NEA. This project consists in developing a wide, comprehensive, internationally recognised and quality insured thermodynamic database for the modelling of phase diagrams and thermodynamic properties of the systems for advanced nuclear fuel materials. Many binary and ternary key systems for the thermodynamic description of the MOX fuel chemistry under irradiation have already been modelled. However, sodium has not been implemented in the database yet.
Therefore, in this section, a review of the existing models is performed to identify the systems already implemented in the TAF-ID database, the missing ones and the high priority systems to be modelled and experimentally studied in the present work.

2.4.1. Na-O-Pu-U

To develop a thermodynamic database on the Na-O-Pu-U system, the binary and ternary sub-systems have to be first modelled.

In this section, only the systems, which are not implemented in the TAF-ID database yet, are presented in details.

As reported in **table 2.7**, except the Na-Pu system, all others binary sub-systems have been modelled. The U-O and Pu-O systems assessed by Guéneau *et al.* [36] and Pu-U by Kurata [37] were already implemented in the TAF-ID database.

Table 2.7: Review of the binary sub-systems binaries of the Na-O-Pu-U system. With "Calphad": Calphad model published in the literature. In green, the Calphad model is implemented in the TAF ID database. In orange, the system is not implemented in the TAF-ID database.

Chemical Element	Na	O	U
O	Calphad [6]		
U	Calphad [6]	Calphad [36]	
Pu		Calphad [36]	Calphad [37]

For the Na-O (**figure 2.13 a)** and Na-U (**figure 2.13 b**) systems, a model has been developed by Smith *et al.* [6] whereas for the Na-Pu system, no phase diagram was reported in the literature.

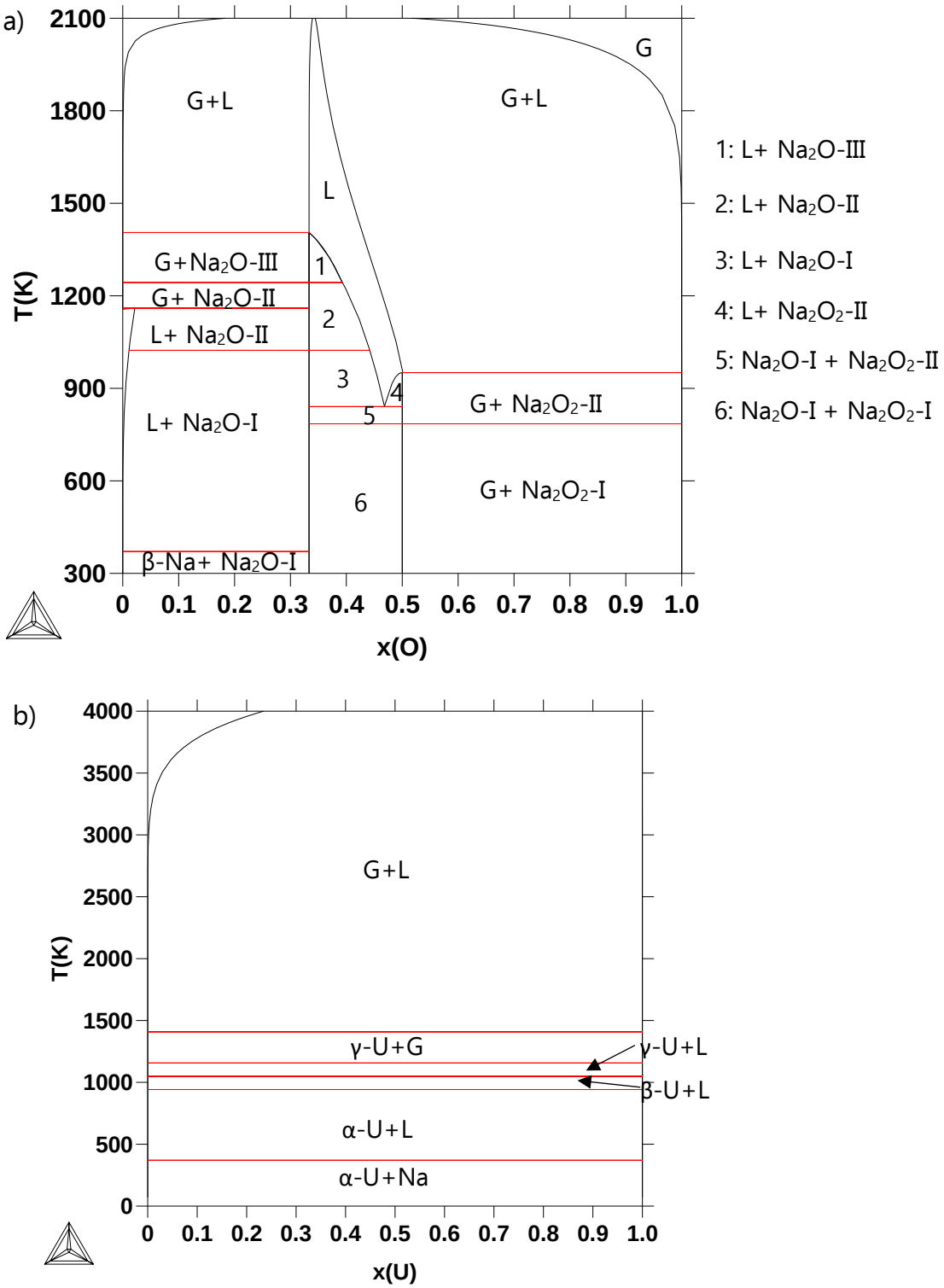

Figure 2.13: Calculated phase diagrams of the Na-O (a) and Na-U (b) systems with the Calphad model reported by Smith *et al.* [6].

For the ternary sub-systems, the Na-O-U system was modelled by Smith *et al.* [6] (see section 2.1.1). For the Na-O-Pu and Na-Pu-U phase diagrams, no model was reported.

As reported in **table 2.8**, the model of the Pu-U-O system derived by Guéneau *et al.* [36] is implemented in the TAF-ID database.

Table 2.8: Review of the ternary sub-systems of the Na-O-Pu-U system. With "Calphad": Calphad model published in the literature. In green, the Calphad model is implemented in the TAF ID database. In orange, the system is not implemented in the TAF-ID.

System	U-O	Pu-O	Pu-U
Na	Calphad, [6]		
U		Calphad [36]	

In **figure 2.14**, calculated isothermal sections of the Na-O-U system using the model of Smith *et al.* [6] are presented. Moreover, the remarkable section Na-UO_2-Na_3UO_4 discussed in section 2.2.1 has been highlighted in blue.

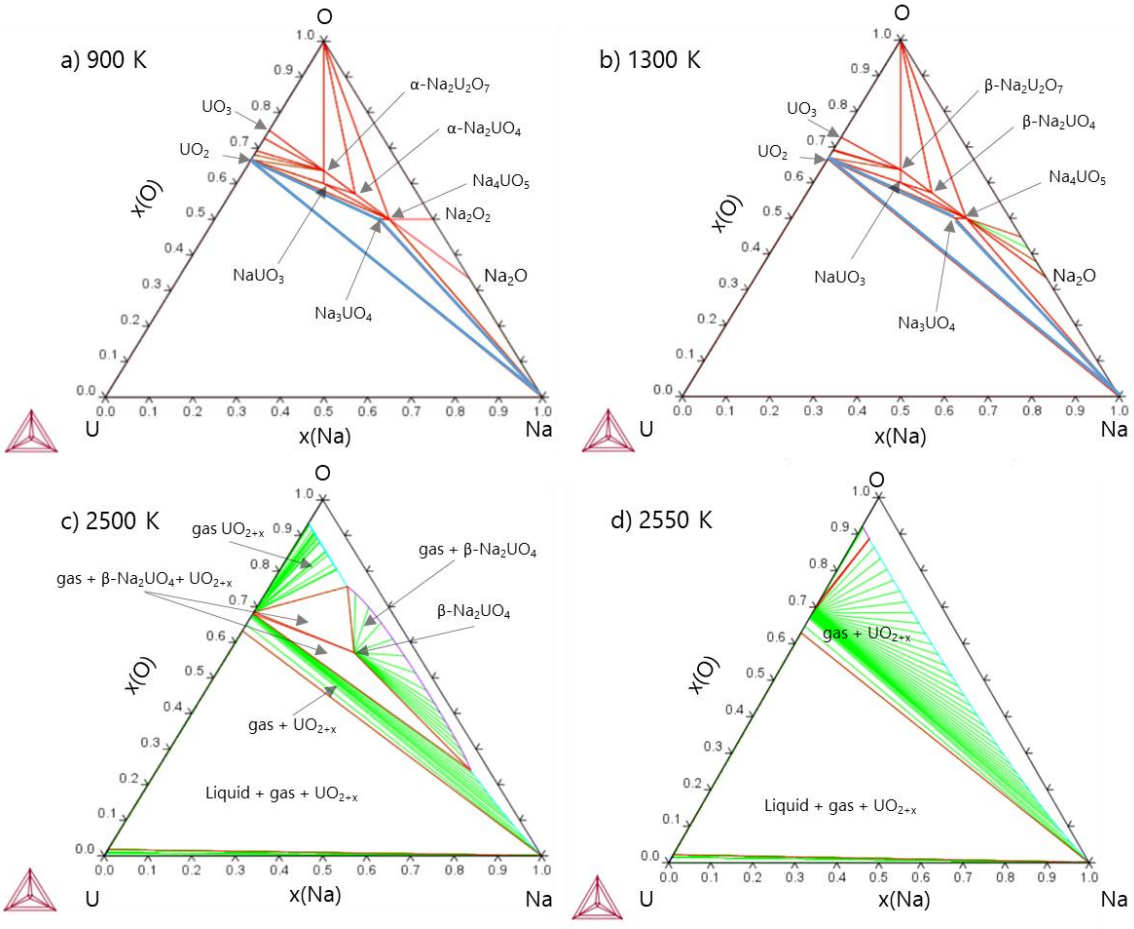

Figure 2.14: Calculated isothermal sections of the Na-O-U system at 900 K (a), 1300K (b), 2500K (c), 2550K (d) using the Calphad model of Smith *et al.* [6]. The stable ternary compounds at the temperature considered are reported on the sections. The UO_2-Na_3UO_4-Na phase field is represented in blue on fig a) and b).

Therefore, to develop a full Calphad model of the quaternary system, the ternary Na-O-Pu has to be modelled.

2.4.2. Na-FP-O with FP: Cs, Ba, I, Mo, Te

In **table 2.9**, the different binary and ternary key sub-systems reported in the literature and of interest for this work are presented.

2.4.2.1. Binary systems

As reported in **table 2.9**, many binary systems have already been modelled and implemented in the TAF-ID database.

For the binaries without sodium, only the Ba-Cs, Ba-Te and I-O systems are not known. The other binary systems are modelled in the TAF-ID database.

Table 2.9: Review of the binary sub-systems of interest in this work. With "Calphad": Calphad model published in the literature, "Diagram": Phase diagram reported in the literature. In green, the Calphad model is implemented in the TAF ID. In orange, the system is not implemented in the TAF-ID database.

Chemical Element	Na	O	Cs	Ba	Mo	Te	I
O	Calphad [6]						
Cs	Calphad [38]						
Ba	Diagram [39]						
Mo		Calphad [40]					
Te	Calphad [41]		Calphad [42]				
I	Calphad [43]						

For the sub-systems containing sodium, the Na-O phase diagram is presented in **figure 2.13a**. For the Na-Mo system, no model was found. However, as reported by Tête [20], no binary compound exists in this system.

The Cs-Na phase diagram was modelled by Ren *et al.* [38]. It is compared with the experimental data of Ott *et al.* [44] in **figure 2.15a**. The Na-Te system was assessed by Chen *et al.* [41] using the critical review of the experimental data performed by Pelton and Petric [32] as reported in **figure 2.15b**. Finally, the Na-NaI system calculated with the model of Dinsdale *et al.* [43] is presented in **figure 2.15c**.

a)

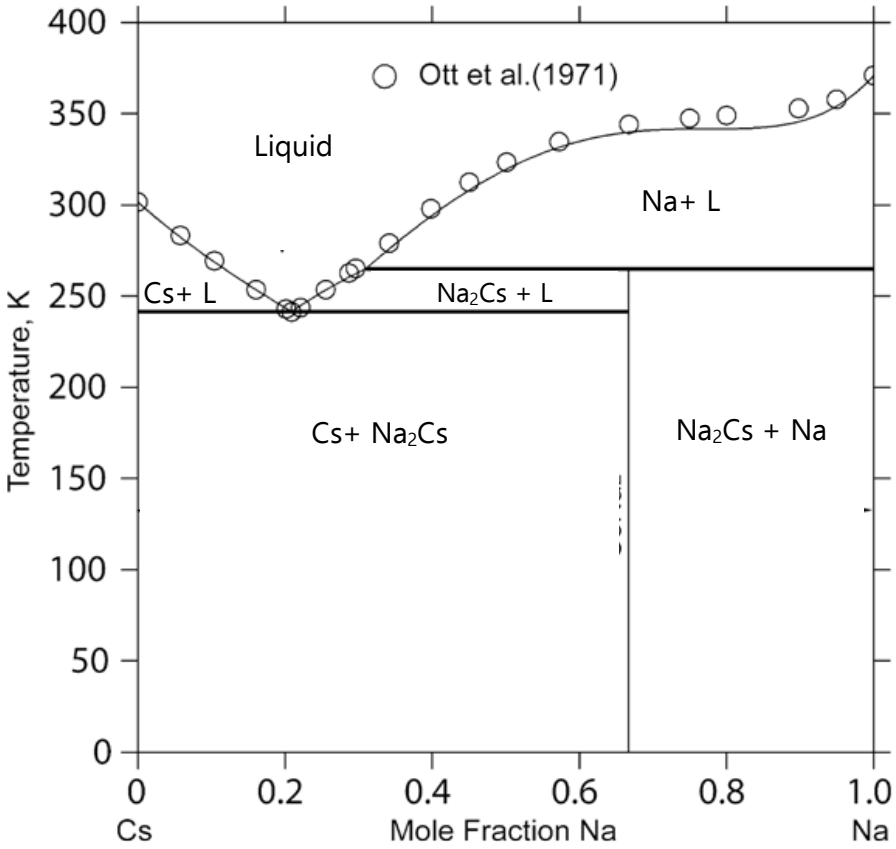
Ott et al.(1971)
Liquid
Na+ L
Cs+ L
Na2Cs + L
Cs+ Na2Cs
Na2Cs + Na
Temperature, K
Mole Fraction Na
Cs
Na

b)

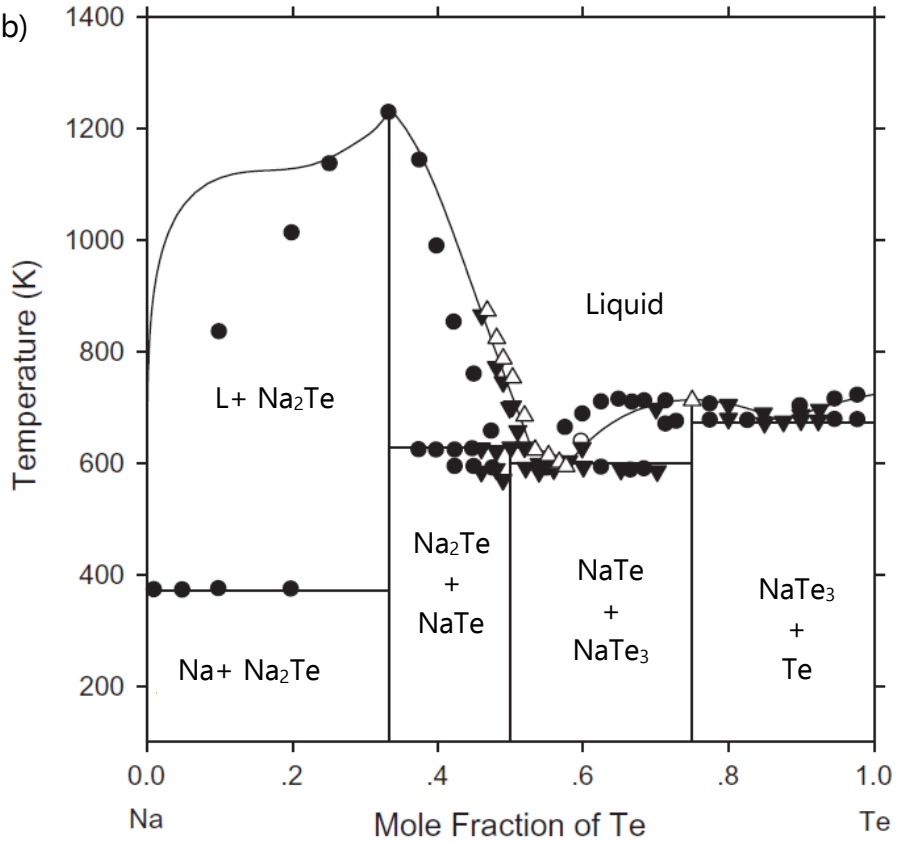
Liquid
L+ Na2Te
Na2Te
+
NaTe
NaTe
+
NaTe3
NaTe3
+
Te
Na+ Na2Te
Temperature (K)
Mole Fraction of Te
Na
Te

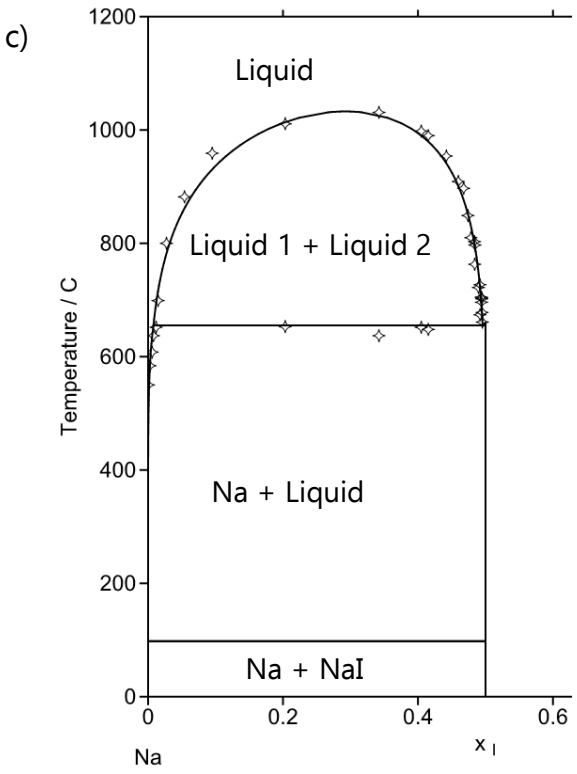

Figure 2.15: Calculated phase diagrams of Cs-Na [38], Na-Te [41] and Na-NaI [43] systems

For the Ba-Na system, the phase diagram data were reviewed by Pelton [39] on the basis of the experimental data of Kanda *et al.* [45] and Addison *et al.* [46] (**figure 2.16)**.

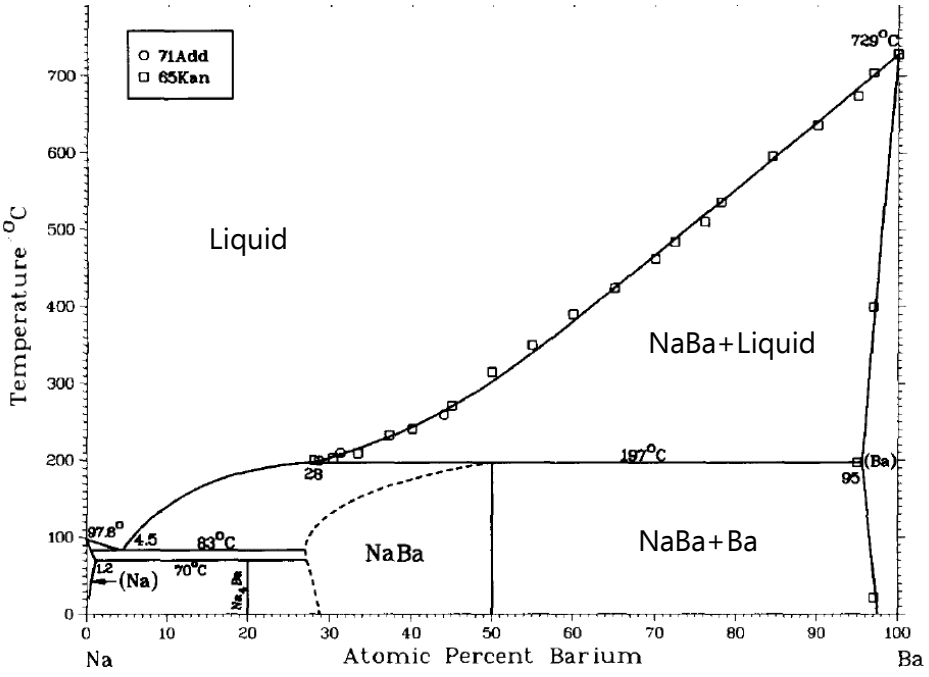

Figure 2.16: Na-Ba phase diagram reported by Pelton [39]

This system has to be modelled using the available experimental data and the review of Pelton [39] (see chapter 7).

To conclude, among the binary sub-systems containing sodium and of interest in this work, only the Ba-Na system has to be modelled.

2.4.2.2. Ternary sub-systems

As previously discussed, the oxygen potential plays a key role on the thermochemistry of the irradiated MOX fuel. Therefore, in this study, a focus on the ternary systems containing oxygen is presented in **table 2.10**.

The models for the Ba-Mo-O and Cs-Mo-O systems, implemented in the TAF-ID database, are described in Chapters 5 and 6.

For other systems, the models are scarce, except for the ternary systems with molybdenum. For the Na-Mo-O system, the pseudo-binary Na_2O-MoO_3 has been assessed by Bordier [47].

Table 2.10: Review of the oxide ternary systems to describe the interaction between sodium and the fission products elements under study in this work. With "Calphad": Calphad model reported in the literature. In green, the Calphad model is implemented in the TAF ID. In orange, the system is not implemented in the TAF-ID database.

System	Na-O	Cs-O	Ba-O	Mo-O	Te-O	I-O
Cs						
Ba						
Mo	Partially known Calphad [47]					
Te			Partially known Calphad [48]			
I						

As shown in **table 2.10**, most of the ternary systems are still unknown. Therefore, priorities in the modelling have to be given to some of these systems.

In this study, the Cs_2O-MoO_3-Na_2O and BaO-Na_2O-MoO_3 pseudo-ternary systems were selected as the main systems to be modelled for the following reasons:

- $BaMoO_4$ and Cs_2MoO_4 are the main compounds forming the JOG which could interact with sodium;
- quaternary compounds were reported to exist in the Ba-Mo-Na-O and Cs-Mo-Na-O systems;
- Na_2O-MoO_3, Cs-Mo-O and Ba-Mo-O sub-systems were modelled and can be used as a starting point to extend the database on both quaternary systems.

2.5. Conclusion

The previous studies on the interaction between sodium and MOX fuel were performed at temperatures from 800 K to 1050 K and no data are available at higher temperatures as the experiments are challenging to perform. Therefore, the approach chosen in the present work is to develop a thermodynamic database with the Calphad method in order to perform calculations in a wide composition and temperature range for severe accident application.

For the Na-O-Pu-U system, experimental data on the Na-O-Pu and Na-O-Pu-U systems are still missing to develop a reliable Calphad model.

Uncertainties remain on the compounds that can form in the Na-O-Pu system. Moreover, the structures of the compounds are not well known and no thermodynamic data have been measured up to now. Thus, a thorough study of the Na-O-Pu system is needed to develop its Calphad model.

For the quaternary system, only one study of the phase diagram was reported with structural data on some quaternary mixed oxides $Na_\alpha(U,Pu)_\beta O_\gamma$. However, only X-ray diffraction analyses were performed. Thus, there is still little knowledge of their crystalline structure. Moreover, the solubility of plutonium and/or uranium in the mixed oxides $Na_\alpha(U,Pu)_\beta O_\gamma$ is not well known and needs to be assessed more precisely. Finally, the thermodynamic properties of these phases have never been measured.

Therefore, a thorough investigation of the Na-O-Pu-U system is needed. The quaternary phases $Na_\alpha(U,Pu)_\beta O_\gamma$ have to be synthesised and characterised. X-ray diffraction experiments coupled with the Rietveld refinement method have to be performed to measure the crystalline structure data for the different phases as a function of the Pu/(U+Pu) ratio. X-ray absorption spectroscopy measurements need also to be performed to determine the oxidation states of uranium and plutonium.

For the fission product systems, many chemical elements are involved. In the present work, the interaction between sodium and the fission products: molybdenum, barium and cesium is investigated. The priority is given to these elements because Cs_2MoO_4 and $BaMoO_4$ are among the main compounds in the JOG layer that could react with sodium in case of an accident. Moreover, the sub-systems Na_2O-MoO_3, Cs-Mo-O and Ba-Mo-O were previously modelled with the Calphad method. These models can be used as a starting point for the development of a database on the Na-Cs-Mo-O and Na-Ba-Mo-O systems.

REFERENCES

[1] P.E. Blackburn., In International Atomic Energy Agency, Proceedings of a Panel on the Behaviour and Chemical State of Irradiated Ceramic Fuels, Organized by International Atomic Energy Agency and Held in Vienna, 7–11 August 1972, IAEA, Vienna, (1974) 393–410.

[2] S. Pillon, Etude des diagrammes de phases U-O-Na, Pu-O-Na, U,Pu-O-Na, 1989.

[3] A.L. Smith, Structural and thermodynamic properties of sodium actinide ternary oxides, PhD Thesis, Department of Materials Science and Metallurgy, University of Cambridge, 2015.

[4] A.L. Smith, P. Martin, D. Prieur, A.C. Scheinost, P.E. Raison, A.K. Cheetham, R.J.M. Konings, Structural Properties and Charge Distribution of the Sodium Uranium, Neptunium, and Plutonium Ternary Oxides: A Combined X-ray Diffraction and XANES Study, Inorg. Chem. 55 (2016) 1569–1579.

[5] A.L. Smith, P.E. Raison, L. Martel, D. Prieur, T. Charpentier, G. Wallez, E. Suard, A.C. Scheinost, C. Hennig, P. Martin, K.O. Kvashnina, A.K. Cheetham, R.J.M. Konings, A New Look at the Structural Properties of Trisodium Uranate Na_3UO_4, Inorg. Chem. 54 (2015) 3552–3561.

[6] A.L. Smith, C. Guéneau, J.-L. Flèche, S. Chatain, O. Beneš, R.J.M. Konings, Thermodynamic assessment of the Na-O and Na-U-O systems: Margin to the safe operation of SFRs, J. Chem. Thermodyn. 114 (2017) 93–115.

[7] P.A.G. O'Hare, W.A. Shinn, F.C. Mrazek, A.E. Martin, Thermodynamic investigation of trisodium uranium(V) oxide (Na_3UO_4), J Chem Thermodyn. 4 (1972) 401–409.

[8] S. Van den Berghe, A. Leenaers, C. Ritter, Antiferromagnetism in MUO_3 (M=Na,K,Rb) studied by neutron diffraction, J. Solid State Chem. 177 (2004) 2231–2236.

[9] Scholder R., Gläser H., Über Lithium- und Natriumuranate(V) und über strukturelle Beziehungen zwischen den Verbindungstypen Li_7AO_6 und Li_8AO_6, Z. Für Anorg. Allg. Chem. 327 (1964) 15–27.

[10] E.H.P. Cordfunke, D.J.W. IJdo, α- and β-Na_2UO_4: Structural and Thermochemical Relationships, J. Solid State Chem. 115 (1995) 299–304. https://doi.org/10.1006/jssc.1995.1137.

[11] D.J.W. IJdo, S. Akerboom, A. Bontenbal, Crystal structure of α- and β-$Na_2U_2O_7$: From Rietveld refinement using powder neutron diffraction data, J. Solid State Chem. 221(2015) 1–4

[12] D.M. Bykov, P.E. Raison, R.J.M. Konings, C. Apostolidis, M. Orlova, Synthesis and crystal structure investigations of ternary oxides in the Na–Pu–O system, J. Nucl. Mater. 457 (2015) 54–62.

[13] M.A. Mignanelli, P.E. Potter, The reactions between sodium and plutonia, urania-plutonia and urania-plutonia containing fission product simulants, J. Nucl. Mater. 125 (1984) 182–201.

[14] C. Keller, L. Koch, K.H. Walter, Die reaktion der oxide der transurane mit alkalioxiden—I: Ternäre oxide der sechswertigen transurane mit lithium und natrium, J. Inorg. Nucl. Chem. 27 (1965) 1205–1223.

[15] M. Housseau, G. Dean, J.P. Marcon, J.F. Marin, Etude hors pile des réactions entre les oxydes d'uranium et de plutonium et le sodium, Note CEA-N-1588. (1973). https://inis.iaea.org/collection/NCLCollectionStore/_Public/04/058/4058558.pdf.

[16] M.G. Adamson, M.A. Mignanelli, P.E. Potter, M.H. Rand, On the oxygen thresholds for the reactions of liquid sodium with urania and urania-plutonia solid solutions, J. Nucl. Mater. 97 (1981) 203–212.

[17] M.A. Mignanelli, P.E. Potter, On the chemistry of the reactions between liquid sodium and urania-plutonia fuel for fast breeder nuclear reactors, Thermochim. Acta. 129 (1988) 143–160.
[18] H. Kleykamp, The chemical state of defective uranium-plutonium oxide fuel pins irradiated in sodium cooled reactors, J. Nucl. Mater. 248 (1997) 209–213.
[19] Y. Guerin, 2.21 - Fuel Performance of Fast Spectrum Oxide Fuel, in: Compr. Nucl. Mater., Elsevier, Oxford, 2012: pp. 547–578.
[20] F. Tête, La réaction Cs_2MoO_4/ Na : Application à l'intéraction combustible / sodium lors d'une rupture de gaine à fort taux de combustion dans un RNR, Université de Provence, 1999.
[21] M. Bober, G. Schumacher, D. Geithoff, Plutonium redistribution in fast reactor mixed oxide fuel pins, J. Nucl. Mater. 47 (1973) 187–197.
[22] Balard, F, Carluec, B, Evaluation of the LMFBR cover gas source terme and synthesis of the associated R & D.
[23] G.L. Cano, G. Karsten, H. Kleykamp, G. Schumacher, Structure and composition changes in nuclear fuel in simulated loss-of-flow transients, J. Nucl. Mater. 127 (1985) 193–204.
[24] A.W. Castleman Jr, I.N. Tang, R.A. Mackay, Fission Product Behavior In Sodium Systems., Brookhaven National Lab., Upton, NY, 1966.
[25] L.E. Herranz, M. García, M.P. Kissane, In-containment source term in accident conditions in sodium-cooled fast reactors: Data needs and model capabilities, Prog. Nucl. Energy. 54 (2012) 138–149.
[26] L.E. Herranz, M.P. Kissane, M. García, Comparison of LWR and SFR in-containment source term: Similarities and differences, Prog. Nucl. Energy. 66 (2013) 52–60.
[27] D.S. Grabaskas, A.J. Brunett, M.D. Bucknor, J.J. Sienicki, T. Sofu, Regulatory Technology Development Plan Sodium Fast Reactor. Mechanistic Source Term Development, 2015.
[28] E.S. Zolotova, Z.A. Solodovnikova, V.N. Yudin, S.F. Solodovnikov, E.G. Khaikina, O.M. Basovich, I.V. Korolkov, I.Yu. Filatova, Phase relations in the Na_2MoO_4 –Cs_2MoO_4 and Na_2MoO_4 –Cs_2MoO_4 –$ZnMoO_4$ systems, crystal structures of $Cs_3Na(MoO_4)_2$ and $Cs_3NaZn_2(MoO_4)_4$, J. Solid State Chem. 233 (2016) 23–29.
[29] A.L. Smith, M.-C. Pignié, L. van Eijck, J.-C. Griveau, E. Colineau, R.J.M. Konings, Thermodynamic study of $Cs_3Na(MoO_4)_2$: Determination of the standard enthalpy of formation and standard entropy at 298.15 K, J. Chem. Thermodyn. 120 (2018) 205–216.
[30] A.L. Smith, G. Kauric, L. van Eijck, K. Goubitz, N. Clavier, G. Wallez, R.J.M. Konings, Structural and thermodynamic study of $Cs_3Na(MoO_4)_2$: Margin to the safe operation of sodium cooled fast reactors, J. Solid State Chem. 269 (2019) 1–8.
[31] A. Förster, H.U. Kreusler, J. Fuchs, Die kristallinen Phasen der Alkalitrimolybdate / The Crystallinic Phases of the Alkali Trimolybdates, Z. Für Naturforschung B. 40 (1985) 1139–1148.
[32] A.D. Pelton, A. Petric, The Na-Te (Sodium-Tellurium) system, J. Phase Equilibria. 11 (1990) 447–451.
[33] H. Kleykamp, The chemical state of the fission products in oxide fuels, J. Nucl. Mater. 131 (1985) 221–246.
[34] T.B. Lindemer, T.M. Besmann, C.E. Johnson, Thermodynamic review and calculations—alkali-metal oxide systems with nuclear fuels, fission products, and structural materials, J. Nucl. Mater. 100 (1981) 178–226.

[35] R. Sabatier, M. Wathlé, J.P. Besse, G. Baud, Perovskites oxyfluorées et oxygénées, J. Inorg. Nucl. Chem. 33 (1971) 1597–1613.
[36] C. Guéneau, N. Dupin, B. Sundman, C. Martial, J.-C. Dumas, S. Gossé, S. Chatain, F.D. Bruycker, D. Manara, R.J.M. Konings, Thermodynamic modelling of advanced oxide and carbide nuclear fuels: Description of the U–Pu–O–C systems, J. Nucl. Mater. 419 (2011) 145–167.
[37] M. Kurata, Thermodynamic Assessment of the Pu-U, Pu-Zr, and Pu-U-Zr Systems, Calphad. 23 (1999) 305–337.
[38] X. Ren, C. Li, Z. Du, C. Guo, Thermodynamic assessments of six binary systems of alkali metals, Calphad. 35 (2011) 446–454.
[39] A.D. Pelton, The Ba- Na (Barium-Sodium) system, Bull. Alloy Phase Diagr. 6 (1985) 26–29.
[40] C. Zhang, M.C. Gao, Y. Yang, F. Zhang, Thermodynamic modeling and first-principles calculations of the Mo–O system, Calphad. 45 (2014) 178–187.
[41] Y. Chen, Y. Liu, M. Chu, L. Wang, Phase diagrams and thermodynamic descriptions for Na–Te and K–Te binary systems, J. Alloys Compd. 588 (2014) 605–610.
[42] T.N. Pham Thi, Caractérisation et modélisation du comportement thermodynamique du combustible RNR-Na sous irradiation, 2014.
[43] A. Dinsdale, J. Gisby, H. Davies, R. Konings, O. Beneŝ, Thermodynamic data to model the interaction between coolant and fuel in gen IV sodium cooled fast reactors, in: 2013 3rd Int. Conf. Adv. Nucl. Instrum. Meas. Methods Their Appl. ANIMMA, 2013: pp. 1–6.
[44] J. Bevan Ott, J. Rex Goates, D. E. Oyler, Solid-liquid phase equilibrium in the sodium-caesium alloy system, Trans. Faraday Soc. 67 (1971) 31–34.
[45] F.A. Kanda, R.M. Stevens, D.V. Keller, The Barium-Sodium Equilibrium System1, J. Phys. Chem. 69 (1965) 3867–3872.
[46] C.C. Addison, G.K. Creffield, P. Hubberstey, R.J. Pulham, The sodium–barium phase diagram, J. Chem. Soc. Inorg. Phys. Theor. (1971) 2688–2691.
[47] S. Bordier, Modélisation thermodynamique des phases insolubles dans les verres nucléaires, (2020) 20.
[48] R. Mishra, S. Phapale, P. Samui, A. Nagaraj, S.R. Dharwadkar, Partial Phase Diagram of $BaO\text{-}TeO_2$ System, J. Phase Equilibria Diffus. 35 (2014) 127–136.

Chapter 3:
Approach

In chapter 1, the key systems that should be studied to describe the interaction between irradiated MOX fuel and sodium were identified:

- Na-O-Pu-U: for the interaction between the MOX fuel and sodium
- Ba-Cs-I-Mo-Na-O-Te: for the interaction between the fission products and sodium.

In this work, the approach is to start the development of a database on these systems using the CALPHAD method with a focus on the binary and ternary sub-systems containing sodium, which is not yet introduced in the TAF-ID database.

However, experimental data are missing on many systems to develop the models.

In chapter 2, after the literature review of the interaction existing with sodium and the selected elements, the following chemical systems were chosen for experimental study:

- Na-O-Pu-U;
- BaO-MoO_3-Na_2O
- Cs_2O-MoO_3-Na_2O.

The investigation of these systems is challenging as the system are highly radioactive and/or sensitive to air and moisture. To perform the experiments, the PhD was organised as summarised in **figure 3.1** and described hereafter.

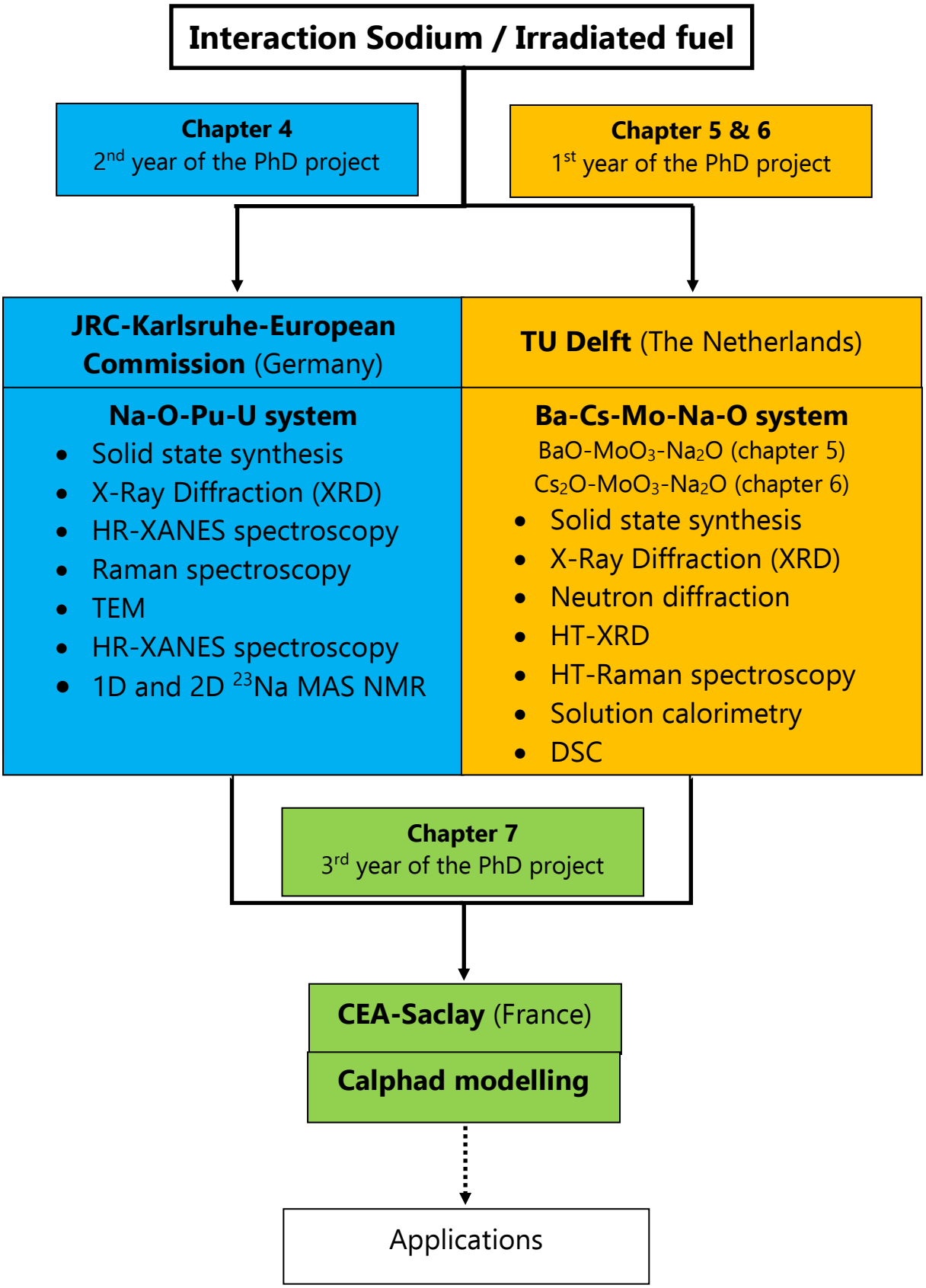

Figure 3.1: The PhD project organisation

During the **first year of the PhD project**, the BaO-MoO_3-Na_2O (Chapter 5) and Cs_2O-MoO_3-Na_2O (Chapter 6) systems were investigated in TU Delft (The Netherlands) in the group of Anna Smith who has a strong experience in the solid state synthesis and thermodynamic measurements on oxide systems and a good knowledge on the Na-O-Pu-U system.

For the BaO-MoO_3-Na_2O system (Chapter 5), a review of the thermodynamic and phase diagram data was first performed.

Then, the $Ba_2NaMoO_{5.5}$ compound was synthesised by solid state synthesis method. The structure of the compound was then characterised by X-ray diffraction (XRD), neutron diffraction, at the 2 MW research reactor of the TU Delft, High Temperature-XRD (HT-XRD), at the JRC-Karlsruhe (European Commission, Germany), and High Temperature Raman spectroscopy (HT-Raman), at Institut de Chimie Séparative de Marcoule (ICSM).

The sample was also analysed by X-ray Analysis Spectroscopy measurements at the European Synchrotron Radiation Facility (ESRF) in Grenoble to investigate the oxidation state and local structure of the molybdenum.

Finally, thermodynamic properties of the compound were measured using Differential Scanning Calorimetry (DSC) and solution calorimetry techniques.

For the Cs_2O-MoO_3-Na_2O system (chapter 6), a literature review was first performed. The different compounds were synthesised by solid state method.

Phase diagram data were measured by DSC in the Cs_2MoO_4-Na_2MoO_4 system.

Then, the structure of the quaternary compounds $CsNaMo_3O_{10}$ and $Cs_3Na(MoO_4)_2$ were characterised by XRD and XAS spectroscopy at the ESRF used for the BaO-MoO_3-Na_2O system.

Finally, DSC experiments to measure the enthalpy of decomposition of the two compounds were performed.

The **second year of the PhD** was dedicated to the experimental study of the Na-O-Pu-U system (chapter 4) at the JRC-Karlsruhe (European Commission, Germany). Experimental work on this system is challenging as it requires the handling of both uranium and plutonium mixed oxide together with sodium. It is the only European facility where such a complex experimental work can be performed. Moreover, high skills, experience and ability on solid state synthesis and thermodynamics measurements on such complex oxide compounds exist there. Karin Popa and Rudy Konings supervised the work at the JRC.

The first step was to synthesise different sodium urano plutonate phases. Batches of nanosized particles of MOX fuels with different Pu/(U+Pu) ratio were produced with the newly developed method by the JRC-Karlsruhe. The interaction products were then synthesised by solid state methods under argon or air atmosphere.

The samples were then characterised using room temperature X-ray diffraction (XRD), solid-state magic angle spinning (MAS) nuclear resonance (NMR) and the two-dimensional multiple quantum MAS (MQ-MAS) methods.

To measure the oxidation state of uranium and plutonium in these compounds, samples were prepared for High energy Resolution-X-ray Analysis Near Edge Spectroscopy (HR-XANES) measurements. The U M_4/Pu M_5 edge HR-XANES spectroscopy measurements were performed at the CAT-ACT beamline for catalysis and actinide research of the KIT synchrotron light source facility (Karlsruhe, Germany).

The **last year of the PhD** was spent at CEA Saclay (France) where Calphad models were developed on the Ba-Na and Cs_2MoO_4-Na_2MoO_4 systems using the data from the literature and experimental data collected during the first year at TU Delft on the Cs_2MoO_4-Na_2MoO_4 system (Chapter 7).

The Calphad model on the Mo-O sub-system had also to be improved to avoid the formation of an unexpected miscibility gap in the liquid state in the ternary systems Cs-Mo-O, Ba-Mo-O and Na-Mo-O.

Finally, the development of a database on the different sodium systems has been started from these models and those available in the literature to be further implemented in the TAF-ID database.

The experimental methods used in this work are described in Appendix A.

Chapter 4:
Experimental study of the Na-O-Pu-U system

As mentioned in Chapter 2, the interaction between sodium and $U_{1-x}Pu_xO_2$ fuel has mainly been studied in the past at temperatures and oxygen potentials corresponding to operating conditions in a nuclear reactor, leading to the formation of the Na_3MO_4 phase. Only Pillon [1] reported data on other phases $Na_\alpha(U_{1-x}Pu_x)_\beta O_\gamma$. However, the experiments were performed for a single Pu/(U+Pu) ratio (x=0.28).

Therefore, in the present study, an experimental structural investigation of several mixed oxides $Na_\alpha(U_{1-x}Pu_x)_\beta O_\gamma$ is carried out, covering a wide range of composition, temperature and oxygen potential conditions. The influence of both the synthesis atmosphere and Pu/(U+Pu) ratio on the structure of the mixed oxides is studied.

Before preparing the sodium urano-plutonate phases, the $U_{1-x}Pu_xO_2$ precursor has to be synthesised. Currently, the Light Water Reactor (LWR) MOX fuel is produced by the MIMAS process ("MIcronized MASter blend") [2], involving several steps and producing a heterogeneous microstructure [3].

A more recent route is used for MOX fuels for Fast Reactors. It is based on the oxalate precipitation and thermal decomposition of the oxalate $(U_{1-x}Pu_x)(C_2O_4)_2{\cdot}nH_2O$ at temperature between 500-800°C [4]. However, in this method, the products are annealed (pre-sintered), resulting in a low specific surface which could be an issue for the investigation of the reaction with sodium. Indeed, from the tests performed by Bykov *et al.* [5] on the Na-Pu-O system and by Pillon [1] on both Na-Pu-O and Na-U-Pu-O systems, it appears that one single phase is challenging to obtain.

Recently, Walter *et al.* [6] developed a new method for the synthesis of AnO_2 (with *An*= Th, U, Np, Pu) and mixed oxides nanocrystals [7] [8]. In this method, the actinide oxalates conversion is performed under an atmosphere of hot compressed water (95-250 °C) and not thermally (thermal decomposition of the oxalate case). The obtained products are spherical shaped agglomerates of nanosized actinide dioxides. With this nanostructure, the specific surface is maximised, which should enhance the reaction between the sodium compound and the nanosized mixed oxide $U_{1-x}Pu_xO_2$. Moreover, this technique is fast, with only small material losses, reproducible, and uses only water as reaction/transport medium. Therefore, this synthesis method was chosen.

In the first section of this chapter, the synthesis and characterisation of the different $U_{1-x}Pu_xO_2$ batches are presented. Then, the syntheses of the ternary $Na_\alpha Pu_\beta O_\gamma$ and quaternary $Na_\alpha(U,Pu)_\beta O_\gamma$ phases are introduced. The structures of the formed phases are also described. Finally, all the structural data are discussed and phase equilibria are suggested.

4.1 Materials synthesis

The uranium and plutonium starting materials were taken from JRC stocks. The isotopic composition of uranium was ^{238}U (natural U) and that of plutonium mainly ^{239}Pu containing about 2% of ^{241}Am.

^{238}U and ^{239}Pu are α-emitters (half-life: 4.47 billion years for ^{238}U and 24131 years for ^{239}Pu) and pose risks if ingested or inhaled. The ^{241}Am coming from the plutonium material is highly radioactive and mainly responsible for the gamma radiations. Therefore, because of the potential health risk, the materials have been handled in glove boxes in properly regulated and controlled radiological facility in JRC-Karlsruhe.

4.1.1 Nanoparticles of $U_{1-x}Pu_xO_2$

For the $U_{1-x}Pu_xO_2$ nanocrystals synthesis, solutions of U^{IV} (0.5 mol/L, obtained by electroreduction of $UO_2(NO_3)_2$ solution in 8 mol/L HNO_3) and Pu^{IV} (0.8 mol/L in 4 mol/L HNO_3) were mixed in the following Pu/(U+Pu) ratio: 0.06; 0.12; 0.25; 0.40. The mixed oxalate $(U_{1-x}Pu_x)(C_2O_4)_2 \cdot nH_2O$ was obtained by direct coprecipitation of the U^{IV} and Pu^{IV} solutions in nitric acid, adding an excess of 1 M solution of oxalic acid. The obtained precipitate was washed several times with distilled water in order to remove any trace of nitrate, which induces the oxidation of U^{IV} to soluble U^{VI} under the working temperature conditions. This method is reported in **figure 4.1** as "Wet route" and compared to the traditional thermal decomposition process. In the following description, the $U_{1-x}Pu_xO_2$ with Pu/(U+Pu) ratio 0.06 will be noted as MOX-6. The MOX-12, MOX-29 and MOX-46 refer to the MOX produced with a theoretical Pu/(U+Pu) ratio =0.12; 0.25; 0.4 respectively.

$$(1\text{-}x)\ UO_2(NO_3)_2 + x\ PuO_2(NO_3)_2 + 2\ H_2C_2O_4 + n\ H_2O$$

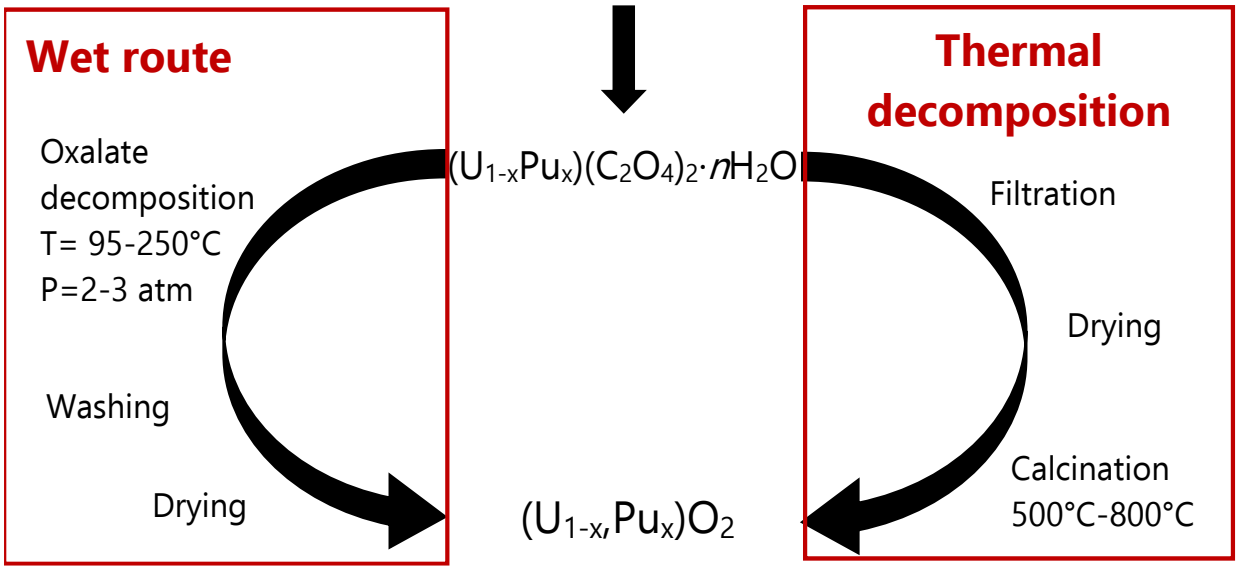

Figure 4.1: Synthesis routes for the $(U_{1-x},Pu_x)O_2$

The oxalate decomposition was then performed in a 25 mL Teflon-lined hydrothermal synthesis autoclave reactor. The thermal treatments were performed by using a heating mantel preheated at the required temperature (200 °C for MOX-6, MOX-12 and MOX-29; 220 °C for MOX-46) while the temperature was controlled by thermocouples. A small amount of water (5 mL) was added to the powder and the obtained suspension mixed by stirring. By heating above the boiling point of water, the added water vaporized and the pressure increased in the autoclave (also due to the gaseous CO and CO_2 formed by decomposition). After a reaction time of four hours, under autogenic pressure (calculated to be of 2-3 bar), the resulting nanocrystals were washed with water, ethanol, and acetone, in order to gradually decrease the polarity of the solution. The work was performed under nitrogen atmosphere, and using small amounts of hydrazine to limit the oxidation of U^{IV}.

The obtained precipitates were then characterised to assess the properties of the $U_{1-x}Pu_xO_2$ nanocrystals.

4.1.1.1. Characterisation by XRD, TEM and ID-TIMS

After the hot compressed water decomposition of the oxalate, the formed nanocrystals of $U_{1-x}Pu_xO_2$ show a fluorite type cubic structure, crystallizing in the $Fm\bar{3}m$ (225) space group. The collected X-ray diffraction patterns are reported in **figure 4.2.** No additional peak was found which shows that the nanocrystals are single phase constituted. More information are reported in **Appendix A.1** on the XRD technique.

The refined cell parameters obtained from the Rietveld refinement of the XRD data are reported in **table 4.1**. In the same table, we report the crystallite sizes for each composition, calculated using the full width at half maximum of at least six selected peaks in the 2θ range between 25 and 100° and measured with TEM (Transmission Electron Microscopy) (see **Appendix A.8**).

The ratio U to Pu of the samples was measured with an ID-TIMS (Isotopic Dilution Thermal Ionisation Mass Spectrometry) measurement (see **Appendix A.7**). The results are also reported in **table 4.1**.

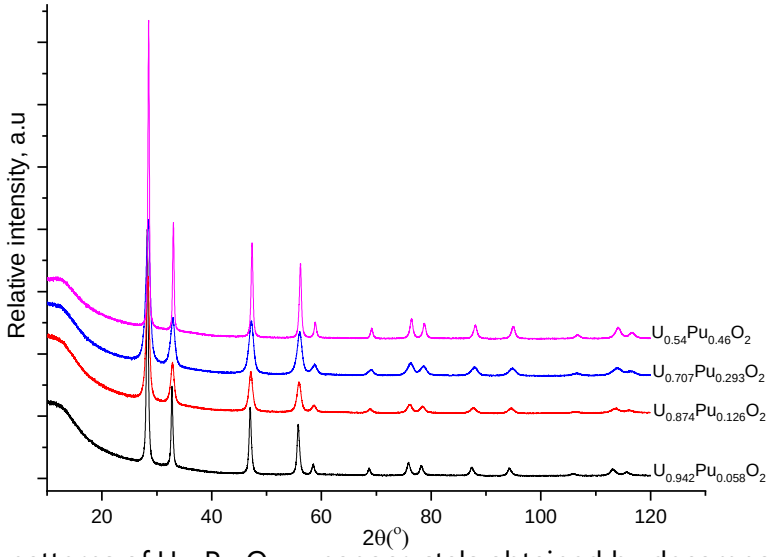

Figure 4.2: XRD patterns of $U_{1-x}Pu_xO_{2(+y)}$ nanocrystals obtained by decomposition of oxalate under the hot compressed water conditions.

Table 4.1: Cell parameters *a* and crystallite diameter *d* obtained from the XRD and TEM results for the different compositions of mixed oxide fuel nanocrystals synthesised

Measured Composition (TIMS)	*a* (Å)	*d* (nm) XRD	*d* (nm) TEM	Reference	Notation
UO_2	5.470 (1)	5.5 ± 0.5	-	[6]	
$U_{0.942}Pu_{0.058}O_2$	5.463 (2)	14 ± 2	11 ± 3 / 55 ± 18	This work	MOX-6
$U_{0.874}Pu_{0.126}O_2$	5.452 (3)	9 ± 1.8	12 ± 3	This work	MOX-12
$U_{0.707}Pu_{0.293}O_2$	5.442 (2)	7 ± 1.4	7 ± 2	This work	MOX-29
$U_{0.54}Pu_{0.46}O_2$	5.436 (1)	19 ± 3	33 ± 12	This work	MOX-46
PuO_2	5.397 (1)	3.6 ± 0.3	-	[6,9]	

The plutonium content for each sample measured by ID-TIMS is consistent with the expected values. The uncertainty on the (Pu/(U+Pu)) content is of 0.005. Nevertheless, a deviation in the Pu/(U+Pu) ratio for MOX-29 and 46 was observed (29 instead of 25 and 46 instead of 40).

The cell parameters refined for all the samples are consistent with Vegard's law. It is apparent in **figure 4.3** that for the MOX-12 and MOX-29 there is a slight deviation from the ideal lattice constant, indicating a possible partial oxidation of the samples.

The TEM analysis reported in **figure 4.4** shows that the nanocrystals are attached to each other forming agglomerates as it has been observed by Popa *et al.* [7] on the pure AnO_2 compounds with An = (Th, U, Np and Pu), and Balice *et al.* [8] on $(U_{1-x},Th_x)O_2$ solid solution. For the mixed oxide MOX-29, the agglomerate sizes are found between 175 and 350 nm.

Moreover, the particle diameter was determined and reported in **table 4.1**. For the MOX-12, MOX-29 and MOX-46, the samples seemed to consist of only one size of particles with a homogeneous distribution, whereas for the MOX-6 two families of particles have been observed. One has an average size of (11±3) nm that fits well with the crystallite size derived from the XRD pattern analysis. The other one has a larger diameter with an average size of (55±18) nm (**figure 4.4*a***). For the three other compositions, there is a good agreement between the two techniques. Moreover, the Pu/(U+Pu) ratios observed in the different nanocrystals did not change substantially, suggesting a homogeneity of the sample.

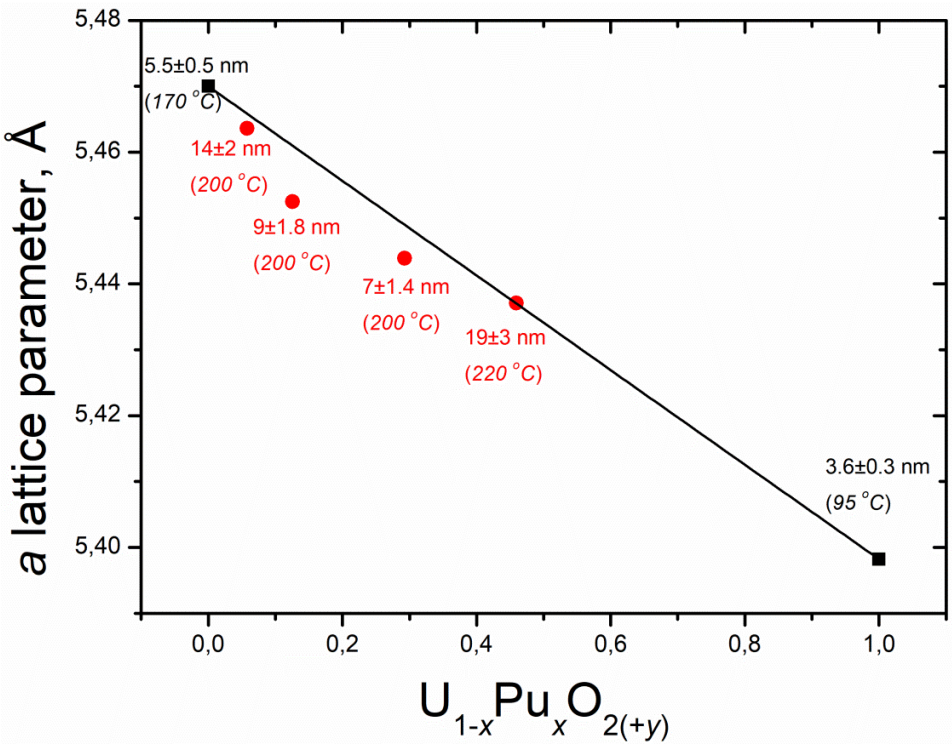

Figure 4.3 Evolution of the lattice parameter as a function of the substitution degree *x* in the $U_{1-x}Pu_xO_{2(+y)}$ solid solutions.

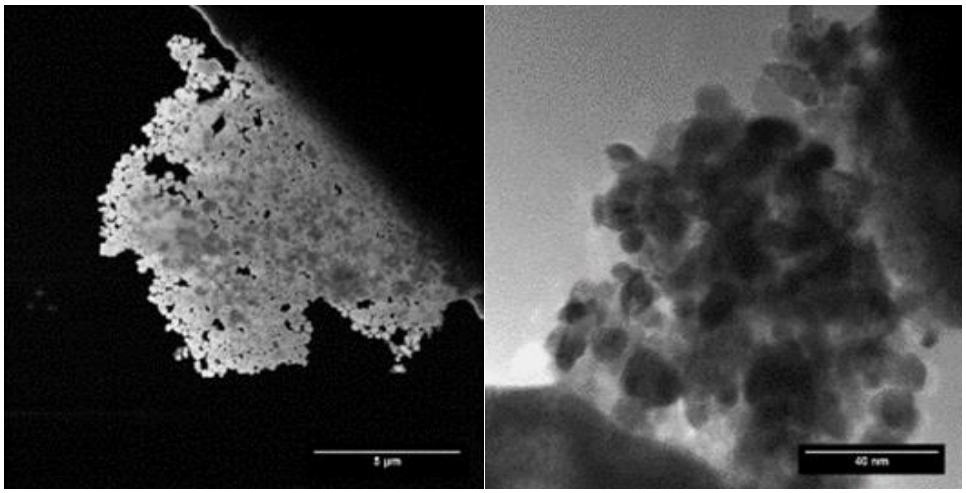

(a) (b)

Figure 4.4: Transmission electron micrographs of nanocrystalline $U_{0.707}Pu_{0.293}O_{2+y}$. In (a), an agglomerate of nanocrystals has been observed; (b) shows a zoom on an agglomerate where nanocrystals can be better observed.

To study the stability of the nanopowders at 800 °C, an annealing treatment of 20 hours under argon atmosphere has been performed for the nanometric $U_{0.707}Pu_{0.293}O_{2+y}$ sample. The XRD pattern is similar to the one before annealing as shown on **figure 4.5**, with increased crystallinity and similar lattice parameter (5.444(1) Å instead of 5.442(2) Å before annealing). After the annealing, a diameter of (33±10) nm was calculated from the XRD experiments, which is in good agreement with the TEM measurements. Moreover, these results follow the trend observed by Popa *et al.* [7] who obtained at 800 °C, a crystallite size ~50 nm for UO_2 and ~20 nm for PuO_2.

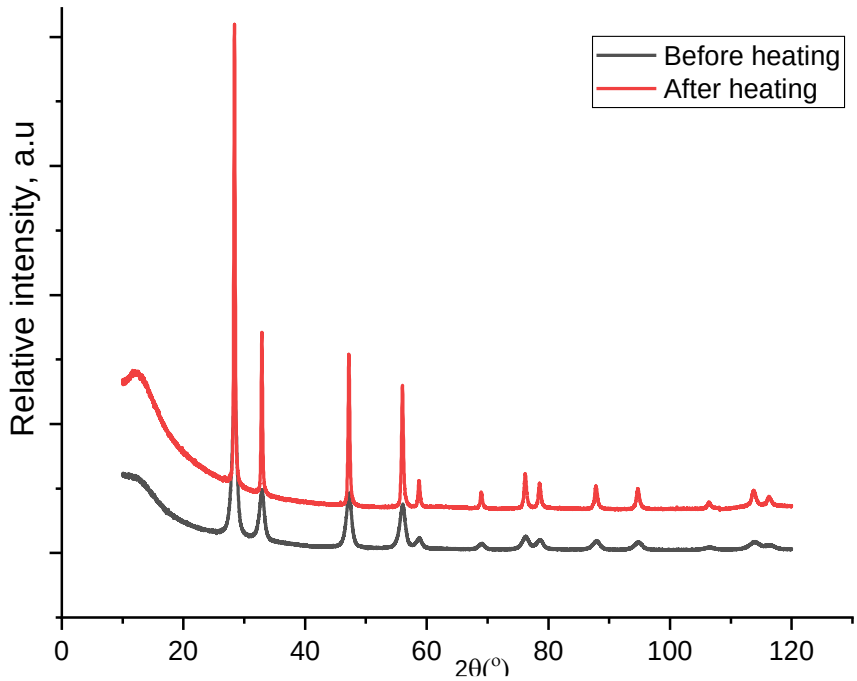

Figure 4.5: XRD pattern of MOX-29 obtained before and after annealing (800°C for 20 h)

4.1.1.2. Characterisation by HR-XANES

Since the 5f valence electrons of U participate in the chemical bonding, changes of electronic structure due to variation of oxidation states and/or atomic environments of the U atoms will be reflected in the U M_4-edge HR-XANES spectrum (see **Appendix A.2.3** for more information on the technique). The U M_4 HR-XANES method mainly probes the bulk of the material and can detect a small amount of one *An* oxidation state in mixtures. One prominent example for *An*-speciation analyses is the ability to clearly resolve U^{V} when it is mixed with U^{IV} [10,11].

Figure 4.6 depicts the U M_4-edge HR-XANES spectra of the three MOX-X (X = 6, 12, 29) compounds synthesised as described previously compared with the bulk $U^{IV}O_2$ and $BiU^{V}O_4$ references.

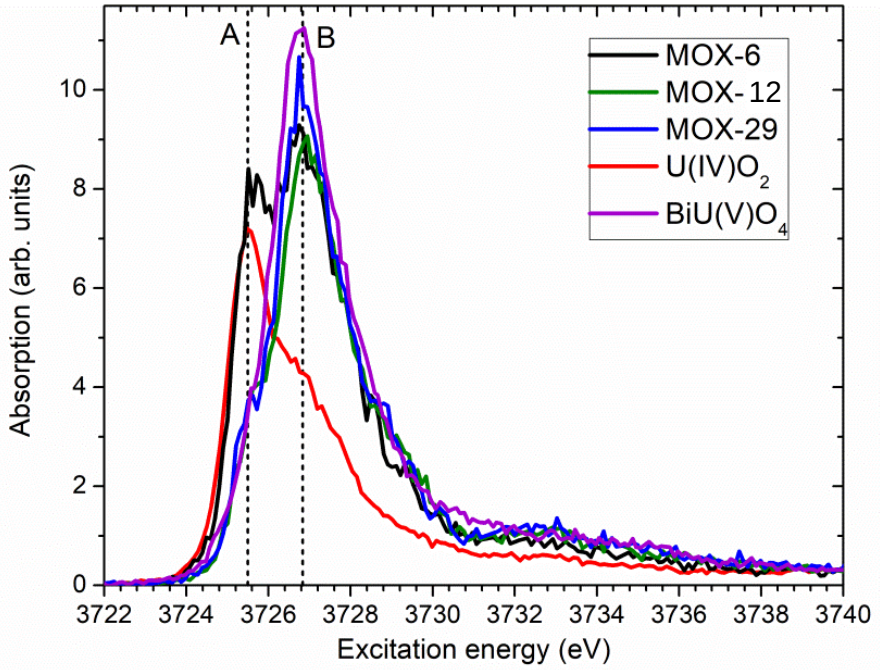

Figure 4.6: U M_4 HR-XANES spectra of the MOX-6, -12 and -29 samples and the $BiU^{V}O_4$ and UO_2 references. Lines A and B mark the peaks characteristic for U^{IV} and U^{V}.

The bulk UO_2 reference contains predominantly U^{IV} and a small amount of U^{V} due to surface oxidation of UO_2 kept in air [10,12]. This is visible in **figure 4.6** since the UO_2 spectrum has a pronounced shoulder on the high energy side of the main absorption peak marked with line B. The energy position of line B is characteristic of the main absorption intensity of U^{V} substituting U^{IV} in the cubic structure of UO_2, *i.e.* UO_{2+y} [10].

The $BiU^{V}O_4$ used as reference, contains U^{V} in a fluorite structure (*Fm-3m*) similarly to U^{IV}/U^{v} in UO_2/UO_{2+y} therefore it is a very suitable U^{V} reference compound [11]. The main absorption peak of the spectrum of $BiU^{V}O_4$ is also located at the energy position of line B.

The spectra contain characteristic peaks for U^{IV} (line A) and U^{V} (line B), which are about 1.1 eV apart. U^{V} dominates in the MOX-29 and MOX-13 samples. U^{V} and U^{IV} have comparable contributions in MOX-6. The smaller particles size of MOX-29 and MOX-13 (7 and 9 nm, respectively) compared to MOX-6 (14 nm) (cf. **Table 4.1**) leads to larger surface area; hence we assume that more U atoms oxidize from U^{IV} to U^{V} on the surface of the particles. This assumption is based on the correlation between the decreases of the size of the particles with the increase of the U^{v} content revealed by the U M_4 edge HR-XANES spectra.

Another contribution to the uranium oxidation from IV to V is given by the presence of about 2% of americium in the original plutonium vector; thus, the MOX-46 would contain close to 1% Am out of the total of the actinides in the sample. It has been shown that substitution of tetravalent uranium with trivalent ions such as americium is compensated by the oxidation of U^{IV} to U^{V}[13]. Moreover, charge compensation in the Am/Pu system is also possible [14] and cannot be excluded at this stage.

4.1.1.3. Conclusion

To conclude, four batches of $U_{1-x}Pu_xO_2$ were synthesised using the hot compressed water decomposition process. The different powders produced were first analysed by X-ray diffraction (XRD) at room temperature in order to (i) check their purity, (ii) to assess the U to Pu ratio derived from Vegard's law and (iii) to evaluate the diameter of the nanocrystals. The Pu/(U+Pu) ratio was also precisely measured by Thermal Ionization Mass Spectrometry (TIMS). Then, to characterize the electronic and structural properties of the prepared mixed oxide fuels, nanocrystals were analysed by U M_4 High-energy Resolution X-ray Absorption Near Edge Spectroscopy (HR-XANES) and Transmission Electron Microscopy (TEM).

This synthesis method is promising for low temperature production of mixed oxides powders and opens research opportunities, which are not accessible using bulk materials. Moreover, they were used as standards in order to study the environmental dispersion of nuclear materials by Colle *et al.* [15].

These samples were then used as precursors to synthesize sodium urano plutonates. It is worth noting that a fifth batch has been prepared with a theoretical Pu/(U+Pu) ratio of 0.85. Nevertheless, only XRD data were collected and unreacted oxalate has been identified. Therefore, the data were not presented here. However, a synthesis test was performed with this MOX-85 composition as reported in the following section.

4.1.2 $Na_\alpha(U_{1-x}Pu_x)_\beta O_\gamma$ phases

As described in chapter 2, the physico-chemical conditions, especially the oxygen potential will have a strong impact on the oxygen stoichiometry and structure of the product obtained after interaction between MOX fuel and sodium. Therefore, syntheses under argon atmosphere are first presented, as this atmosphere is closer to the in-pile conditions. However, to develop a Calphad model, all the compounds have to be studied, thus syntheses under air atmosphere have also been performed to form compounds with higher actinide oxidation states and oxygen content. In the following section the composition are noted $Na_\alpha M_\beta O_\gamma$ with $M=(U_{1-x},Pu_x)$. Unfortunately, the Pu/(U+Pu) ratio in these mixed oxides cannot be assessed from the XRD analysis.

4.1.2.1. Ternary compounds Na_2PuO_3 and Na_4PuO_5

Na_2PuO_3 compound was synthesised by reaction between stoichiometric amounts of PuO_2 nano-powder provided from the stocks of JRC-Karlsruhe and sodium hydroxide NaOH (Sigma-Aldrich, >97%, pellet) stored under nitrogen atmosphere. The mixture was placed in alumina crucible and heated at 850°C in a tubular furnace under argon flow during 24 hours with an intermediate regrinding step. No reaction was observed between the mixture and the crucible.

(1) $2\ NaOH + PuO_2 \xrightarrow{Argon,850°C,12h+12h} Na_2PuO_3 + H_2O$

A similar procedure was applied for the Na_4PuO_5 compound with a mixture heated under air flow at 850°C.

(2) $4\ NaOH + PuO_2 \xrightarrow{Air,850°C,12h+12h} Na_4PuO_5 + 2\ H_2O$

The compounds were then analysed by XRD. No additional peaks in the Na_2PuO_3 sample was found whereas ~5% of unreacted PuO_2 was observed in the Na_4PuO_5 XRD analysis.

4.1.2.2. Quaternary phases under argon

As a preliminary test, MOX-6 was used to prepare the different phases Na_2MO_3, Na_3MO_4 and Na_4MO_5 phases with (1:1), (1.5:1) and (2:1) ratio of Na_2O/ $U_{0.942}Pu_{0.058}O_{2+y}$ (MOX-6).

As pure Na_2O is not available commercially, Na_2O was produced in situ by thermal decomposition of NaOH [16] or Na_2CO_3 as shown in equations (3) and (4).

(3) $4\ NaOH + MO_{2+y} \rightarrow 2\ Na_2O + 2\ H_2O + MO_{2+y}$

(4) $2\ Na_2CO_3 + MO_{2+y} \rightarrow 2\ Na_2O + 2\ CO_2 + MO_{2+y}$

Precisely weighted amounts of NaOH (Sigma-Aldrich, >97%, pellet) or Na_2CO_3 (Sigma-Aldrich,>99.5%) stored under nitrogen atmosphere, were ground together with the

MO_{2+y} nanopowders. The mixtures were then heated in a tubular furnace under argon flow at 800°C during 24 hours with a regrinding step.

For the (1:1) and (1.5:1) ratios, many peaks were observed and no single phase was obtained. Thus, the results are not discussed in this work.

In that section, the expected compound forming is highlighted in bold in the different tables (**Tables 4.2 to 4.5**) describing the phases observed from the Le Bail refinement (see **Appendix A.1**) of the XRD data. Furthermore, the phases are organised from the main phase observed to the lowest one based on the peak intensities.

Only the batches with (2:1) ratios produced a single mixed oxide phase corresponding to the Na_4MO_5 phase. For the batch defined as "NaOH-test" (corresponding to the product obtained after reaction of NaOH precursor in a (2:1) ratio), no MOX phase remained, whereas in the "Na_2CO_3-test" unreacted MOX fuel was observed.

As a single phase was obtained after the reaction with NaOH in a (2:1) ratio of Na_2O/ $U_{0.942}Pu_{0.058}O_{2+y}$ (MOX-6), the (2:1) ratio and NaOH reagent were chosen for syntheses of Na_4MO_5 with MOX-12, 29 and 46. The synthesis attempts of Na_4MO_5 and the XRD results are reported in **table 4.2**.

Table 4.2: Experimental conditions for the syntheses of Na_4MO_5 under argon at 800°C.

Pu/(U+Pu)	Batch Name	Ratio Na_2O/MO_2	Heating (°C) /dwell (h)	Phases observed
0.058	NaOH-test	(2:1)	800/12+12	**Na_4MO_5**
0.058	Na_2CO_3-test	(2:1)	800/12+12	**Na_4MO_5** + MO_2
0.058	Batch 1.2	(2:1)	800/12+50	**Na_4MO_5** + Na_3MO_4 + $NaMO_3$ + MO_2
	Batch 1.3	excess Na_2O	800/20	**Na_4MO_5** + MO_2
0.126	Batch 1.2	(2:1)	800/12+50	Na_3MO_4 +**Na_4MO_5** + MO_2
	Batch 1.3	excess Na_2O	800/20	**Na_4MO_5**
0.126	Batch 2	(2.1:1)	800/20	**Na_4MO_5** + MO_2
0.293	Batch 1.2	(2:1)	800/12+50	**Na_4MO_5** + MO_2
	Batch 1.3	excess Na_2O	800/20	**Na_4MO_5** + Na_2MO_3 + MO_2
0.293	Batch 2	(2.2:1)	800/20	**Na_4MO_5** + Na_2MO_3
0.46	Batch 1.2	(2:1)	800/12+50	MO_2 + Na_3MO_4 + **Na_4MO_5**
	Batch 1.3	excess Na_2O	800/20	Na_2MO_3 + **Na_4MO_5**
0.46	Batch 2	(2.2:1)	800/20	Na_2MO_3
0.85	Batch 2	(2.4:1)	800/20	Na_2MO_3

The mixtures of NaOH and MO_{2+y} (MOX-6, 12, 29 and 46) were thermally treated in a furnace under argon flow at 800°C to form the Na_4MO_5 phase as described in **table 4.2**.

In the first synthesis attempt, "Batch 1.1" (800 °C / 12 hours), two cubic phases were observed with lattice parameters corresponding to the values of Na_3MO_4 and MO_2 as reported in **table 4.3**.

After the long thermal treatment (800°C / 50 hours, Batch 1.2), the tetragonal phase assigned to the Na_4MO_5 phase was formed as reported in **table 4.2**. In "Batch 1.2", the fraction of Na_4MO_5 increased while the intensity of the peaks assigned to Na_3MO_4 structure decreased, and the peaks corresponding to MO_2 remained similar to those observed in the XRD data obtained after the first thermal treatment.

To try to obtain a single phase, as a similar amount of unreacted MO_2 was found after the first (Batch 1.1) and second heat treatment (Batch 1.2), an excess of Na_2O corresponding approximatively to the quantity of unreacted MOX (estimated from Rietveld refinement) was added to the "Batch 1.2" and heated at 800°C for 20 hours (Batch 1.3). The different observed phases for "Batch 1.3" are reported in **table 4.2**.

Other batches where NaOH was added in excess from the beginning (ratio (2.1:1), (2.2:1) and (2.4:1)) before a 20 hours thermal treatment were synthesized and are called "Batch 2" in **table 4.2**.

In these different tests, Na_4MO_5 was obtained as one single phase for Pu/(U+Pu)=0.06 and a (2:1) ratio and Pu/(U+Pu)=0.126 with a ratio in (Na_2O:MO_2) higher than the (2:1) ratio. For other compositions, a mixture of several phases was obtained.

Finally, a test with MOX-85 and an excess of NaOH was performed and is therefore reported as "Batch 2" in **table 4.2**. The pure Na_2MO_3 was obtained. It is worth noting that Na_2MO_3 phase was also obtained as a one single phase for a (2.2:1) ratio at and Pu/(U+Pu)=0.46.

To identify the phases in the samples, XRD patterns were refined using the Le Bail method. The composition, structure and cell parameters of the obtained phases are discussed in section 4.2.2.

In "Batch 1.1" the cubic phase Na_3MO_4 was observed. However, residual MO_2 remained for all Pu contents in the MOX as reported in **table 4.3**.

Table 4.3: Experimental conditions for the Na_3MO_4 syntheses at 800°C.

Pu/(U+Pu)	Batch Name	Ratio Na_2O/MO_2	Heating (°C) /dwell (h)	Phases observed
0.058	Batch 1.1	(2:1)	800/12	**Na_3MO_4** + MO_2
0.058	Na_2CO_3-3h	(2:1)	800/3	**Na_3MO_4** + MO_2 + Na_2CO_3 + Na_2MO_3 + $NaMO_3$
0.126	Batch 1.1	(2:1)	800/12	**Na_3MO_4** + MO_2
0.126	Na_2CO_3-3h	(2:1)	800/3	**Na_3MO_4** + MO_2 + Na_2CO_3 + Na_2MO_3 + $NaMO_3$
0.293	Batch 1.1	(2:1)	800/12	**Na_3MO_4** + MO_2
0.293	Na_2CO_3-3h	(2:1)	800/3	**Na_3MO_4** + MO_2 + Na_2CO_3 + Na_2MO_3 + $NaMO_3$
0.46	Batch 1.1	(2:1)	800/12	**Na_3MO_4** + MO_2
0.46	Na_2CO_3-3h	(2:1)	800/3	**Na_3MO_4** + MO_2 + Na_2CO_3

After a second thermal treatment (Batch 1.2), the phase Na_4MO_5 phase was formed (see **table 4.2**). The actinide is more oxidised in this compound than in Na_3MO_4. Therefore, in the attempt to synthesise a batch with a single phase Na_3MO_4, a reaction with Na_2CO_3 was also tested, as CO_2 is released instead of water, leading to less oxidizing conditions.
Precisely weighted amounts of Na_2CO_3 were mixed in stoichiometric ratio with $U_{1-x}Pu_xO_2$ batches. The mixtures were heated for 3 hours at 800°C, under argon flow inside a tubular furnace. This short reaction time was used to minimize the possible oxidation of the sample observed after a long time. The obtained samples were constituted of several phases (Na_3MO_4, Na_2MO_3, $NaMO_3$), unreacted MOX and Na_2CO_3 as shown in **table 4.3**.

Therefore, the equilibrium after 3 hours reaction at 800°C was not reached, as Na_2CO_3 and MO_2 were observed.

To synthesize a single phase of Na_3MO_4, a 12 hours thermal treatment at 1000°C was performed, as Pillon [1] reported that the formation reaction of Na_3MO_4 was total at this temperature. In our case, the Na_3MO_4 phase disappeared and the phases (Na_4MO_5 and Na_2MO_3) were obtained as presented in **table 4.4**.

Therefore, it was not possible to synthesize the pure Na_3MO_4 phase.

Table 4.4: Experimental conditions for the Na_4MO_5 syntheses at 1000°C.

X(Pu)	Batch Name	Ratio Na_2O/MO_2	Heating (°C) /dwell (h)	Phases observed
0.058	Na_2CO_3	(2:1)	800/3+1000/12	**Na_4MO_5**
0.126	Na_2CO_3	(2:1)	800/3+1000/12	**Na_4MO_5** + Na_2MO_3
0.293	Na_2CO_3	(2:1)	800/3+1000/12	**Na_4MO_5** + Na_2MO_3
0.46	Na_2CO_3	(2:1)	800/3+1000/12	**Na_4MO_5** + Na_2MO_3 + MO_2

4.1.2.3. Quaternary phases under air

Finally, syntheses under air were performed to prepare phases with higher oxygen content such as Na_2MO_4 (1:1) or $Na_2M_2O_7$ (1:2). Precisely weighted amounts of NaOH were ground together with the MO_{2+y} nanopowders and heated under air at 800°C for 20 hours. The obtained phases are reported in **table 4.5**.

Pure compounds Na_2MO_4 for MOX-6 and $Na_2M_2O_7$ for MOX-6 and MOX-12 were successfully obtained whereas a mixture of three phases was found for MOX-46.

Table 4.5: Experimental conditions for the sodium mixed oxide syntheses at 800°C under air.

X(Pu)	Batch Name	Ratio Na_2O/MO_2	Heating (°C) /dwell (h)	Phases observed
0.058	NaOH	(1:1)	800/20	**Na_2MO_4**
0.058	Na_2CO_3	(1:1)	800/20	**Na_2MO_4**
0.058	NaOH	(1:2)	800/20	**$Na_2M_2O_7$**
0.126	NaOH	(1:1)	800/20	**Na_2MO_4** + MO_2
0.126	NaOH	(1:2)	800/20	**$Na_2M_2O_7$**
0.46	NaOH	(1:1)	800/20	**Na_2MO_4** + Na_4MO_5 + MO_2
0.46	NaOH	(1:2)	800/20	**$Na_2M_2O_7$** + Na_2MO_4 + MO_2

4.1.2.4. Conclusion

After the heat treatments under argon, the Na_4MO_5 phase was successfully obtained pure only for MOX-6 and MOX-12. At high Pu/(U+Pu) ratio (MOX-46 and 85), the Na_2MO_3 phase was also synthesised pure.

The Na_3MO_4 phase was always observed with residual MO_2. After subsequent attempts to form pure Na_3MO_4, the Na_4MO_5 phase was obtained.

After the heat treatments under air, the Na_2MO_4 and $Na_2M_2O_7$ phases were successfully prepared pure for MOX-6 (Na_2MO_4 and $Na_2M_2O_7$) and MOX-12 ($Na_2M_2O_7$), respectively.

Some of the synthesis attempts led to pure phases. However, in most cases, mixtures of sodium urano-plutonate phases were obtained.

In the next section, the XRD results for each phases are discussed separately.

4.2 Structural investigation

The characterisations of the phases using XRD are discussed in this section (see **Appendix A.1** for the description of the technique). Moreover, when possible, HR-XANES at U M_4-edge and Pu M_5-edge, solid-state magic angle spinning (MAS) nuclear resonance (NMR) and the two-dimensional multiple quantum MAS (MQ-MAS) experiments were performed. Information on the NMR techniques are reported in **Appendix A.3**.

4.2.1 $Na_\alpha Pu_\beta O_\gamma$ compounds

To understand the structural evolution of the mixed oxides with plutonium content, a thorough knowledge of the structure of the end-members is mandatory. Many open questions are remaining on the Na-O-Pu ternary phase diagram, which is not modelled yet. Therefore, a structural study of the Na_2PuO_3 and Na_4PuO_5 compounds is presented hereafter.

4.2.1.1. The Na_2PuO_3 compound

As described in the literature review, a discrepancy between the works of Smith [17] and Bykov *et al.* [5] exists on the structure of Na_2PuO_3. Bykov *et al.* [5] refined the compound in $R\bar{3}m$ space group with two sodium sites whereas Smith [17] refined it in the *C2/c* space group with four sodium sites as shown in **tables 4.6** and **4.7**, respectively. The structure proposed by Bykov et al. [17] were not reproducing the reflexions observed at 2θ angles between 17 and 23°.

To solve this discrepancy, pure Na_2PuO_3 was synthesised in this work (see section 4.1.2.1). The two possible structures were tested and the present XRD pattern was finally refined in the *C2/c* space group as "goodness of the fit was better" (see **figure 4.7** and **table 4.9**). This structure was also supported by the ^{23}Na-NMR results presented hereafter. As shown in **table 4.8 and 4.9**, the obtained cell parameters and atomic positions are in good agreement with the values reported by Smith [17].

Table 4.6: Na_2PuO_3 structure reported by Bykov *et al* [5]

Atom	Wyckoff	x	y	z	B_0(Å^2)	Occ.
Na1	3a	0	0	0	1.529	1
Na2	3b	0	0	0.5	3.834	0.333
Pu	3b	0	0	0.5	0.235 (3)	0.667
O	6c	0	0	0	1.2	1

Table 4.7 Na_2PuO_3 structure reported by Smith [17].

Atom	Oxidation State	Wyckoff	x	y	z	$B_0(Å^2)$	Occ.
Pu1	+4	4e	0	0.835(5)	0.25	0.27 (2)	0.35
Na1	+1	4e	0	0.835(5)	0.25	0.27 (2)	0.65
Pu2	+4	4e	0	0.169(3)	0.25	0.27 (2)	0.65
Na2	+1	4e	0	0.169(3)	0.25	0.27 (2)	0.35
Pu3	+4	4e	0	0.498(2)	0.25	0.27 (2)	1
Na3	+1	4a	0	0	0	0.27 (2)	1
Na4	+1	8f	0.036(4)	0.340(4)	0.013(2)	0.27 (2)	1
O1	-2	8f	0.247(8)	0.495(9)	0.142(4)	1.00 (8)	1
O2	-2	8f	0.249(9)	0.141(5)	0.175(3)	1.00 (8)	1
O3	-2	8f	0.271 (9)	0.839(9)	0.132(4)	1.00 (8)	1

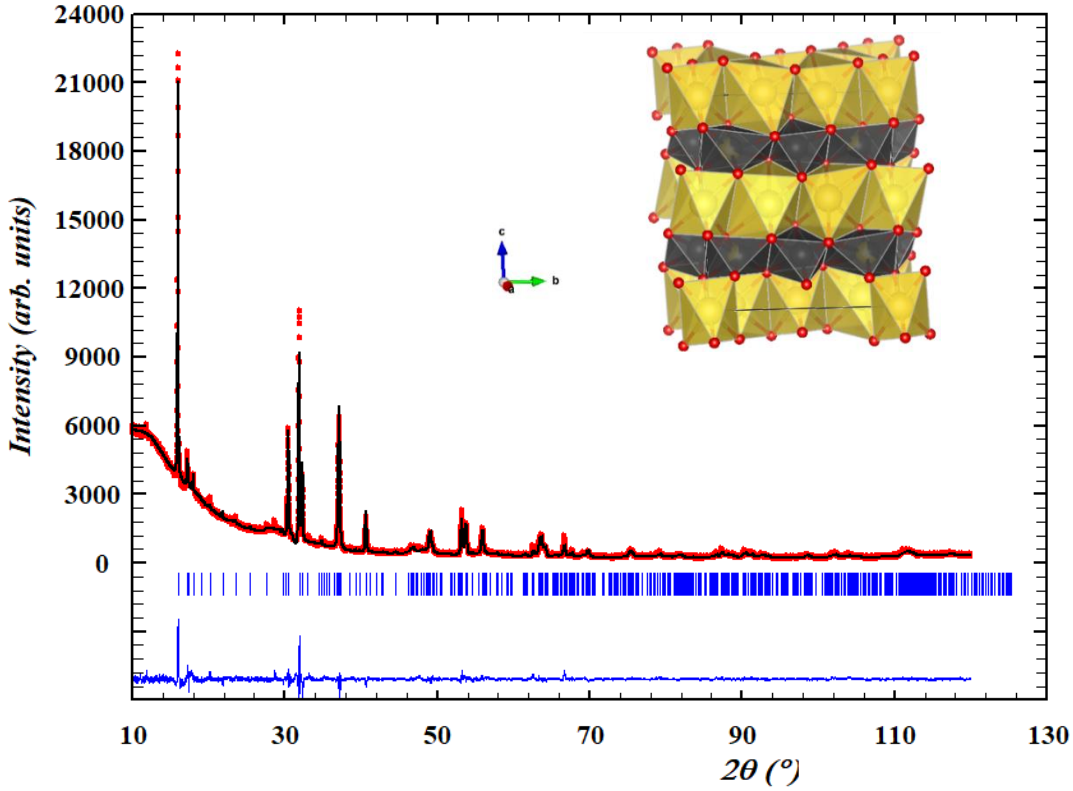

Figure 4.7: Comparison between the observed (Y_{obs}, in red) and calculated (Y_{calc}, in black) X-ray diffraction patterns of Na_2PuO_3. Y_{obs}-Y_{calc}, in blue, is the difference between the experimental and calculated intensities. The Bragg reflections' angular positions are marked in blue. Measurement at λ=Cu-Kα1.

Table 4.8: Na_2PuO_3 cell parameters in *C2/c* space group

a (Å)	b (Å)	c (Å)	β (°)	Ref
5.965 (3)	10.313 (3)	11.772 (3)	109.97 (1)	Smith [17]
5.964 (3)	10.312 (4)	11.778 (4)	109.93 (3)	This work

Table 4.9: Refined atomic positions of Na_2PuO_3 in *C2/c* space group
R_{wp} = 20.9, R_{exp} = 10.98, χ^2 = 3.63

Atom	Oxidation State	Wyckoff	x	Y	z	B_0(Å^2)	Occ.
Pu1	+4	4e	0	0.843 (8)	0.25	0.27	0.35
Na1	+1	4e	0	0.843 (8)	0.25	0.27	0.65
Pu2	+4	4e	0	0.171 (6)	0.25	0.27	0.65
Na2	+1	4e	0	0.171 (6)	0.25	0.27	0.35
Pu3	+4	4e	0	0.500 (6)	0.25	1.1 (4)	1
Na3	+1	4a	0	0	0	0.27	1
Na4	+1	8f	0.004 (5)	0.344 (2)	0.012(2)	0.27	1
O1	-2	8f	0.282 (6)	0.497 (5)	0.132(3)	1.00	1
O2	-2	8f	0.26(1)	0. 83(5)	0.154(3)	1.00	1
O3	-2	8f	0.238 (78)	0.126(3)	0.177(3)	1.00	1

As mentioned previously, the compound was also analysed using 1D and 2D ^{23}Na MAS NMR experiments. As shown in **figure 4.8**, by combining these two experiments four sodium sites were identified and differentiated (red squares) in the structure. There is an inherent disorder for all four sites. As four crystallographic sites contain sodium atoms, these results support the statement that Na_2PuO_3 crystallizes in the *C2/c* space group as suggested by Smith [17].

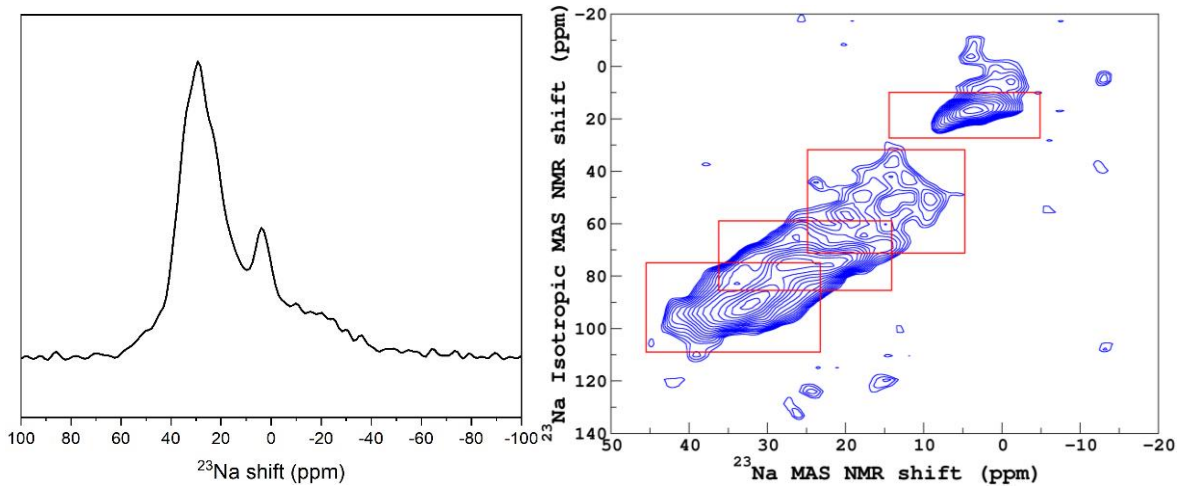

Figure 4.8: ^{23}Na central transition MAS-NMR spectra of $Na_2Pu^{IV}O_3$ recorded using a) a single $\pi/12$ impulsion and b) an MQMAS experiment. In red rectangles, we identify the four different sodium sites.

In **figure 4.9**, the HR-XANES measurement of Na_2PuO_3 sample at Pu M_5-edge is reported. As for uranium, the 5f valence electrons of plutonium participate in the chemical bonding. Therefore, the changes of electronic structure due to variation of oxidation states and/or atomic environments of the plutonium atoms will be well reflected in the Pu M_5-edge HR-XANES spectra [18].

The white line (maximum intensity) of the Na_2PuO_3 compound is at the same energy as the $Pu^{IV}O_2$ used as reference for Pu^{IV}, and the specific features (in dashed line) of the Pu^{IV} are found in the post-edge region. Therefore, in $Na_2Pu^{IV}O_3$, plutonium is in the +IV oxidation state and can be used as a reference for sodium plutonate with Pu^{IV}.

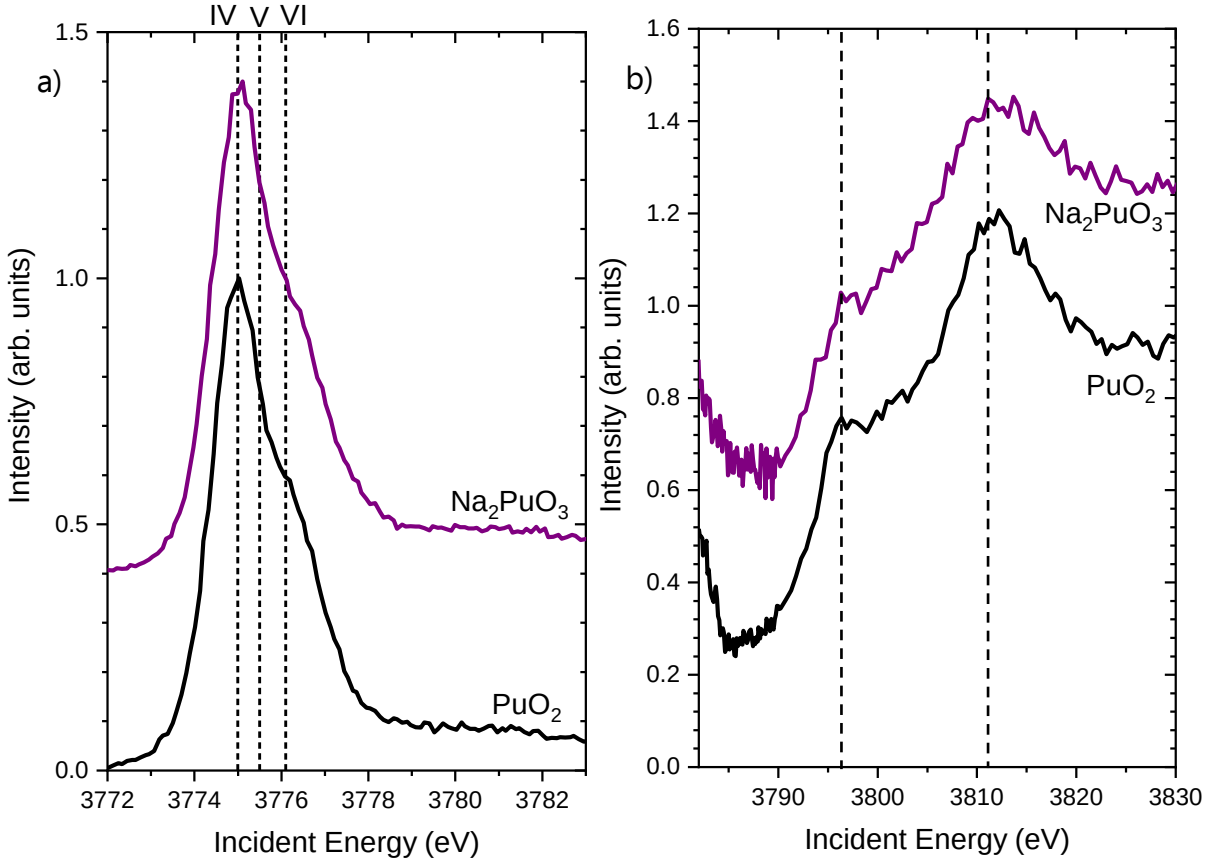

Figure 4.9: Pu M_5-edge HR-XANES (a) and post-edge (b) spectra of $Na_2Pu^{IV}O_3$ sample and $Pu^{IV}O_2$ reference. (Spectra have been shifted on the y axis to better distinguish the different measurement)

The discrepancy raised between the previous works and the re-assessment of the $Na_2Pu^{IV}O_3$ structure made by Smith [17] has been solved combining several methods: XRD, HR-XANES, 1D and 2D ^{23}Na MAS NMR methods, which confirm the *C2/c* space group for the Na_2PuO_3 compound synthesized here under argon at 850°C. Therefore, the Na_2PuO_3 end-member and Na_2MO_3 solid solutions obtained in this work are refined in the *C2/c* space group.

4.2.1.2. The Na_4PuO_5 compound

Bykov *et al.* [5] managed to synthesize Na_4PuO_5 using Na_2CO_3 as precursor under air atmosphere, which is isostructural with Na_4UO_5 in space group *I4/m* (n°87). However, the cell parameters were higher than the one previously reported by Keller *et al.* [19] who used Na_2O_2 as sodium source in the synthesis (**table 4.10)**. While attempting a direct synthesis using Na_2O as starting reagent under air, Pillon [1] obtained similar cell parameters as Bykov *et al.* [5], which are both reported in **table 4.10**. Due to the handling restrictions on samples containing plutonium, these different works only reported XRD data.

Finally, Smith *et al.* [20] performed XANES spectroscopy measurement on Na_4PuO_5 at the Pu L_3-edge. Nevertheless, no Pu^{VI} reference was measured and the oxidation state was attributed based on the energy shift (0.8 eV) of the inflexion point from the one of Pu^{IV} observed. Conradson *et al.* [21] measured several reference compounds and found a shift of 1.4 eV for Pu^{VI} compounds. As the uncertainty of the measurement is 0.5 eV for the XANES spectroscopy measurements of Smith *et al* [21], the energy of the inflexion point of the Na_4PuO_5 was attributed to Pu^{VI}.

Nevertheless, the white line reported by Smith *et al.* [20] for Na_4PuO_5 is lower than the PuO_2 reference measured (energy shift -0.3). The negative shift for Pu^{V} compound is reported in the work of Conradson *et al.* [21] and Kvashnina et al. [22] (energy shift -1.4 and -1.7 eV, respectively) whereas the Pu^{VI} compound is reported with a positive shift (energy shift +1.2 eV). Therefore, the shift reported by Smith *et al.* [20] for the Na_4PuO_5 is not consistent with the work of Conradson *et al.* [21].

Kvashnina *et al.* [22] finally precisely attributed the oxidation state of plutonium compound using HR-XANES experiments at the Pu $M_{4,5}$-edges as more information on the oxidation state and electronic structure are obtained at $M_{4,5}$-edges than at the L_3-edge (see **Appendix A.2.3**). Therefore, a structural re-investigation of the compound using complementary techniques, especially HR-XANES at Pu M_5-edge, has been initiated here.

The Na_4PuO_5 synthesised in this work (see section 4.1.2.1) has been obtained with only minor amounts of unreacted PuO_2 (5.6% weight fraction from the Rietveld analysis) as shown in **figure 4.10**. A Rietveld refinement using the structure reported by Bykov *et al.* [5] with one sodium site has been performed. The reported cell parameters and structure are similar to those reported by Pillon [1], Smith *et al.* [20] and Bykov *et al.* [5] as shown in **table 4.10 and 4.11**.

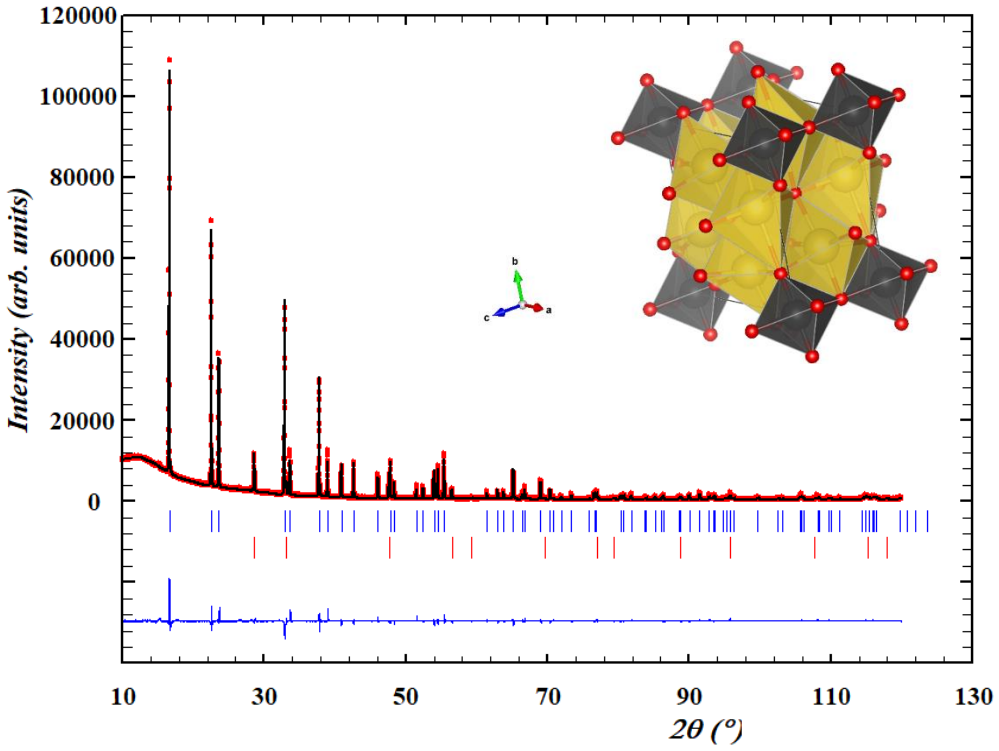

Figure 4.10: Comparison between the observed (Y_{obs}, in red) and calculated (Y_{calc}, in black) X-ray diffraction patterns of Na_4PuO_5 (blue) and PuO_2 (red). Y_{obs}-Y_{calc}, in blue, is the difference between the experimental and calculated intensities. The Bragg reflections' angular positions are marked in blue. Measurement at λ=Cu-Kα.

Table 4.10: Na_4PuO_5 cell parameters comparison

a (Å)	c (Å)	Ref
7.449(5)	4.590(5)	Keller *et al.* [19]
7.5167(5)	4.6192(5)	Pillon [1]
7.519(2)	4.619 (1)	Bykov *et al.* [5]
7.519(2)	4.619 (1)	Smith *et al.* [20]
7.518 (1)	4.616 (1)	This work

Table 4.11: Refined atomic positions of Na_4PuO_5 in *I4/m* space group
R_{wp} = 16.1, R_{exp} = 5.22, χ^2 = 9.49

Atom	**Wyckoff**	**x**	**y**	**z**	**B_0(Å^2)**	**Occ.**
Pu	2a	0	0	0	1.75(2)	1
Na	8h	0.792 (6)	0.603(6)	0	3.0(1)	1
O1	2b	0	0	0.5	1.407	1
O2	8h	0.77(1)	0.919(9)	0	2.2(2)	1

To better understand the structure, ^{23}Na-NMR and HR-XANES measurements have been performed as shown respectively on **figure 4.11** and **4.12**.

In **figure 4.11**, the ^{23}Na MAS NMR spectrum of Na_4PuO_5 is compared with the one of Na_4UO_5 [23] as the compounds are isostructural. Due to their identical crystallographic structure and coordination number (CN), the spectra are very similar. Moreover, the line broadening (C_Q) parameter for both spectra are also close and the asymmetry parameter identical. Smith et al. [23] attributed such a low η_Q value to the symmetry of NaO_6 close to a regular octahedron, consistent with the structure proposed. The only main difference is the peak position (δ) as shown in **table 4.12**. Only one sodium signal is detected as represented by the fit in red dashed lines in agreement with the unique crystallographic site in the theoretical structure refined by Bykov *et al* [5].

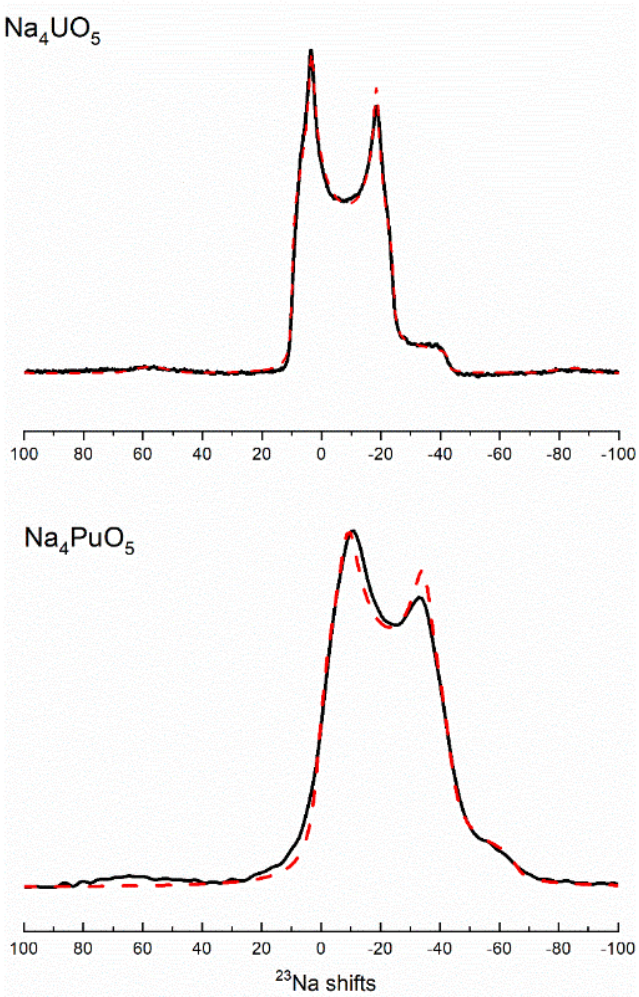

Figure 4.11: ^{23}Na MAS NMR spectra of Na_4UO_5 from Smith *et al.* [23] and Na_4PuO_5 (black line) and their corresponding fits (red dashed line).

Table 4.12: ^{23}Na shift (δ), quadrupolar coupling constant (C_Q), asymmetry parameter (η_Q).

	Na_4UO_5 [23]	Na_4PuO_5
δ (ppm)	15.1	6.6
C_Q (MHz)	3.2	3.5
η_Q	0.2	0.2

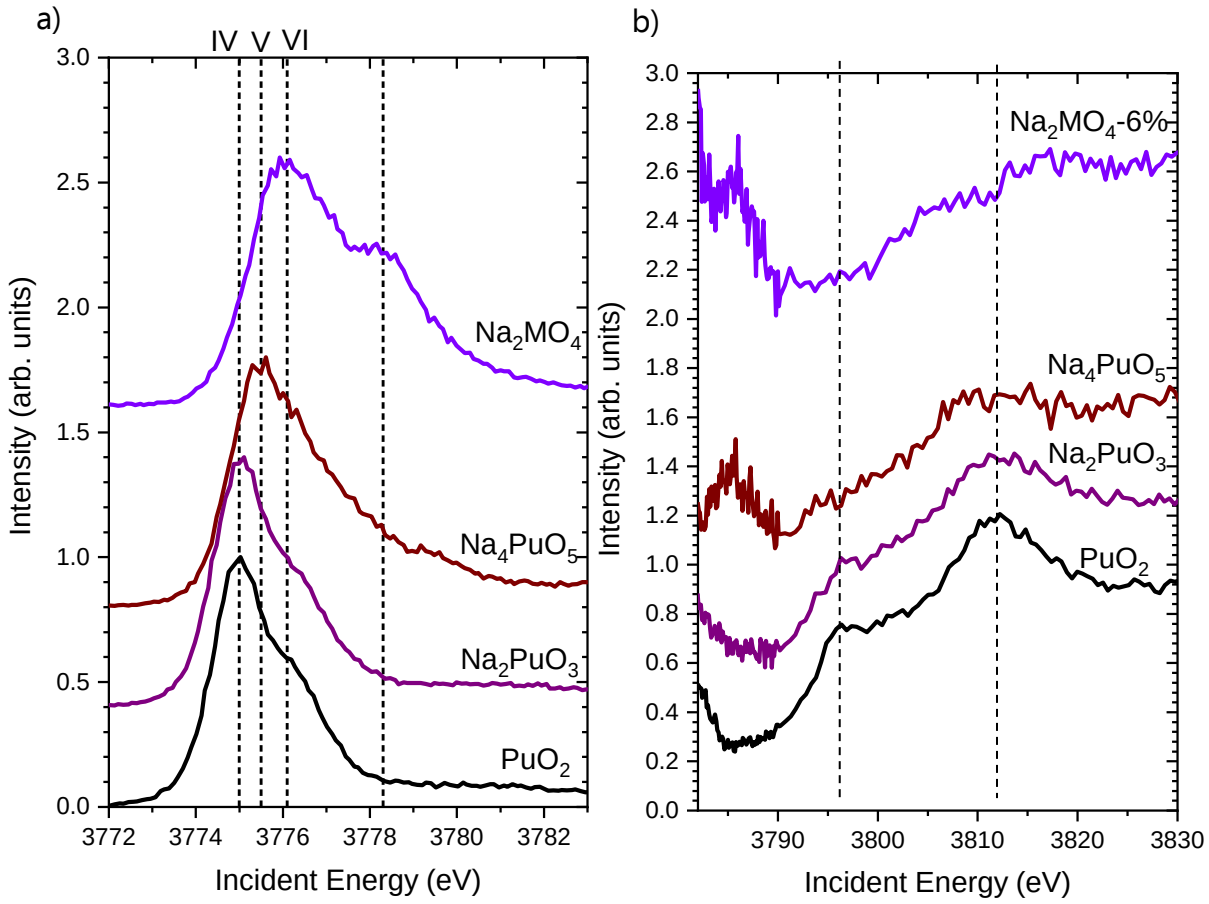

Figure 4.12: Pu M_5-edge HR-XANES (a) and post-edge (b) spectra of Na_2PuO_3, Na_4PuO_5 and Na_2MO_4-6% (Pu^{VI} reference) samples and PuO_2 reference. (Spectra have been shifted on the y axis to better distinguish the different measurements).

As shown in **figure 4.12**, the white line of Pu^{V} has been added based on the shift of the Pu^{V} compounds from the Pu^{IV} reference (+0.4 eV) measured at the Pu M_5-edge in the work Kvashnina *et al.* [22]. For the Pu^{VI} white line, no solid compound with Pu^{VI} was measured at the Pu M_5-edge. Therefore, the results of the Na_2MO_4 presented in section 4.2.2 were added in **figure 4.12** as pure Pu^{VI} was observed in the compound. **Table 4.13** reports the energies of white line and post-edge feature observed in **figure 4.12.**

Table 4.13: Energies of the White Lines and post-edge features of the PuO_2, Na_2PuO_3, Na_4PuO_5 and Na_2MO_4-6 samples at the Pu M_5-edge.

Sample	WL (eV)		Post edge		Ref
$Pu^{IV}O2$	3775.0		*3796.4*	*3811.5*	This work
$Na_2Pu^{IV}O_3$	3775.1		*3796.3*	*3811.5*	
Na_4PuO_5	**3775.5**		***3785.8***		
Na_2MO_4-6	3776.1	*3778.3*	*3786*		

The Na_4PuO_5 has its white line between the ones for Pu^{IV} and Pu^{VI}. The shift observed for the Na_4PuO_5 compound from the $Pu^{IV}O_2$ used as reference for Pu^{IV} is +0.5 eV, which is consistent with the shift reported by Kvashnina *et al.* [22] for Pu^{V}. Unfortunately, as Pu^{V} references are extremely challenging to synthesise and measure, no reference was available for the present measurement. Moreover, the Pu^{IV} specific features in the post-edge section for Pu^{IV} (dashed lines on **figure 4.12 b**)) and the second maximum after the white line characteristic of Pu^{VI} in uranyl configuration (see **figure 4.14** in section 4.2.2) have not been found. Nevertheless, the post-edge region of Na_2MO_4 used as reference for Pu^{VI} and the post-edge region of Na_4PuO_5 seem similar.

Based on the present observations, the synthesised Na_4PuO_5 compound could be attributed to mainly Pu^{V}. However, small amounts of Pu^{VI} might exist in the compound.

If the plutonium is in +V oxidation state, a charge compensation mechanism has to be introduced to keep the charge neutrality of the compound. Smith *et al.* [24] faced the same problem with the "$Na_3U^{V}O_4$" compound, which they found to contain U^{VI} by HR-XANES at the U M_4-edge. Thanks to neutron diffraction data and ^{23}Na-NMR, the authors showed that the charge compensation mechanism was operated by excess sodium on the actinide crystallographic site, corresponding to the formula $Na_{3.16}U0_{.84}{}^{V}O_4$. However, this explanation has to be rejected here as only one sodium site has been found by ^{23}Na-NMR measurement.

Another possibility could be a charge balance realised by both sodium and oxygen leading to the theoretical formula $Na_3Pu^{V}O_4$. However, the Na_3PuO_4 phase has already been reported with cubic and orthorhombic symmetry in space groups $Fm\bar{3}m$ (225) [25] and $Fmmm$ (69) [17], respectively. This hypothesis is thus unlikely.

Pillon [1] reported the formation of several compounds with different compositions: Na_4PuO_4, Na_3PuO_4 or $Na_{3.5}PuO_{4.5}$ using a similar synthesis method as we used for Na_4PuO_5. Therefore, we can assume a charge balance made by oxygen vacancies leading to a theoretical formula $Na_4Pu^{V}O_{4.5}$, which would be an intermediate compound between the $Na_4Pu^{IV}O_4$ and $Na_4Pu^{VI}O_5$. As the synthesis has been performed with stoichiometric amount of sodium compound, the most probable charge compensation mechanism is the introduction of oxygen vacancies and the compound will be written $Na_4Pu^{V}O_{4.5}$.

As mentioned previously, Keller *et al.* [19] used Na_2O_2 under air to synthesise the Na_4PuO_5 compound whereas in the other works the synthesis was performed under air but with either Na_2CO_3 (Bykov *et al.* [5], Smith *et al.* [20]), Na_2O (Pillon [1]) or NaOH (this work). The three cell parameters reported for these compounds are similar and can be attributed to pentavalent plutonium whereas Keller *et al.* [19] obtained a compound with lower cell parameters. The ionic radius of Pu^{V} is higher than the one of Pu^{VI}. Therefore, the Na_4PuO_5 with hexavalent plutonium should have lower cell parameters than the one with Pu^{V}. In Keller *et al.* [19], a strong oxidant reagent Na_2O_2

was used, whereas in other works the reagents were less oxidising, and higher cell parameters were obtained. Therefore, Keller *et al.* [19] might have synthesised $Na_4Pu^{VI}O_5$ whereas other authors the $Na_4PuO_{4.5}$ with Pu^{V}.

4.2.1.3. Conclusion

The Na-Pu-O system is one of the key systems to study in the Na-O-Pu-U system. However, as experiments are challenging to perform, only few data are available. Moreover, some discrepancies have been raised between the different studies for the Na_2PuO_3 and Na_4PuO_5 compounds.

Thanks to the use of several techniques XRD, ^{23}Na-NMR and MQ-MAS, the Na_2PuO_3 compound was refined in the *C2/c* space group with four sodium crystallographic sites. Finally, the HR-XANES measurements, confirmed that the formed compound can be used as pure Pu^{IV} reference.

For the Na_4PuO_5, the Na-NMR results confirmed that sodium was only found on one crystallographic site as expected from the theoretical structure proposed by Bykov *et al.* [5]. The HR-XANES measurements showed that the oxidation state of the plutonium was most probably +V, and not +VI as expected from the theoretical formula. However, to establish with certainty the exact chemical formula, the charge compensation mechanism must be determined. This would require performing complementary local structure measurements, for instance using EXAFS at the Pu L_3-edge.

4.2.2 $Na_\alpha(U,Pu)_\beta O_\gamma$ compounds

In this section, the results on the different mixed oxide compounds are discussed. Generally, refinements were performed using the Le Bail method as the crystallographic positions of the atoms have not been assessed. With this refinement method, it is not possible to assess the weight fraction of the phases when several phases are observed. When a hypothetical structure was proposed, a Rietveld refinement was performed.

In Na_2MO_4, plutonium was found as pure Pu^{VI} and was used as reference in the previous section for the HR-XANES analysis. Therefore, the first compounds described hereafter are Na_2MO_4 and $Na_2M_2O_7$ containing high oxygen content and synthesised under air.

4.2.2.1. The Na_2MO_4 and $Na_2M_2O_7$ phases

In the Na-O-U and Na-O-Pu systems, the compounds Na_2UO_4, $Na_2U_2O_7$ and $Na_2Pu_2O_7$ were reported. However, as described in Chapter 2, the "Na_2PuO_4" end-member does not exist as a stable phase. Therefore, to determine the plutonium solubility and the evolution of the structure with an increase in the plutonium content, the mixed compounds $Na_2(U_{1-x}Pu_x)O_4$ are studied in this section.

Table 4.14 reports the cell parameters of the $Na_2(U_{1-x}Pu_x)O_4$ solid solution synthesised according to the conditions listed in **table 4.5**.

Table 4.14: $Na_2U_{1-x}Pu_xO_4$ cell parameters evolution with the Pu/(U+Pu) ratio

x(Pu)	Ratio Na_2O/MO_2	a (Å)	b (Å)	c (Å)	Batch	Ref
0	(1:1)	9.762	5.729	3.496	-	[26]
0.058	(1:1)	9.753(1)	5.7277(4)	3.4916 (2)	NaOH	This work
	(1:1)	9.753(1)	5.7275(4)	3.4914 (3)	Na_2CO_3	
0.126	(1:1)	9.757 (1)	5.7275 (5)	3.4918 (3)	NaOH	
0.46	(1:1)	9.772 (2)	5.732 (1)	3.493 (1)	NaOH	
0.46	(1:2)	9.785 (2)	5.731 (1)	3.4924 (4)	NaOH	

As seen in **table 4.14**, the change in the cell parameters is only significant for the *a* parameter in the $Na_2U_{1-x}Pu_xO_4$ solid solution. Therefore, only the *a* cell parameter evolution is represented in **figure 4.13**. When more than one phase was observed, the symbol on the graphic is half filled.

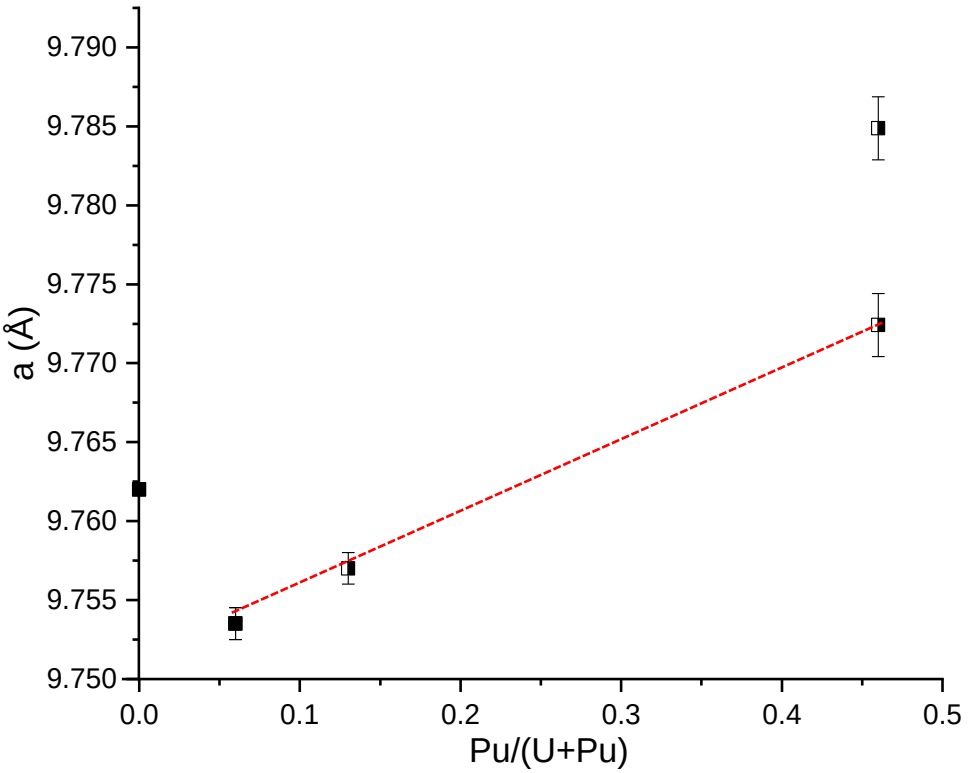

Figure 4.13: Evolution of the *a* cell parameter in the solid solution $Na_2U_{1-x}Pu_xO_4$ with the Pu/(U+Pu) ratio. Symbols are half filled when several phases were observed.

A decrease in the *a* lattice parameter is observed in the mixed compositions for x=0.06 compared to Na_2UO_4. After, this decrease, the lattice parameter increases with the Pu/(U+Pu) ratio in the MOX. Moreover, as shown by the dashed line in **figure 4.13** for the values obtained with a (1:1) ratio in (Na_2O:MO_2) (Na_2MO_4 composition targeted) the increase of the cell parameter seems to follow a linear trend.

The Na_2MO_4 solid solution composition at 46% was also observed in the batch synthesised with a ratio (1:2) in (Na_2O:MO_2) ($Na_2M_2O_7$ composition targeted). The cell parameter is higher than the one obtained with a (1:1) ratio (**figure 4.13**) and not following the linear trend. Nevertheless, no additional characterisations were performed on these batches.

Finally, it is worth noting that only the solid solution at 6% was obtained as a single phase.

For the $Na_2(U_{1-x}Pu_x)_2O_7$ phase, the evolution of the cell parameters (**table 4.15**) with the Pu/(U+Pu) ratio is difficult to analyse parameter by parameter as the evolution does not seem to follow a consistent pattern. Therefore, the change in the cell volume with composition is directly reported in **figure 4.14**.

Table 4.15: $Na_2(U_{1-x}Pu_x)_2O_7$ cell parameters evolution with the plutonium content

x(Pu)	a (Å)	b (Å)	c (Å)	β (°)	Batch	Ref
0	12.796	7.822	6.896	111.42	-	Smith [17]
0.058	12.781 (2)	7.851 (1)	6.868 (1)	111.13 (2)	NaOH	This work
0.126	12.805 (3)	7.833 (2)	6.881 (2)	111.19 (2)	NaOH	
0.46	12.828 (5)	7.737 (3)	6.873 (2)	110.05 (5)	NaOH	

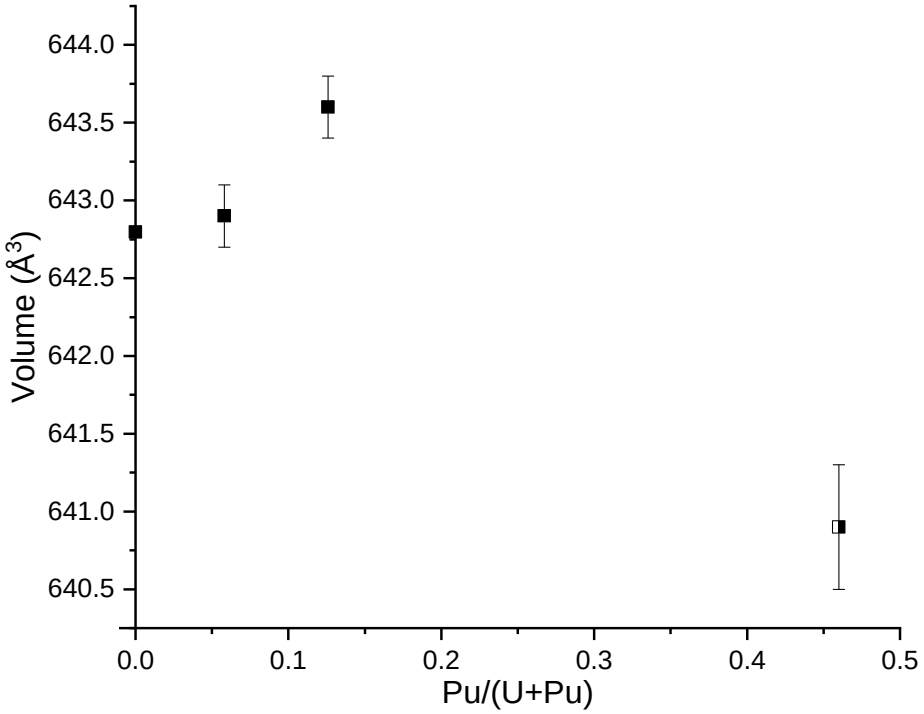

Figure 4.14: Volume evolution in the solid solution $Na_2(U_{1-x}Pu_x)_2O_7$ with the Pu/(U+Pu) ratio. Symbols are half filled when several phases were observed.

A general increase in the cell volume is observed for $Na_2(U_{1-x}Pu_x)_2O_7$ up to a 12% plutonium content. At 46% plutonium content, the second phase $Na_2U_{1-x}Pu_xO_4$ (reported in **table 4.14** and **figure 4.13**) appears and the volume of $Na_2(U_{1-x}Pu_x)_2O_7$ decreases.

The $Na_2U_{1-x}Pu_xO_4$ phase with a 6% plutonium content in the starting MOX and the $Na_2(U_{1-x}Pu_x)_2O_7$ at 6% and 12% were obtained as pure phases. Therefore, HR-XANES measurements have been performed on these pure phases to obtain more information on the actinide oxidation state and interpret the observed trends.

The HR-XANES spectra at Pu M_5-edge are reported in **figure 4.15**. On the graphs in this section the $(U_{1-x}Pu_x)$ content has been written M with the Pu/(U+Pu) ratio in the starting MOX at the end of the compound's formula for better readability. **Table 4.16** reports the energies of white line and post-edge feature observed in **figure 4.15**.

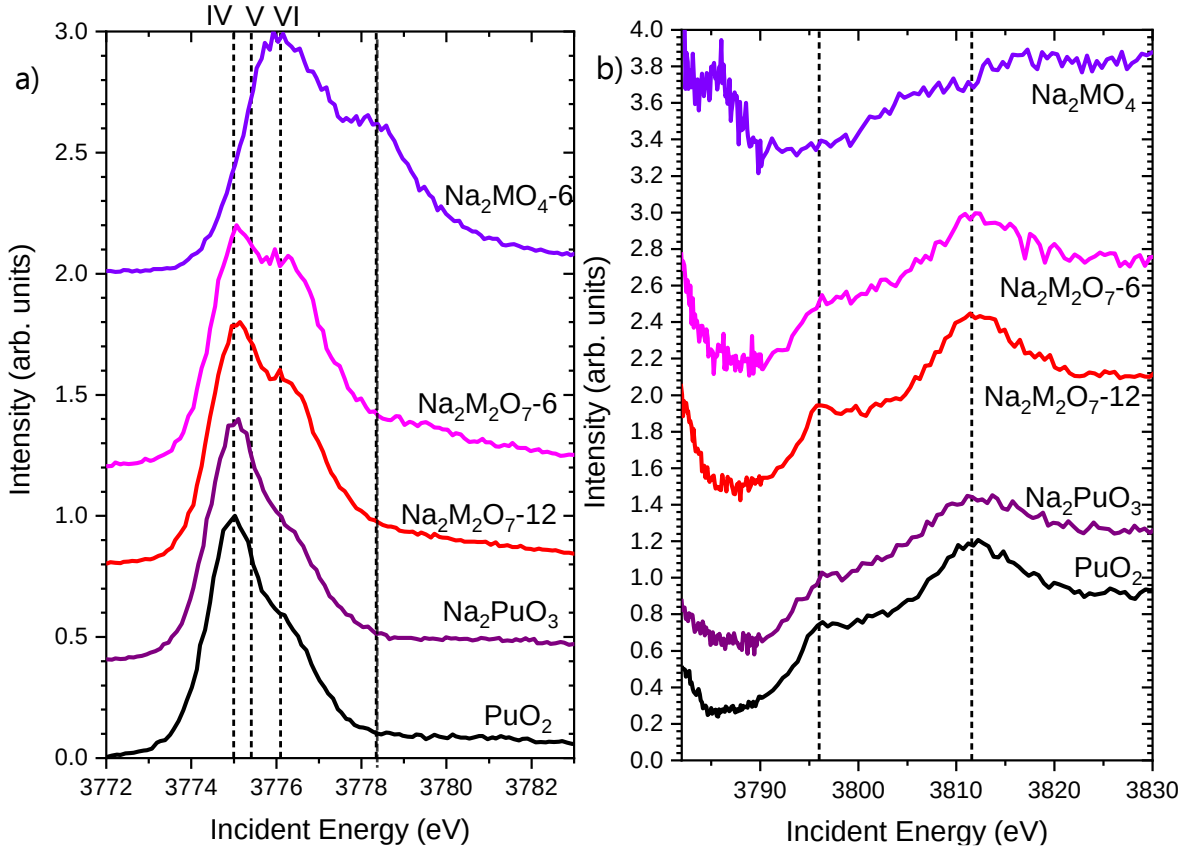

Figure 4.15: Pu M_5-edge HR-XANES (a) and post-edge (b) spectra of $Na_2U_{1-x}Pu_xO_4$-6%, $Na_2(U_{1-x}Pu_x)_2O_7$-6% and $Na_2(U_{1-x}Pu_x)_2O_7$-12% samples and PuO_2 reference. (Spectra have been shifted on the y axis to better distinguish the different measurements).

Table 4.16: Energies of the White Lines and post-edge features of the PuO_2, Na_2PuO_3, $Na_2M_2O_7$-6, $Na_2M_2O_7$-12 and Na_2MO_4-6 samples at the Pu M_5-edge.

Sample	WL (eV)		Post edge		Ref
$Pu^{IV}O_2$	3775.0		*3796*	*3811*	This work
$Na_2Pu^{IV}O_3$	3775.1		*3796.3*	*3811.5*	
$Na_2M_2O_7$-6	**3775.1**	***3776.1***	***3796***	***3811***	
$Na_2M_2O_7$-12	**3775.1**	***3776.1***	***3796***	***3811***	
Na_2MO_4-6	3776.1	*3778.3*	*3786*	-	

For the Na_2MO_4-6 sample, the white line (energy maximum) is shifted by 1eV compared to the energy reported for Pu^{IV}. Moreover, a second local maximum after the white line at 3778.3 eV is observed which is characteristic of Pu^{VI} with a plutonyl configuration PuO_2^{2+}[27]. Therefore, this compound can be assigned to pure Pu^{VI} and will be used as a pure Pu^{VI} reference.

In the $Na_2M_2O_7$ phases, the white line is aligned with the PuO_2 reference and the specific features of Pu^{IV} are observed in the post-edge region. Nevertheless, a feature is observed at the Pu^{VI} energy. However, the specific second local maximum of plutonyl configuration is not observed as shown in **figure 4.15**. Therefore, the compound is most likely pure Pu^{IV}. Nevertheless, local structure experiments should be done to confirm this statement as the mixte Pu^{IV}/Pu^{VI} oxidation state was not possible to reject.

Finally, the samples have also been characterised by HR-XANES at U M_4-edge. The spectra are reported in **figure 4.16**. The white line corresponds to the energy of U^{VI} and the specific features of the $U^{VI}O_2^{2+}$ uranyl ions with short axial bond lengths are observed as reported in **table 4.17** [28–30]. This is consistent with the $Na_2U^{VI}_2O_7$ [31] and $Na_2U^{VI}O_4$ structures which both have a uranyl configuration with U-O distances of 1.871 and 1.903 respectively. Only for Na_2MO_4-6, a shift in the local maximum energies on **figure 4.16** is observed which is due to short distances between axial oxygen and actinides atoms [32]. This could come from the insertion of Pu^{VI} in the structure on the crystallographic site of uranium as the ionic radius of Pu^{VI} is lower than the U^{VI} leading to a decrease in the bond lengths.

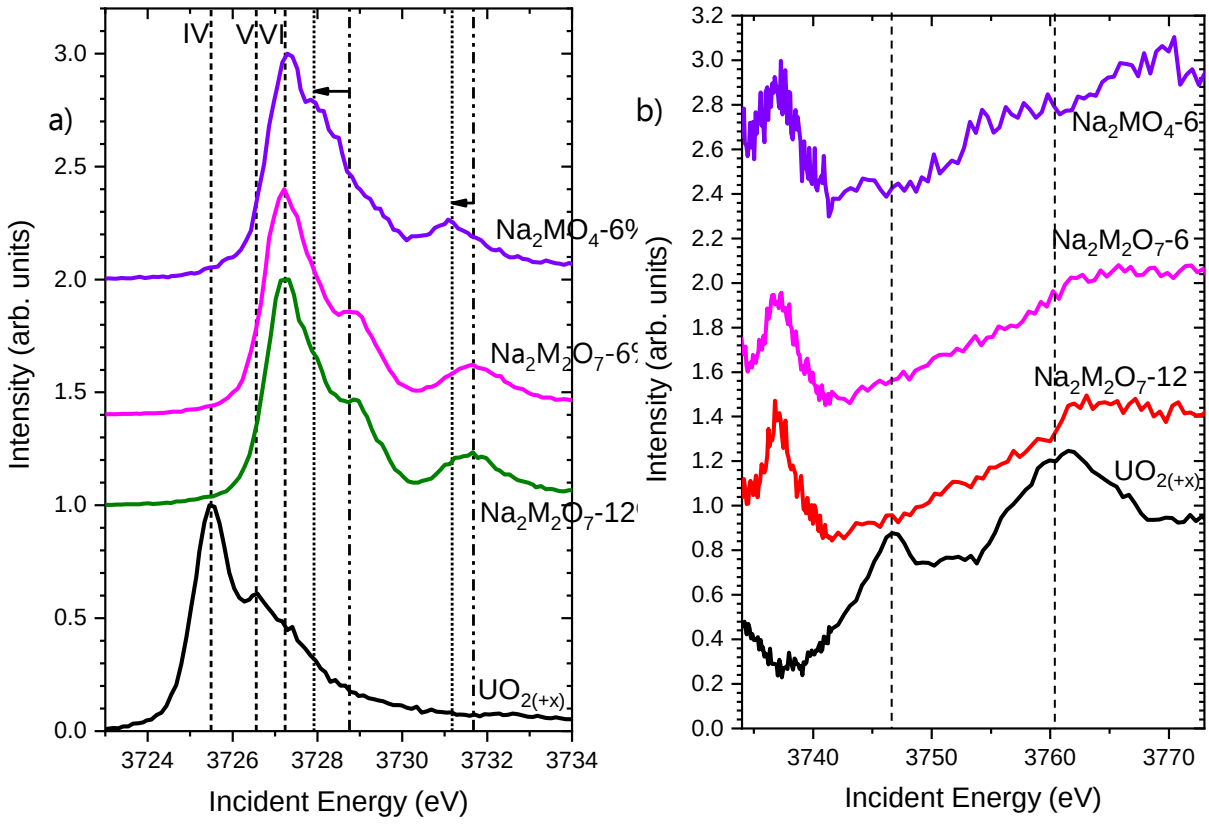

Figure 4.16: U M_4-edge HR-XANES (a) and post-edge (b) spectra of Na_2MO_4-6%, $Na_2M_2O_7$-6% and $Na_2M_2O_7$-12% samples and UO_2 reference. (Spectra have been shifted on the y axis to better distinguish the different measurement)

Table 4.17: Energies of the White Lines and post-edge features of the PuO_2, Na_2PuO_3, $Na_2M_2O_7$-6, $Na_2M_2O_7$-12 and Na_2MO_4-6 samples at the U M_4-edge.

Sample	WL(eV)			Post edge (eV)		Ref
$U^{IV}O_{2(+x)}$	3725.5	3726.6		*3746.7*	*3761.0*	This work
$Na_2M_2O_7$-6	**3727.2**	***3728.8***	***3731.7***	***3736.8***	-	
$Na_2M_2O_7$-12	**3727.3**	***3728.8***	***3731.7***	***3736.8***	-	
Na_2MO_4-6	**3727.3**	***3727.9***	***3731.2***	***3737.4***	-	

Thanks to the HR-XANES measurement of the $Na_2U_{1-x}Pu_xO_4$ solid solution, plutonium and uranium have been found hexavalent, as expected from the theoretical formula. Therefore, a Rietveld refinement has been performed using the $Na_2U^{VI}O_4$ structure as starting model. The plutonium atom has been added on the crystallographic site of the uranium in this compound, and the occupancy fixed to the starting MOX Pu/(U+Pu) ratio. The obtained results are reported in **figure 4.17** and in **table 4.18**.

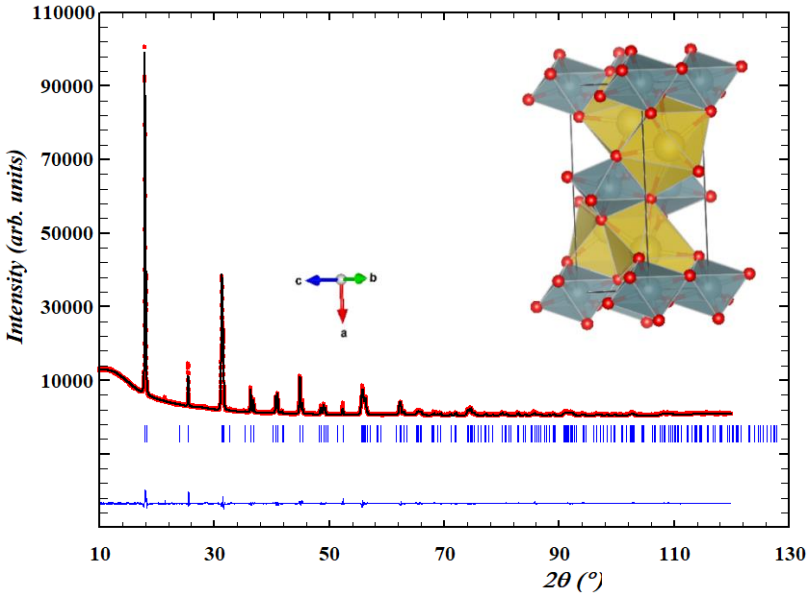

Figure 4.17: Comparison between the observed (Y_{obs}, in red) and calculated (Y_{calc}, in black) X-ray diffraction patterns of $Na_2U^{VI}_{0.94}Pu^{VI}_{0.06}O_4$ (blue). Y_{obs}-Y_{calc}, in blue, is the difference between the experimental and calculated intensities. The Bragg reflections' angular positions are marked in blue. Measurement at λ=Cu-Kα1.

Table 4.18: Refined atomic positions of $Na_2U^{VI}_{0.94}Pu^{VI}_{0.06}O_4$
R_{wp} = 10.9, R_{exp} = 4.6, χ^2 = 5.6

Atom	Oxidation State	Wyckoff	x	Y	z	B_0(Å^2)	Occ.
U	+6	2a	0	0	0	1.38 (2)	0.94
Pu	+6	2a	0	0	0	1.38 (2)	0.06
Na	+1	4h	0.189 (5)	0.44 (1)	0.5	2.7 (2)	1
O1	-2	4g	0.15 (1)	0.12 (2)	0	2.5 (2)	1
O2	-2	4h	-0.06 (1)	0.16 (2)	0.5	4.8 (3)	1

The $Na_2U^{VI}_{0.94}Pu^{VI}_{0.06}O_4$ phase shows infinite chains of corner-sharing AnO_6 octahedra along the c axis. These chains are held together by NaO_7 polyhedra. The octahedra presents two short axial oxygen-actinide bond lengths of 1.63(8) Å, which is lower than the usual uranyl bond lengths (1.903(2) Å for example in Na_2UO_4 [20]) in agreement with the HR-XANES measurements. The four other oxygen atoms are in the equatorial plane at 2.05(5) Å (2.191(1) Å in Na_2UO_4 [20]) forming the same conventional local environment as observed around U^{VI} in Na_2UO_4.

Conclusion

Thanks to the combination of XRD and HR-XANES methods, the plutonium solubility in Na_2MO_4 is estimated to be at least 6 %, as for the Pu/(U+Pu)=0.06 ratio, a single phase was obtained. In the mixed oxide Na_2MO_4, the inserted plutonium is hexavalent and shares the crystallographic site with the uranium.

For the $Na_2(U_{1-x}Pu_x)_2O_7$, HR-XANES revealed the presence of Pu^{IV} in the phases obtained with Pu/(U+Pu)=0.06 and 0.12 which was not expected from the theoretical structure. The possible occurrence of a mixed valence state IV/VI of plutonium has been discussed, but it was not possible to conclude on this point based on the available information.

The phase diagram data obtained on the sodium mixed oxides compositions formed under air are reported in **table 4.19**.

Table 4.19: Summary of the phase diagram data obtained on the samples heated under air

Structure	Temperature	Solubility of Pu (Pu/(U+Pu))	Equilibrium with
$Na_2(U^{VI}_{1-x}Pu^{VI}_x)O_4$	800°C	0.06	Na_4MO_5 and MO_2
$Na_2(U_{1-x}Pu_x)_2O_7$	800°C	0.12	MO_2 and Na_2MO_4

Finally, only one synthesis attempt has been performed for these compounds. Therefore, more trials should be performed to study the trend as a function of the Pu content in the MOX under oxidising conditions.

The results obtained under argon atmosphere are presented in the next section. The first structure discussed hereafter is the cubic Na_3MO_4. Indeed, as presented in chapter 2, this is the main phase expected to form in case of sodium / irradiated fuel interactions under operational conditions.

4.2.2.2. The Na_3MO_4 phase

As described in the synthesis section (section 4.1.2), the cubic Na_3MO_4 compound has been observed in two batches. In the Batch 1.1, the compound was found together

with cubic MO_2 (**figure 4.18**) whereas in"Na_2CO_3-3h", it was formed together with several other phases as described in **table 4.3**.

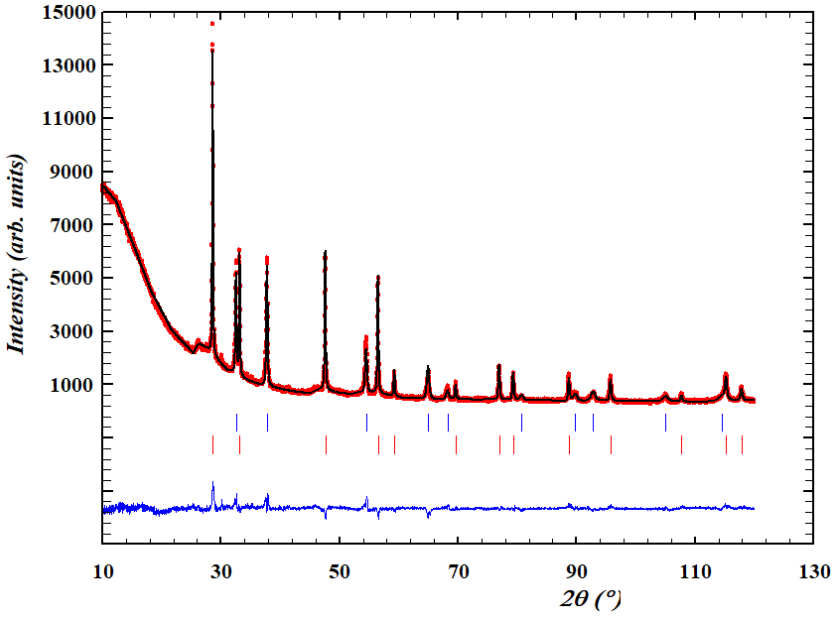

Figure 4.18: Comparison between the observed (Y_{obs}, in red) and calculated (Y_{calc}, in black) X-ray diffraction patterns of the "NaOH-12h" batch sample synthesized with MOX-46. Y_{obs}-Y_{calc}, in blue, is the difference between the experimental and calculated intensities. The Bragg reflections' angular positions are marked in blue for Na_3MO_4 and in green for MO_2. Upper: Na_3MO_4, Lower: MO_2. Measurement at λ=Cu-Kα1

The lattice parameters for both cubic phases are reported in **table 4.20** together with the data of Pillon [1], Housseau [33] for the sodium urano plutonates and Scholder and Gläser [34] and Mignanelli and Potter [25] for the end-members. These data are represented on **figure 4.19**. Moreover, the cell parameter values of cubic Na_4UO_5 and Na_4PuO_5 reported by Smith *et al.* [24], Keller *et al.* [19], respectively, and the cubic phases obtained by Bykov *et al.* in the Na-O-Pu system [5] have also been added for comparison in **figure 4.19**.

Table 4.20: Cubic phases cell parameters in the NaOH-12h and Na_2CO_3-3h samples

Pu/(U+Pu)	Batch 1.1		Na_2CO_3-3 hours		Literature
	a($Na_3U_{1-x}Pu_xO_4$) (Å)	a($U_{1-x}Pu_xO_2$) (Å)	a($Na_3U_{1-x}Pu_xO_4$) (Å)	a($U_{1-x}Pu_xO_2$) (Å)	a($Na_3U_{1-x}Pu_xO_4$) (Å)
0		5.470 (1) [6]		5.470 (1) [6]	4.77 [34]
0.058	4.767 (1)	5.397 (2)	4.782 (2)	5.433	
0.126	4.767 (1)	5.400 (2)	4.784 (2)	5.426	
0.2					4.77 [33]
0.28					4.795 [1]
0.29	4.763 (2)	5.400 (3)	4.777 (1)	5.412	
0.46	4.760 (1)	5.395 (1)	4.766 (3)	5.413	
1		5.397 (1) [6,9]		5.397 (1) [6,9]	4.87 [25]

XRD data obtained for the "Batch 1.1" samples showed a cell parameter for the unreacted MOX phase close to the one for PuO_2. As the oxygen stoichiometry is not known, we cannot attribute the remaining MOX phase to pure PuO_2 using only XRD data. Nevertheless, a plutonium enrichment in the MOX phase is expected.

For syntheses made with Na_2CO_3, many phases were observed as reported in **table 4.3** in section 4.1.2.2. The observed unreacted MOX phase presented a less marked plutonium enrichment than the one reported for the "Batch 1.1".

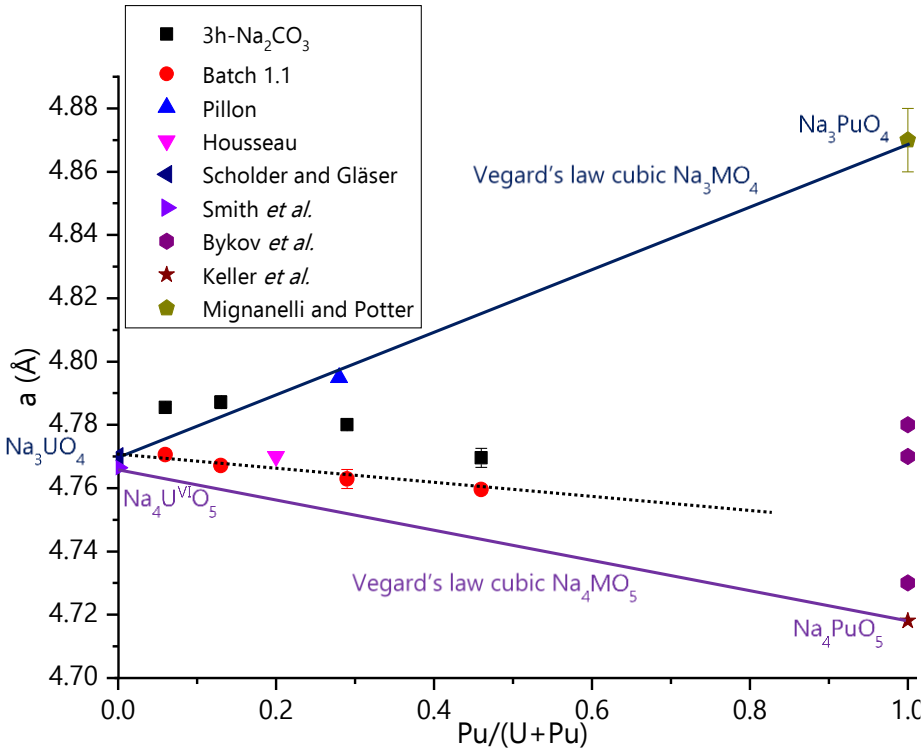

Figure 4.19: Cell parameters reported for the mixed oxide cubic phases attributed to $Na_3U_{1-x}Pu_xO_4$. Comparison with the data of Scholder and Gläser [34] (Na_3UO_4), Smith *et al.* [24] (Na_4UO_5), Mignanelli and Potter [25] (Na_3PuO_4), Keller *et al.* [19] (Na_4PuO_5) and Bykov *et al.* [5] for the cubic end-members and Pillon [1] and Housseau [33] for the cubic Na_3MO_4 mixed oxides.

For the Batch 1.1, a slight decrease in the Na_3MO_4 cell parameter is observed as shown by the black dashed line in **figure 4.19**. Plutonium has a smaller ionic radius in six-fold coordination, compared to uranium for a same oxidation state as shown in **table 4.21**. Therefore, the decrease in the cell parameters could be related to the plutonium content increase in the sodium mixed oxide. Nevertheless, it could also be explained by uranium oxidation as the ionic radius of uranium decreases when the uranium oxidises. As none of the phases were obtained pure, only XRD measurements have been performed. Thus, it is not possible to determine the plutonium content in the mixed oxide phases, nor the actinide oxidation states. Therefore, it can only be

concluded that this decrease suggests an increase in the Pu/(U+Pu) ratio and/or actinide oxidation state in Na_3MO_4.

Table 4.21: Uranium and plutonium ionic radii for a six-fold coordination as a function of the actinide oxidation state [35].

Oxidation state	U ionic radius (pm)	Pu ionic radius (pm)
IV	89	86
V	76	74
VI	73	71

For the batch called "Na_2CO_3-3h", the Na_3MO_4 phase with 6 and 12 % plutonium fraction in MOX followed Vegard's law reported for the Na_3MO_4 trend as shown on **figure 4.19**. Nevertheless, since plutonium has a lower ionic radius than the uranium for the same oxidation state, the positive slope of the suggested Vegard's law trend is extremely surprising. No precise structural investigation has been done on the actinide oxidation state but one explanation could be that the plutonium in the cubic "Na_3PuO_4" compound reported by Keller [19] is at the valence state +IV. Supposing this hypothesis was verified, the plutonium would be also +IV in the 6% and 12% compounds, with a charge compensation operated by either uranium oxidation (to U^{VI}) or sodium and/or oxygen stoichiometry (leading to a different composition than the reported formula Na_3MO_4).

For the 29 and 46% plutonium contents, the refined cell parameters are higher than the ones obtained with the Batch 1.1 experiments. However, they are not following the trend of Vegard's law between cubic Na_3UO_4 and Na_3PuO_4. Therefore, a mixed plutonium oxidation state between IV and V can be suggested.

Conclusion

In the ternary Na-U-O and Na-Pu-O systems, cubic structures for Na_3UO_4, Na_3PuO_4, $Na_4U^{VI}O_5$ and Na_4PuO_5 were reported in the literature (all for phases obtained at low temperatures). However, only the cubic $Na_4U^{VI}O_5$ was precisely characterised.

For the cubic sodium urano-plutonates Na_3MO_4, lattice parameters data were reported in the literature and in the present work. However, pure compounds are challenging to synthesise and the final composition (sodium and oxygen stoichiometry) of both cubic $U_{1-x}Pu_xO_2$ and supposedly, $Na_3U_{1-x}Pu_xO_4$ cannot be determined from only XRD data. Under the experimental conditions used to perform the syntheses, the oxygen potential cannot be precisely controlled. From the data obtained, the actinides seem to adopt several oxidation states (from IV to VI). However, the precise structure and composition of the formed compounds cannot be determined.

It is worth noting that the lattice parameters of the $Na_3U_{1-x}Pu_xO_4$ solid solution from the "Batch 1.1" stay close to the one of pure uranium compound for low plutonium

contents (<20%). This is consistent with literature studies concluding that the ternary Na-O-U system is suitable to model the interaction with sodium coolant, forming the Na_3MO_4 composition under operating conditions.

4.2.2.3. The Na_4MO_5 phase

As seen in section 4.1.2, the tetragonal Na_4MO_5 compound was the product obtained in most of the syntheses performed under argon with a (2:1) ratio for (Na_2O:$U_{1-x}Pu_xO_2$). The cell parameters obtained after Le Bail refinement of the samples described in **table 4.2** are reported in **table 4.22**. Moreover, the cell parameters of the Na_4MO_5 obtained under argon at 1000°C were also added and referenced as "Batch Na_2CO_3" in **table 4.22**. Finally, the lattice parameters for Na_4MO_5 obtained under air for Pu/(U+Pu)=0.46 with a (1:1) ratio have also been added.

Several cell parameter data were reported in the literature for Na_4UO_5. The results obtained in this work will be compared with the ones of Pillon [1] (which are in good agreement with the ones of Smith *et al.* [36]) because the analysis method and the compound synthesis conditions are the closest to the ones reported in this work.

Table 4.22: Lattice parameters of the Na_4MO_5 phase obtained by Le Bail refinement of the XRD patterns obtained for each sample with Pu/(U+Pu), the plutonium content.

Pu/(U+Pu)	a (Å)	c (Å)	Batch	Ref
0	7.5455(3)	4.6371(3)	-	Pillon [1]
0.058	7.5489 (4)	4.6355 (3)	Na_2CO_3-test	This work
	7.559 (1)	4.6300 (6)	NaOH-test	
	7.5507 (3)	4.6365 (2)	1.3	
	7.5498 (3)	4.6345 (2)	Na_2CO_3	
0.126	7.548 (3)	4.645(2)	1.3	
	7.5504 (3)	4.6347 (2)	Na_2CO_3	
	7.5519 (6)	4.6375 (5)	2	
0.28	7.547(1)	4.632(1)	-	Pillon [1]
0.293	7.5587 (6)	4.6342 (4)	1.2	This work
	7.567 (2)	4.635 (5)	1.3	
	7.5513 (7)	4.6352 (5)	Na_2CO_3	
	7.5548 (6)	4.6395 (5)	2	
0.46	7.565 (2)	4.647 (3)	1.2	
	7.5492 (5)	4.6358 (4)	Na_2CO_3	
	7.556 (1)	4.6342 (6)	Air	
1	7.519(2)	4.619(1)	-	Bykov *et al.* [5]
	7.522(1)	4.617(1)	-	This work

As the temperature and starting reagents for the Na_4MO_5 syntheses in the various batches are different, the results obtained with Na_2CO_3 will be discussed separately from the ones obtained with NaOH.

Figure 4.20 reports the cell parameters of Na_4MO_5 obtained with Na_2CO_3 starting reagent.

Na_4MO_5 compounds synthesised with Na_2CO_3

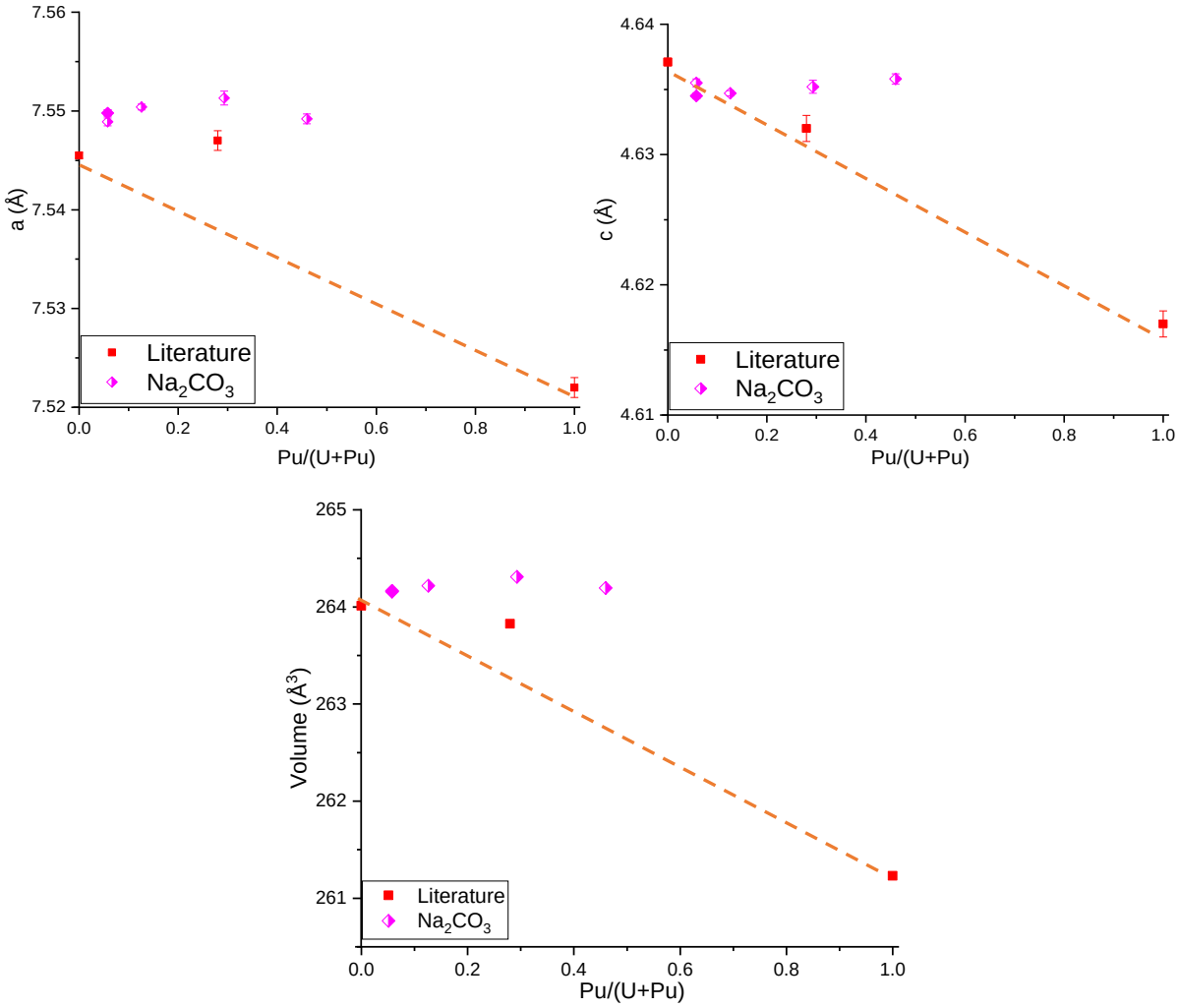

Figure 4.20: Cell parameters and volume of Na_4MO_5 obtained after Lebail refinement of the Na_2CO_3 sample XRD data, compared with data of Pillon [1] for Na_4UO_5 and Na_4MO_5 and Bykov *et al.* [5] for $Na_4PuO_{4.5}$. Symbols are half filled when several phases were observed

The cell parameters obtained at 1000°C are the same for all plutonium contents. As the phase with a starting Pu/(U+Pu)=0.06 ratio was obtained as a single phase sample. The plutonium solubility in the structure obtained with Na_2CO_3 at 1000°C is of 0.06 minimum in (Pu/(U+Pu)).

To have a better understanding of the structure of the mixed oxide, ^{23}Na MAS-NMR and HR-XANES were performed on the Na_4MO_5-6 as it has been synthesised pure. On

figure 4.21, the spectra obtained for Na_4UO_5 from Smith *et al.* [24] and the one obtained for Na_4PuO_5 (described in figure 4.11) were added for comparison.

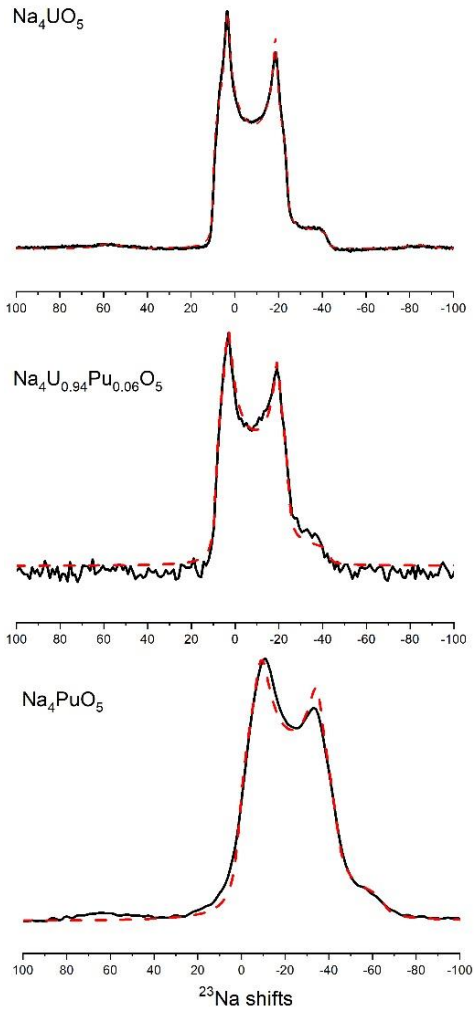

Figure 4.21: ^{23}Na MAS NMR spectra of data from Smith *et al.* [24], Na_4MO_5-6 and Na_4PuO_5 and their corresponding fits (red dashed line).

From the ^{23}Na MAS-NMR analyses reported in **figure 4.21**, only one sodium signal as represented by the fit in dashed line, is observed meaning that only one crystallographic site contains a sodium atom. It is worth noting that the obtained signal for Na_4MO_5-6 is nearly identical to the one obtained for Na_4UO_5 by Smith *et al.* [24] as is evident from the similar values reported in **table 4.23**.

Table 4.23: ^{23}Na shift (δ), quadrupolar coupling constant (C_Q), asymmetry parameter (η_Q).

	Na_4UO_5 [24]	Na_4MO_5-6
δ (ppm)	15.1	14.3
C_Q (MHz)	3.2	3.2
η_Q	0.2	0.2

The Na_4MO_5-6 sample was also analysed by HR-XANES at the U M_4-edge and Pu M_5-edge. The results at the U M_4-edge are reported in **Appendix B** as conventional pure U^{VI} was observed. The results at Pu M_5-edge are reported in **figure 4.22**. To compare with the $Na_2Pu^{IV}O_3$ and $Pu^{IV}O_2$ references and $Na_4PuO_{4.5}$ compound, the different spectra obtained were also added and the energies of white line and post-edge feature observed in **figure 4.22** are reported in **table 4.24**.

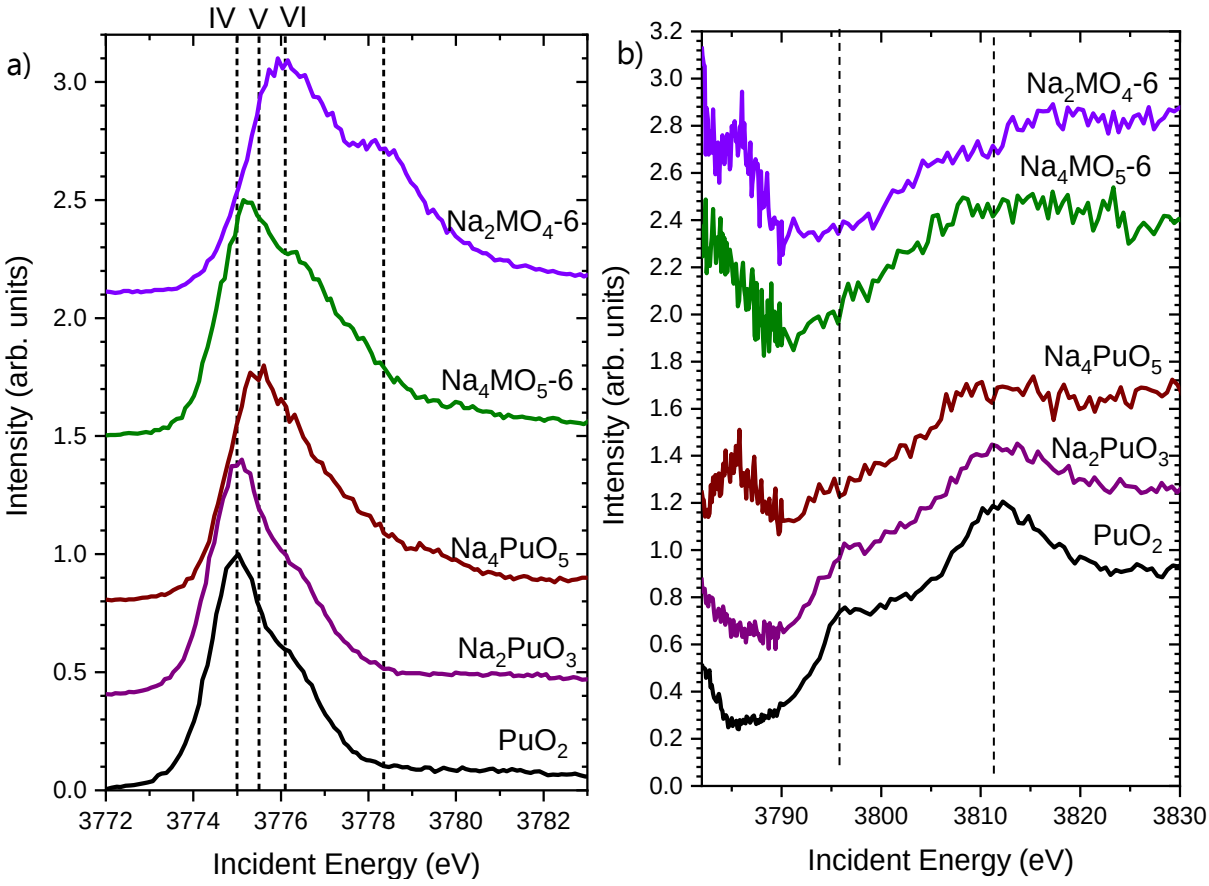

Figure 4.22: Pu M_5-edge HR-XANES (a) and post-edge (b) spectra of $Na_2Pu^{IV}O_3$, $Na_4Pu^{V}O_{4.5}$, Na_2MO_4-6, Na_4MO_5-6 samples and $Pu^{IV}O_2$ reference. (Spectra have been shifted on the y axis to better distinguish the different measurement)

Table 4.24: Energies of the White Lines and post-edge features of the PuO_2, Na_2PuO_3, Na_4PuO_5, Na_4MO_5-6, and Na_2MO_4-6 samples at the Pu M_5-edge.

Sample	WL (eV)		Post edge		Ref
$Pu^{IV}O_2$	3775.0	-	*3796*	*3811*	This work
$Na_2Pu^{IV}O_3$	3775.1	-	*3796*	*3811*	
Na_4PuO_5	3775.5	-	*3786*	-	
Na_4MO_5-6	**3775.2**	-	-	-	
Na_2MO_4-6	3776.1	*3778.3*	*3786*	-	

As shown on **figure 4.22**, the maximum intensity reported for Na_4MO_5-6 is shifted towards higher energies compared to the $Na_2Pu^{IV}O_3$ and $Pu^{IV}O_2$ references. Moreover, in the post-edge region the two local maxima characterising Pu^{IV} are not observed. Therefore, plutonium in Na_4MO_5-6 is more oxidised than in the compounds $Na_2Pu^{IV}O_3$ and $Pu^{IV}O_2$.

Conclusion

In the Na_4MO_5 phases synthesised with Na_2CO_3 as precursor at 1000°C, the lattice parameters are constant and a single phase is observed for Pu/(U+Pu)=0.06. Plutonium shares the crystallographic site with the uranium atom as only one sodium crystallographic site was found from ^{23}Na-NMR results. Uranium is in +VI oxidation state whereas, plutonium is in lower oxidation state than the +VI suggested in the literature. Therefore, the charge compensation mechanism should be related to the actinide local environment. To conclude, XAS analyses at U and Pu L_3-edge have to be performed.

Na_4MO_5 compounds synthesized with NaOH

The cell parameters obtained after Le Bail refinement of the XRD patterns of the samples synthesised with NaOH are reported in **figure 4.23**. The data of Pillon [1] for Na_4UO_5 and Na_4MO_5-20 and of Bykov *et al.* [5] for $Na_4Pu^{V}O_{4.5}$ have also been added in the figures.

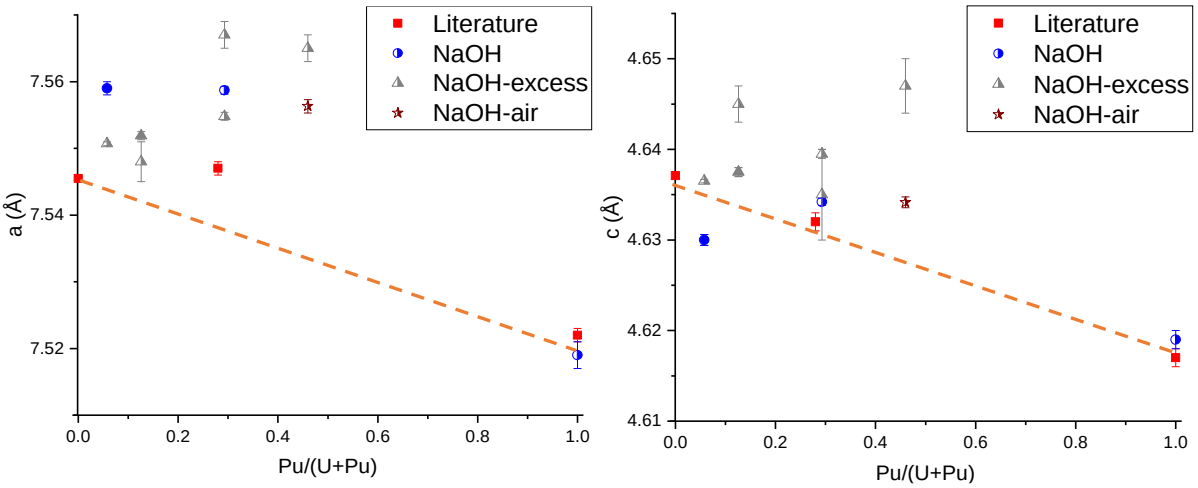

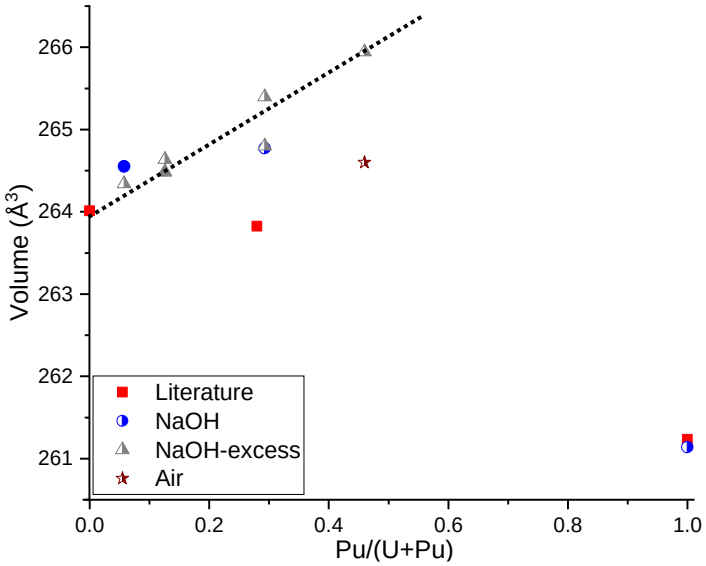

Figure 4.23: Cell parameters of Na_4MO_5 obtained after Lebail refinement of the XRD data of the NaOH sample and volume evolution with the Pu/(U+Pu) ratio. The data of Pillon [1] for Na_4UO_5 and Na_4MO_5 and Bykov *et al.* [5] for $Na_4PuO_{4.5}$ have also been added. Symbols are half filled when several phases were observed. The dashed line represents the linear increase observed for the volume of Na_4MO_5 synthesised with sodium excess.

The results can be summarised as follows:

- The cell parameter measurements obtained with NaOH in excess, suggest a positive deviation from Vegard's law for both parameters. Nevertheless, the data are very scattered.
- For the results obtained when sodium was added in excess from the beginning "Batch 2", no sample was synthesised pure. Therefore, only XRD measurements have been performed. The volume increase with the plutonium content seems to be linear as shown by the dashed line in **figure 4.23**.
- For MOX-46, in one attempt under air, the Na_4MO_5 structure was observed with lower cell parameters than the ones obtained with NaOH in excess under argon.

In these results two samples are particularly striking. For Pu/(U+Pu) ratio=0.06 and 0.12, a single phase Na_4MO_5 sample was obtained (full symbols in **figure 4.23**). The former shows a low cell parameter *c* and a high *a* parameter compared to XRD results obtained on other batches. For the latter, the cell parameter c is extremely high. To understand these trends, complementary analyses were performed as the samples were synthesised pure.

Discussion on pure Na_4MO_5-6

To get further information on the structure, HR-XANES measurements were performed. Spectra measured at the U M_4 and Pu M_5-edge are reported in **figure 4.24**. This measurement was performed during a different measurement campaign from the HR-

XANES experiments therefore, the $Na_2Pu^{IV}O_3$ and $Na_4PuO_{4.5}$ reference spectra were not added on **figure 4.24**. Unfortunately, not enough material was left for ^{23}Na-NMR experiments.

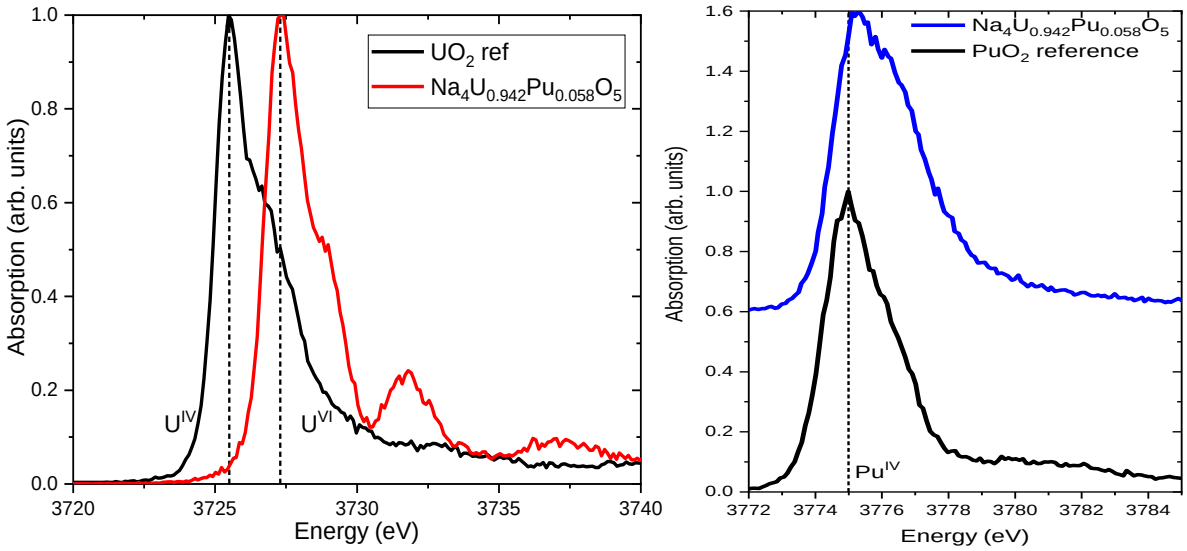

Figure 4.24: U M_4-edge and Pu M_5-edge HR-XANES spectra of Na_4MO_5-6% sample and UO_2 or PuO_2 reference.

From the maximum intensities reported in **figure 4.24**, plutonium seems to be Pu^{IV} and uranium U^{VI}. Therefore, as in the compounds synthesised with Na_2CO_3, a charge compensation mechanism is suggested to occur.

As observed in **figure 4.23**, there is a decrease in the *c* parameter. In the Na_4MO_5, infinite chains of corner-sharing AnO_6 octahedra are existing in the *c* direction. If oxygen vacancies around the actinide were introduced around the actinide, this would lead to a decrease of the average oxygen distances in the octahedra and therefore a strong decrease in the cell parameter *c*.

In the structural description of $Na_4U^{VI}O_5$, which is isostructural with Na_4MO_5, two oxygen sites exist. One is in *2b* crystallographic site and the other one is in *8h*. A Rietveld refinement of the XRD pattern of Na_4MO_5-6 has been tested by introducing oxygen vacancies either on the *2b* or the *8h* crystallographic sites. The results reported in **figure 4.25** and **table 4.25** are the ones obtained with oxygen vacancies on the *8h* crystallographic site, where all thermal displacements could be refined. Moreover, the "goodness of the fit" was better with the oxygen vacancies on the *8h* site than on the one obtained with vacancies on the *2b* site.

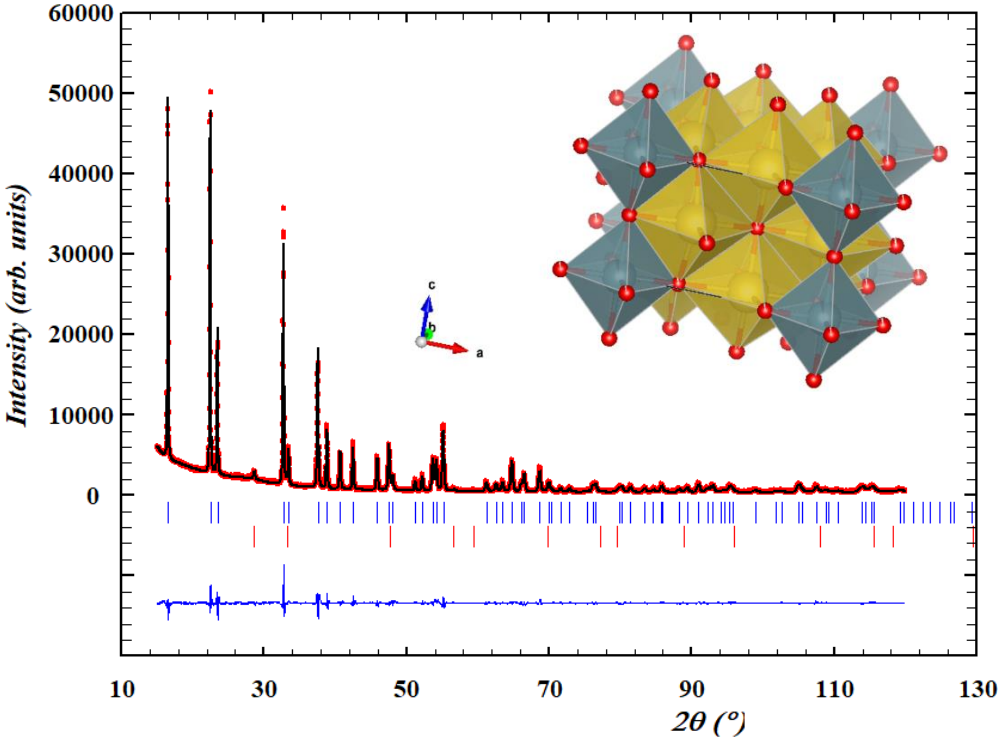

Figure 4.25: Comparison between the observed (Y_{obs}, in red) and calculated (Y_{calc}, in black) X-ray diffraction patterns of the $Na_4U^{VI}_{0.94}Pu^{IV}_{0.06}O_{4.94}$ compound with ~1 wt% of unreacted MOX. Y_{obs}-Y_{calc}, in blue, is the difference between the experimental and calculated intensities. The Bragg reflections' angular positions are marked in blue for $Na_4U^{VI}_{0.94}Pu^{IV}_{0.06}O_{4.94}$ and in green for MO_2. Upper: $Na_4U^{VI}_{0.94}Pu^{IV}_{0.06}O_{4.94}$, Lower: MO_2. Measurement at λ=Cu-Kα1

Table 4.25: Refined atomic positions, isotropic thermal displacement factor B_0 and occupancy in the $Na_4U_{0.94}Pu_{0.06}O_5$ compound (noted Occ. in the table) derived from the XRD refinement. Background: Linear interpolation between operator-selected points in the pattern with refinable heights. R_{wp}=11 R_{exp}=4.52 χ^2=5.92

Atom	Oxidation State	Wyckoff	X	y	z	B_0(Å^2)	Occ.
U	+6	2a	0	0	0	1.00 (2)	0.94
Pu	+4	2a	0	0	0	1.00 (2)	0.06
O1	-2	2b	0	0	0.5	2.3 (3)	1
Na	+1	8h	0.806 (1)	0.593 (1)	0	0.90(1)	1
O2	-2	8h	0.727 (1)	0.917 (1)	0	3.2 (2)	0.98 (1)

The oxygen occupancy in the *8h* crystallographic site was refined whereas the occupancy of uranium and plutonium atom were kept constant. The occupancy obtained for the *8h* oxygen leads to the theoretical formula $Na_4U^{VI}_{0.94}Pu^{IV}_{0.06}O_{4.92}$ giving as general formula $Na_4U^{VI}_{1-x}Pu^{IV}_xO_{5-x}$. Nevertheless, for a more accurate determination of the occupancy, neutron diffraction experiments or EXAFS analysis should be performed.

Discussion on pure Na_4MO_5-12

For the single phase structure obtained with 12% plutonium content, the lattice parameter of the c axis is higher compared to the other data obtained at low plutonium content (Pu/(U+Pu)=0.06 and 0.12). 1D and 2D ^{23}Na MAS NMR experiments and HR-XANES measurements were performed on this sample to understand this trend.

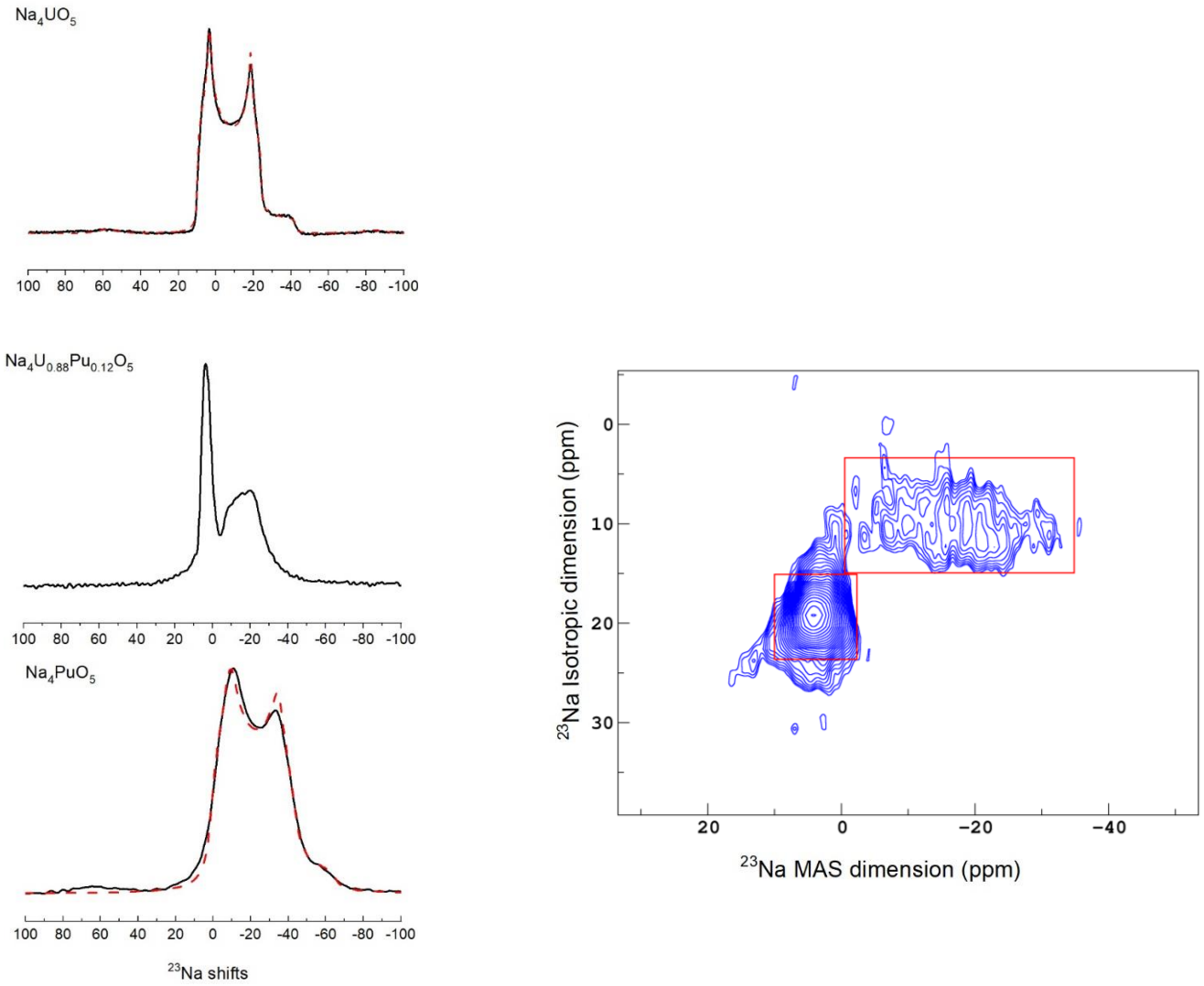

Figure 4.26: ^{23}Na central transition MAS-NMR spectra of Na_4MO_5-12% and end members recorded using a) a single π/12 impulsion and b) an MQ-MAS experiment of Na_4MO_5-12%. In red rectangles, we identify two different sodium sites.

The ^{23}Na MAS NMR results for Na_4MO_5-12% are reported in **figure 4.26**. The-one dimensional experiments were recorded using a single π/12 pulse and to increase the spectral resolution of the MOX a bi-dimensional experiment -MQ-MAS- was also performed. In the red rectangles, we can clearly identify two distinct sodium sites, whereas in the Na_4UO_5 structure, only one sodium exists. Moreover, both sites present an inherent disorder.

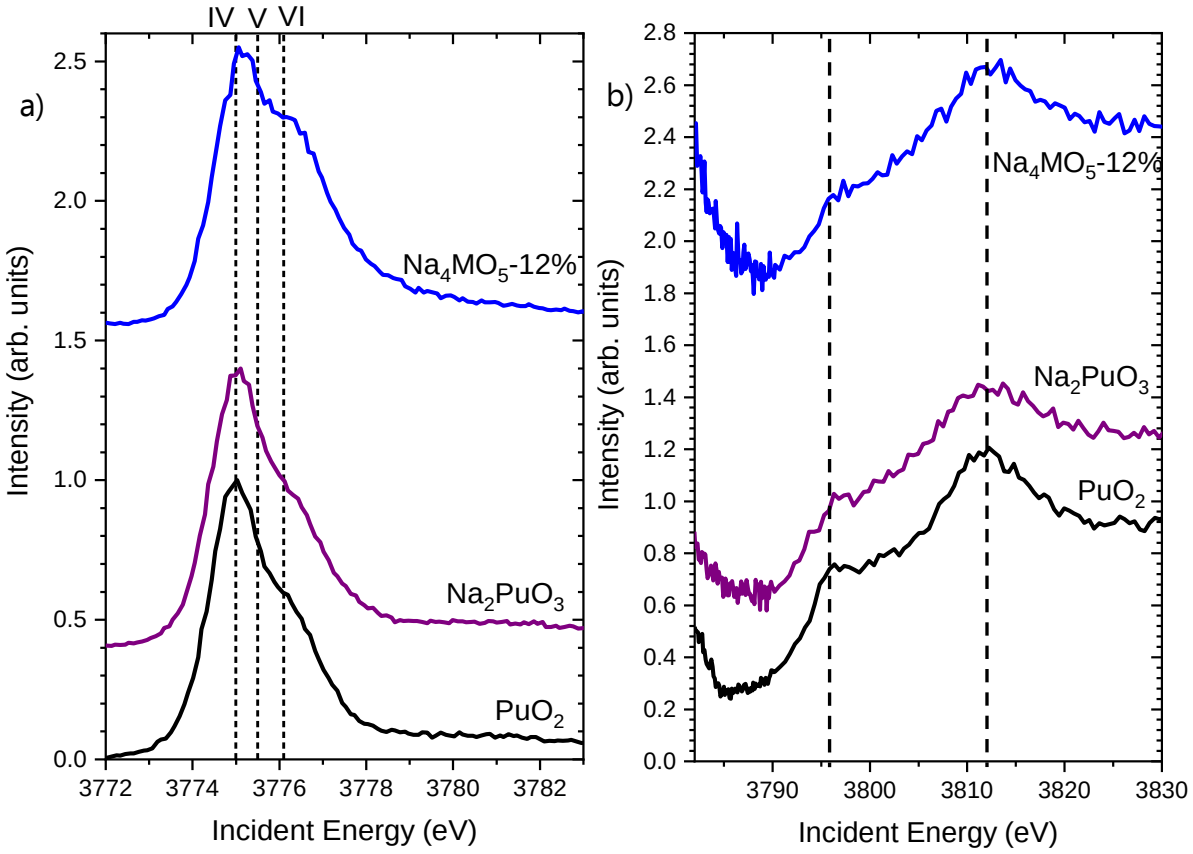

Figure 4.27: Pu M_5-edge HR-XANES (a) and post-edge (b) spectra of Na_2PuO_3, Na_4PuO_5, Na_4MO_5-12% samples and PuO_2 reference. (Spectra have been shifted on the y axis to better distinguish the different measurements).

Table 4.26: Energies of the White Lines and post-edge features of the PuO_2, Na_2PuO_3 and Na_4MO_5-12 samples at the Pu M_5-edge.

Sample	WL (eV)		Post edge		Ref
$Pu^{IV}O_2$	3775.0	-	*3796*	*3811*	This work
$Na_2Pu^{IV}O_3$	3775.1	-	*3796*	*3811*	
Na_4MO_5-12	**3775.0**	***3776.3***	***3796***	***3811***	

Figure 4.27 shows the HR-XANES spectrum of the Na_4MO_5-12 and its post-edge region (**figure 4.27 b**). In the figure, the maximum intensity corresponds to the presence of Pu^{IV} as confirmed by the two local intensity maxima in the post edge region reported in **table 4.26**. Therefore, as in Na_4MO_5-6, a charge compensation mechanism occurs. Nevertheless, cell parameters are extremely different and a second sodium site appears. Therefore, the charge compensation mechanism used by Smith *et al.* [24] for the $Na_{3+x}UO_4$ might be applicable here. Moreover, Pillon also reports the existence of a composition range for the $Na_{4+x}MO_5$ phase.

Using the charge compensation mechanism described by Smith *et al.* [24], the added sodium in the Na_4MO_5 structure will share the crystallographic site of the actinides. As the ionic radius of sodium atoms is larger than those of uranium or plutonium, the cell parameter *c* and the volume V will strongly increase as observed in the XRD results. This would lead to the theoretical formula $Na_4(U^{VI}_{1-x},Na_{2x},Pu^{IV}_x)O_5$.

Finally, the strong linear volume increase observed for "Batch 2" samples could be explained by the introduction of sodium into the structure as suggested for the Na_4MO_5-12. The samples were synthesised with sodium excess and follow the volume lattice increase trend, therefore, they can be attributed to the composition $Na_4(U^{VI}_{1-x},Na_{2x},Pu^{IV}_x)O_5$. Nevertheless, a batch of single phase material should be synthesised to confirm this interpretation.

Conclusion

A structural study of the Na_4MO_5 solid solutions has been performed using XRD, HR-XANES, ^{23}Na-NMR and MQ-MAS experiments when a pure sample was obtained. We showed that in this phase, the uranium was always hexavalent whereas the plutonium could be either tetravalent or in a more oxidised state. Therefore, different charge compensation mechanisms have been considered, with either the addition of sodium or oxygen vacancies in the structure as reported in **figure 4.28**.

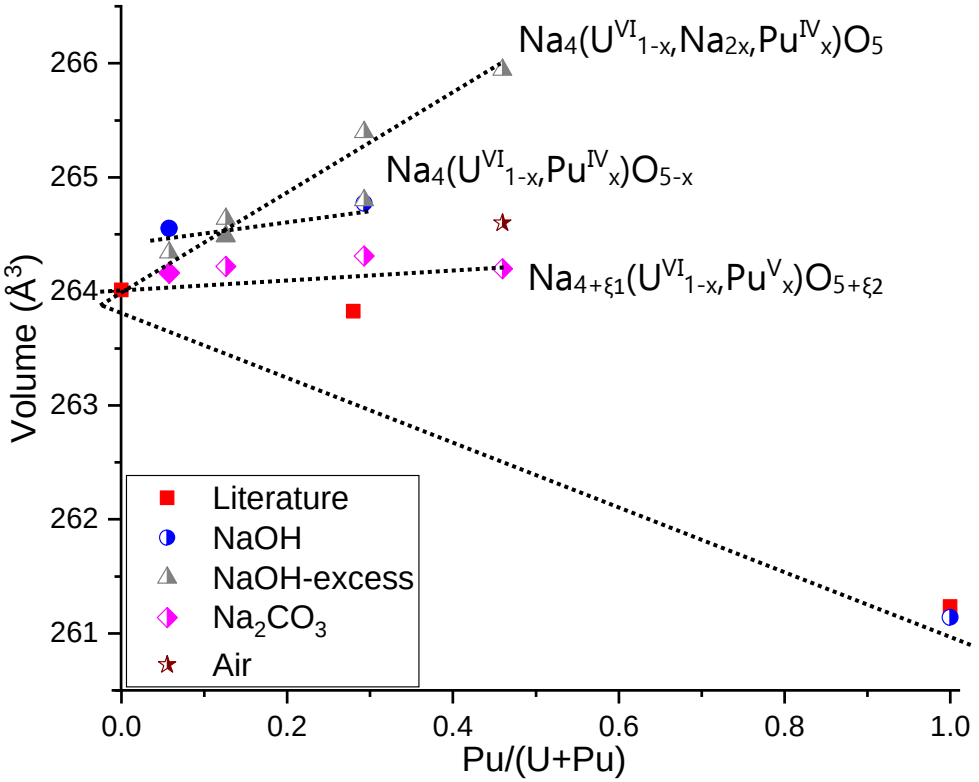

Figure 4.28: Lattice volume evolution of the Na_4MO_5 compositions with the starting Pu/(U+Pu) ratio of the MOX. The data of Pillon [1] for Na_4UO_5 and Na_4MO_5 and Bykov *et al.* [5] for $Na_4PuO_{4.5}$ have also been added.

For $Na_4U_{1-x}Pu_xO_5$ obtained with Na_2CO_3 at 1000°C, the phase seemed to be similar to the $Na_4Pu^{V}O_{4.5}$ compound formed in section 4.2.1. However, the charge compensation mechanism could not be determined.

For the syntheses with NaOH at 800°C, a general increase in the cell parameters compared to Vegard's law was observed except for the composition with Pu/(U+Pu)=0.06. This pure phase structure was refined with oxygen vacancies. However, to discuss the local environment of the plutonium, XAS analyses have to be performed.

The second sample studied in detail was the pure $Na_4U_{1-x}Pu_xO_5$ with Pu/(U+Pu)=0.12 ratio. The cell parameters were higher compared to other low plutonium content phases (Pu/(U+Pu)=0.06 and 0.12). Thanks to XRD, ^{23}Na-NMR, MQ-MAS and HR-XANES spectroscopy, this trend was explained by sodium insertion on the actinide crystallographic site. Finally, the compositions synthesised with a sodium excess added before the first thermal treatment ("Batch 2") were also attributed to the composition $Na_4(U^{VI}_{1-x},Na_{2x},Pu^{IV}_x)O_5$.

Thanks to the studies of single-phase materials, the mixed oxides synthesized in different conditions were attributed to different charge compensation mechanisms.

As in the SFR reactor, the conditions are reducing, the phases obtained under argon with high sodium content were extensively studied in this work. However, to develop the Calphad models, the same study has to be performed for oxidizing conditions (under air). Indeed, from the results of Pillon and those obtained in this work on the Na_4MO_5 phase observed at 46% under air, other phases should exist on the phase diagram for those oxidising conditions.

The phase diagram data obtained on the different Na_4MO_5 structures formed under argon are reported in **table 4.27**.

Table 4.27: Summary of the phase diagram data obtained on Na_4MO_5 compositions after the structural analyses

Structure	Temperature	Solubility of Pu (Pu/(U+Pu))	Equilibrium with
$Na_4(U^{VI}_{1-x},Na_{2x},Pu^{IV}_x)O_5$	800°C	>0.12	Na_2MO_3
$Na_4(U^{VI}_{1-x},Pu^{IV}_x)O_{5-x}$	800°C	>0.06	MO_2 and Na_2MO_3
$Na_{4+\xi1}(U^{VI}_{1-x},Pu^{V}_x)O_{5+\xi2}$	1000°C	>0.06	Only Na_2MO_3 Pu/M<0.29 MO_2 and Na_2MO_3 Pu/M=0.46

To conclude, the structures of the Na_4MO_5 phases are extremely sensitive to the physico-chemical conditions of the synthesis. To assess the charge compensation mechanisms, in many cases, a local structure investigation around the actinide atoms is needed.

Finally, for many compositions, it was not possible to obtain a pure phase. Indeed, an equilibrium between Na_4MO_5 and Na_2MO_3 phases has often been observed as reported in section 4.2.2. In the following section, the results obtained on the Na_2MO_3 phase are presented.

4.2.2.4. The Na_2MO_3 phase

In many synthesis attempts at high Pu/(U+Pu) ratio, a mixture of Na_4MO_5 and Na_2MO_3 was observed. Moreover, the Na_2MO_3 solid solution is also extremely interesting to study as the uranium end-member "Na_2UO_3" does not exist. Therefore, when the solubility limit of plutonium into the Na_4MO_5 phase is reached, the plutonium will either remain in the MOX form, generally enriched in plutonium, or react with sodium to form Na_2MO_3.

The lattice parameters of the Na_2MO_3 phase obtained after Le Bail refinement of the XRD patterns obtained for all the samples are reported in **table 4.28**.

Table 4.28: Lattice parameters of the Na_2MO_3 phase obtained by Le Bail refinement of the XRD patterns obtained for each sample with Pu/(U+Pu) ratio.

Pu/(U+Pu)	a (Å)	b (Å)	c (Å)	β (°)	Batch	Ref
0.126	5.8776 (6)	10.125 (1)	11.650 (2)	110.26 (2)	Na_2CO_3	This work
0.293	5.774 (2)	10.167 (2)	11.672 (2)	110.39 (2)	1.2	
	5.879 (1)	10.141 (2)	11.653 (2)	110.14 (1)	Na_2CO_3	
	5.883 (2)	10.143 (2)	11.646 (2)	109.85 (2)	2	
0.46	5.878 (1)	10.146 (2)	11.663 (2)	109.93 (2)	1.2	
	5.895 (2)	10.171 (4)	11.668 (4)	109.99 (3)	Na_2CO_3	
	5.879 (1)	10.155 (2)	11.664 (2)	109.96 (2)	2	
0.85	5.867 (2)	10.045 (3)	11.673 (3)	111.18 (2)		
1	5.965 (3)	10.313 (3)	11.772 (3)	109.97 (1)	-	Smith [17]
	5.964 (3)	10.312 (4)	11.778 (4)	109.93 (3)	-	This work

As reported in section 4.2.1.1, the Na_2PuO_3 compound has a complex structure. Therefore, only the volume evolution with the plutonium content is reported in **figure 4.29**.

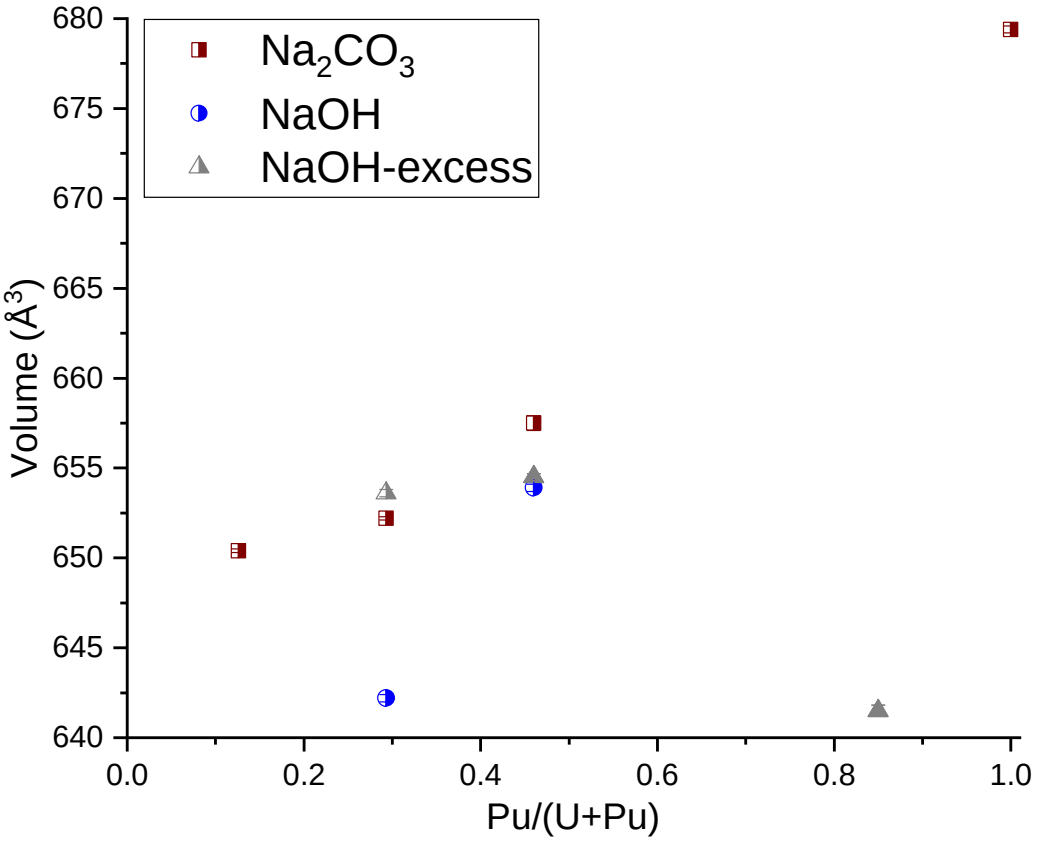

Figure 4.29: Lattice volume evolution of the Na_2MO_3 compositions with the starting plutonium content in the MOX. Symbols are half filled when several phases were observed.

As observed in **figure 4.29**, starting from Na_2PuO_3 volume, a general decrease of the unit cell volume is observed in Na_2MO_3 solid solution when the plutonium content decreases. Moreover, the volume difference (~25 Å^3) between the sodium mixed oxides Na_2MO_3 and Na_2PuO_3 is high. Finally, two samples, i.e. one obtained for Pu/(U+Pu)=0.29 and the other one for Pu/(U+Pu)=0.85, show lower volumes than the other ones. However, they were not investigated further due to a lack of time.

The only sample investigated with HR-XANES measurement at the U M_4 and Pu M_5-edges was the single phase Na_2MO_3 sample, obtained with starting MOX-46 and NaOH added in excess. The data are reported in **figure 4.30** and **table 4.29**.

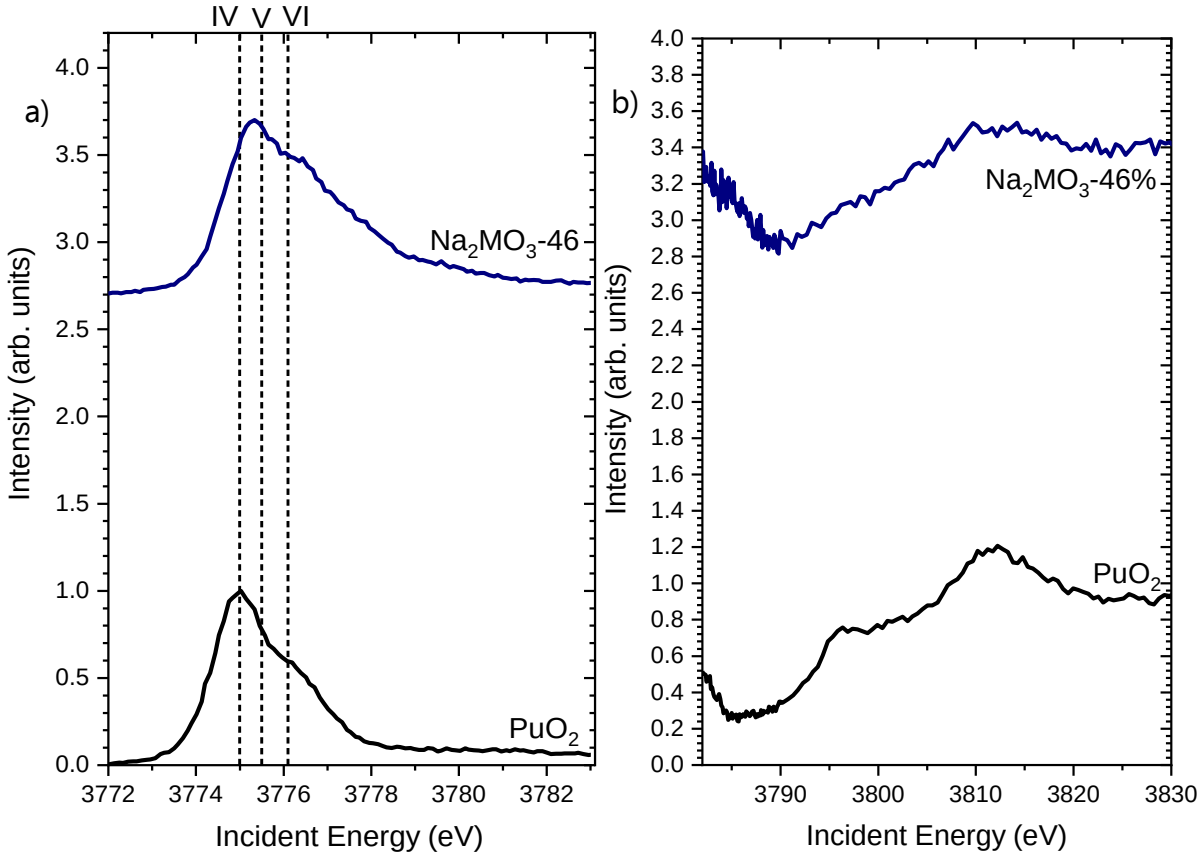

Figure 4.30: Pu M_5-edge HR-XANES (a) and post-edge (b) spectra of Na_2MO_3-46% and PuO_2 reference. (Spectra have been shifted on the y axis to better distinguish the different measurements).

Table 4.29: Energies of the White Lines and post-edge features of the PuO_2 and Na_2MO_3-46 samples at the Pu M_5-edge.

Sample	WL (eV)		Post edge		Ref
$Pu^{IV}O_2$	3775.0	-	*3796*	*3811*	This work
Na_2MO_3-46	**3775.4**	-	-	-	

The uranium is in the U^{VI} valence state (see **Appendix B**) which is not expected from the theoretical formula. As shown in **figure 4.30**, the plutonium is not tetravalent but close to the theoretical +V oxidation state as the shift is +0.4 eV. As Pu^{V} and U^{VI} have lower ionic radii than Pu^{IV}, this could explain the large volume difference observed between $Na_2Pu^{IV}O_3$ and the mixed oxides. Moreover, the ionic radius of U^{VI} is smaller than that of Pu^{V}. Therefore, this would be consistent with the slight decrease of the volume between Pu/(U+Pu)=0.46 and 0.13, observed in **figure 4.29**. As the measured actinide oxidation state is different from the theoretical Pu^{IV}, a charge compensation mechanism should also be introduced for these compositions. However, because of the few data and analyses performed on these phases, this is not discussed in this work.

Conclusion

The structure of $Na_2Pu^{IV}O_3$ is extremely complex with sodium and plutonium atoms sharing two crystallographic sites as described previously. Only few data were obtained on the Na_2MO_3 solid solution compositions and no direct conclusion on the charge compensation mechanisms can be deduced from these data. To study in details the structure of Na_2MO_3 solid solution, syntheses at high plutonium content should be performed and single phase samples should be analysed with complementary techniques as described for the Na_4MO_5 samples.

Thanks to detailed analyses of the different solid phases and the phase equilibria obtained with the different compositions in plutonium, an experimental phase diagram can be tentatively drawn as discussed in the next section.

4.3 Phase equilibria in the Na-O-Pu-U system

In the previous section, the structures of the $Na_\alpha M_\beta O_\gamma$ phases have been studied in detail, especially for the Na_4MO_5 phase in which several charge compensation mechanisms were identified.

As the final objective is to develop a thermodynamic model for the Na-O-Pu-U system, this section is dedicated to the determination of the phase equilibria that can be suggested from the results of the thermal treatments and phase characterizations in the previous section. **Table 4.30** is summarising the phase diagram data obtained in section 4.2 on the different samples.

These suggested phase equilibria data are compared with the phase diagram proposed by Pillon [1] in **figure 4.31**.

Since after a long thermal treatment, the Na_3MO_4 phase disappeared, this phase is not reported on the phase diagram. It is considered as a metastable phase which was observed after the MOX / sodium interaction under normal conditions as reported by Pillon [1].

Moreover, Pillon reported two different tetragonal phases Na_4MO_5 and $Na_{4+x}MO_5$. In this work, we have shown that it is a single phase $Na_{4+\xi1}(M,Na)O_{5+\xi2}$ with a large composition range which was thoroughly investigated (blue region). Plutonium solubility limits of Pu/(U+Pu)>0.12, in excess sodium, and of Pu/(U+Pu)>0.06 with a deficit in oxygen, were deduced. However, the phase boundaries are not yet well defined.

For the other phase boundaries there is a good agreement with the diagram of Pillon [1].

Finally, the $Na_2M_2O_7$ and Na_2MO_4 phases synthesized under air were also added. The plutonium solubilities were found as $Pu/(U+Pu)>0.12$ for $Na_2M_2O_7$ and $Pu/(U+Pu)>0.06$ for Na_2MO_4.

This region of the phase diagram was not investigated in the work of Pillon [1]. Therefore, it is the first time that these phases are characterised.

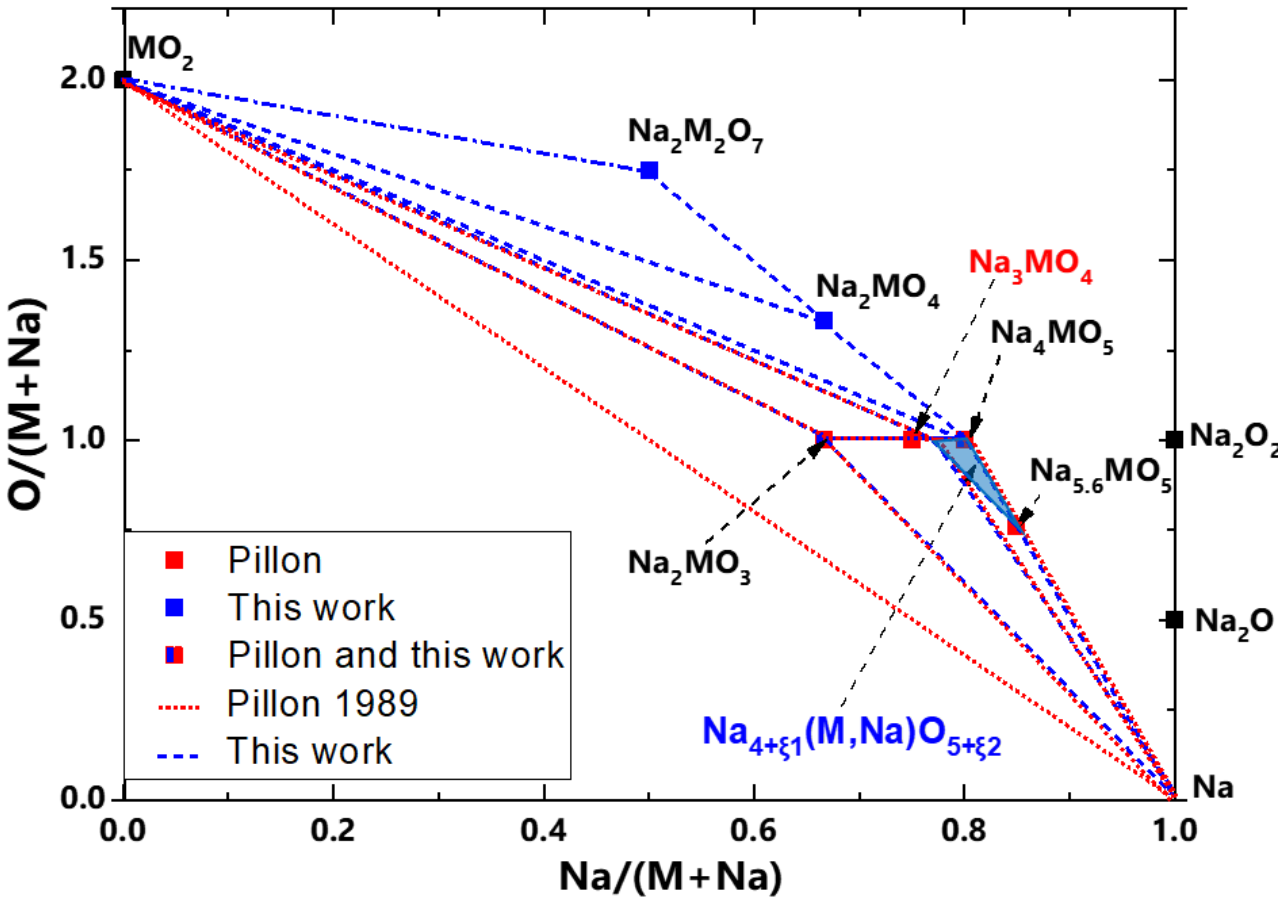

Figure 4.31: Comparison between the Na-M-O phase diagram at 1073 K with M=(U,Pu) reported by Pillon [1] and the one suggested from the results obtained in this work. In red, the stable phases reported by Pillon with the phase fields boundaries in red dashed lines. In blue the stable phases observed in this work with the phase fields boundaries in blue dashed lines and the composition domain of $Na_{4+\xi1}(M,Na)O_{5+\xi2}$

Table 4.30: Summary of the experimental phase diagram data obtained in the Na-O-Pu-U system

Pu/(U+Pu) in MOX	Ratio Na_2O:MOX	T(°C)	Phases	Conditions
0.06	1:2	800	$Na_2M_2O_7$	Air
	1:1		Na_2MO_4	Air
	2:1		Na_4MO_5	Argon
	2:1	1000	Na_4MO_5	Argon
0.12	1:2	800	$Na_2M_2O_7$	Air
	1:1		$Na_2MO_4 + MO_2$	Air
	Not known		Na_4MO_5	Argon Excess Na
	2.1:1		$Na_4MO_5 + MO_2$	Argon
	2:1	1000	$Na_4MO_5 + Na_2MO_3$	Argon
0.29	2:1	800	$Na_4MO_5 + MO_2$	Argon
	Not known		$Na_4MO_5 + Na_2MO_3 + MO_2$	Argon Excess Na
	2.2:1		$Na_4MO_5 + Na_2MO_3$	Argon Excess Na
	2:1	1000	$Na_4MO_5 + Na_2MO_3$	Argon
0.46	1:2	800	$Na_2M_2O_7 + Na_2MO_4 + MO_2$	Air
	1:1		$Na_2MO_4 + Na_4MO_5 + MO_2$	Air
	Not known		$Na_2MO_3 + Na_4MO_5$	Argon Excess Na
	2.2:1		Na_2MO_3	Argon
	2 :1	1000	$Na_4MO_5 + Na_2MO_3 + MO_2$	Argon

As shown in section 4.2.2.1, pure U^{VI} was found in all the investigated samples. Therefore, a pseudo-ternary phase diagram with the $U^{VI}O_3$ end-member representing pure U^{VI} can be considered.

For the plutonium, several oxidation states were found among the samples. However, as in most of the samples, plutonium was found as Pu^{IV}, and as the lattice parameter of the MO_2 phase was close to the one of PuO_2, the pseudo-ternary Na_2O-$U^{VI}O_3$-$Pu^{IV}O_2$ section is tentatively drawn in **figure 4.32**. The dashed lines represent the hypothetical phases boundaries.

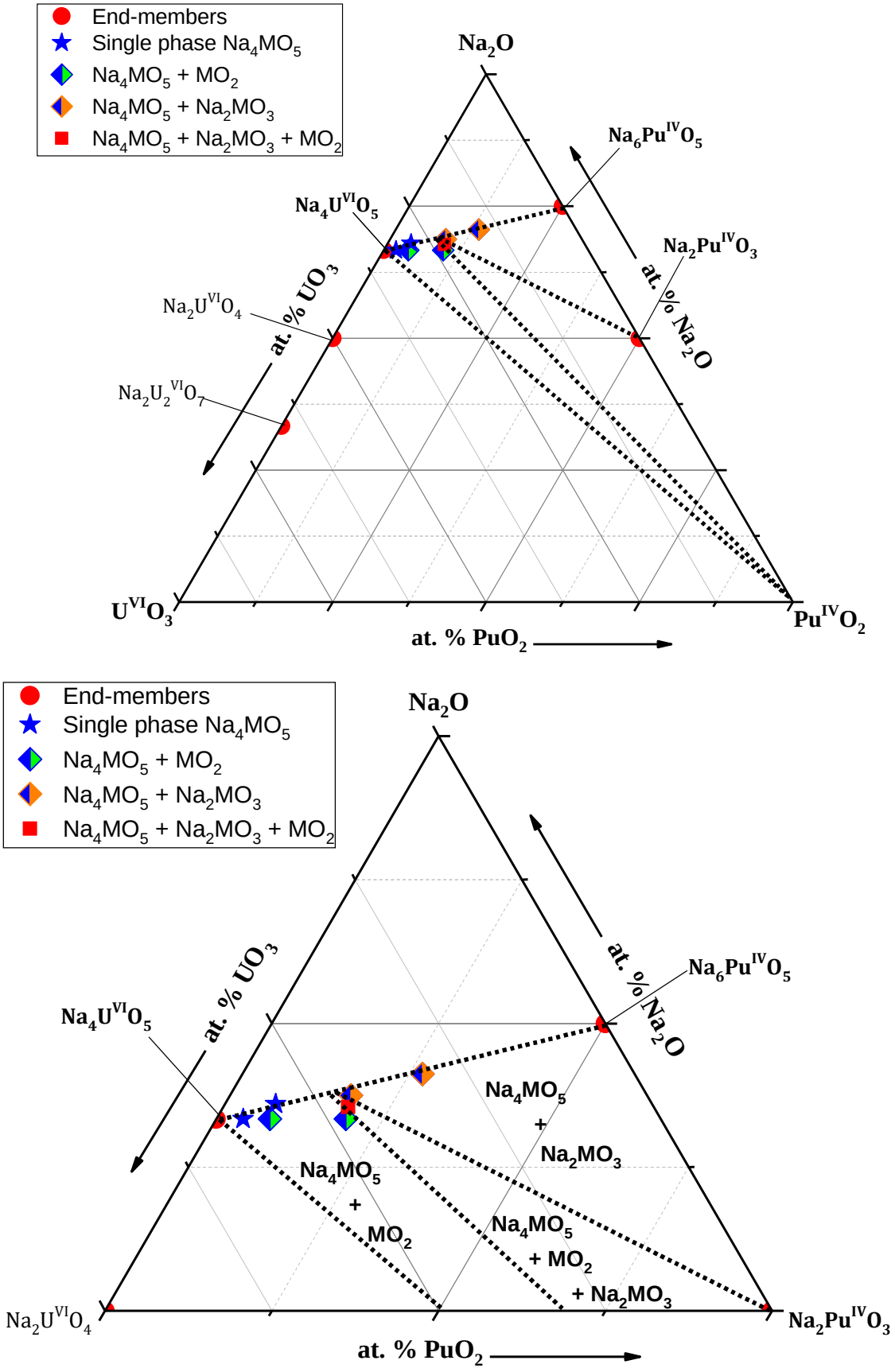

Figure 4.32: Experimental phase diagram at 800°C of the Na_2O-UO_3-PuO_2 section. In figure b) a zoom on the Na_2O-$Na_2U^{VI}O_4$-Na_2PuO_3 section is shown.

In this work, thanks to the wide plutonium composition range for the starting MOX and the different atmospheres for the synthesis, the phase diagram on the Na-O-Pu-U system as reported in **figure 4.31** and **4.32** has been improved.

However, the composition in plutonium, uranium, sodium and oxygen of the different phases is missing. Local characterization methods are necessary to measure these data. Moreover, to improve the accuracy of the phase diagram data, long thermal treatments with controlled oxygen potential should be performed. Nevertheless, these experiments are extremely challenging with compounds containing sodium and plutonium.

4.4 Conclusion

In this chapter, the synthesis of the nanosized MOX particles was reported and the products that were obtained thoroughly characterized. Then, they were used as starting reagents to perform the syntheses of sodium urano-plutonates, obtained after reaction between Na_2O (formed in situ) and nanosized PuO_2 and $U_{1-x}Pu_xO_2$ with different Pu/(U+Pu) ratio. The structure of the single phase products were characterised with XRD, ^{23}Na-NMR, MQ-MAS and HR-XANES spectroscopy.

In the Na-O-Pu system, the discrepancy on the structure of the Na_2PuO_3 compound was solved. Na_2PuO_3 was finally refined with a monoclinic symmetry in the *C2/c* space group. For the Na_4PuO_5 compound, the measured cell parameters are in good agreement with the ones reported in the literature. However, the determination of the actinide oxidation state using HR-XANES spectroscopy leads to Pu^{V} instead of Pu^{VI} as theoretically expected. The most probable mechanism is the introduction of oxygen vacancies leading to the $Na_4PuO_{4.5}$ composition.

In the Na-O-Pu-U system, a sodium urano-plutonate with pure Pu^{VI} was obtained under air: the $Na_2U^{VI}_{0.94}Pu^{VI}_{0.06}O_4$ solid solution. This phase is the first reference phase for sodium urano-plutonates with Pu^{VI}. The other structures obtained under oxidizing atmosphere are the $Na_2M_2O_7$ phase obtained pure for Pu/(U+Pu)= 0.06 and 0.12. The HR-XANES analyses showed that Pu^{IV} was found but a mixture of Pu^{IV}/Pu^{VI} could not be totally excluded for these samples.

Under argon atmosphere, the Na_4MO_5 phase was obtained in many syntheses. However, the plutonium oxidation state and the charge compensation mechanisms were found to be different depending on the sodium and oxygen contents in the phases. When the plutonium remains as Pu^{IV}, the charge compensation is (i) either made by insertion of sodium atoms on the crystallographic site of the actinide, leading to $Na_4(U^{VI}_{1-x}Na_{2x}Pu^{IV}_x)O_5$ with a strong volume increase or (ii) by oxygen vacancies introduction leading to $Na_4(U^{VI}_{1-x}Pu^{IV}_x)O_{5-x}$. When plutonium is oxidised, the charge compensation mechanism could not be assessed. Finally, a large composition range was found for this phase.

A short discussion on the Na_2MO_3 structure was then presented. In some samples with high plutonium content, this compound was obtained in equilibrium with Na_4MO_5. Only one sample was constituted of pure Na_2MO_3, in which plutonium was found more oxidised than Pu^{IV}. However, experiments with high plutonium content and accurate sodium stoichiometry are needed to study this phases in details.

Using the newly determined structural data on the Na-O-Pu-O system, the table summarising the structural data on sodium mixed oxides compounds, reported in the literature (see **table 2.4** in Chapter 2 section 2.1.4.) can be completed as shown hereafter in **table 4.31**.

Table 4.31: Structural data on the Na-M-O phases and endmembers

Composition	Uranium End member	Ref	Phase MOX	Ref	Plutonium End member	Ref
Na_2MO_3	-	-	Cubic	[1]	-	
			Monoclinic, *C2/c* (15) $Na_2(U^{VI},Pu^{V})O_3$ Charge compensation mechanism not determined	This work	Monoclinic *C2/c* (15)	[18], This work
$NaMO_3$	Orthorhombic	[38]	?	[39]	-	-
Na_3MO_4	Cubic (metastable)	[40]	Cubic Pu/(U+Pu)<0.3	[26,41]	Cubic	[5]
	-	-	Tetragonal Pu/(U+Pu) ≥ 0.3	[26,41]	-	-
	Monoclinic	[18]	Orthorhombic (metastable)	[1]	Orthorhombic	[18]
$Na_{3+\varepsilon}M_{1+\varepsilon}O_{4+2\varepsilon}$	Monoclinic	[25]	Cubic	[1]	Rhombohedral	[1]
$Na_2M_2O_7$	Monoclinic, *P21/a* (14)	[42]	Monoclinic, *P21/a* (14) Solubility >Pu/(U+Pu)=0.12 (800°C) Pu oxidation state IV or mixture of Pu^{IV}/Pu^{VI}	This work	Monoclinic	[5]
Na_2MO_4	Orthorhombic *Pbam* (55)	[27]	Orthorhombic, *Pbam* (55) Solubility >Pu/(U+Pu)=0.06 (800°C)	This work	-	-
Na_4MO_5	Tetragonal, *I4/m*	[1]	Tetragonal, *I4/m* (87) $Na_4(U^{VI}_{1-x},Pu^{IV}_{x})O_{5-x}$ Solubility > Pu/(U+Pu)=0.06 (800°C) $Na_4(U^{VI},Pu^{V})O_5$ (1000°C) Charge compensation mechanism not determined	This work	Tetragonal, *I4/m* (87) Mainly Pu^{V} but mixture Pu^{V}/Pu^{VI} possible Charge compensation mechanism not determined	This work
	Cubic (metastable)	[18]	-	-	Cubic	[5]
$Na_{4+x}MO_5$	$Na_{5.33}UO_5$ Tetragonal	[1]	$Na_4(U^{VI}_{1-x},Pu^{IV}_{x},Na_{2x})O_5$ Tetragonal, *I4/m* (87) Solubility > Pu/(U+Pu)=0.12 (800°C)	This work	$Na_5Pu^{V}O_5$ Monoclinic	[1]
					$Na_6Pu^{IV}O_5$?	[1]

Our phase equilibria data at 800°C were compared with the phase diagram drawn by Pillon [1]. The Na_3MO_4 phase was not reported because it was found metastable in this work. Moreover, the wide composition range of $Na_{4+\xi1}(M,Na)O_{5+\xi2}$, the $Na_2M_2O_7$ and Na_2MO_4 phases were added. A hypothetical Na_2O-$Pu^{IV}O_2$-$U^{VI}O_3$ pseudo-ternary phase diagram was also proposed.

These new data improve the knowledge on the Na-O-Pu-U phase diagram. It will be extremely useful for the future Calphad model development of the Na-O-Pu-U system. However, to assess more accurately the phase boundaries reported in this phase diagram and the solubility limits of plutonium in the different phases, experiments with precisely controlled sodium amounts and oxygen potential should be performed together with long thermal treatments. The exact composition of the phases have to be also measured.

Finally, measurements of the thermodynamic properties of these phases would also be extremely useful to understand how the stability of those compounds changes with the plutonium and oxygen contents.

REFERENCES

[1] S. Pillon, Etude des diagrammes de phases U-O-Na, Pu-O-Na, U,Pu-O-Na, 1989. http://www.iaea.org/inis/collection/NCLCollectionStore/_Public/21/052/21052450.

[2] D. Haas, A. Vandergheynst, J. van Vliet, R. Lorenzelli, J.-L. Nigon, Mixed-Oxide Fuel Fabrication Technology and Experience at the Belgonucléaire and CFCa Plants and Further Developments for the MELOX Plant, Nucl. Technol. 106 (1994) 60–82.

[3] Z. Talip, S. Peuget, M. Magnin, M. Tribet, C. Valot, R. Vauchy, C. Jégou, Characterization of un-irradiated MIMAS MOX fuel by Raman spectroscopy and EPMA, J. Nucl. Mater. 499 (2018) 88–97.

[4] R.M. Orr, H.E. Sims, R.J. Taylor, A review of plutonium oxalate decomposition reactions and effects of decomposition temperature on the surface area of the plutonium dioxide product, J. Nucl. Mater. 465 (2015) 756–773.

[5] D.M. Bykov, P.E. Raison, R.J.M. Konings, C. Apostolidis, M. Orlova, Synthesis and crystal structure investigations of ternary oxides in the Na–Pu–O system, J. Nucl. Mater. 457 (2015) 54–62.

[6] O. Walter, K. Popa, O.D. Blanco, Hydrothermal decomposition of actinide(IV) oxalates: a new aqueous route towards reactive actinide oxide nanocrystals, Open Chem. 14 (2016) 170–174.

[7] K. Popa, O. Walter, O. Dieste Blanco, A. Guiot, D. Bouëxière, J.-Y. Colle, L. Martel, M. Naji, D. Manara, A low-temperature synthesis method for AnO_2 nanocrystals (An = Th, U, Np, and Pu) and associate solid solutions, CrystEngComm. 20 (2018) 4614–4622.

[8] L. Balice, D. Bouëxière, M. Cologna, A. Cambriani, J.-F. Vigier, E. De Bona, G.D. Sorarù, C. Kübel, O. Walter, K. Popa, Nano and micro $U_{1-x}Th_xO_2$ solid solutions: From powders to pellets, J. Nucl. Mater. 498 (2018) 307–313.

[9] D. Bouëxière, K. Popa, O. Walter, M. Cologna, Kinetic study on the grain growth of PuO_2 nanocrystals, RSC Adv. 9 (2019) 6542–6547.

[10] K.O. Kvashnina, S.M. Butorin, P. Martin, P. Glatzel, Chemical State of Complex Uranium Oxides, Phys. Rev. Lett. 111 (2013) 253002.

[11] K. Popa, D. Prieur, D. Manara, M. Naji, J.-F. Vigier, P.M. Martin, O. Dieste Blanco, A.C. Scheinost, T. Prüßmann, T. Vitova, P.E. Raison, J. Somers, R.J.M. Konings, Further insights into the chemistry of the Bi–U–O system, Dalton Trans. 45 (2016) 7847–7855.

[12] S.B. Donald, M.L. Davisson, Z. Dai, S.K. Roberts, A.J. Nelson, Relative impact of H_2O and O_2 in the oxidation of UO_2 powders from 50 to 300 °C, J. Nucl. Mater. 496 (2017) 353–361.

[13] S. M. Butorin, K. O. Kvashnina, D. Prieur, M. Rivenet, P. M. Martin, Characteristics of chemical bonding of pentavalent uranium in La-doped UO_2, Chem. Commun. 53 (2017) 115–118.

[14] E. Epifano, M. Naji, D. Manara, A.C. Scheinost, C. Hennig, J. Lechelle, R.J.M. Konings, C. Guéneau, D. Prieur, T. Vitova, K. Dardenne, J. Rothe, P.M. Martin, Extreme multi-valence states in mixed actinide oxides, Commun. Chem. 2 (2019) 1–11.

[15] J.-Y. Colle, S. Stohr, B. Cremer, S. Van Winckel, G. Rasmussen, O.D. Blanco, T. Wiss, R.J.M. Konings, Uranium–plutonium partitioning in aerosols produced from $(U,Pu)O_2$ mixed oxide by laser heating, J. Aerosol Sci. 148 (2020) 105588.

[16] M. Shao-Yu, R. Xiao-Xia, Z. Zhao-Hui, Synthesis and Crystal Structure of Na2TiO3, JIEGOU HUAXUE. 27 (2008) 5.

[17] A.L. Smith, Structural and thermodynamic properties of sodium actinide ternary oxides, PhD Thesis, Department of Materials Science and Metallurgy, University of Cambridge, 2015.
[18] S. Bahl, A. Bauer, E. Bohnert, K. Dardenne, E. González-Robles, M. Herm, V. Krepper, V. Metz, I. Pidchenko, J. Rothe, M. Vespa, T. Vitova, Development of actinide speciation methods, 6.
[19] C. Keller, L. Koch, K.H. Walter, Die reaktion der oxide der transurane mit alkalioxiden—I: Ternäre oxide der sechswertigen transurane mit lithium und natrium, J. Inorg. Nucl. Chem. 27 (1965) 1205–1223.
[20] A.L. Smith, P. Martin, D. Prieur, A.C. Scheinost, P.E. Raison, A.K. Cheetham, R.J.M. Konings, Structural Properties and Charge Distribution of the Sodium Uranium, Neptunium, and Plutonium Ternary Oxides: A Combined X-ray Diffraction and XANES Study, Inorg. Chem. 55 (2016) 1569–1579.
[21] S.D. Conradson, K.D. Abney, B.D. Begg, E.D. Brady, D.L. Clark, C. den Auwer, M. Ding, P.K. Dorhout, F.J. Espinosa-Faller, P.L. Gordon, R.G. Haire, N.J. Hess, R.F. Hess, D.W. Keogh, G.H. Lander, A.J. Lupinetti, L.A. Morales, M.P. Neu, P.D. Palmer, P. Paviet-Hartmann, S.D. Reilly, W.H. Runde, C.D. Tait, D.K. Veirs, F. Wastin, Higher Order Speciation Effects on Plutonium L_3 X-ray Absorption Near Edge Spectra, Inorg. Chem. 43 (2004) 116–131.
[22] K.O. Kvashnina, A.Y. Romanchuk, I. Pidchenko, L. Amidani, E. Gerber, A. Trigub, A. Rossberg, S. Weiss, K. Popa, O. Walter, R. Caciuffo, A.C. Scheinost, S.M. Butorin, S.N. Kalmykov, A Novel Metastable Pentavalent Plutonium Solid Phase on the Pathway from Aqueous Plutonium(VI) to PuO_2 Nanoparticles, Angew. Chem. Int. Ed. 58 (2019) 17558–17562.
[23] A.L. Smith, P.E. Raison, L. Martel, T. Charpentier, I. Farnan, D. Prieur, C. Hennig, A.C. Scheinost, R.J.M. Konings, A.K. Cheetham, A ^{23}Na Magic Angle Spinning Nuclear Magnetic Resonance, XANES, and High-Temperature X-ray Diffraction Study of $NaUO_3$, Na_4UO_5, and $Na_2U_2O_7$, Inorg. Chem. 53 (2014) 375–382.
[24] A.L. Smith, P.E. Raison, L. Martel, D. Prieur, T. Charpentier, G. Wallez, E. Suard, A.C. Scheinost, C. Hennig, P. Martin, K.O. Kvashnina, A.K. Cheetham, R.J.M. Konings, A New Look at the Structural Properties of Trisodium Uranate Na_3UO_4, Inorg. Chem. 54 (2015) 3552–3561.
[25] M.A. Mignanelli, P.E. Potter, The reactions between sodium and plutonia, urania-plutonia and urania-plutonia containing fission product simulants, J. Nucl. Mater. 125 (1984) 182–201.
[26] E.H.P. Cordfunke, D.J.W. IJdo, α- and β-Na_2UO_4: Structural and Thermochemical Relationships, J. Solid State Chem. 115 (1995) 299–304.
[27] I. Pidchenko, Characterization of structural properties of U and Pu in model systems by advanced synchrotron based X-ray spectroscopy, KIT, 2016.
[28] T. Vitova, J.C. Green, R.G. Denning, M. Löble, K. Kvashnina, J.J. Kas, K. Jorissen, J.J. Rehr, T. Malcherek, M.A. Denecke, Polarization Dependent High Energy Resolution X-ray Absorption Study of Dicesium Uranyl Tetrachloride, Inorg. Chem. 54 (2015) 174–182.
[29] Y. Podkovyrina, I. Pidchenko, T. Prüßmann, S. Bahl, J. Göttlicher, A. Soldatov, T. Vitova, Probing Covalency in the UO_3 Polymorphs by U M_4 edge HR- XANES, J. Phys. Conf. Ser.
[30] I. Pidchenko, K.O. Kvashnina, T. Yokosawa, N. Finck, S. Bahl, D. Schild, R. Polly, E. Bohnert, A. Rossberg, J. Göttlicher, K. Dardenne, J. Rothe, T. Schäfer, H. Geckeis, T. Vitova, Uranium

Redox Transformations after U(VI) Coprecipitation with Magnetite Nanoparticles, Environ. Sci. Technol. 51 (2017) 2217–2225.
[31] M. Gasperin, $Na_2U_2O_7$: Synthèse et structure d'un monocristal, J. Common Met. 119 (1986) 83–90.
[32] I. Pidchenko, F. Heberling, K. Kvashnina, N. Finck, D. Schild, E. Bohnert, T. Schäfer, J. Rothe, H. Geckeis, T. Vitova, Aqueous U(VI) interaction with magnetite nanoparticles in a mixed flow reactor system: HR-XANES study, J. Phys. Conf. Ser. 712 (2016) 012086.
[33] M. Housseau, G. Dean, J.P. Marcon, J.F. Marin, Etude hors pile des réactions entre les oxydes d'uranium et de plutonium et le sodium, Note CEA-N-1588. (1973). https://inis.iaea.org/collection/NCLCollectionStore/_Public/04/058/4058558.
[34] R. Scholder, H. Gläser, Über Lithium- und Natriumuranate(V) und über strukturelle Beziehungen zwischen den Verbindungstypen Li_7AO_6 und Li_8AO_6, Z. Für Anorg. Allg. Chem. 327 (1964) 15–27.
[35] Shannon-Prewitt Effective Ionic Radius - Part 3 | The Elements Handbook at KnowledgeDoor,http://www.knowledgedoor.com/2/elements_handbook/shannon-prewitt_effective_ionic_radius_part_3.html
[36] A.L. Smith, P.E. Raison, R.J.M. Konings, Synthesis and crystal structure characterisation of sodium neptunate compounds, J. Nucl. Mater. 413 (2011) 114–121.

Chapter 5: Experimental study of the BaO-MoO_3-Na_2O system

The experimental data and the thermodynamic models available in the literature on the BaO-MoO_3-Na_2O system are first reviewed. Then, an experimental study on both structural and thermodynamic properties of the $Ba_2NaMoO_{5.5}$ compound is presented.

5.1. Literature review

Data on the BaO-MoO_3, MoO_3-Na_2O, BaO-Na_2O and BaO-MoO_3-Na_2O systems are reviewed to identify gaps in knowledge, thus which systems and compounds should be experimentally investigated.

A schematic view of the BaO-MoO_3-Na_2O section is presented in **figure 5.1**, showing the different compounds that are stable in this pseudo-ternary system.

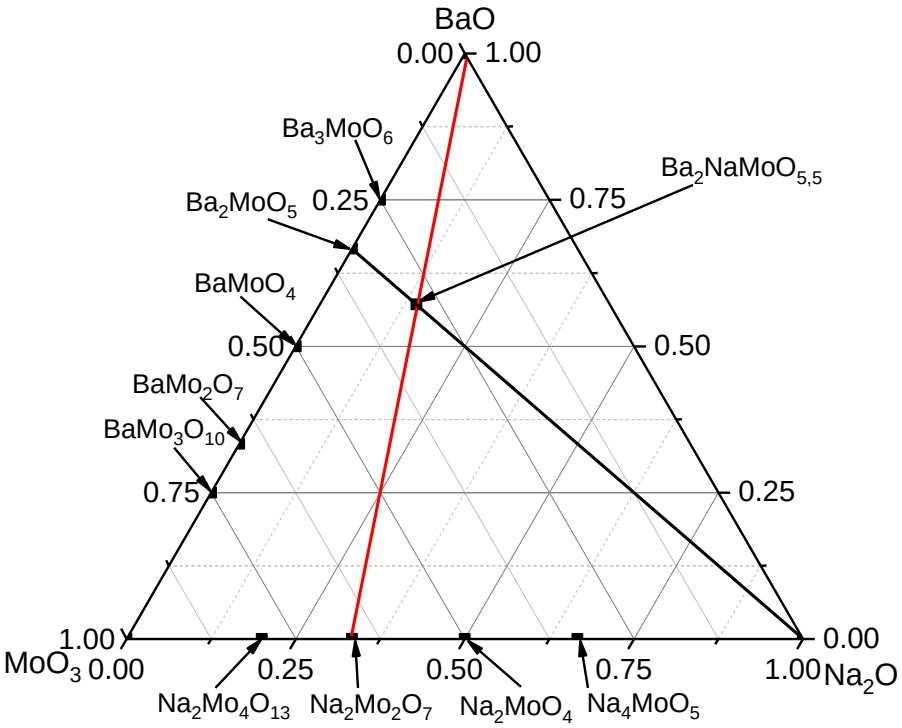

Figure 5.1: Sketch of the pseudo-ternary phase diagram BaO-MoO_3-Na_2O

Firstly, the pseudo-binary systems are described, followed by the BaO-Na_2O-MoO_3 phase diagram section and the $Ba_2NaMoO_{5.5}$ quaternary compound.

BaO-MoO₃

In the BaO-MoO_3 pseudo-binary system, many ternary compounds have been reported: Ba_3MoO_6, Ba_2MoO_5, $BaMoO_4$, $BaMo_2O_7$ and $BaMo_3O_{10}$ in the different studies reported by Cavalcante et al. [1], Veksler and Zhukovskij [2], Gao et al. [3] and Werner et al. [4].

Smith [5] performed a thermodynamic assessment of this system using the CALPHAD method within the TAF-ID project (**figure 5.2**), based on the different data reported by Yanushkevich *et al.* [6], Dash *et al.* [7], Zhukovskii and Petrov [8], Zhukovskii *et al.* [9], and Cordfunke and Konings [10].

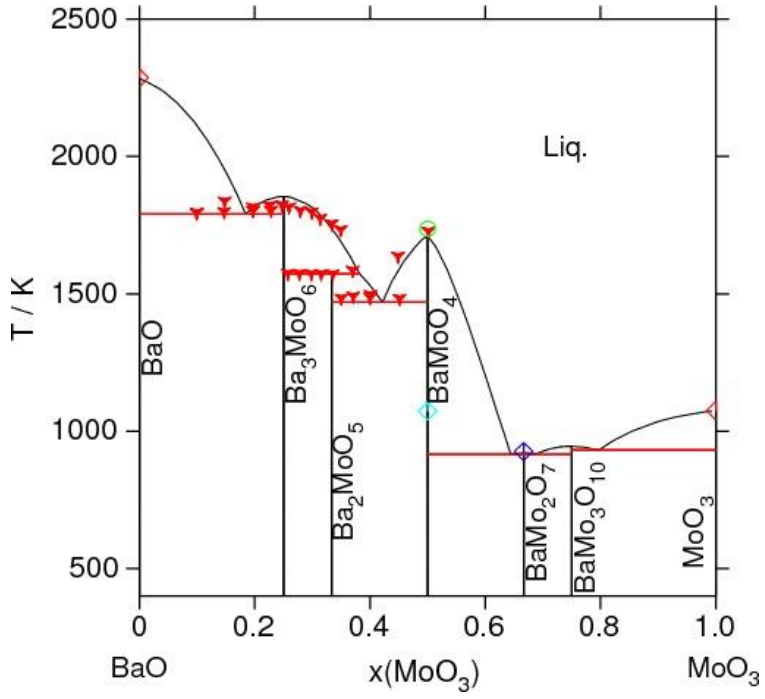

Figure 5.2: Calculated BaO-MoO_3 pseudo-binary phase diagram. Model developed by Smith [5] within the TAF-ID project with the data of ▼ Yanushkevich *et al.* [6], ○ Dash *et al.* [7], ◇ Zhukovskii and Petrov [8], ◇ Zhukovskii *et al.* [9], ◇ Cordfunke and Konings [10].

In terms of thermodynamic data available, the $BaMoO_4$ is well known in this system as reported in the review by Dash *et al.* [7]. For the other compositions, the reported thermodynamic data are mainly based on estimations.

The Calphad model is in good agreement with the phase diagram data reported for the BaO-$BaMoO_4$ pseudo-binary. But the knowledge on the $BaMoO_4$-MoO_3 pseudo-binary section is more limited. Therefore, this system still requires further experimental investigations.

Na_2O-MoO_3

The Na_2O-MoO_3 pseudo-binary section is described in the PhD work of Bordier [11], reporting the existence and the structure of the following compounds: Na_4MoO_5, Na_2MoO_4, $Na_2Mo_2O_7$ and $Na_2Mo_4O_{13}$. The calculated phase diagram with the Calphad model developed by Bordier [11] is presented in **figure 5.3**. However, the optimised parameters for the Mo-O sub-system in the description of Bordier [11] are not compatible with the current descriptions in the TAF-ID database [12], and is further described in Chapter 7.

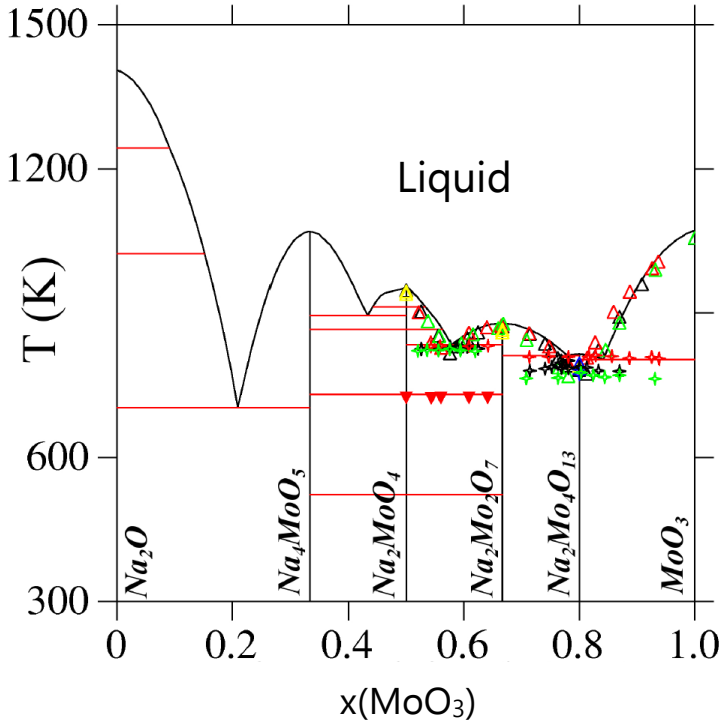

Figure 5.3: Calculated Na_2O-MoO_3 pseudo-binary phase diagram using the thermodynamic modelling assessment of Bordier [11], compared with the liquidus data of △ Groschuff [13], △ Hoermann [14], △ Caillet [15], △ Balashov [16] and solidus data of ✦ Groschuff [13], ✦ Hoermann [14], ✦ Caillet [15], △ Mudher *et al.* [17] and the allotropic transition data of ▼ Caillet [15].

In this system, the Na_2MoO_4-MoO_3 pseudo-binary section has been extensively studied, while thermodynamic data have been collected on the Na_2MoO_4 and $Na_2Mo_2O_7$ compounds as reported by the review of Bordier [11]. As for the Na_2O-Na_4MoO_5 section and the thermodynamic data for Na_4MoO_5 and $Na_2Mo_4O_{13}$, only few data have been reported on the structure of the compounds and the Gibbs energy of formation by Mudher *et al.* [17], Sridaran *et al.* [18] and Gnanasekaran *et al.* [19]. Thermodynamic data for these compounds were estimated and the Calphad model developed is in good agreement with the phase diagram data from the literature reported by Groschuff [13], Hoermann [14], Caillet [15], Balashov [16] and Mudher *et al.* [17].

BaO-Na_2O

The BaO-Na_2O pseudo-binary section was never reported in the literature. Nevertheless, the pseudo-ternary phase diagrams BaO-Na_2O-Nb_2O_5 and BaO-Na_2O-SiO_2 were experimentally studied by Giess *et al.* [20] and Gunawardan *et al.* [21], respectively. The first system was studied by Differential Thermal Analysis (DTA) and crystal melt growth. The second system was carefully characterised by a static-equilibrium technique, and the equilibrium phases were identified by optical microscopy and XRD measurements. In these two pseudo-ternary phase diagrams, no

compound was reported on the pseudo-binary section BaO-Na_2O. Therefore, we will consider that no compound exists in-between the Na_2O and BaO end-members.

To conclude, this system is not well known and would need further investigation.

$BaO-Na_2O-MoO_3$

A study of the Na_2MoO_4-$BaMoO_4$ phase diagram has recently been reported by Danilushkina *et al.* [22]. The phase diagram exhibits one eutectic point at T_E=951 K at a composition of 9.7 equivalent. % of $BaMoO_4$. Moreover, barium is soluble into the Na_2MoO_4 structure up to 4% at 967 K forming the solid solution $(Na,Ba)_2MoO_4$ [23]. Unfortunately, the phase diagram is not reported in their study.

Finally, the Na_2MoO_4-$BaMoO_4$-MoO_3 pseudo-ternary section was studied by Garkushin *et al.* [24] by Differential Thermal Analysis. The results obtained on the section AB with A (20% $BaMoO_4$ + 80% Na_2MoO_4) and B (20% $BaMoO_4$ + 80% MoO_3) are reported in **figure 5.4.** In this figure, D_1 and D_2 represent $Na_2Mo_2O_7$ and $Na_2Mo_4O_{13}$, respectively. The pseudo-binary section is finally represented by the red line in the Na_2MoO_4-$BaMoO_4$-MoO_3 section in **figure 5.5**.

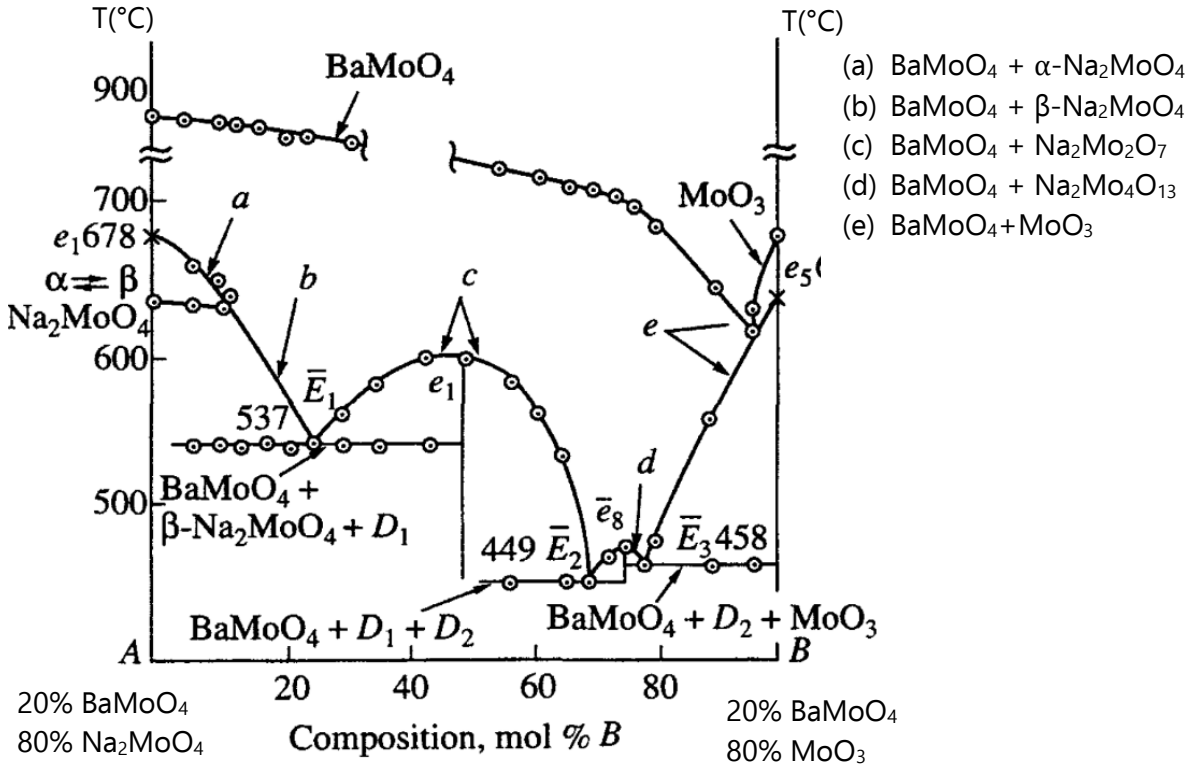

Figure 5.4: Phase diagram of the AB section with A (20% $BaMoO_4$ + 80% Na_2MoO_4) and B (20% $BaMoO_4$ + 80% MoO_3) reported by Garkushin *et al.* [24]

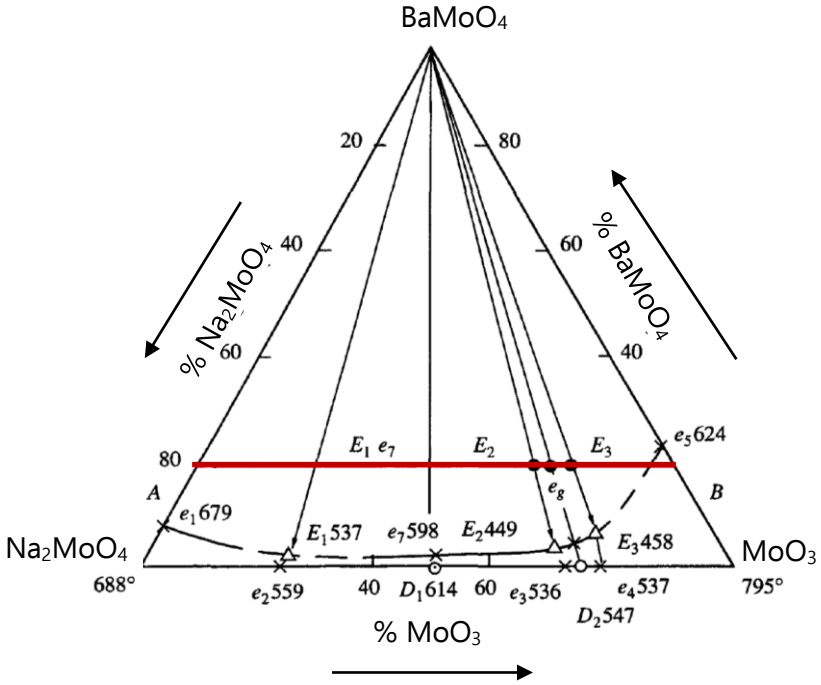

Figure 5.5: Na_2MoO_4-$BaMoO_4$-MoO_3 section reported by Garkushin *et al.* [24]. The AB section is represented in red.

$Ba_2NaMoO_{5.5}$

As reported in **figure 5.1**, the quaternary compound $Ba_2NaMoO_{5.5}$ exists in the BaO-MoO_3-Na_2O system. This compound crystallises with a perovskite structure, like the BaMoO3 compound found in the "grey phase" $(Ba,Sr)(Zr,Mo,U)O_3$ in the irradiated fuel as described in Chapter 1 and 2. Nevertheless, a slight structural difference exists: the quaternary compound is $Fm\bar{3}m$ (225) whereas $BaMoO_3$ is $Pm\bar{3}m$ (221). Sabatier *et al.* [25] and Thangarudai *et al.* [26] reported XRD measurements with a slight difference in the cell parameter (a=8.330(2) Å for Sabatier *et al.* and 8.319(3) Å for Thangarudai *et al* [26]). The second study also reports a ^{23}Na MAS NMR investigation of the compound showing that only one oxygen site exists and that the oxygen sites are not ordered. Nevertheless, the structure of the compound is still not well known as the presence of oxygen vacancies in the compound were only described from XRD measurements. Moreover, no thermodynamic data have been reported on this phase to this date.

Conclusion

To conclude, the pseudo-binary systems BaO-MoO_3 and Na_2O-MoO_3 are relatively well known and CALPHAD models are available. However, the CALPHAD model for the Mo-O sub-system in the Na_2O-MoO_3 description from Bordier [11] is not compatible with the one in the TAF-ID [12]. Moreover, the Mo-O model in the TAF-ID database had to be slightly modified to correct some issues encountered when calculating ternary systems such as Ba-Mo-O, Cs-Mo-O, etc. (more specifically the appearance of

unexpected miscibility gaps) systems. Thus, a new Mo-O model has been developed in this work, and the updated versions of BaO-MoO_3 and MoO_3-Na_2O are presented in Chapter 7.

The phase equilibria in the BaO-Na_2O system are not known but the priority will not be given to this system because the reaction between $BaMoO_3$ and $BaMoO_4$ and sodium is key for the understanding of the fission product phases / sodium coolant interaction.

As for the current knowledge on the pseudo-ternary system, the $BaMoO_4$-Na_2MoO_4 section and the $BaMoO_4$-Na_2MoO_4-MoO_3 section were investigated and phase diagram data collected.

For the quaternary compound $Ba_2NaMoO_{5.5}$, only a few structural and no thermodynamic data are available. This compound could be formed in case of interaction between fission products compounds and sodium as detailed in the next section. Therefore, to take this compound into account in the modelling assessments, thermodynamic data are needed. Hence, the structural and thermodynamic investigation of $Ba_2NaMoO_{5.5}$ was performed and is presented hereafter.

5.2. Characterisation of the $Ba_2NaMoO_{5.5}$ compound

Before starting a detailed investigation of $Ba_2NaMoO_{5.5}$, large batches of pure compound had to be synthesised. In this section, the synthesis method is first described. Then, the structural characterisation of the compound is presented and finally, measurements of thermodynamic data are described.

5.2.1. Synthesis

The starting reagent $BaMoO_4$ was synthesized by grinding together barium carbonate $BaCO_3$ (Fluka, >99%) and molybdenum trioxide MoO_3 (Alfa Aesar, >99.5%) in stoichiometric ratio. The powdered mixture was then heated under dry oxygen for 45 hours at 1073 K with one intermediate regrinding step. The purity of the sample was checked by X-ray diffraction at room temperature (see **figure 5.6**).

$Ba_2NaMoO_{5.5}$ was then synthesized by reaction between powdered $BaMoO_4$, stoichiometric amounts of barium carbonate $BaCO_3$ (Fluka, >99%) and anhydrous sodium carbonate Na_2CO_3 (Sigma-Aldrich, >99.5%). The stoichiometric mixture was heated under oxygen flow for 60 hours at 973 K with one intermediate regrinding step.

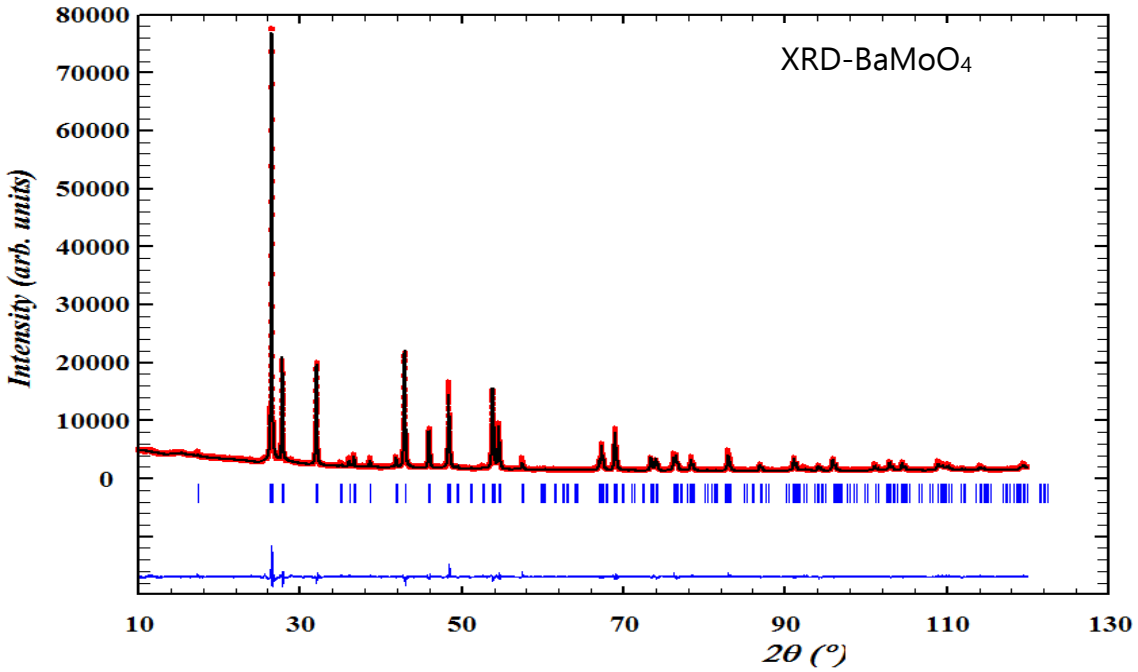

Figure 5.6: Comparison between the calculated (Y_{calc}, in black) and observed (Y_{obs}, in red) XRD patterns of $BaMoO_4$. Y_{obs}-Y_{calc} in blue, is the difference between the experimental and calculated intensites. The angular positions of Bragg reflections are shown in blue. The measurement has been performed at λ=Cu-Kα

5.2.2. Structural Investigation

The synthesised quaternary compound was then examined by X-ray diffraction (XRD) at room temperature to assess its purity, its lattice parameters and compare with the results from the literature. Then, neutron diffraction and XAS measurements were performed (**Appendix A.1 and A.2**). Finally, the evolution of the structure of the compound at high temperatures has been studied using HT-XRD and HT-Raman spectroscopy (**Appendix A.6**).

5.2.2.1. XRD and neutron diffraction at room temperature

As reported in section 5.1.1, at room temperature, $Ba_2NaMoO_{5.5}$ crystallizes with a cubic perovskite structure in space group $Fm\bar{3}m$ (225) [25]. The collected X-ray and neutron diffraction patterns are reported in **figures 5.7** and **5.8**. The resulting parameters are reported in **table 5.1**.

The refined cell parameters obtained by the Rietveld method from the XRD data, a=8.3156(4) Å, are in good agreement with the reported values by Thangarudai *et al.* [26] a=8.319(3) Å. The neutron diffraction data (a=8.305(1) Å at λ=1.667 Å) are consistent with the XRD results as seen in **table 5.1**.

The atomic positions obtained after the Rietveld refinement of the neutron diffraction data are reported in **table 5.2** (data measured at λ=1.667 Å).

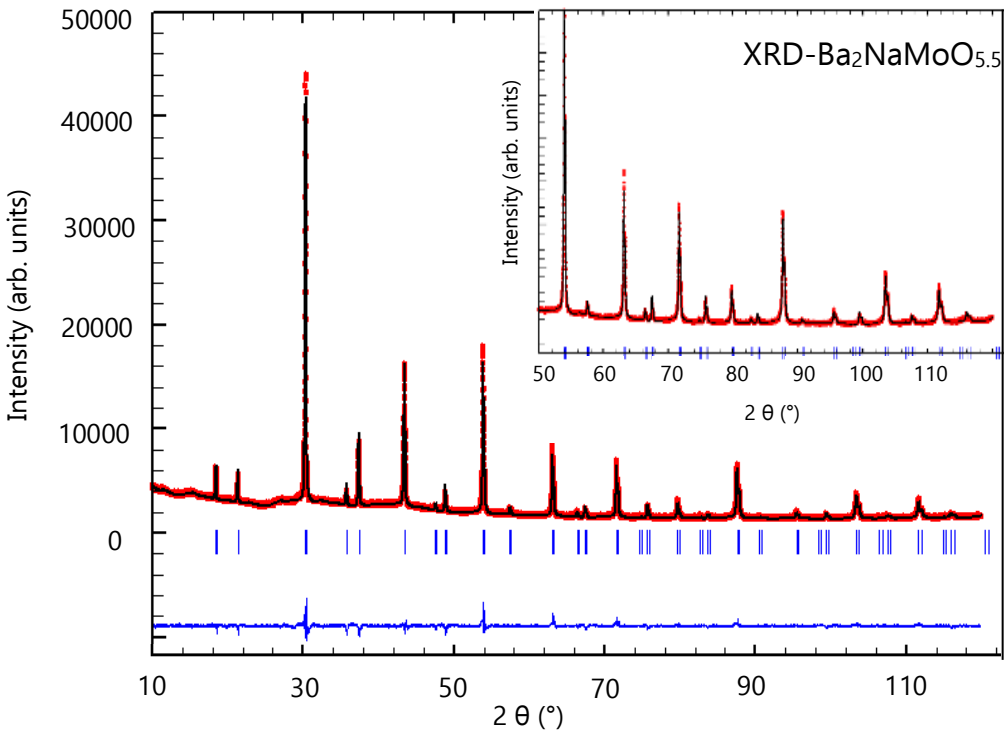

Figure 5.7: Comparison between the calculated (Y_{calc}, in black) and observed (Y_{obs}, in red) XRD patterns of $Ba_2NaMoO_{5.5}$. Y_{obs}-Y_{calc} in blue, is the difference between the experimental and calculated intensities. The angular positions of Bragg reflections are shown in blue. The measurement has been performed at λ=Cu-Kα

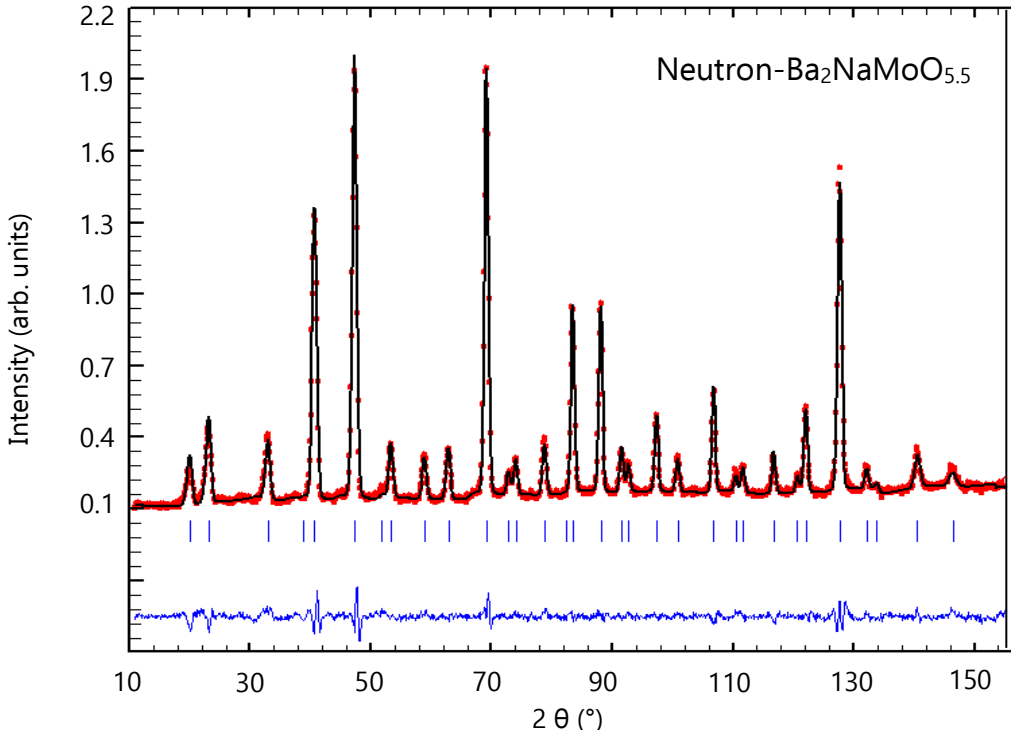

Figure 5.8: Comparison between the calculated (Y_{calc}, in black) and observed (Y_{obs}, in red) neutron diffraction patterns of $Ba_2NaMoO_{5.5}$. Y_{obs}-Y_{calc} in blue, is the difference between the experimental and calculated intensities. The angular positions of Bragg reflections are shown in blue. The measurement has been performed at λ=1.667 Å

Table 5.1: Profile parameters of $Ba_2NaMoO_{5.5}$ obtained with XRD and neutron diffraction methods

Chemical Formula	$Ba_2NaMoO_{5.5}$	
Source	XRD	Neutron
Formula weight ($g.mol^{-1}$)	481.6	
Temperature (K)	(293 ± 3)	
Wavelenght λ (Å)	1.541/1.544	1.667
Crystal system	Cubic	
Space group (No.)	$Fm\bar{3}m$ (225)	
a (Å)	8.3156(4)	8.305(1)
Cell volume V ($Å^3$)	575.01(8)	572.9(3)
Z	4	
d-space range (Å)	0.89-8.84	0.78-8.35
χ^2	6.59	3.85
R_p	18.4	10.1
R_{wp}	13.3	5.14

Definition of R factors hereafter: N is the number of observations, P the number of parameters, w_k the weights of the observations, y_{ck} is the calculated counts, y_{ok} is the observed counts at the k step:
$\chi^2 = \Sigma_k w_k (y_{ck} - y_{ok})^2 / (N-P)$
Profile factor Rp: $Rp^2 = \Sigma_k (y_{ck} - y_{ok})^2 / \Sigma_k (y_{ok})^2$
Weighted Profile Factor R_{wp} : $R_{wp}^2 = \Sigma_k w_k (y_{ck} - y_{ok})^2 / \Sigma_k (y_{ok})^2$

Table 5.2: Refined atomic positions, isotropic thermal displacement factor B_0 and occupancy factor in the $Ba_2NaMoO_{5.5}$ compound (noted Occ. in the table) derived from the neutron diffraction pattern refinement at λ=1.667 Å.
Background obtained by linear interpolation between operator-selected points in the pattern with refinable heights.

Atom	Oxidation State	Wyckoff	X	y	z	$B_0(Å^2)$	Occ.
Ba	+2	8c	0.25	0.25	0.25	1.34(3)	1
Na	+1	4a	0	0	0	0.80(8)	1
Mo	+6	4b	0.5	0.5	0.5	1.38(5)	1
O	-2	24e	0.2673(2)	0	0	1.98(2)	0.91(1)

As shown in **figure 5.9**, $Ba_2NaMoO_{5.5}$ shows a perovskite-type structure with infinite chains of alternating corner-sharing MoO_6 and NaO_6 regular octahedra along the *a*, *b* and *c* axes. These regular octahedra have distances of 2.220(2) Å for Na-O bonds and 1.933(2) Å for Mo-O bonds.

Moreover, the existence of oxygen vacancies is assessed for the first time by the refined occupancy factor on the site *24e* of the oxygen. The refined occupancy, i.e. 0.91(1), yields a chemical composition corresponding to 5.46(6) oxygen atoms per formula unit, which is consistent with the theoretical formula (5.5).

Barium atoms are located in the centre of a cube formed by the alternating NaO_6/MoO_6 octahedra as illustrated in **figure 5.9**, in coordination 12, with Ba-O distances of 2.940(1) Å and distances of 3.596(1) Å for both Ba-Mo and Ba-Na.

The thermal displacement factors B_0 for the sodium atom in both refinements of neutron diffraction patterns are lower than for the other atoms. This could be related to the ordering of this crystallographic site as observed for the cobalt site in the La_2CoMnO_6 perovskite compound by Kumar et Sathe [27].

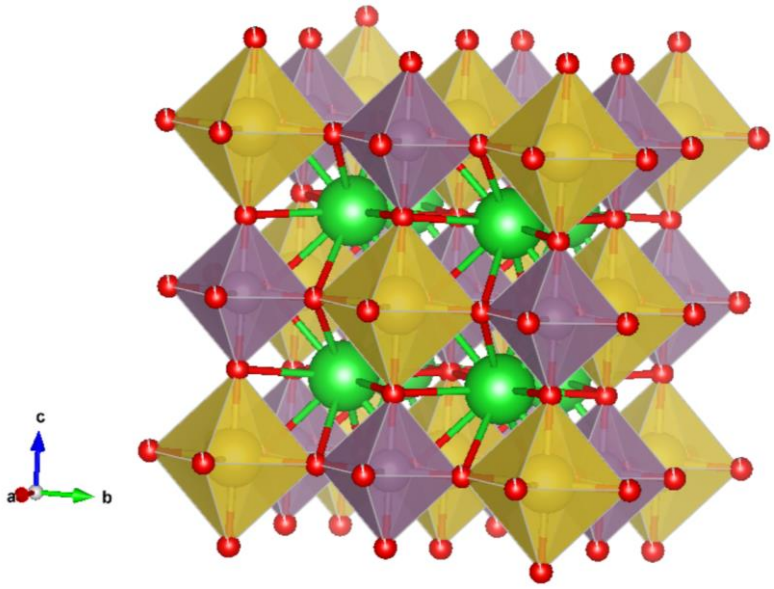

Figure 5.9: Sketch of the structure of $Ba_2NaMoO_{5.5}$. The octahedra around the atoms of molybdenum and sodium are represented in purple and yellow, respectively. Barium atoms are represented in green, and oxygen atoms in red.

5.2.2.2. *X-ray Absorption Spectroscopy*

$Ba_2NaMoO_{5.5}$ was characterised by X-ray Absorption Spectroscopy, to analyse the valence state of molybdenum (XANES analysis) and the local structure (coordination number and bond lengths) around Mo (EXAFS analysis) (Appendix A.2).

X-ray Absorption Near Edge Structure analysis (XANES)

The XANES spectrum of $Ba_2NaMoO_{5.5}$, collected at the Mo K-edge, is reported in **figure 5.10** together with that of Mo^0 metal, $Mo^{IV}O_2$ and $Mo^{VI}O_3$, used as reference materials to determine the oxidation state of the molybdenum.

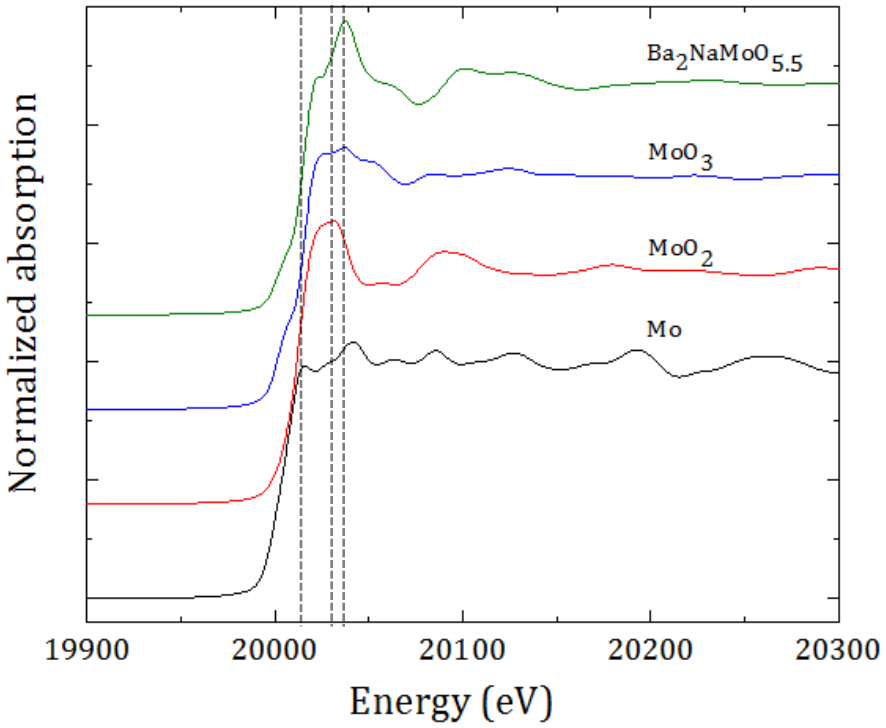

Figure 5.10: XANES spectra of the $Ba_2NaMoO_{5.5}$ compound obtained at the Mo K-edge and comparison with spectra of Mo^0, $Mo^{IV}O_2$ and $Mo^{VI}O_3$ used as reference compounds

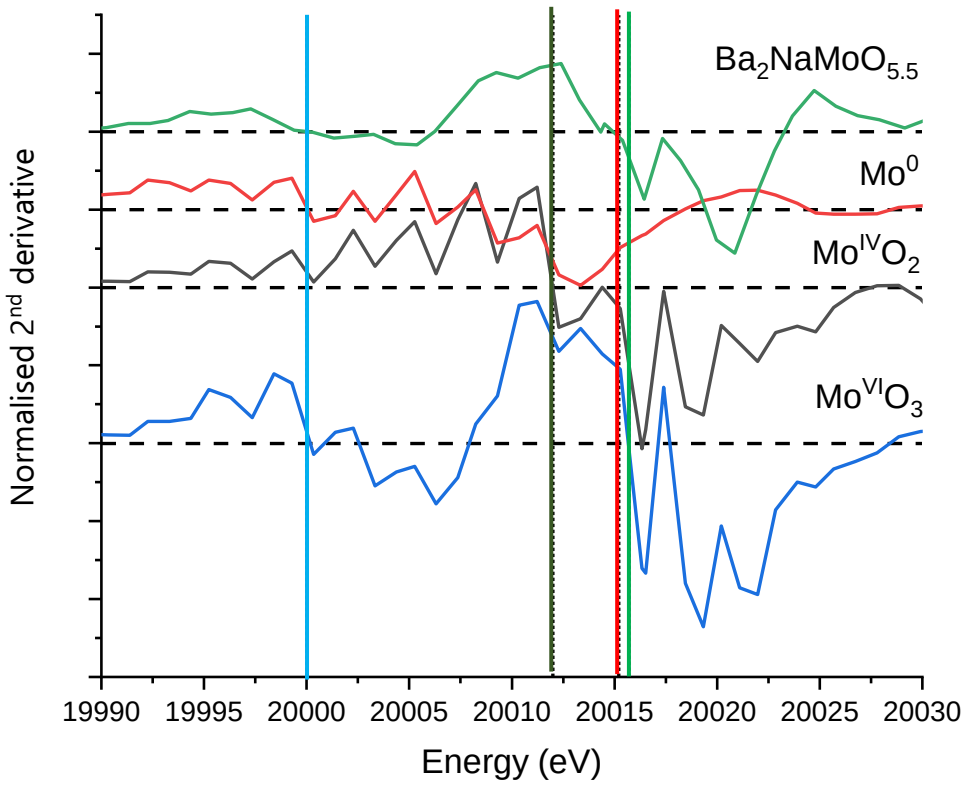

Figure 5.11: Normalised second derivative of the Mo K-edge absorption of $Ba_2NaMoO_{5.5}$ compound and comparison with the ones of Mo^0, $Mo^{IV}O_2$ and $Mo^{VI}O_3$ used as references. The horizontal dashed lines mark the zero value for each shifted spectra. The vertical one is the energy position of the inflexion point.

On **figure 5.10**, the white line of $Ba_2NaMoO_{5.5}$ and MoO_3 are well aligned. Moreover, the energy positions of the inflexion points E_0 of the different XANES spectra, listed in **table 5.3** were determined from the second derivative of the XANES spectra represented in **figure 5.11**. The E_0 value for $Ba_2NaMoO_{5.5}$ is close to that of MoO_3, confirming the oxidation state +VI of molybdenum in this compound. This result was expected given that the synthesis reaction consisted in the stoichiometric reaction between $BaMo^{VI}O_4$, $BaCO_3$ and Na_2CO_3 starting materials under oxygen flow. The $BaMo^{VI}O_4$ starting material was itself prepared from hexavalent $Mo^{VI}O_3$ and $BaCO_3$ materials. In **table 5.3**, a shift of E_0 to higher energies is observed with increasing oxidation state as expected at the Mo K-edge. When the oxidation state of the molybdenum increases, the energy of the inflexion point increases as observed by Cramer *et al.* [28].

Table 5.3: Energy positions of the inflexion points for the reference materials and $Ba_2NaMoO_{5.5}$

Compound	**$Ba_2NaMoO_{5.5}$**	**$Mo^{VI}O_3$**	**$Mo^{IV}O_2$**	**Mo^0**
E_0 (eV)[a]	20015.2	20015.7	20012.0	20000.0

[a] The standard uncertainties u on the energy position of the inflection points are $u(E_0) = 1$ eV.

EXAFS analysis

The Mo K-edge fitted and experimental EXAFS spectra and their Fourier transform are reported hereafter in **figure 5.12**. Using the starting model obtained after the Rietveld refinement of XRD and neutron data, the experimental data were fitted as described in **Appendix A.2**. The Fourier transform of the spectra presents two main peaks. One is at ~1.9 Å and the other one at ~3.6 Å. From the X-Ray and neutron diffraction measurements, they can be attributed to Mo-O and Mo-Ba bonds, respectively. The contribution of the six sodium atoms surrounding the molybdenum does not clearly appear on the Fourier transform and was found of low intensity from the calculations of the FEFF program in the Athena software. Therefore, the range of the fit called "Window" in **figure 5.12** was chosen to exclude the sodium atoms from fitting calculations. Finally, in the "Window" considered, the fit is in good agreement with the experimental data as shown by the low value of the "goodness of fit" parameter ($\frac{\sum_k (dataa_k - fit_k)^2}{\sum_k (data_k)^2}$ =0.017). Finally, the results are reported in **table 5.4** and compared to neutron diffraction data.

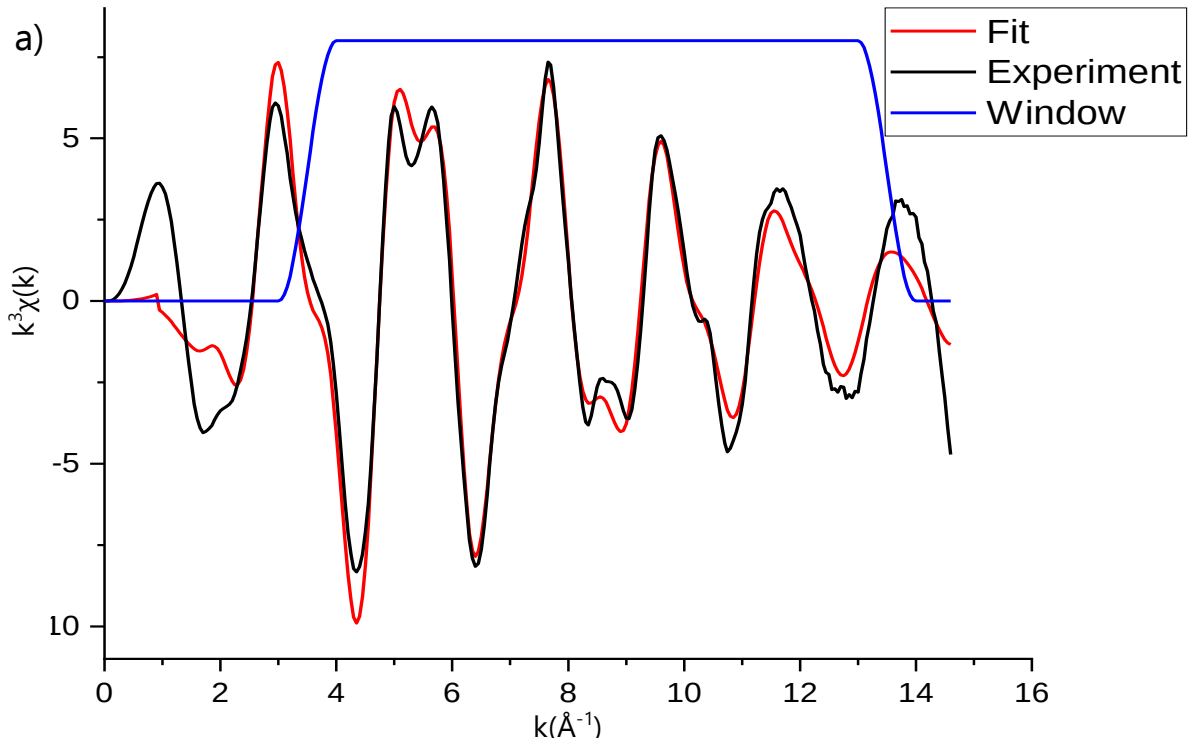

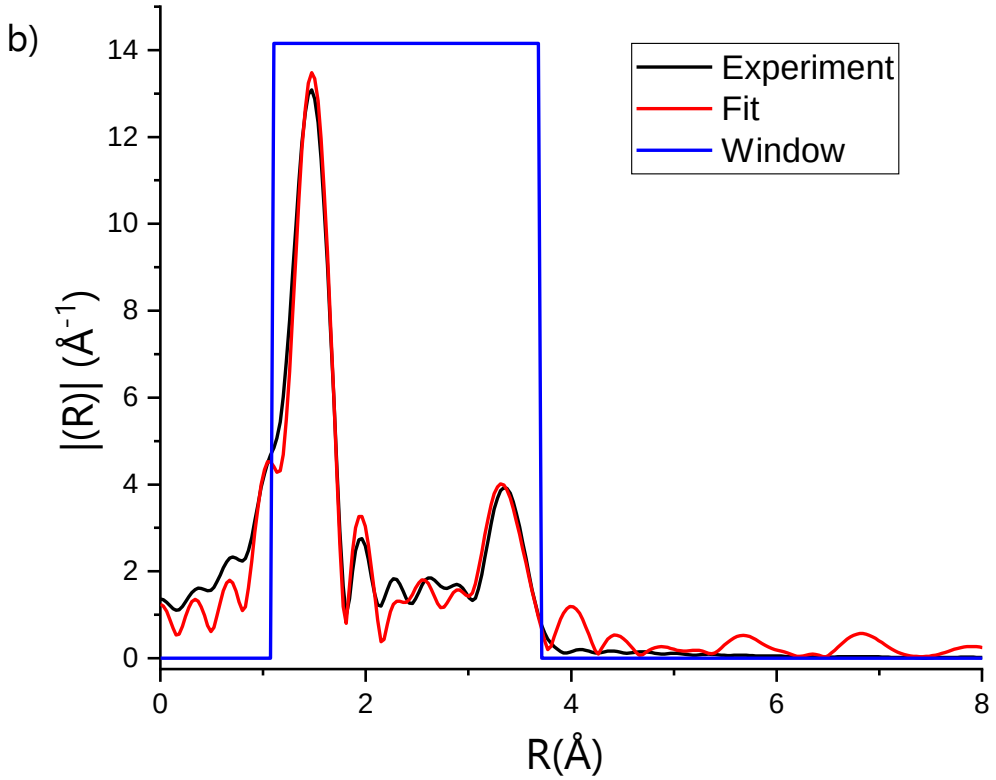

Figure 5.12: Fitted (red) and experimental (black) $k^3\chi(k)$ spectra (a) and Fourier transform (b) of $Ba_2NaMoO_{5.5}$ obtained at room temperature. (Fourier Transform boundaries 3.5-13.5 $Å^{-1}$, dk = 1 $Å^{-1}$).

The number of oxygen (5.6(2)) and barium (8) atoms in the first and second coordination shells around Mo determined by EXAFS are consistent with the theoretical formula and the neutron diffraction data (5.46(6) and 8, respectively).

The Mo-Ba distances obtained by EXAFS and neutron diffraction measurements, reported in **table 5.4**, are in good agreement within uncertainties.

For the oxygen atoms, the Mo-O bond lengths derived by EXAFS are slightly lower than the ones obtained by neutron diffraction for the first sphere, as mentioned in **table 5.5**. To have a good agreement between the experimental data and the fit, a multi-scattering path Mo-O-Mo-O[#] designed hereafter by "path*", had to be added, corresponding to the doubling of the Mo-O path (see **figure 5.13**), as suggested by its high amplitude in the EXAFS signal calculated by FEFF (35 % for Mo-O-Mo-O compared to 37% for Mo-Ba path). Nevertheless, to minimize the refined parameter during the fitting process, the coordination number of the multi scattering "path*" was fixed to the value taken for the first coordination shell, as both oxygen atoms involved are from this shell. For the single scattering path the Mo-O bond length was refined at 1.89(1) Å

[#] 4 legs multi-scattering "path*" details : Mo(c) -> O(1) (180°) → Mo(c) 0° → O(2) 180 °→ Mo(c))

whereas for the double path, the Mo-O bond length was finally optimised at 3.98(2) Å leading to a single bond length of 3.98(2)/2= 1.99(1) Å. Hence, the bond length finally optimised for path* (3.98 Å) was found longer than twice the value obtained for the single scattering Mo-O path.

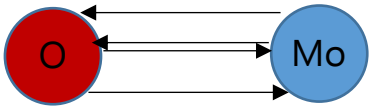

Figure 5.13: Scheme of the multi-scattering "path*".

This difference between single and multiple-scattering paths within the BO_6 unit of a ABO_3 perovskite has already been observed in $La_{2-x}Sr_xCu_{1-y}Ru_yO_{4-\delta}$ [29]. In such material, the BO_6 octahedra are known to rotate or tilt to adjust for different sizes of A cations [30] which induces a slight loss of linearity (0° angle) of the O(1)-Mo-O(2) section of the multi-scattering "path*". Such phenomenon would then induce an increase of the associated distance [31] compared to the strict sum of the two single-scattering Mo-O path. To check the validity of such hypothesis, the average Mo-O bond distances of single (1.89(1) Å) and multi-scattering "paths*" (1.99(1) Å) have to be compared to the 1.933(2) Å given by neutron diffraction measurements, representing the average Mo-O bond observed (as neutron diffraction can only yield an average value). Finally, the average Mo-O distance given by EXAFS is equal to 1.94(2) Å, similar to the neutron diffraction value. Hence, this is consistent with the hypothesis of octahedra tilting in the structure of $Ba_2NaMoO_{5.5}$.

Table 5.4: Bond lengths R_E (Å) of $Ba_2NaMoO_{5.5}$ obtained from EXAFS and neutron diffraction data (R_N). For the EXAFS fitting (ΔE_0=3.1, goodness of fit = $\frac{\sum_k (data a_k - fit_k)^2}{\sum_k (data_k)^2}$ =0.017). Standard deviations are given in parenthesis. σ^2 is the Debye-Waller factor, N is the number of atoms in each shell.

Bond	N	R_E (Å)	σ^2	R_N (Å)
Mo-O	5.6(2)	1.89 (1)	0.0047 (8)	1.933(2)
Mo-Ba	8	3.62 (2)	0.014 (2)	3.596(1)
Mo-O-Mo-O	5.6(2)	3.98 (2)	0.017 (2)	3.866(4)

5.2.2.3. High temperature Raman Spectroscopy

High Temperature Raman Spectroscopy measurements (Appendix A.6) have been performed on the $Ba_2NaMoO_{5.5}$ compound to study the local structure evolution as a function of temperature.

Five sets of bands associated with the internal modes of vibration of the MoO_6 units are observed in the $Ba_2NaMoO_{5.5}$ Raman spectrum at room temperature (**figure 5.14**).

This is consistent with the data reported for $MeMoO_4$ (Me = Ba, Ca, Pb, Sr) [32] [33] [34] and for $Cs_3Na(MoO_4)_2$ [35].

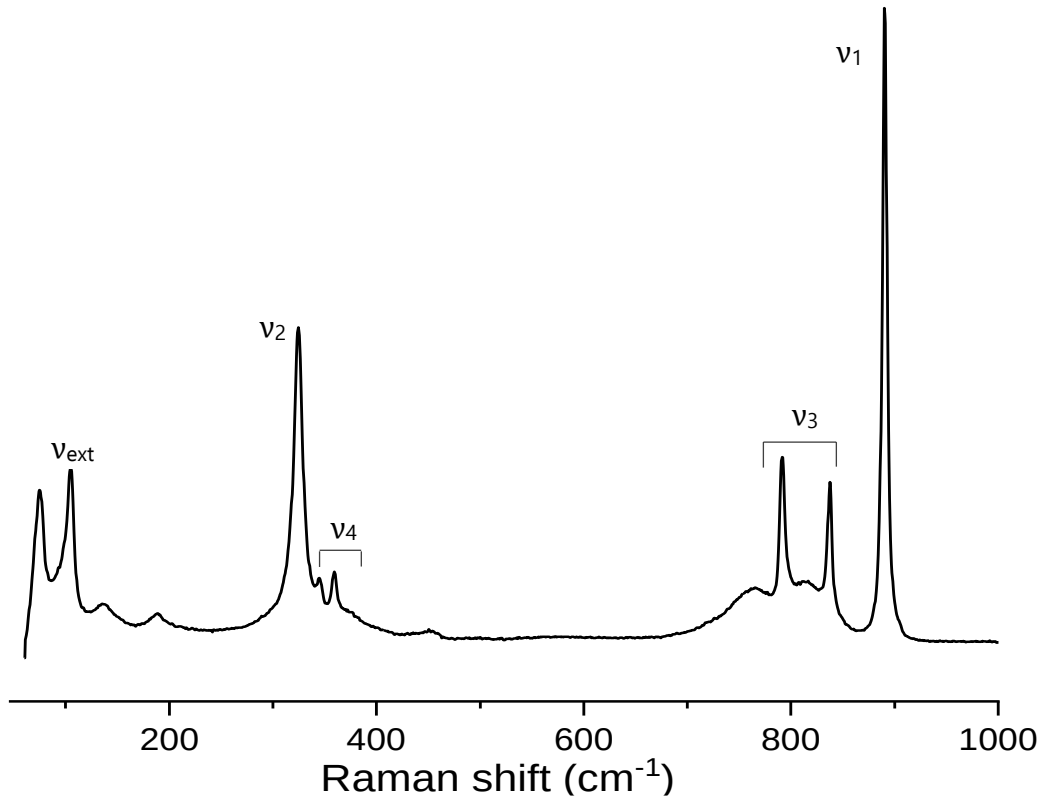

Figure 5.14: Raman spectrum of $Ba_2NaMoO_{5.5}$ at room temperature

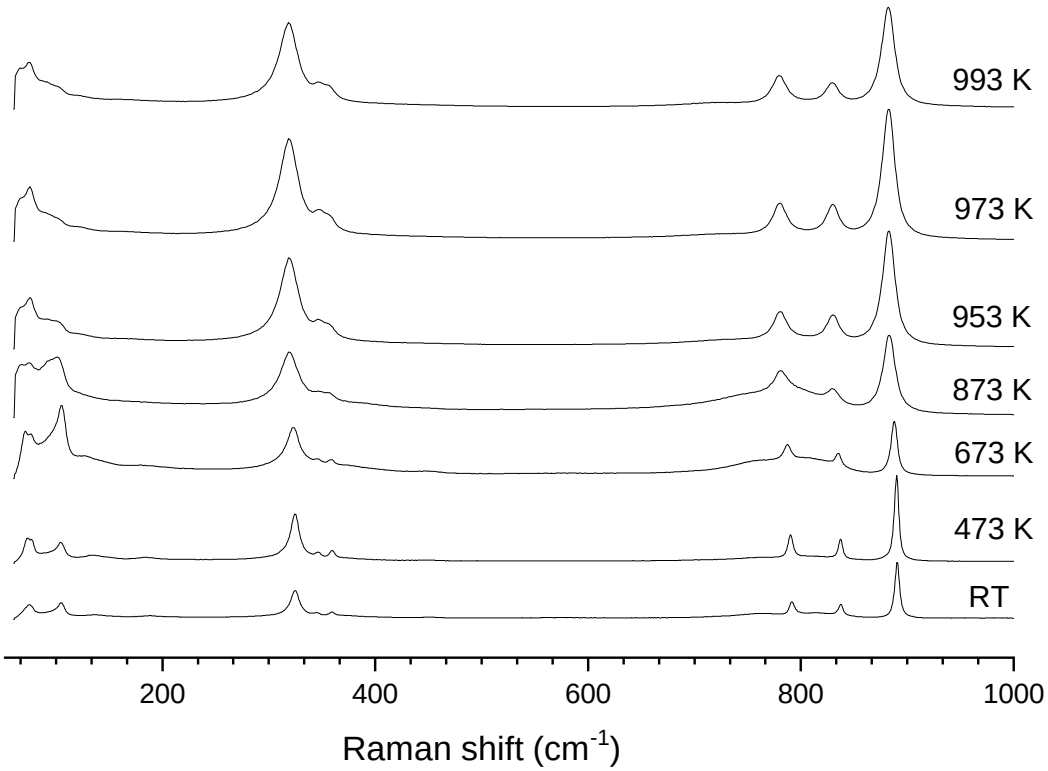

Figure 5.15: Variation of the Raman spectrum of $Ba_2NaMoO_{5.5}$ versus temperature

Liegeois-Duyckaerts and Tarte [32] studied $A_2B^{II}B^{VI}O_6$ (A=Ba, Pb, Sr; B=Ba, Sr, Ca, Cd, Zn, Cu, Co, Ni, Mg) ordered perovskites with Raman spectroscopy. In the different spectra obtained, they attributed the highest-frequency band with a strong intensity (ν_1 ~ 891 cm^{-1}) to the totally symmetric stretching of the MoO_6 octahedron in the internal modes approximation.

The vibrations between 780 and 850 cm^{-1} (ν_3) correspond to the antisymmetric stretching of the MoO_6 octahedron. In this range of frequencies, a wide feature is also observed related to the defects of the octahedron which partly break the symmetry [36]. This is consistent with the neutron diffraction and EXAFS results (oxygen vacancies and tilting of the angles of the Mo-O-Mo-O bond).

The peaks found between 300 and 380 cm^{-1} correspond to the symmetric (ν_2) and antisymmetric (ν_4) bending modes.

The external modes found at low frequencies (between 50 and 110 cm^{-1}) correspond to the translation of the Na^+ cation [32] [37] [35].

No noticeable change in the spectrum is observed between room temperature and 993 K as observed in **figure 5.15**, except a slight widening of the peaks and shift in the wavenumber due to anharmonic effects appearing with increasing temperature, as observed by Kokanyan *et al.* [38]. Moreover, the bands position shift with temperature follows a linear function as reported in **table 5.5** and **figure 5.16**. Therefore, no phase transition was observed with the Raman spectroscopy technique.

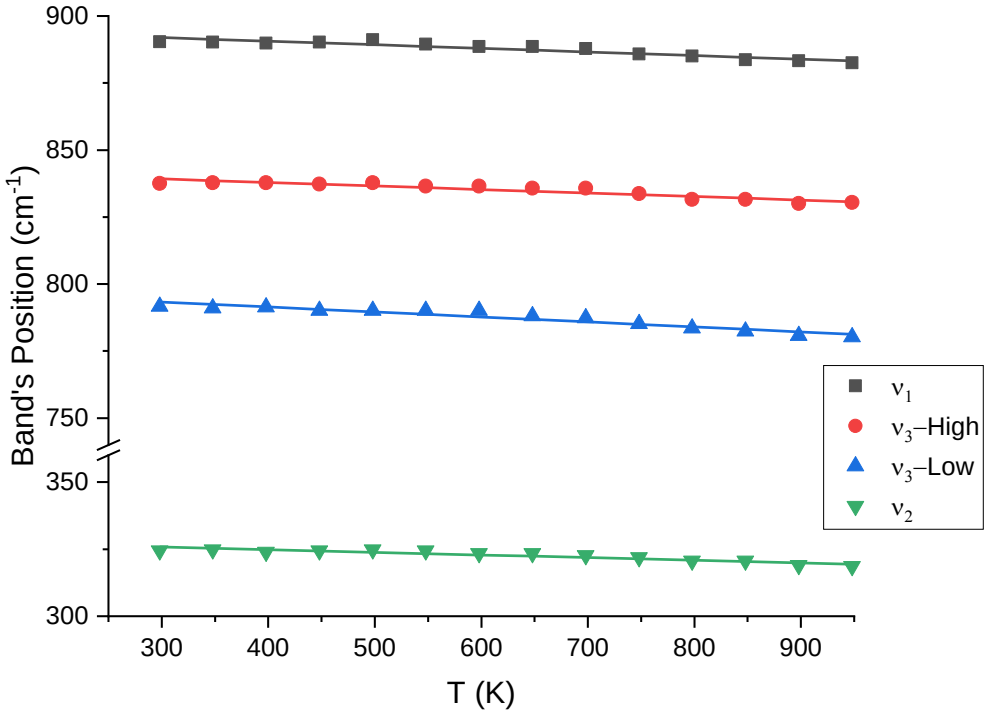

Figure 5.16: Evolution of the Raman band's position of $Ba_2NaMoO_{5.5}$ as a function of temperature

Table 5.5: Linear thermal expansion of the different band positions in the $Ba_2NaMoO_{5.5}$ compound

Frequency	ν_1	ν_3-High	ν_3-Low	ν_2
Linear thermal expansion ($K^{-1}.cm^{-1}$)	-0.0134	-0.0131	-0.0186	-0.01

5.2.3. Thermal expansion

The evolution of the cell parameters as a function of temperature was determined by Rietveld refinement of HT-XRD data.

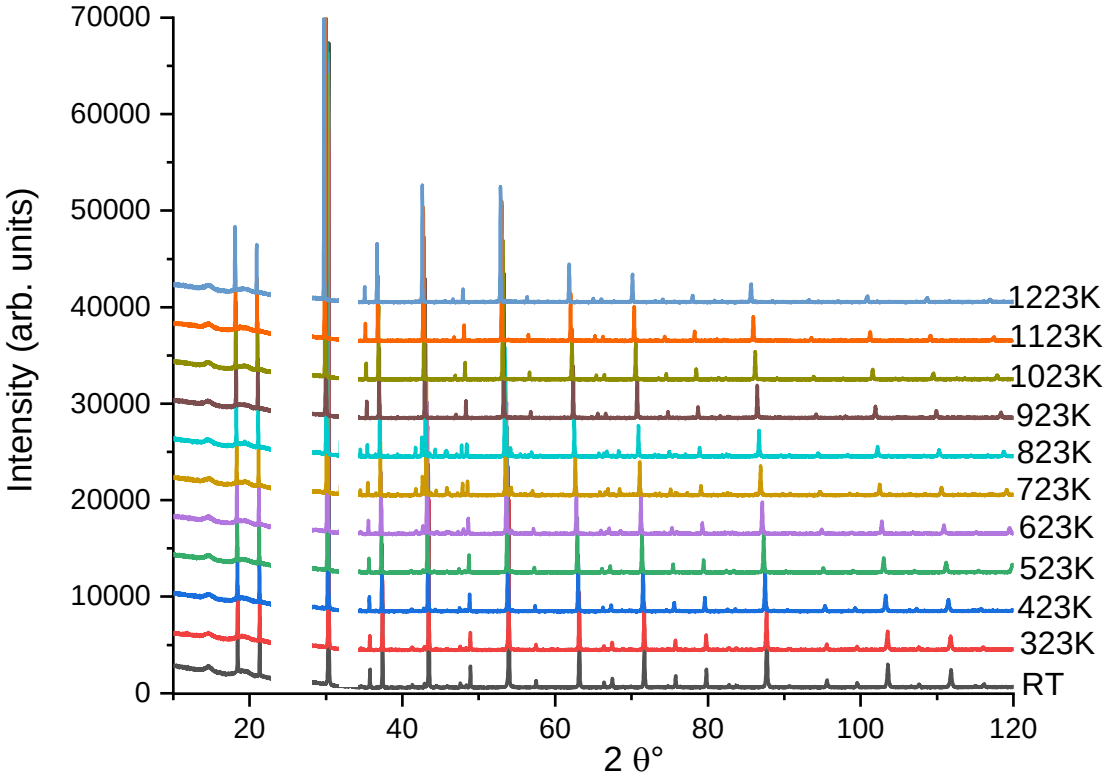

Figure 5.17: XRD patterns of the $Ba_2NaMoO_{5.5}$ compound measured from room temperature up to 1223K. Two sections were deleted, where no peaks were coming from the phase measured, but additional peaks were coming from the sample holder.

No major change was observed in the XRD patterns of $Ba_2NaMoO_{5.5}$ obtained up to the maximum temperature of the measurement T = 1223 K (**figure 5.17**). Only a shift to lower 2θ values was observed following the expansion of the unit cell as shown in **table 5.6**. These results are in good agreement with the high temperature Raman spectroscopy measurements (section 5.2.2), which also do not reveal any phase transition nor melting up to 993 K. Moreover, a DSC measurement performed in this work up to 1473 K also did not show any phase transition nor melting of the compound. Hence, the quaternary $Ba_2NaMoO_{5.5}$ compound is found stable up to at least 1473 K.

Table 5.6: Evolution of the cell parameters and unit cell volume of $Ba_2NaMoO_{5.5}$ with temperature

Temperature (K)	Lattice parameter (Å)	V (Å^3)
303	8.3183 (5)	575.6 (1)
323	8.3209 (2)	576.11 (4)
423	8.3354 (3)	579.14 (6)
523	8.3496 (3)	582.09 (6)
623	8.3644 (3)	585.19 (6)
723	8.3805 (5)	588.6 (1)
823	8.3965 (5)	592.0 (1)
923	8.4140 (4)	595.67 (8)
1023	8.4357 (5)	600.3 (1)
1123	8.4552 (5)	604.5 (1)
1223	8.4793 (6)	609.6 (2)

The relative thermal expansion of the unit lattice parameters, derived from the HT-XRD patterns, is reported in **figure 5.18** between room temperature and T = 1223 K. The mean relative linear thermal expansion coefficient $\frac{dl}{l_0}$, where $l = (abc)^{1/3}$ and $l_0 = (a_0 b_0 c_0)^{1/3}$ is the reference length at 303 K, can be expressed as a polynomial function of the temperature T (K):

$$\frac{dl}{l_0} = -3.69 \cdot 10^{-3} + 1.0047 \cdot 10^{-5}\, T + 6.74121 \cdot 10^{-9}\, T^2 \qquad (1)$$

The plots of relative thermal expansion data $\frac{l-l_0}{l_0} = f(T)$ for the compounds $Ba_2NaMoO_{5.5}$, $BaMoO_4$ [39] and $BaMoO_3$ [40] are shown hereafter in **figure 5.18**:

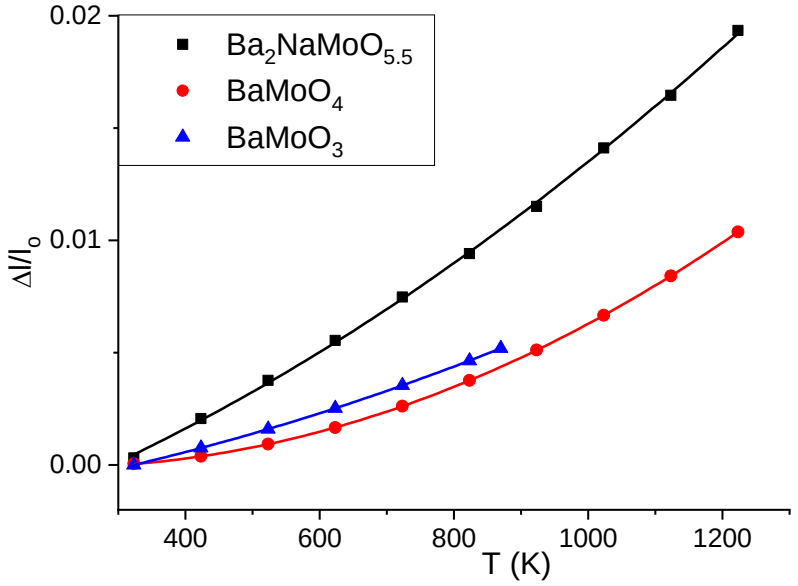

Figure 5.18: Relative thermal expansion of $Ba_2NaMoO_{5.5}$, compared to $BaMoO_4$ [39] and $BaMoO_3$ [40].

The mean relative thermal expansion of the quaternary compound is about two times higher than that of the two barium molybdates $BaMoO_3$ and $BaMoO_4$. The average volumetric thermal expansion of $BaMoO_4$ and $BaMoO_3$ are equal to α_V = 26.6 10^{-6} K^{-1} and 28.4 10^{-6} K^{-1} in the temperature ranges 298-1273 K, and 298-873 K, respectively [39],[40]. In comparison, the value for $Ba_2NaMoO_{5.5}$ is about twice higher: 55.8·10^{-6} K^{-1} in the temperature range 303-1223 K.

This high relative thermal expansion of the quaternary compound can be explained by the difference in the local structure properties coming from the sodium atoms insertion.

In $BaMoO_3$, the Mo atoms are octahedrally coordinated and form a 3-dimensional structure of corner-sharing MoO_6 octahedra. The barium atoms are found in between the chains in 12-fold cuboctahedral coordination. The continuous 3D lattice of strong Mo-O bonds ensures the structure's rigidity and constrains the expansion of the weaker Ba-O bonds.

The quaternary $Ba_2NaMoO_{5.5}$ compound shows the same 3-dimensional arrangement, except that half of the MoO_6 octahedra are replaced by NaO_6 octahedra. The Mo^{VI}-O bonds alternating with much weaker Na^{I}-O bonds result in a much stronger thermal expansion. The Ba-O bond length in $Ba_2NaMoO_{5.5}$ is also higher than in $BaMoO_3$ as observed by neutron diffraction (2.940(1) Å in this work vs 2.857 Å as reported by Nassif *et al.* [41]), which indicates weaker Ba-O bonds in the quaternary compound. This property, together with the less restraining octahedral network, explains a significantly higher swelling. An increased swelling of the irradiated fuel is therefore expected in case of the formation of this quaternary phase following the interaction with the sodium coolant.

5.2.4. Standard enthalpy of formation

The results obtained in section 5.2.1 demonstrate that $Ba_2NaMoO_{5.5}$ was obtained as a pure phase. Therefore, thermodynamic data are now possible to measure. In this section, the determination of the enthalpy of formation by solution calorimetry measurements is presented. In this method, all the compounds involved in the selected thermochemical cycle ($Na_2Mo_2O_7$, BaO and $Ba_2NaMoO_{5.5}$) have to be soluble in the same solvent (here nitric acid). Therefore, to perform these measurements, the $Na_2Mo_2O_7$ had to be synthesized and its purity assessed by XRD and DSC analysis as presented hereafter. Then the solution calorimetric measurements will be detailed.

5.2.4.1. *$Na_2Mo_2O_7$ synthesis*

$Na_2Mo_2O_7$ was synthesized by heating a stoichiometric mixture of powders of anhydrous Na_2MoO_4 (Sigma-Aldrich, 99.5%) and MoO_3 (Alfa Aesar, >99.5%) under dry oxygen for 60 hours at 773 K with intermediate regrinding. The purity of the sample was checked by XRD and DSC (see **Appendix A.4**) measurements (see **figure 5.19** and **5.20**).

On the refined XRD pattern, no secondary phases were found.

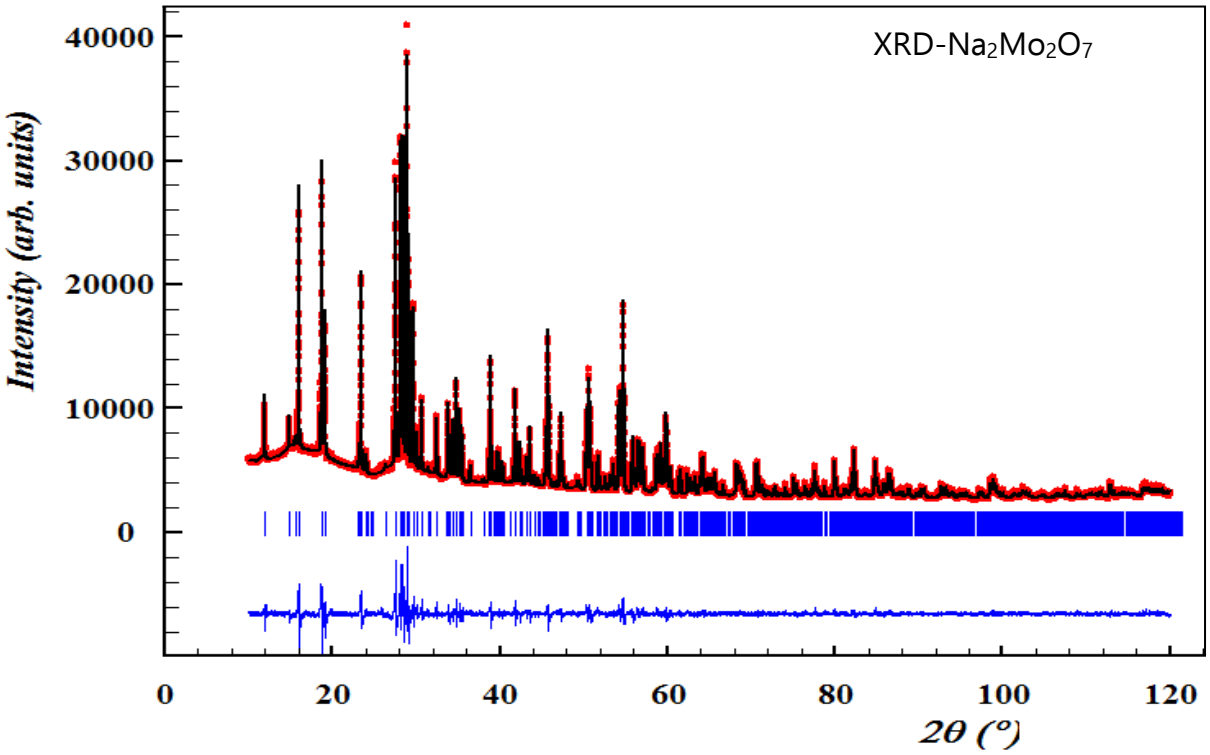

Figure 5.19: Comparison between the calculated (Y_{calc}, in black) and observed (Y_{obs}, in red) XRD patterns of $Na_2Mo_2O_7$. Y_{obs}-Y_{calc} in blue, is the difference between the experimental and calculated intensities. The angular positions of Bragg reflections are shown in blue. The measurement has been performed at λ=Cu-Kα

On the DSC curve, reported in **figure 5.20**, two events are observed at (830 ± 5) K and (872 ± 5) K, corresponding to the allotropic phase transition and the melting of $Na_2Mo_2O_7$, respectively, which are in very good agreement with the values reported in the literature by Mudher *et al.* [17], i.e. (830 ± 5) K and (873 ± 5) K. It is worth noting that the allotropic phase transition of $Na_2Mo_2O_7$ has only been reported in the study of Mudher *et al.* [17]. Moreover, as the structure of the compound is unknown and only the temperature of the phase transition was reported, the allotropic phase transition was not taking into account in the thermodynamic modelling assessment of Bordier [11]. Therefore, from the DSC analysis of the $Na_2Mo_2O_7$ sample, the existence of the

allotropic phase transition in $Na_2Mo_2O_7$ is confirmed and in good agreement with the value reported by Mudher *et al.* [17].

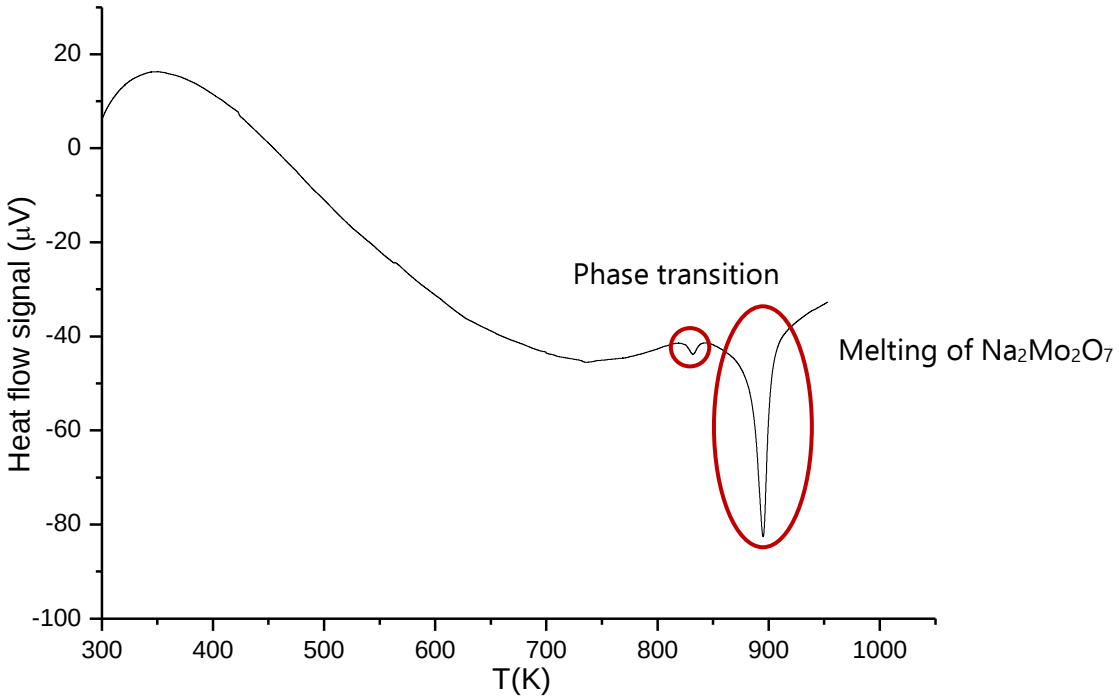

Figure 5.20: DSC curve of a sample of $Na_2Mo_2O_7$ (80.7 mg) in an alumina liner heated from 300 K up to 953K at 5K/min.

Thanks to these two characterisations, the $Na_2Mo_2O_7$ compound is pure and can be used for solution calorimetry measurements.

5.2.4.2. Solution calorimetry measurement

Solution calorimetry is an analysis technique measuring the temperature change (ΔT) produced by an interaction during mixing of two solutions or a solid and a liquid. As detailed in **Appendix A.5**, the standard enthalpy of formation of a compound can be determined.

The enthalpy of formation of $Ba_2NaMoO_{5.5}$ at 298.15K was obtained in 2 mol/L HNO_3 solution (VWR Chemicals, 99.5%) using the thermodynamic cycle detailed in **table 5.7**.

Table 5.7: Thermodynamic cycle used for the calorimetric measurement

Cycle	Reaction
(1)	$Ba_2NaMoO_{5.5}$(s) + *x* HNO_3 = sol. 1
(2a)	2 BaO(s) + *x* HNO_3 = sol. 2
(2b)	1/2 $Na_2Mo_2O_7$(s) + sol. 2 = sol. 3
(3)=(2a)+(2b)-(1)	2 BaO(s) + 1/2 $Na_2Mo_2O_7$(s) = $Ba_2NaMoO_{5.5}$(s)

In the cycle, the final compositions of solution 1 and solution 3 in **table 5.7** have to be identical. Therefore, precisely weighted amounts of samples, reported in **table 5.8**, were dissolved forming solution 1, 2 and 3. The dissolutions of $Ba_2NaMoO_{5.5}$ (reaction 1), BaO (reaction 2a) and $Na_2Mo_2O_7$ (reaction 2b) in nitric acid (2 M HNO_3 solution (VWR chemicals, 99.5%)) were in all cases instantaneous and complete. The weight, temperature change, specific heat capacity, energy and enthalpy of reactions of dissolution are reported in **table 5.8**. The measurements were performed five times to determine the uncertainty on the resulting values obtained. The results show a good agreement and a good reproducibility.

Table 5.8: Calorimetric results for the dissolution of $Ba_2NaMoO_{5.5}$ (M = 481.6 g.mol^{-1}), BaO (M = 153.3 g.mol^{-1}) and $Na_2Mo_2O_7$ (M = 349.9 g.mol^{-1}) in 2[a] M HNO_3 at 298.15 K. Solution calorimetry measurements were performed at a pressure p = (0.105 ± 0.005[b]) MPa, and in the temperature interval T = (298.15 ± 0.30[b]) K.

No.	m($Ba_2NaMoO_{5.5}$)[c]/mg	ΔT[d]/mK	Cp[e]/J·K^{-1}	Q[f]/J	$\Delta_rH°_m$ (298.15K)[g]/kJ·mol^{-1}
1	44.0	61.445	411.728	-25.298	-276.90
2	44.0	61.306	411.102	-25.203	-275.86
3	44.0	61.477	411.592	-25.303	-276.96
4	44.0	61.639	410.585	-25.308	-277.01
5	43.9	60.740	411.520	-24.996	-274.22
No.	**m(BaO)[c]/mg**	**ΔT[d]/mK**	**Cp[e]/J·K^{-1}**	**Q[f]/J**	**$\Delta_rH°_m$ (298.15K)[g]/kJ·mol^{-1}**
1	28.0	411.156	126.268	-51.916	-284.29
2	28.0	411.353	126.234	-51.927	-284.35
3	28.0	411.654	125.998	-51.868	-284.03
4	28.0	411.365	126.066	-51.859	-283.98
5	28.0	411.152	126.273	-51.917	-284.30
No.	**m($Na_2Mo_2O_7$)[c]/mg**	**ΔT[d]/mK**	**Cp[e]/J·K^{-1}**	**Q[f]/J**	**$\Delta_rH°_m$ (298.15K)[g]/kJ·mol^{-1}**
1	16.0	409.511	3.257	-1.334	-29.17
2	15.9	411.617	3.157	-1.299	-28.40
3	16.0	411.108	3.226	-1.326	-28.99
4	16.0	409.800	3.263	-1.337	-29.24
5	15.9	410.749	3.189	-1.31	-28.82

m is the sample mass, ΔT the temperature change caused by the dissolution, Cp the energy equivalent of the calorimeter, Q the amount of heat generated by the dissolution, ΔrH°m (298.15 K) the corresponding molar enthalpy of reaction.

[a] The standard uncertainties u on the molar concentrations are u(C) = 0.002 M.

[b] The quoted uncertainty corresponds to the standard uncertainty.

[c] The standard uncertainties u on the weights are u(m) = 0.1 mg.

d The relative standard uncertainties on ΔT are $u_r(\Delta T) = 0.2$

e The relative standard uncertainties on Cp are $u_r(Cp) = 0.2$.

[f] The relative standard uncertainties on Q are $u_r(Q) = 0.3$.

[g] The relative standard uncertainties on $\Delta_rH°_m$ (298.15K) are $u_r(\Delta_rH°_m(298.15K)) = 0.4$.

From these measurements, the enthalpy of formation from the constituting oxides BaO and $Na_2Mo_2O_7$ corresponding to the reaction (3) in **table 5.7**
(½ $Na_2Mo_2O_{7(cr)}$ + 2 $BaO_{(cr)}$ = $Ba_2NaMoO_{5.5\,(cr)}$) is equal to:

$\Delta_rH°_m = \Delta_rH°_{2a} + \Delta_rH°_{2b} - \Delta_rH°_1 = -(306.24 \pm 0.65)$ kJ.mol^{-1},

Finally, to derive the standard enthalpy of formation, the standard enthalpy of formation reaction of BaO [42] and $Na_2Mo_2O_7$ [43] from the constituting standard references $Ba_{(s)}$, $Na_{(s)}$, $Mo_{(s)}$ and $O_{2(g)}$ have to be added to the cycle as reported in **table 5.9**.

The enthalpy of dissolution of $BaO_{(s)}$ in a 1 M HCl solution has been measured in the work of Fitzgibbon *et al.* [42]. The authors measured $\Delta_rH°_m$ (298.15K) = -(273.17 ± 0.96) kJ.mol^{-1}, which is consistent with the present data measured in a solution of 2 M HNO_3, i.e. –(284.19 ± 0.17) kJ.mol^{-1}.
No measurements of the dissolution of $Na_2Mo_2O_7$ in acidic solution are reported in the literature to compare with the value obtained in this work. Nevertheless, Tangri *et al.* [43] measured the enthalpy of dissolution in 0.024 mol.L^{-1} NaOH solution.

Combining with the standard enthalpy of formation of standard element, the authors determined the standard enthalpy of formation of $BaO_{(s)}$ [42], and $Na_2Mo_2O_{7(s)}$ [43]. Using these results, the standard enthalpy of formation of $Ba_2NaMoO_{5.5}$ at 298.15 K from the pure elements is finally derived as **$\Delta_fH°_m$ = -(2524.75 ± 4.15) kJ·mol^{-1}** as reported in **table 5.9**

Table 5.9: Thermochemical cycle used for the determination of the enthalpy of formation of $Ba_2NaMoO_{5.5}$. Solution calorimetry measurements were performed at a pressure p = (0.105 ± 0.005) MPa, and in the temperature interval T = (298.15 ± 0.30[a]) K.

Cycle	Reaction	$\Delta_rH°_m$ (298.15K)/ kJ·mol^{-1}	Uncertainty[a]	Ref
(1)	$Ba_2NaMoO_{5.5}$(s) + *x* HNO_3 = sol. 1	-276.68	0.55	This work
(2a)	2 BaO(s) + *x* HNO_3 = sol. 2	-568.38	0.34	This work
(2b)	1/2 $Na_2Mo_2O_7$(s) + sol. 2 = sol. 3	-14.55	0.09	This work
(3)	Ba(s) + 1/2 O_2(g) = BaO(s)	-548.00	2.00	[42]
(4)	2 Na(s)+2 Mo(s)+7/2 O_2(g) = $Na_2Mo_2O_7$(s)	-2245.02	1.81	[43]
(5)	**2Ba(s)+Na(s)+Mo(s) +11/4 O_2(g)=$Ba_2NaMoO_{5.5}$(s)**	**-2524.75**	**4.15**	This work

[a] The quoted uncertainty corresponds to the standard uncertainty

5.3. Conclusion

In this chapter, a review of the literature data and the experimental investigation of the BaO-MoO_3-Na_2O system are presented. The BaO-MoO_3 and MoO_3-Na_2O pseudo-binary systems are relatively well known and CALPHAD models are available. Nevertheless, small modifications of the Mo-O model for these systems had to be done and are described in Chapter 7. For the modelling of the pseudo-ternary system, the existing models will be used after the modification.

The experimental study of the system Ba-Mo-Na-O was dedicated to the characterisation of the quaternary compound $Ba_2NaMoO_{5.5}$ for which no thermodynamic data was reported in the literature to this date.

An extensive study of the crystal structure of the $Ba_2NaMoO_{5.5}$ quaternary perovskite phase is reported by combining XRD, neutron diffraction, Raman spectroscopy and EXAFS methods. The +VI molybdenum oxidation state has been confirmed from XANES spectroscopy measurements at the Mo K-edge. Using neutron diffraction, for the first time, the position and occupancy of the oxygen atoms were assessed, confirming the presence of oxygen vacancies.

HT-XRD measurements performed in the temperature range 303-1223 K have allowed to derive the volumetric thermal expansion coefficient $\alpha_{vol} = 55.8 \cdot 10^{-6}\ K^{-1}$, which is about twice higher than the ones of ternary barium molybdate compounds $BaMoO_3$ and $BaMoO_4$ formed as secondary oxide phases in the irradiated fuel. The high thermal expansion of $Ba_2NaMoO_{5.5}$ compared to the one of $BaMoO_3$ was explained by the difference in the local structural arrangement. Moreover, this quaternary perovskite phase was found stable up to at least 1473 K. Therefore, in case of an interaction between the irradiated MOX fuel and the sodium, the formation of this quaternary compound is possible, which could lead to a higher swelling compared to $BaMoO_3$ and $BaMoO_4$ phases.
Numerous analysis techniques were applied to the $Ba_2NaMoO_{5.5}$ compound, leading to an extensive characterisation of the compound's structure with agreement between all results coming from the different techniques. These investigations have been reported in the publication "*Structural and Thermodynamic Investigation of the Perovskite $Ba_2NaMoO_{5.5}$*" [44].

Finally, for the first time, the standard enthalpy of formation of $Ba_2NaMoO_{5.5}$ has been measured by solution calorimetry. This thermodynamic data is key for the Calphad modelling of the BaO-MoO_3-Na_2O system.

REFERENCES

[1] L.S. Cavalcante, J.C. Sczancoski, R.L. Tranquilin, M.R. Joya, P.S. Pizani, J.A. Varela, E. Longo, $BaMoO_4$ powders processed in domestic microwave-hydrothermal: Synthesis, characterization and photoluminescence at room temperature, J. Phys. Chem. Solids. 69 (2008) 2674–2680.

[2] S.P. Veksler, V.M. Zhukovskij, Synthesis of barium molybdates of Ba_2MoO_5 and Ba_3MoO_6 type, Zhurnal Neorganicheskoj Khimii. 19 (1974) 3224.

[3] P. Gao, Y. Xie, L. Ye, Y. Chen, Z. Li, Synthesis of Single-crystal $BaMo_2O_7$ Nanowire Bundles: A General, Low-temperature Hydrothermal Approach to 1D Molybdenum Oxide-based Nanostructures, Chem. Lett. 35 (2005) 162–163. https://doi.org/10.1246/cl.2006.162.

[4] P.E. Werner, M. Moustiakimov, B.O. Marinder, K.S. Knight, Crystal structure of $BaMo_3O_{10}$ solved from powder diffraction data in: Zeitschrift für Kristallographie - Crystalline Materials Volume 212 Issue 9 (1997), Z. Für Krist. 212 (1997) 665–670.

[5] A.L. Smith, Assessment of the ternary Ba-Mo-O system, internal report, TAF-ID, https://www.oecd-nea.org/science/taf-id/, (2017).

[6] T.M. Yanushkevich, V.M. Zhukovskij, Phase diagram of the $BaMoO_4$-BaO system, Izv. Akad. Nauk SSSR Neorganicheskie Mater. 8 (1972) 2039–2040.

[7] S. Dash, Z. Singh, R. Prasad, V. Venugopal, Computer calculation of the 700 K isothermal section of the Ba-Mo-O system from thermodynamic data, 1999.

[8] V.M. Zhukovskii, A.N. Petrov, 1969 Russ. J. Phys. Chem. 43 1715- 1717.

[9] V.M. Zhukovskii, E.V. Tkachenko, T.A. Rakova, PHASE DIAGRAMS OF THE SYSTEMS MoO_3-$MeMoO_4$ (Me = Mg, Ca, Sr, Ba)., Zh Neorg Khim 15 3326-8Dec 1970. (1970).

[10] E.H.P Cordfunke, R.J.M Konings, Thermochemical data for reactor materials and fission products, Elsevier Science Publishers B.V., 1990.

[11] S. Bordier, Modélisation thermodynamique des phases insolubles dans les verres nucléaires. Application à la vitrification du molybdène et des produits de fission platinoïdes.

[12] NEA Nuclear Science Committee, Thermodynamics of Advanced Fuels - International Database (TAF-ID), https://www.oecd-nea.org/science/tafid/.

[13] E. Groschuff, Über Wasserfreie Molybdate I, Z. Für Anorg. Chem. 58 (1908) 113–119.

[14] F. Hoermann, Beitrag zur Kenntnis der Molybdate und Wolframate. Die binären Systeme: Li_3MoO_4-MoO_3, Na_2MoO_4-MoO_3, K_3MoO_4-MoO_3, Li_2WO_4-WO_3, Na_2WO_4-WO_3, K_2WO_4-WO_3, Li_2MoO_4-Na_2MoO_4, Li_2WO_4-Na_2WO_4, Li_2MoO_4-K_2MoO_4, Z. Für Anorg. Allg. Chem. 177 (1929) 145–186.

[15] P. Caillet, Polymolybdates et polytungstates de sodium ou de potassium anhydres, Bull. Sociétée Chim. Fr. (1967).

[16] V.A. Balashov, A.A. Majer, Synthesis and some properties of sodium- and- scandium-double molybdate, Neorganicheskie Mater. 6 (1970) 1450–1453.

[17] K.D. Singh Mudher, M. Keskar, K. Krishnan, V. Venugopal, Thermal and X-ray diffraction studies on Na_2MoO_4, $Na_2Mo_2O_7$ and $Na_2Mo_4O_{13}$, J. Alloys Compd. 396 (2005) 275–279.

[18] R. Sridharan, D. Krishnamurthy, C.K. Mathews, Thermodynamic properties of ternary oxides of alkali metals from oxygen potential measurements, J. Nucl. Mater. 167 (1989)

[19] T. Gnanasekaran, K.H. Mahendran, G. Periaswami, C.K. Mathews, H.U. Borgstedt, Stability of ternary oxygen compounds of molybdenum in liquid sodium, J. Nucl. Mater. 150 (1987)

[20] E.A. Giess, B.A. Scott, B.L. Olson, G. Burns, D.F. O'kane, Tungsten Bronze Field and Melt Growth of Crystals in the Na_2O-BaO-Nb_2O_5 System, J. Am. Ceram. Soc. 53 (1970) 14–17.
[21] R.P. Gunawardane, F.P. Glasser, Phase Equilibria and Crystallization of Melts in the System Na_2O-BaO-SiO_2, J. Am. Ceram. Soc. 57 (1974) 201–204.
[22] E.G. Danilushkina, I.K. Garkushin, D.S. Ryzhkova, Investigation of the Ternary Reciprocal System Na,Ba||Br,MoO_4, Russ. J. Inorg. Chem. 64 (2019) 1047–1053.
[23] B.D. Babaev, A.M. Gasanaliev, Quaternary system Li_2MoO_4-Na_2MoO_4-$CaMoO_4$-$BaMoO_4$, Inorg. Mater. 36 (2000) 954–958.
[24] K. Garkushin, A.S. Trunin, T.T. Miftakhov, Study of the Ternary System Na_2MoO_4-$BaMoO_4$-MoO_3, (1995) 4.
[25] R. Sabatier, M. Wathlé, J.P. Besse, G. Baud, Perovskites oxyfluorées et oxygénées, J. Inorg. Nucl. Chem. 33 (1971) 1597–1613.
[26] V. Thangadurai, A.K. Shukla, J. Gopalakrishnan, Oxide-ion conduction in anion-deficient double perovskites, $Ba_2BB'O_{5.5}$ (B=Li, Na; B'=Mo, W, Te), Solid State Ion. 104 (1997) 277–283.
[27] D. Kumar, V.G. Sathe, Raman spectroscopic study of structural transformation in ordered double perovskites La_2CoMnO_6 bulk and epitaxial film, Solid State Commun. 224 (2015) 10–14.
[28] S.P. Cramer, T.K. Eccles, F.W. Kutzler, K.O. Hodgson, L.E. Mortenson, Molybdenum x-ray absorption edge spectra. The chemical state of molybdenum in nitrogenase, J. Am. Chem. Soc. 98 (1976) 1287–1288.
[29] S. Ebbinghaus, M. Fröba, A. Reller, The "Realstruktur" of the System $La_{2-x}Sr_xCu_{1-y}Ru_yO_{4-\delta}$ Studied by Rietveld and Extended X-ray Absorption Fine Structure Spectroscopy †, J. Phys. Chem. B. 101 (1997) 9909–9915.
[30] S.G. Ebbinghaus, A. Weidenkaff, R.J. Cava, Structural Investigations of $ACu_3Ru_4O_{12}$ (A=Na, Ca, Sr, La, Nd)—A Comparison between XRD-Rietveld and EXAFS Results, J. Solid State Chem. 167 (2002) 126–136.
[31] P.M. Martin, R.C. Belin, P.J. Valenza, A.C. Scheinost, EXAFS study of the structural phase transition in the americium zirconate pyrochlore, J. Nucl. Mater. 385 (2009) 126–130.
[32] M. Liegeois-Duyckaerts, P. Tarte, Vibrational studies of molybdates, tungstates and related compounds—II: New Raman data and assignments for the scheelite-type compounds, Spectrochim. Acta Part Mol. Spectrosc. 28 (1972) 2037–2051.
[33] T.T. Basiev, A.A. Sobol, Yu.K. Voronko, P.G. Zverev, Spontaneous Raman spectroscopy of tungstate and molybdate crystals for Raman lasers, Opt. Mater. 15 (2000) 205–216.
[34] G. Wallez, P.E. Raison, A.L. Smith, N. Clavier, N. Dacheux, High-temperature behavior of dicesium molybdate Cs_2MoO_4: Implications for fast neutron reactors, J. Solid State Chem. 215 (2014) 225–230.
[35] A.L. Smith, G. Kauric, L. van Eijck, K. Goubitz, N. Clavier, G. Wallez, R.J.M. Konings, Structural and thermodynamic study of $Cs_3Na(MoO_4)_2$: Margin to the safe operation of sodium cooled fast reactors, J. Solid State Chem. 269 (2019) 1–8.
[36] B.E. Scheetz, W.B. White, Characterization of Anion Disorder in Zirconate $A_2B_2O_7$ Compounds by Raman Spectroscopy, J. Am. Ceram. Soc. 62 (1979) 468–470.
[37] G.D. Saraiva, W. Paraguassu, M. Maczka, P.T.C. Freire, F.F. de Sousa, J. Mendes Filho, Temperature-dependent Raman scattering studies on $Na_2Mo_2O_7$ disodium dimolybdate, J. Raman Spectrosc. 42 (2011) 1114–1119.

[38] N. Kokanyan, D. Chapron, M.D. Fontana, Temperature dependence of Raman scattering and anharmonic properties in $LiNbO_3$, Appl. Phys. A. 117 (2014) 1147–1152.
[39] M. Sahu, K. Krishnan, B.K. Nagar, D. Jain, M.K. Saxena, C.G.S. Pillai, S. Dash, Characterization and thermo physical property investigations on $Ba_{1-x}Sr_xMoO_4$ (x=0, 0.18, 0.38, 0.60, 0.81, 1) solid-solutions, J. Nucl. Mater. 427 (2012) 323–332.
[40] M. Sahu, K. Krishnan, M.K. Saxena, S. Dash, Thermophysical properties of $Ba_{1-x}Sr_xMoO_{3\ (s)}$, J. Nucl. Mater. 457 (2015) 29–35.
[41] V. Nassif, R.E. Carbonio, J.A. Alonso, Neutron Diffraction Study of the Crystal Structure of $BaMoO_4$: A Suitable Precursor for Metallic $BaMoO_3$ Perovskite, J. Solid State Chem. 146 (1999) 266–270.
[42] G.C. Fitzgibbon, E. J. Hubert, JR., C.E. Holley, JR., The enthalpy of formation of barium monoxide, J Chem Thermodyn. (1973) 577–582.
[43] R.P. Tangri, V. Venugopal, D.K. Bose, Standard molar enthalpies of formation of sodium molybdates ($Na_2Mo_nO_{3n+1}$ with n = 1, 2, 3 or 4) at 298.15 K by solution calorimetry, Thermochim. Acta. 198 (1992) 259–265.
[44] G. Kauric, E. Epifano, P.M. Martin, L. van Eijck, D. Bouëxière, N. Clavier, C. Guéneau, A.L. Smith, Structural and Thermodynamic Investigation of the Perovskite $Ba_2NaMoO_{5.5}$, Inorg. Chem. 59 (2020) 6120–6130.

Chapter 6: Experimental study of the Cs_2O-MoO_3-Na_2O system

In this chapter, phase diagram data on the quaternary Cs_2O-MoO_3-Na_2O system and its sub-systems are first reviewed. Then, key missing data in these systems are listed. Finally, the experimental investigation of the Cs_2MoO_4-Na_2MoO_4 pseudo-binary section and the characterisation of two quaternary compounds formed in the Cs-Mo-Na-O system are presented.

6.1. Literature review

A schematic view of the Cs_2O-MoO_3-Na_2O ternary pseudo system is presented in **figure 6.1** with all the compounds reported to exist.

To identify the missing phase diagram and thermodynamic data, a literature review is presented hereafter starting with the pseudo-binary systems.

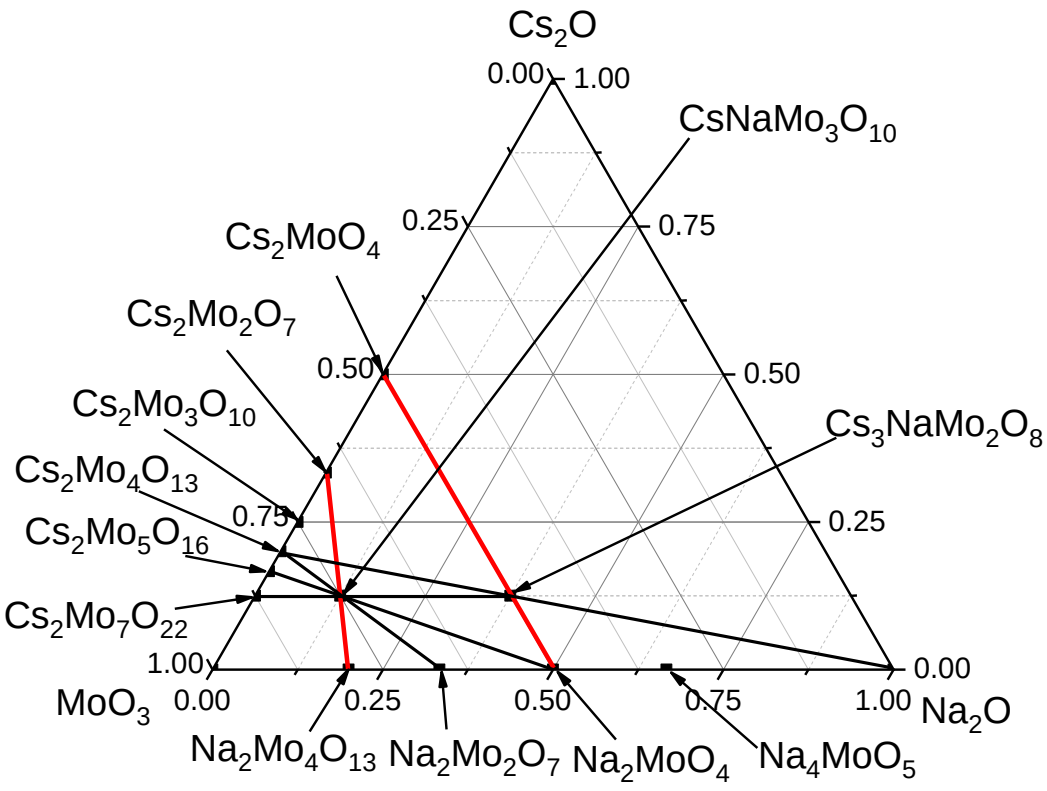

Figure 6.1: Sketch of the pseudo-ternary phase diagram Cs_2O-MoO_3-Na_2O

The pseudo-binary phase diagram forming this system are Cs_2O-MoO_3, Cs_2O-Na_2O and MoO_3-Na_2O.

Pseudo-binary phase diagrams

The description of the Na_2O-MoO_3 system is reported in section 5.1 in Chapter 5.

For the Cs_2O-Na_2O pseudo-binary section, no phase diagram was found and no ternary compound was reported to exist in the literature.

For the Cs_2O-MoO_3 system, numerous compounds exist: Cs_2MoO_4, $Cs_2Mo_2O_7$, $Cs_2Mo_3O_{10}$, $Cs_2Mo_4O_{13}$, $Cs_2Mo_5O_{16}$ and $Cs_2Mo_7O_{22}$. Thermodynamic properties of the different phases and phase diagram data on the Cs_2MoO_4-MoO_3 section were reported and discussed in the work of Pham Thi [1]. Using the experimental thermodynamic data on Cs_2MoO_4 and $Cs_2Mo_2O_7$, and the phase diagram data of Hoekstra *et al.* [2], the author developed a Calphad model for the Cs_2MoO_4-MoO_3 system. Then, this model was later re-assessed by Dupin in the framework of the TAF-ID project [3]. The phase diagram obtained with the re-assessed database is presented in **figure 6.2**.

The Cs_2O-Cs_2MoO_4 section was not studied experimentally. Nevertheless, a Calphad model was developed for the ternary Cs-Mo-O system.

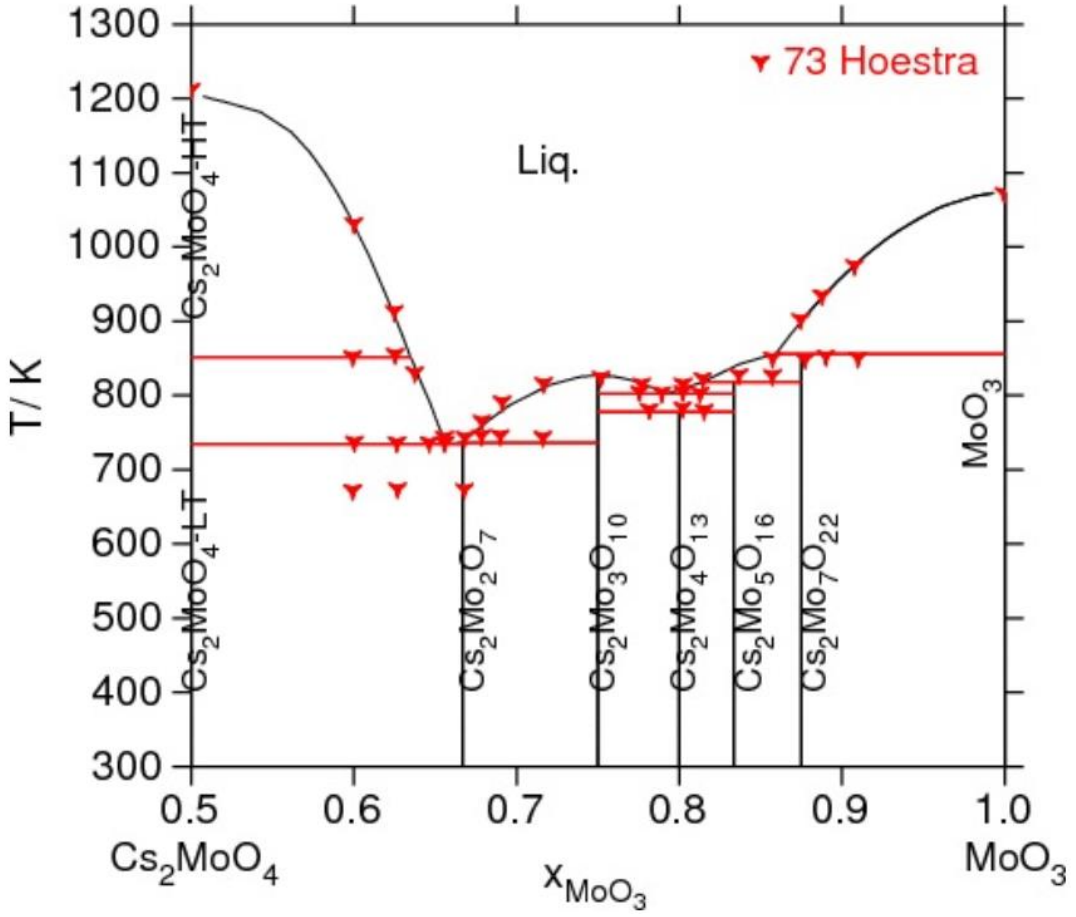

Figure 6.2: Calculated Cs_2MoO_4-MoO_3 pseudo-binary phase diagram using the TAF-ID database with the experimental phase diagram data of Hoekstra *et al.* [2].

Cs_2O-MoO_3-Na_2O pseudo-ternary

For the pseudo-binary section Cs_2MoO_4-Na_2MoO_4, Samuseva *et al.* [4] reported a phase diagram with three eutectoids (e1, e2, e3) and one eutectic point (E) at 753 K and 42.5 mol% of Cs_2MoO_4 as shown on **figure 6.3**. A solubility of both Cs_2MoO_4 into Na_2MoO_4 and of Na_2MoO_4 into Cs_2MoO_4 was found. Moreover, on the reported phase diagram, three polymorphs of Cs_2MoO_4 named as α, β and γ were represented and observed by XRD.

Zueva *et al.* [5] reinvestigated the Cs_2MoO_4-Na_2MoO_4 phase diagram and reported an eutectic point at 37 mol% Cs_2MoO_4 at 747 K, in relatively good agreement with the measurements of Samureva *et al.* [4]. However, no phase diagram was proposed by the authors.

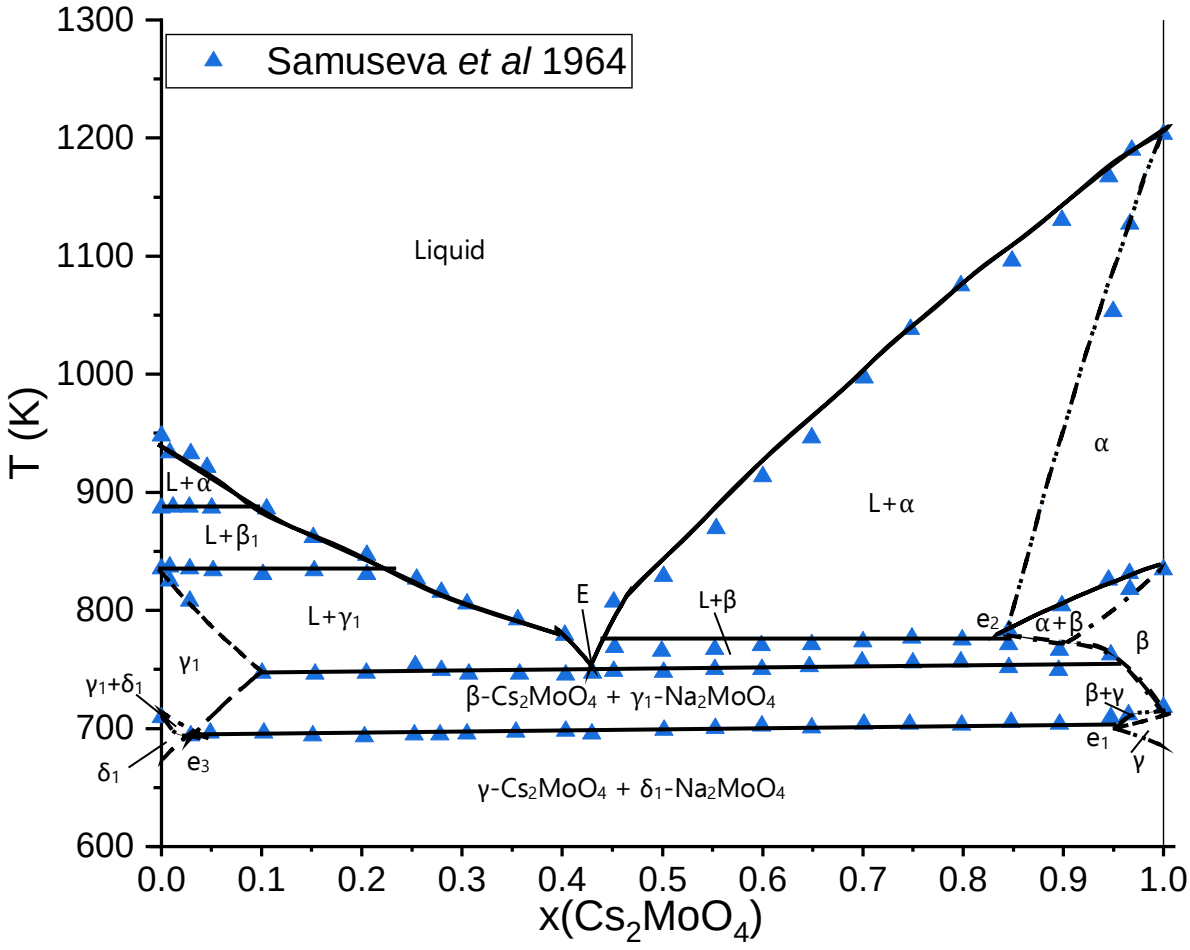

Figure 6.3: Na_2MoO_4-Cs_2MoO_4 phase diagram reported by Samuseva *et al* [4].

However, several studies showed that Cs_2MoO_4 exists with only two crystallographic structures as suggested by Hoekstra *et al.* [2], in disagreement with Samuseva *et al.* [4]. Recently, Wallez *et al.* [6] refined the high temperature crystallographic form of Cs_2MoO_4 in hexagonal symmetry, confirming that only one allotropic phase transition

exists, in the temperature range from 300 to 1200 K, in contradiction with the phase diagram proposed by Samuseva *et al.* [4].

Recently, Zolotova *et al.* [7], showed the existence of the quaternary compound $Cs_3Na(MoO_4)_2$ as reported in **figure 6.1**. Therefore, the authors reinvestigated the phase diagram Cs_2MoO_4-Na_2MoO_4, (**figure 6.4**). Mixtures of (Na_2MoO_4:Cs_2MoO_4) were annealed at 623-723 K for 100-250 hours. The phase diagram was finally assessed from DTA results and the co-existing phase fields checked with the XRD results for the sintered samples. The formation of the quaternary compound was observed in the sintered samples. As Samuseva *et al.* [4], they reported a solubility of Na_2MoO_4 into Cs_2MoO_4 whereas no solubility of Cs_2MoO_4 was measured in Na_2MoO_4. Moreover, the authors report the incongruent melting of $Cs_3Na(MoO_4)_2$ at 783 K and an allotropic phase transition at low temperature (663 K). Nevertheless, the XRD patterns measured after annealing of the compound at a temperature lower than the allotropic phase transition did not show any change. Finally, the existence of a small miscibility gap in the liquid state is assumed between 30 and 45 mol% equivalent in Cs_2MoO_4 as shown on **figure 6.4**. Nevertheless, the observed phase fields by XRD measurements after quenching in the Cs_2MoO_4-Na_2MoO_4 compositions by Zolotova *et al.* [7] were not reported by the authors.

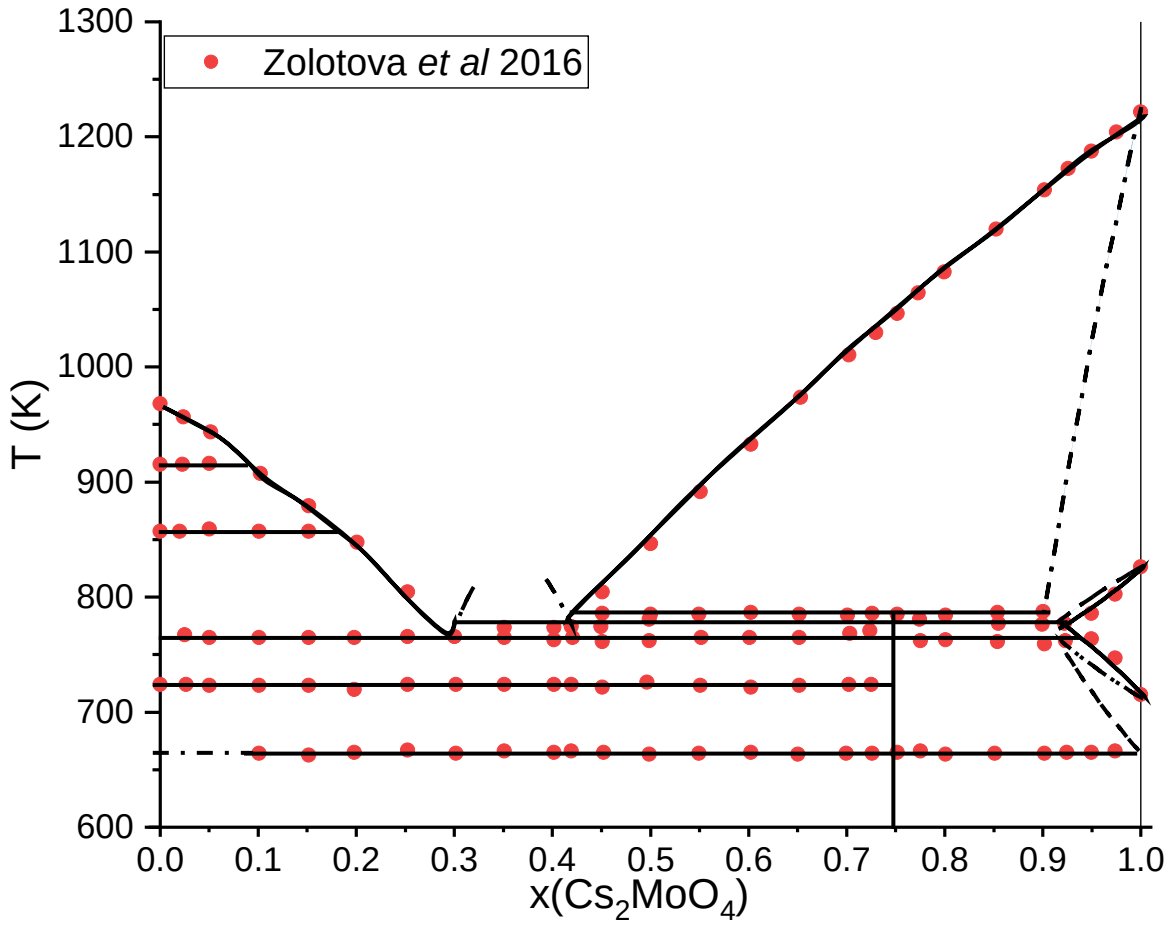

Figure 6.4: Na_2MoO_4-Cs_2MoO_4 phase diagram reported by Zolotova *et al.* [7].

On **figure 6.5**, the two datasets coming from the works of Samuseva *et al.* [4] and Zolotova *et al.* [7] are superposed for comparison. For the liquidus data and the measurements in the region rich in Na_2MoO_4, there is a relatvely good agreement between both studies, except for the solubility of Cs_2MoO_4 into Na_2MoO_4 and the phase transition temperatures for Na_2MoO_4 that seem to be lower (~50 K) for Samuseva *et al.* [4] than the ones reported by Zolotova *et al.* [7]. For $x(Cs_2MoO_4)>0.4$, the two studies are reporting different phase fields as shown on **figure 6.3** and **6.4**. However, the reported temperatures of the events between 750 and 800 K are close and the phase field attribution is unclear in this region. Therefore, a re-investigation with determination of the stable phase fields would be useful for the assessment of the phase diagram.

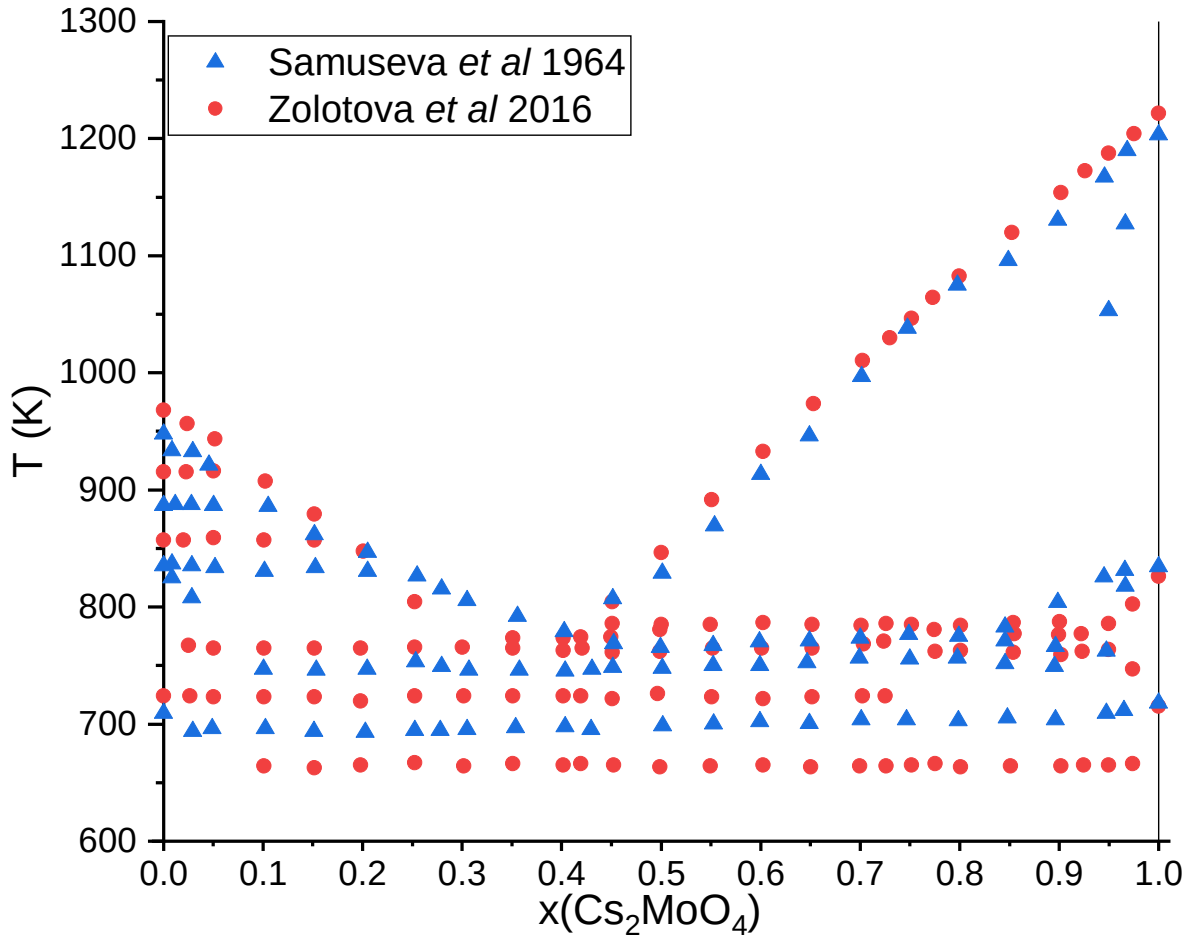

Figure 6.5: Na_2MoO_4-Cs_2MoO_4 pseudo-binary phase diagram with the data of Samureva *et al.* [4] and the one of Zolotova *et al.* [7]

The recent re-investigation of the quaternary compound $Cs_3Na(MoO_4)_2$ by Smith *et al.* [8] showed that no allotropic phase transition exists in this compound. The authors found out a decomposition temperature of (777±5) K for the pure compound, in agreement with the data reported by Zolotova *et al.* [7]. Moreover, Smith *et al.* [8,9] measured the standard enthalpy of formation $\Delta_fH°_m$ and standard entropy $S°_m$ and heat capacity $Cp°_m$ at low temperatures (1.9-299.6 K) of the $Cs_3Na(MoO_4)_2$ compound. These

data, very useful for the Calphad modelling of the Na_2MoO_4-Cs_2MoO_4 system are reported in **table 6.1**. Therefore, enough thermodynamic and phase diagram are available to model the Na_2MoO_4-Cs_2MoO_4 system as reported in Chapter 7.

Table 6.1 : Thermodynamic data on the $Cs_3Na(MoO_4)_2$ reported by Smith *et al.* [9]

$\Delta_f H°_m$ (298K)/ kJ.mol^{-1}	$\Delta_f S°_m$ (298K)/ J.K^{-1}.mol^{-1}	$S°_m$ (298K)/ J.K^{-1}.mol^{-1}	$Cp°_m$ (298K)/ J.K^{-1}.mol^{-1}
-2998.6 ± 3.0	-717.5 ± 5.2	467.2 ± 6.8	296.3 ± 3.3

According to Förster *et al.* [10], a second quaternary compound, $NaCsMo_3O_{10}$, exists in the Cs_2O-MoO_3-Na_2O system [10]. However, only the space group *Pnma* (n°62) and cell parameters of the compound (a=7.69 Å, b=7.60 Å, c=15.52 Å) have been reported. No structural analysis of the atomic positions, and no diffraction pattern are reported. Moreover, no thermodynamic data exist on this compound.

Finally, Zueva *et al.* [5] studied the liquidus surface of the Cs_2MoO_4-Na_2MoO_4-MoO_3 section by Differential Thermal Analysis (**figure 6.6**). No quaternary compound was reported on their phase diagram.

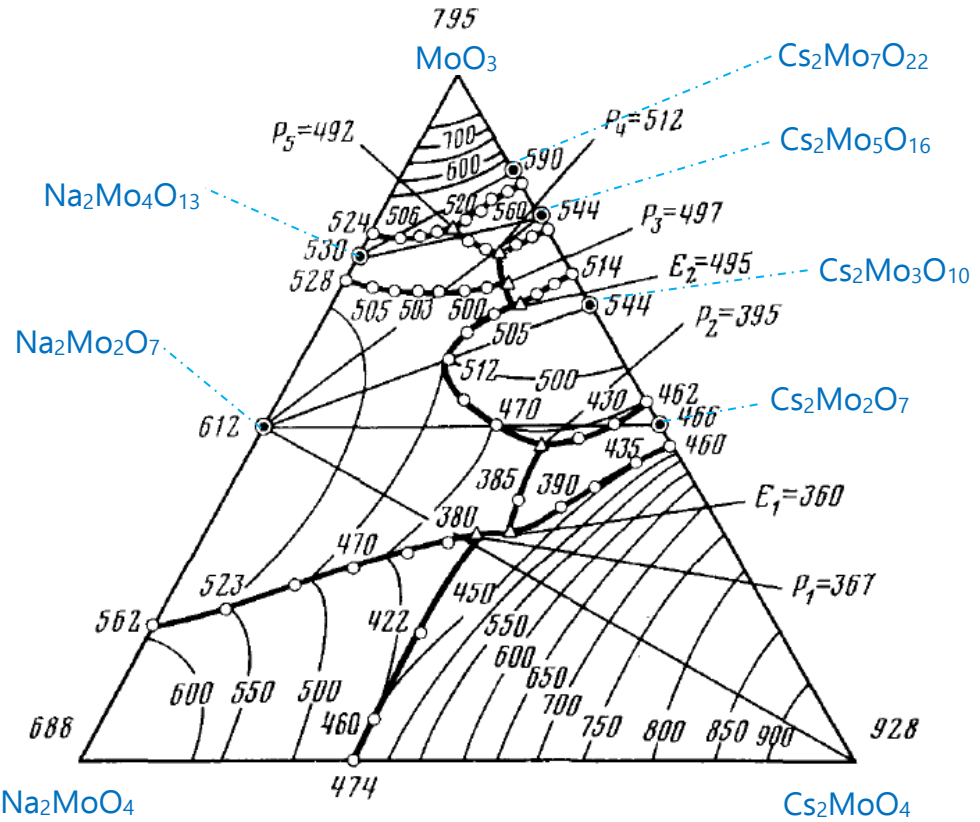

Figure 6.6: Projection of the crystallisation surface of the Na_2MoO_4-Cs_2MoO_4-MoO_3 system reported by Zueva *et al.* [5]. The temperature are in °C. The ternary compounds have been added in blue on the pseudo-binary systems.

Conclusion

To conclude, the pseudo-binary systems Cs_2O-MoO_3 and Na_2O-MoO_3 are well known and CALPHAD models are available. Nevertheless, as mentioned in Chapter 5 the CALPHAD model of the Mo-O sub-system had to be updated, leading to minor changes in the modelling of Cs_2O-MoO_3 and Na_2O-MoO_3 systems, reported in Chapter 7.

The Cs_2O-Na_2O section is not known but the priority was given to the reactions involving Cs_2MoO_4, as it is the main compound of the JOG likely reacting with the sodium coolant.

Regarding the pseudo-ternary system Cs_2O-MoO_3-Na_2O, the Cs_2MoO_4-Na_2MoO_4 pseudo-binary section was studied by three different authors. However, some discrepancies have been raised in the reported phase fields. Moreover, the quaternary compound $Cs_3Na(MoO_4)_2$ was only observed by Zolotova *et al.* [7] and Smith *et al.* [8,9]. Therefore, an experimental re-investigation of the Cs_2MoO_4-Na_2MoO_4 pseudo-binary is proposed to settle down on the different equilibria and transitions observed. Finally, the development of a Calphad model of the Cs_2MoO_4-Na_2MoO_4 system is reported in Chapter 7.

Finally, liquidus data on the Cs_2MoO_4-Na_2MoO_4-MoO_3 pseudo-ternary section have been reported. However, in a first step, the quaternary compound $CsNaMo_3O_{10}$ has been studied in this work to assess its structure and thermal stability. These data will be extremely valuable in the Calphad model development of the Cs_2MoO_4-Na_2MoO_4-MoO_3 pseudo-ternary phase diagram, not performed in the frame of the present work due to a lack of time.

6.2. Phase transition data in the Cs_2MoO_4-Na_2MoO_4 system

In this section, the investigation of the Cs_2MoO_4-Na_2MoO_4 system by Differential Scanning Calorimetry (DSC) (**see Appendix A.4**) is described to solve the discrepancies raised in the previous section.

DSC measurements were performed on fifteen compositions of (Cs_2MoO_4:Na_2MoO_4) mixtures (see **table 6.2**). Precisely weighted amounts of Cs_2MoO_4 (prepared by solid state synthesis as reported in Wallez et al. [6]) and anhydrous Na_2MoO_4 (Na_2MoO_4 anhydrous, 99.9% trace metal basis, Sigma-Aldrich) were grinded together under the dry-atmosphere of an argon-filled glove box. Each sample was introduced in a nickel liner and encapsulated for calorimetric measurements in a stainless steel crucible closed with a screw bold, as described by Benes *et al.* [11]. This technique was used to avoid both vaporization at high temperature and oxygen and water contamination of

the samples (Cs_2MoO_4 and anhydrous Na_2MoO_4 are extremely hygroscopic compounds). Examples of heat flow curves are shown in **figure 6.7**.

The melting temperatures of pure compounds and transition temperature for all mixtures were derived on the heating ramp as the onset temperature using tangential analysis of the recorded heat flow curve. The liquidus temperatures for mixtures were taken as the extremum of the last thermal event as recommended by Boettinger *et al.* [12]. The uncertainty on the measured temperatures is estimated to be 5 K on the pure compounds (Cs_2MoO_4 and Na_2MoO_4) and 10 K for the mixtures (corresponding to the standard uncertainty). Four successive heating/cooling cycles were performed with a heating rate between 2 and 10 K/min and cooling rates of 12-10-8-5 K/min.

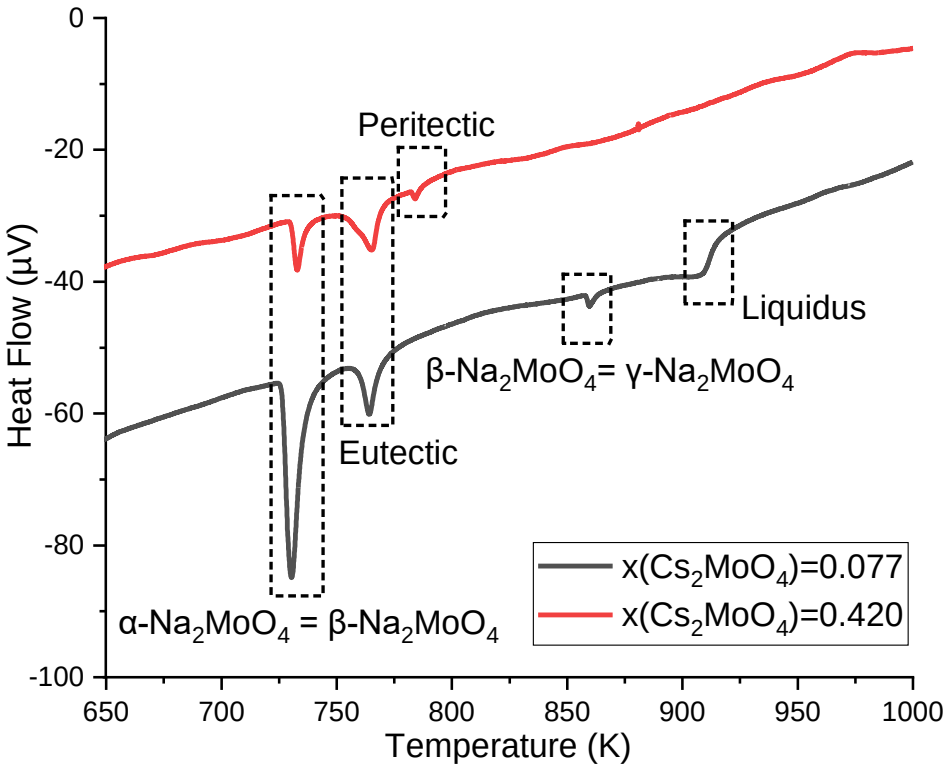

Figure 6.7: Heat flow curve versus temperature of two samples with compositions $x(Cs_2MoO_4)=0.077$ ($m_{sample}=107$ mg) and $x(Cs_2MoO_4)=0.420$ ($m_{sample}=78$ mg)

The reported data in **table 6.2** are the temperatures obtained after averaging the temperatures measured for the four cycles. The equilibria were only attributed based on the interpretation of the DSC signals, and consistently with the data of Samuseva *et al.* [4] and Zolotova *et al.* [7] as no XRD data after thermal treatment were collected. The data collected in this work are also compared with the phase diagram data of Samuseva *et al.* [4] and Zolotova *et al.* [7] **in figure 6.8**.

In the rich part section in Cs_2MoO_4, the equilibria are still unclear and are discussed in Chapter 7.

Table 6.2: Results of the DSC measurements on the pseudo-binary Na_2MoO_4-Cs_2MoO_4 section

x(Cs_2MoO_4)[a]	T (K)[b]	Equilibrium	Equilibrium reaction
0	728	Allotropic transition	α-Na_2MoO_4 = β-Na_2MoO_4
	853	Allotropic transition	β-Na_2MoO_4= γ-Na_2MoO_4
	912	Allotropic transition	γ-Na_2MoO_4 = δ-Na_2MoO_4
	957	Congruent melting	δ-Na_2MoO_4 = L
0.039	723	Allotropic transition	α-Na_2MoO_4 = β-Na_2MoO_4
	751	Eutectic	L= β-Na_2MoO_4 + $Cs_3Na(MoO_4)_2$
	856	Allotropic transition	β-Na_2MoO_4= γ-Na_2MoO_4
	915	Allotropic transition	γ-Na_2MoO_4 = δ-Na_2MoO_4
	941	Liquidus	δ-Na_2MoO_4 + L′ = L
0.077	721	Allotropic transition	α-Na_2MoO_4 = β-Na_2MoO_4
	754	Eutectic	L= β-Na_2MoO_4 + $Cs_3Na(MoO_4)_2$
	852	Allotropic transition	β-Na_2MoO_4= γ-Na_2MoO_4
	915	Liquidus	γ -Na_2MoO_4 + L′ = L
0.100	723	Allotropic transition	α-Na_2MoO_4 = β-Na_2MoO_4
	752	Eutectic	L= β-Na_2MoO_4 + $Cs_3Na(MoO_4)_2$
	856	Allotropic transition	β-Na_2MoO_4= γ-Na_2MoO_4
	899	Liquidus	γ -Na_2MoO_4 + L′ = L
0.151	720	Allotropic transition	α-Na_2MoO_4 = β-Na_2MoO_4
	753	Eutectic	L= β-Na_2MoO_4 + $Cs_3Na(MoO_4)_2$
	855	Allotropic transition	β-Na_2MoO_4= γ-Na_2MoO_4
	875	Liquidus	γ -Na_2MoO_4 + L′ = L
0.210	718	Allotropic transition	α-Na_2MoO_4 = β-Na_2MoO_4
	752	Eutectic	L= β-Na_2MoO_4 + $Cs_3Na(MoO_4)_2$
	853	Allotropic transition	β-Na_2MoO_4= γ-Na_2MoO_4
	860	Liquidus	γ -Na_2MoO_4 + L′ = L
0.295	721	Allotropic transition	α-Na_2MoO_4 = β-Na_2MoO_4
	757	Eutectic	L= β-Na_2MoO_4 + $Cs_3Na(MoO_4)_2$
	795	Liquidus	β -Na_2MoO_4 + L′ = L
0.321	721	Allotropic transition	α-Na_2MoO_4 = β-Na_2MoO_4
	751	Eutectic	L= β-Na_2MoO_4 + $Cs_3Na(MoO_4)_2$
	768	Liquidus	β -Na_2MoO_4 + L′ = L
0.358	719	Allotropic transition	α-Na_2MoO_4 = β-Na_2MoO_4
	749	Eutectic	L= β-Na_2MoO_4 + $Cs_3Na(MoO_4)_2$
	779	Peritectic	$Cs_3Na(MoO_4)_2$ = L + Cs_2MoO_4
0.398	721	Allotropic transition	α-Na_2MoO_4 = β-Na_2MoO_4
	757	Eutectic	L= β-Na_2MoO_4 + $Cs_3Na(MoO_4)_2$
	779	Peritectic	$Cs_3Na(MoO_4)_2$ = L + Cs_2MoO_4
0.420	719	Allotropic transition	α-Na_2MoO_4 = β-Na_2MoO_4
	752	Eutectic	L= β-Na_2MoO_4 + $Cs_3Na(MoO_4)_2$
	779	Peritectic	$Cs_3Na(MoO_4)_2$ = L + Cs_2MoO_4

0.509	720	Allotropic transition	α-Na_2MoO_4 = β-Na_2MoO_4
	757	Eutectic	L= β-Na_2MoO_4 + $Cs_3Na(MoO_4)_2$
	779	Peritectic	$Cs_3Na(MoO_4)_2$ = L + Cs_2MoO_4
	858	Liquidus	h-Cs_2MoO_4 + L′ = L
0.640	720	Allotropic transition	α-Na_2MoO_4 = β-Na_2MoO_4
	752	Eutectic	L= β-Na_2MoO_4 + $Cs_3Na(MoO_4)_2$
	778	Peritectic	$Cs_3Na(MoO_4)_2$ = L + Cs_2MoO_4
	959	Liquidus	h-Cs_2MoO_4 + L′ = L
0.850	760	Peritectoïd	o-$(Cs,Na)_2MoO_4$ + $Cs_3Na(MoO_4)_2$ = h-$(Cs,Na)_2MoO_4$
	780	Peritectic	$Cs_3Na(MoO_4)_2$ = L + Cs_2MoO_4
	1153	Liquidus	h-Cs_2MoO_4 + L′ = L
0.918	754	Peritectoïd	o-$(Cs,Na)_2MoO_4$ + $Cs_3Na(MoO_4)_2$ = h-$(Cs,Na)_2MoO_4$
	795	Peritectic	o-$(Cs,Na)_2MoO_4$ = o-$(Cs,Na)_2MoO_4$ + h-$(Cs,Na)_2MoO_4$
	826	Solidus ?	h-$(Cs,Na)_2MoO_4$ = L + h-$(Cs,Na)_2MoO_4$
	1180	Liquidus	h-Cs_2MoO_4 + L′ = L
0.960	812	o-$(Cs,Na)_2MoO_4$ phase boundary ?	o-$(Cs,Na)_2MoO_4$ = o-$(Cs,Na)_2MoO_4$ + h-$(Cs,Na)_2MoO_4$
	833	h-$(Cs,Na)_2MoO_4$ phase boundary ?	o-$(Cs,Na)_2MoO_4$ + h-$(Cs,Na)_2MoO_4$ = h-$(Cs,Na)_2MoO_4$
	1206	Liquidus	h-Cs_2MoO_4 + L′ = L
1	841	Allotropic transition	o-Cs_2MoO_4 = h-Cs_2MoO_4
	1229	Congruent melting	h-Cs_2MoO_4 = L

[a] Standard uncertainties u are u (x(Cs_2MoO_4))=0.005

[b] Standard uncertainties u are u (T)=5 K for the pure end-members, u (T) = 10 K for mixtures

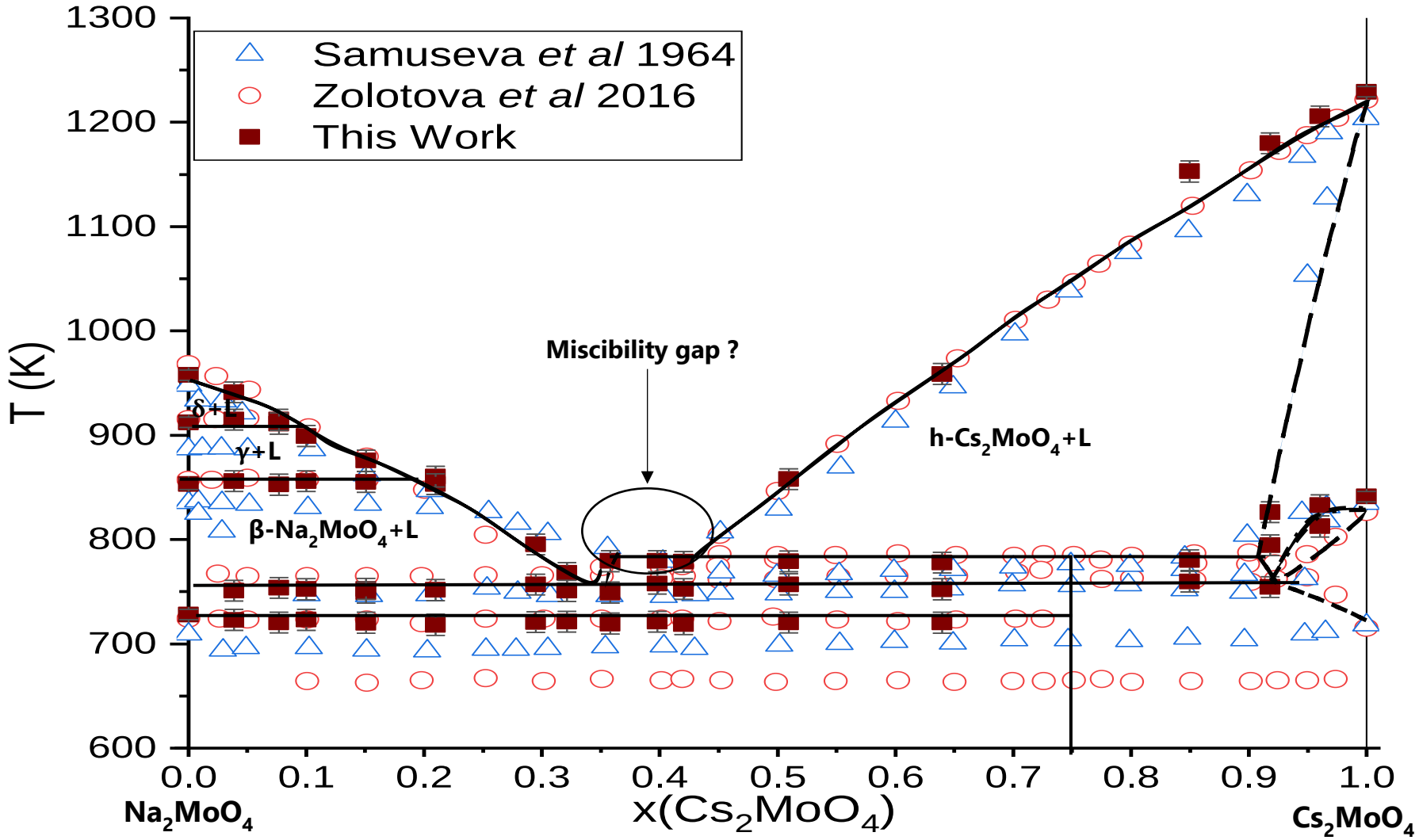

Figure 6.8: Na_2MoO_4-Cs_2MoO_4 pseudo-binary phase diagram with the experimental data measured by Samuseva *et al.* [4] and Zolotova *et al.* [7] and in this work

The study in this work is very consistent with the results of Zolotova *et al.* [7]. However, the low temperature phase transition of the quaternary compound found by Zolotova *et al.* [7] has not been observed, which is consistent with the study of Smith *et al.* [8].

The present liquidus data are in good agreement with both Samuseva *et al.* [4] and Zolotova *et al.* [7]. A possible eutectic point is found at ~35 mol. % Cs_2MoO_4 in good agreement with the data reported by Zueva *et al.* [5]. Moreover, the peculiar liquidus shape between 35 and 45 mol. % Cs_2MoO_4 observed by Zolotova *et al.* [7] has also been observed in our study and would suggest the existence of a small miscibility gap. Finally, the solubility of sodium into Cs_2MoO_4 reported by Samuseva *et al.* [4] and Zolotova *et al.* [7] has also been observed in this work.

As in Zolotova *et al.* [7], no solubility of cesium into Na_2MoO_4 was observed in disagreement with the data of Samuseva *et al.* [4]

The present data are used in the Calphad modelling of the pseudo-binary system Cs_2MoO_4-Na_2MoO_4 (see Chapter 7).

Nevertheless, complementary studies involving long thermal heat treatments followed by quenching tests and XRD characterisations should be performed to more precisely assess the identity of the different phase fields.

6.3. Synthesis and structural analysis of the quaternary compounds

In this section, the synthesis and analysis of the two quaternary compounds of the Cs-Mo-Na-O system are described. Because of the hygroscopic nature of the molybdates, handling of the samples was carried out exclusively under dry atmosphere in an argon-filled glove box. The structure of the $CsNaMo_3O_{10}$ compound has been thoroughly investigated before determining its decomposition temperature and associated enthalpy of transition. Moreover, the enthalpy of the $Cs_3Na(MoO_4)_2$ peritectic decomposition has also been measured, therefore, the compound's synthesis is also be presented in this section.

6.3.1. $CsNaMo_3O_{10}$

The experimental X-ray diffraction pattern of $CsNaMo_3O_{10}$ has never been reported in the literature. In this section, the synthesis method and structural investigation are detailed.

Synthesis

Cesium molybdate, Cs_2MoO_4, was grinded with an accurately weighted amount of sodium molybdate (Na_2MoO_4 anhydrous, 99.9% trace metal basis, Sigma-Aldrich) and

molybdenum trioxide (MoO_3, >99.5%, Sigma-Aldrich) according to the reaction:

$$\frac{1}{2}\,Cs_2MoO_{4\,(s)} + \frac{1}{2}\,Na_2MoO_{4\,(s)} + \,2\,MoO_{3\,(s)} = CsNaMo_3O_{10\,(s)}$$

This stoichiometric mixture was then heated under dry oxygen at 723K for 120 hours with an intermediate regrinding step.

Förster *et al.* [10] studied in detail the structure of the $RbNaMo_3O_{10}$ compound. The authors refined the structure in space group *Pnma* (n°62) with cell parameters *a*=7.584 Å, *b*=7.589 Å, *c*=15.475 Å and mentioned that the cesium compound $CsNaMo_3O_{10}$ is isostructural to the rubidium one. Therefore, the rubidium compound was used as starting model to refine the structure of $CsNaMo_3O_{10}$. The obtained results are reported in **figure 6.9** and **table 6.3**. The refined lattice parameters are *a*=7.7707 (6) Å, *b*=7.6242 (5) Å, *c*=15.615(1) Å. The cell parameters are higher than the one ones reported for $RbNaMo_3O_{10}$ as expected, due to the increase in the ionic radius (in coordination 9, the ionic radius of rubidium is 1.63 Å whereas the one of cesium is 1.78 Å [13])

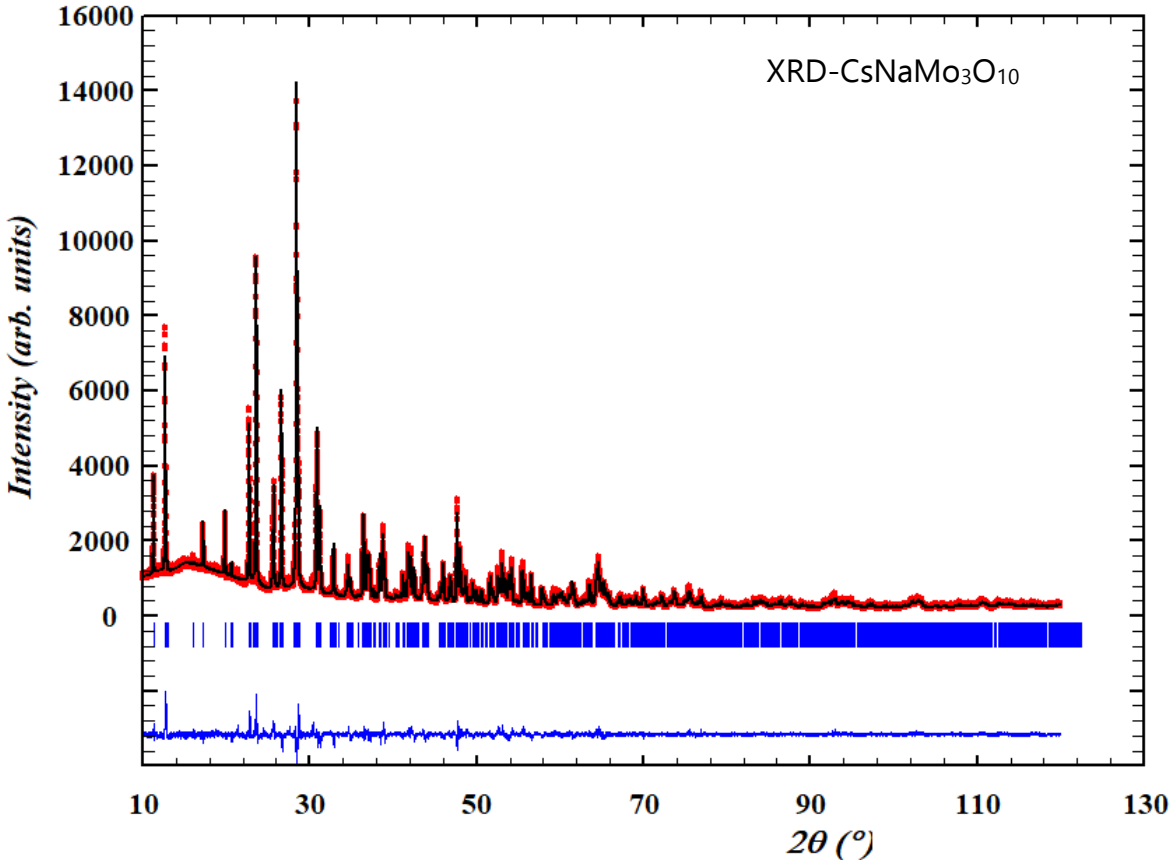

Figure 6.9: Comparison between the calculated (Y_{calc}, in black) and observed (Y_{obs}, in red) XRD patterns of $CsNaMo_3O_{10}$. Y_{obs}-Y_{calc} in blue, is the difference between the experimental and calculated intensities. The angular positions of Bragg reflections are shown in blue. The measurement has been performed λ=Cu-Kα.

Table 6.3: Refined atomic positions, isotropic thermal displacement factor B_0 the $CsNaMo_3O_{10}$ derived from the XRD refinement

with χ^2 = 3.15, R_p= 15.5 R_{wp}= 15.6.

Atoms	Wyckoff	X	y	z	B_0(Å^2)
Cs	4c	0.8538 (3)	0.25	0.1485 (2)	2.92 (5)
Mo1	4c	0.7710 (3)	0.25	0. 5551 (2)	1.43 (5)
Mo2	8d	0.3907 (2)	0.5034 (3)	0.1008 (1)	1.56 (3)
Na	4c	0.442 (2)	0.25	0.723 (1)	4.0 (3)
O1	4c	0.068 (2)	0.25	0.593 (1)	1.6(4)
O2	4c	0.886 (2)	0.25	0.422 (1)	0.8*
O3	8d	0.338 (1)	0.034 (1)	-0.037 (1)	0.8*
O4	8d	0.191 (2)	0.555 (2)	0.132 (1)	2.3(3)
O5	8d	0.488 (2)	0.465 (2)	0.194 (1)	4.7(5)
O6	4c	0.595 (3)	0.25	0.516 (2)	7.7(7)
O7	4c	0.740 (2)	0.25	0.664 (2)	4.7(6)

*non refined parameters

The structure of the compound is shown in **figure 6.10**. It is constituted of chains of corner-sharing sodium and cesium polyhedra along the *a* axis with a coordination number of 6 and 9, respectively. Infinite chains of corner-sharing molybdenum octahedra are formed along the *b* axis. The selected bond lengths obtained from the XRD refinement are reported in **table 6.4**. The average bond lengths for Na-O and Mo2-O octahedra are similar as the rubidium compound (2.44 Å and 1.96 Å respectively for the cesium compound and 2.41(3) Å and 1.95(2) Å for the rubidium). For the Cs-O octahedra, a increase was reported (3.28 Å compared to 3.12(2) Å) whereas for the Mo1-O, a slight decrease was observed (1.89 Å compared to 1.98(3) Å) that could be explained from the short Mo1-O6 distance observed for the cesium compound (1.50(3) Å vs 1.69(3) Å). Nevertheless, for more accurate values neutron diffraction and/or EXAFS measurements should be performed.

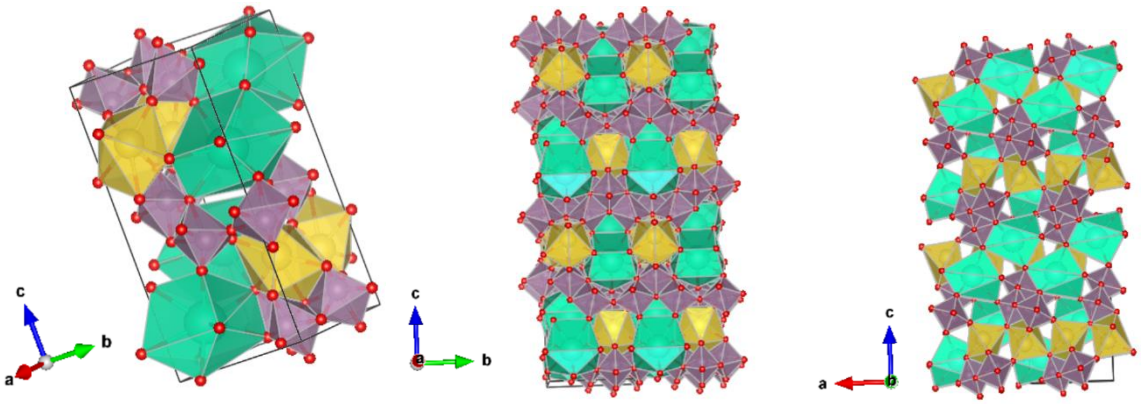

Figure 6.10: Representation of the structure of $CsNaMo_3O_{10}$. The octahedrons around the atoms of molybdenum and sodium are represented in purple and yellow, respectively. The polyhedrons around the cesium atoms are represented in green, and oxygen atoms in red.

Table 6.4: Selected bond lengths of the Cs, Mo or Na atoms of $CsNaMo_3O_{10}$

Cs (l in Å)		Mo1 (l in Å)		Mo2 (l in Å)		Na (l in Å)	
l(Cs-O3)	3.15(1)	l(Mo1-O1)	2.38(2)	l(Mo2-O1)	1.913(3)	l(Na-O4)	2.31(2)
l(Cs-O3)	3.15(1)	l(Mo1-O2)	2.26(2)	l(Mo2-O2)	1.966(3)	l(Na-O4)	2.31(2)
l(Cs-O4)	3.52(1)	l(Mo1-O3)	1.75(1)	l(Mo2-O3)	2.22(1)	l(Na-O5)	2. 58(2)
l(Cs-O4)	3.52(1)	l(Mo1-O3)	1.75(1)	l(Mo2-O3)	2.34(1)	l(Na-O5)	2. 58(2)
l(Cs-O5)	3.14(2)	l(Mo1-O6)	1.50(3)	l(Mo2-O4)	1.70(1)	l(Na-O7)	2.37(3)
l(Cs-O5)	3.14(2)	l(Mo1-O7)	1.71(3)	l(Mo2-O5)	1.67(2)	l(Na-O7)	2.49(2)
l(Cs-O5)	3.36(2)						
l(Cs-O5)	3.36(2)						
l(Cs-O6)	3.18(3)						
Coordination	9	Coordination	6	Coordination	6	Coordination	6
Average bond length	3.28(2)	Average bond length	1.89(2)	Average bond length	1.96 (2)	Average bond length	2.44 (2)

The $CsNaMo_3O_{10}$ compound has been synthesised and analysed by XRD. However, for confirmation of the molybdenum valence state and thus compound stoichiometry, X-ray Absorption Near Edge Structure spectroscopy measurements were performed.

X-ray Absorption Near Edge Structure analysis

The XANES spectrum of $CsNaMo_3O_{10}$, collected at the Mo K-edge is reported in **figure 6.11**. The white lines of $CsNaMo_3O_{10}$ and MoO_3 are well-aligned. Moreover, the energy position of the inflection point for the quaternary compound is close to the one for MoO_3 used as a reference for molybdenum +VI as shown in **figure 6.12** and reported in **table 6.5**. Therefore, the oxidation state of the molybdenum in the quaternary compound is +VI as expected from the synthesis route and the octahedral oxygen environment surrounding the molybdenum atom.

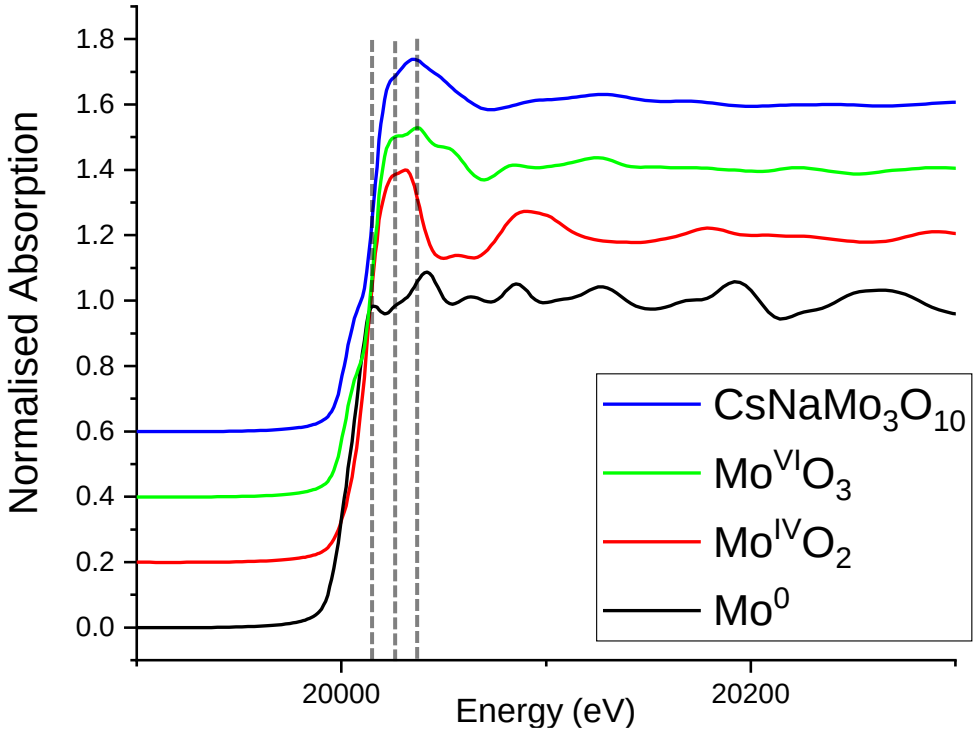

Figure 6.11: XANES spectra of the $CsNaMo_3O_{10}$ compound obtained at the Mo K-edge and comparison with spectra of Mo^0, $Mo^{IV}O_2$ and $Mo^{VI}O_3$ used as reference

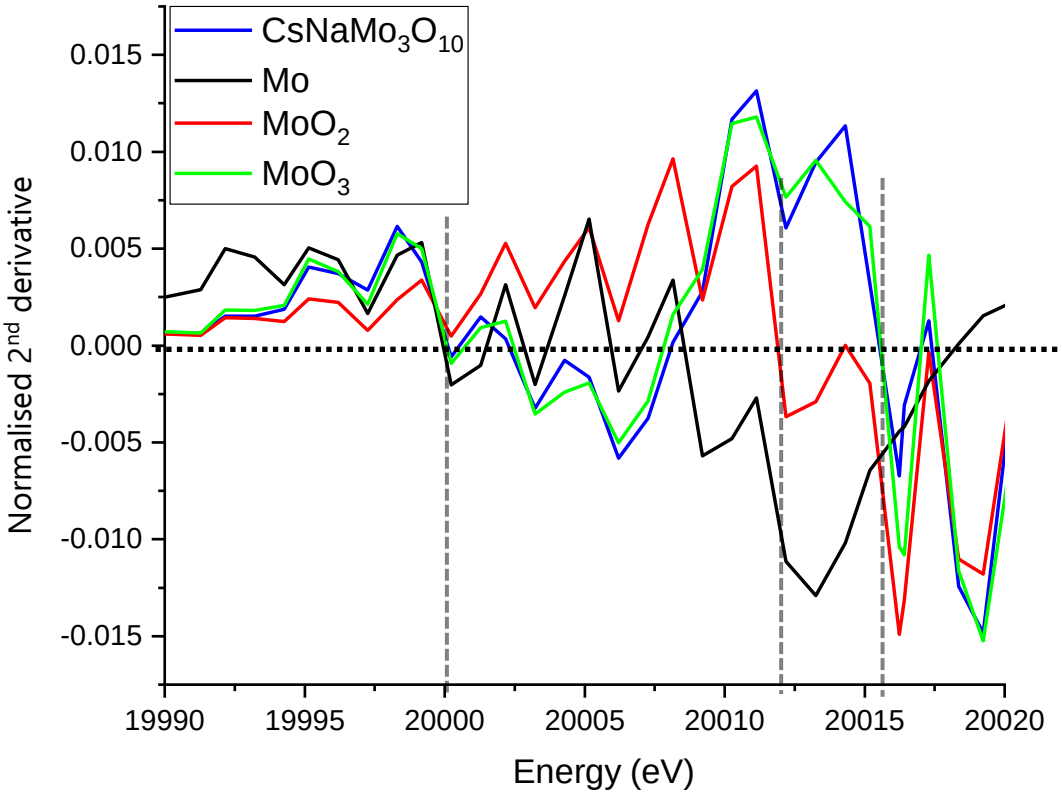

Figure 6.12: Normalised second derivative of the Mo K-edge absorption of $CsNaMo_3O_{10}$ compound and comparison with the ones of Mo^0, $Mo^{IV}O_2$ and $Mo^{VI}O_3$ used as references. The horizontal dashed lines mark the zero value for each shifted spectra. The vertical one is the energy position of the inflexion point.

Table 6.5: Energy position of the inflection points for the reference materials and for $CsNaMo_3O_{10}$.

Compound	**$CsNaMo_3O_{10}$**	**$Mo^{VI}O_3$**	**$Mo^{IV}O_2$**	**Mo^0**
E_0 (eV)[a]	20015.7	20015.7	20012.0	20000.0

The $CsNaMo_3O_{10}$ phase was synthesised pure and then analysed by XRD and XANES measurements. The obtained compound will then be used for thermodynamic measurements in section 6.2.3.

6.3.2. $Cs_3Na(MoO_4)_2$

$Cs_3Na(MoO_4)_2$ was synthesized in a closed stainless steel container under argon flow by reaction between accurately weighted powdered samples of cesium molybdate Cs_2MoO_4 and Na_2MoO_4 (99.9% min, Sigma Aldrich). The stoichiometric mixture was then heated at 723 K for 120 hours with intermediate regrinding steps.

The purity of the quaternary compound was examined by X-ray diffraction at room temperature (**figure 6.13**).The cell parameters measured for the compound are *a*=6.3469(4) Å, *c*=8.2216(6) Å in good agreement with the data reported by Smith *et al.* [8].

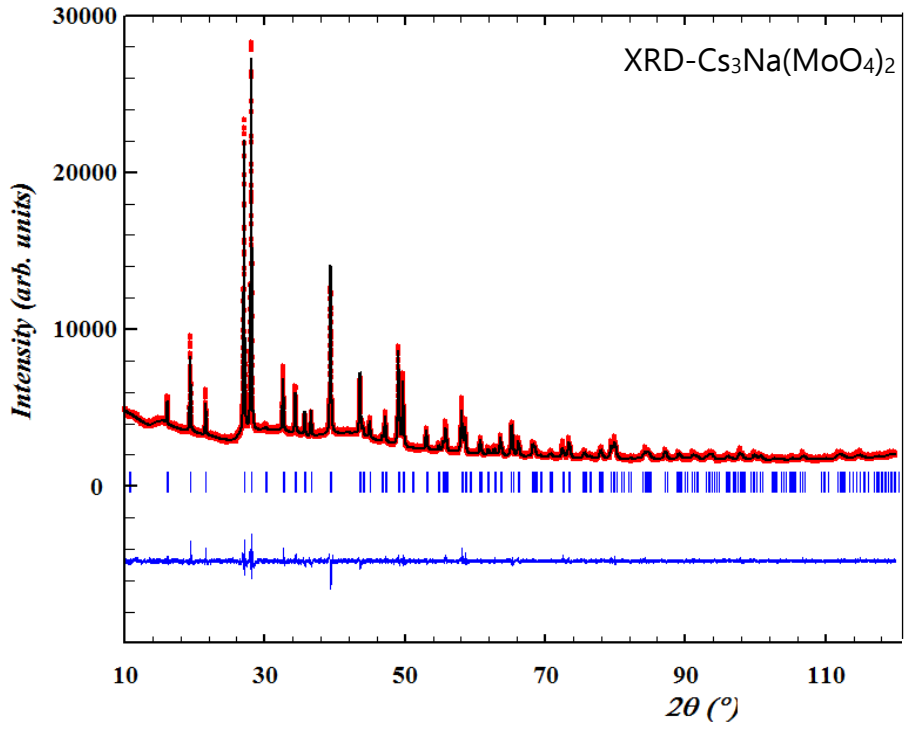

Figure 6.13: Comparison between the observed (Y_{obs}, in red) and calculated (Y_{calc}, in black) X-ray diffraction patterns of $Cs_3Na(MoO_4)_2$. Y_{obs}-Y_{calc}, in blue, is the difference between the experimental and calculated intensities. The angular positions of Bragg reflections are shown in blue. The measurement has been performed λ=Cu-Kα.

Both the $CsNaMo_3O_{10}$ and $Cs_3Na(MoO_4)_2$ compounds were obtained pure. Moreover, the amount of material produced was sufficient to perform thermodynamic measurements as presented in the following section.

6.4. Transition enthalpy measurement

Thermodynamic data on the transition temperatures of compounds are useful in the development of Calphad models. However, they are generally difficult to measure as large batches of pure samples are needed for precise measurements. As reported, in the previous section, we managed to synthesise $CsNaMo_3O_{10}$ and $Cs_3Na(MoO_4)_2$ pure with enough material to perform the measurement of the temperature and enthalpy of the decomposition reaction for both quaternary compounds.

The measurement was performed by Differential Scanning Calorimeter (DSC). A pure metal with a known enthalpy of fusion (lead for Na_2MoO_4 and $Cs_3Na(MoO_4)_2$ and aluminium for $CsNaMo_3O_{10}$) was added in the reference crucible which serves as an internal calibration standard as described in the work of Epifano *et al.* [14].

The sensitivity S in $\mu V.mW^{-1}$ of the detector is defined as: $S = \frac{A_{ref} \times M_{ref}}{\Delta H_{ref} \times m_{ref}}$ where A is the area of the peak associated with the transition of the reference material in μV.s, M the molar mass of the reference in $g.mol^{-1}$, ΔH the enthalpy of reaction in $J.mol^{-1}$ and m the weight of the reference in mg. This value is detector dependent, therefore the enthalpy of melting or phase transition of the compound can be written as:

$$\Delta H_{sample} = \frac{A_{sample} \times M_{sample} \times m_{ref}}{A_{ref} \times M_{ref} \times m_{sample}} \Delta H_{ref}$$

Where A_{sample}, M_{sample}, ΔH_{sample} and m_{sample} refer to the sample under measurement and A_{ref}, M_{ref}, ΔH_{ref} and m_{ref} to the reference.

6.4.1. Na_2MoO_4

Before applying this method to unknown compounds, we have validated it on Na_2MoO_4, whose allotropic transition (α-Na_2MoO_4 = β-Na_2MoO_4) is well known and energetic. Three measurement cycles, carried out with the same sample, were performed and averaged to determine the uncertainty on the obtained value. Each cycle consisted in a heating cycle of the sample up to 830K, followed by cooling down to room temperature. Both heating and cooling rates were of 10K/min. The maximum temperature was chosen in order to be above the first allotropic phase transition temperature (α-Na_2MoO_4 = β-Na_2MoO_4) at ~730 K, but still under the second phase transition occurring at ~866 K (β-Na_2MoO_4= γ-Na_2MoO_4).

Lead was used for the reference, as its melting temperature is 600.6 ±0.1 K , which is in the same temperature range but not superposed with any phase transitions of Na_2MoO_4. Both reactions are endothermic. However, as the opposite directions for the sample and metal peaks used as reference was placed in the reference crucible, the melting of the metal appears as a positive peak in the measured heat flow signal on **figure 6.14**. For the sample, placed in the measurement crucible, the peak is negative. The phase transition temperature was found at T=732 ± 5 K, in good agreement with Sugawara and Jin (2018) [15]. They used the phase transition temperature previously reported in the literature to give an average value of T=728 ± 4 K. The measured peaks areas for the first (A_1), second (A_2) and third cycles (A_3) and the experimental parameters are reported in **table 6.6**.

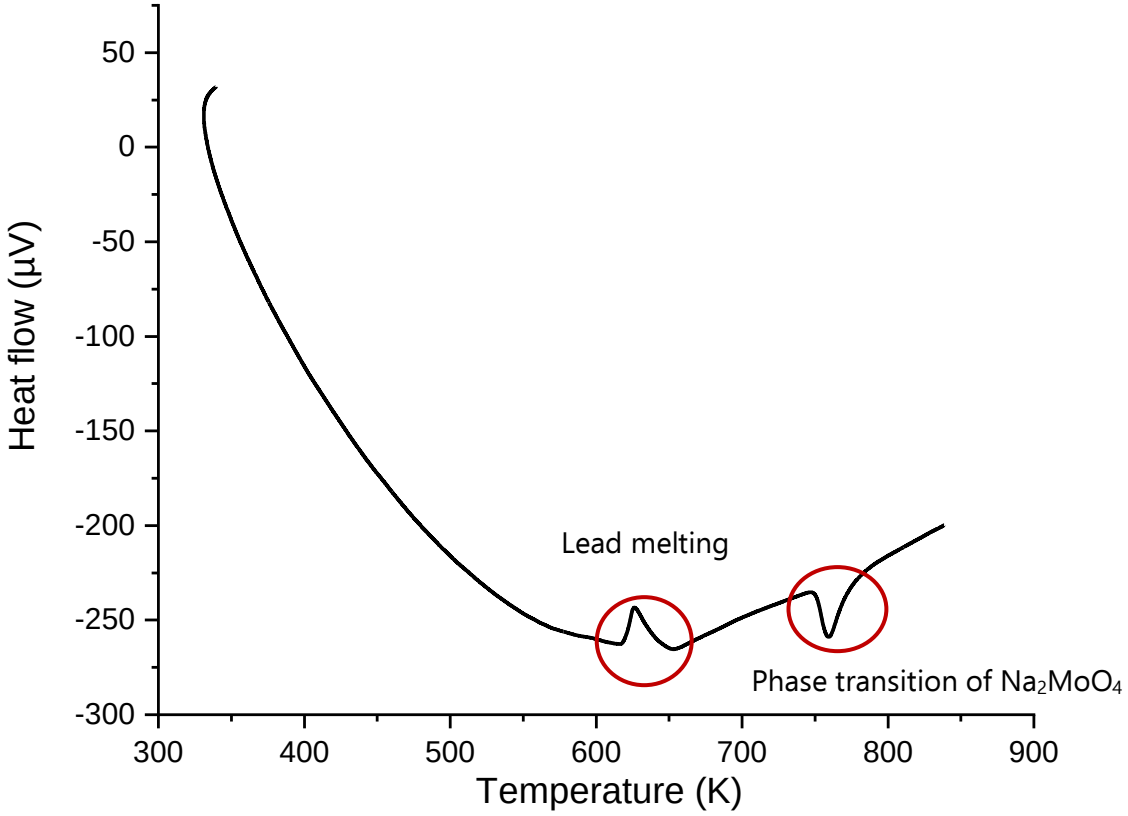

Figure 6.14: DSC measurement of Na_2MoO_4 with a lead sample used as reference. The first peak is the melting of the lead sample in the reference crucible. The second event is the allotropic transition of Na_2MoO_4.

Table 6.6: Raw data obtained after analysing DSC measurements of Na_2MoO_4

Compound	m (mg)	A_1 (µV.s)	A_2(µV.s)	A_3(µV.s)	M(g/mol)	ΔH(J/mol)
Pb	184.7(1)	1484	1366	1430	207.2	4773.9
Na_2MoO_4	70.7(1)	2855	2524	2541	205.9	-

Table 6.7: Comparison between the enthalpy of the first allotropic transition of Na_2MoO_4 measured in this work and the one suggested in the work of Sugawara and Jin (2018) [15]

Reference	ΔH(kJ/mol)
Cycle 1	23.8
Cycle 2	22.9
Cycle 3	22.0
This work	23 ± 1
Sugawara and Jin (2018) [15]	22.6 ± 0.5

The value obtained for the first allotropic transition enthalpy of Na_2MoO_4 is in good agreement with the value reported by Sugawara and Jin [15] in **table 6.7**. Therefore, we will use the same method for the quaternary compounds.

6.4.2. $Cs_3Na(MoO_4)_2$

For the $Cs_3Na(MoO_4)_2$ compound, the measurement was performed with lead in the reference crucible. The measured data (a single cycle in this case) and the heat flow curve are reported in **table 6.8** and in **figure 6.15**, respectively. From the measurements reported in section 6.2.1, the measured transition can be identified to correspond to the peritectic decomposition {$Cs_3Na(MoO_4)_2$ = Liq + Cs_2MoO_4}.

Table 6.8: Raw data obtained after analysing the DSC measurement of $Cs_3Na(MoO_4)_2$

Compound	m (mg)	A (µV.s)	M(g/mol)	ΔH(kJ/mol)
Pb	184.7	1407.3	207.2	4.77
$Cs_3Na(MoO_4)_2$	82.9	1466.9	741.6	39.7

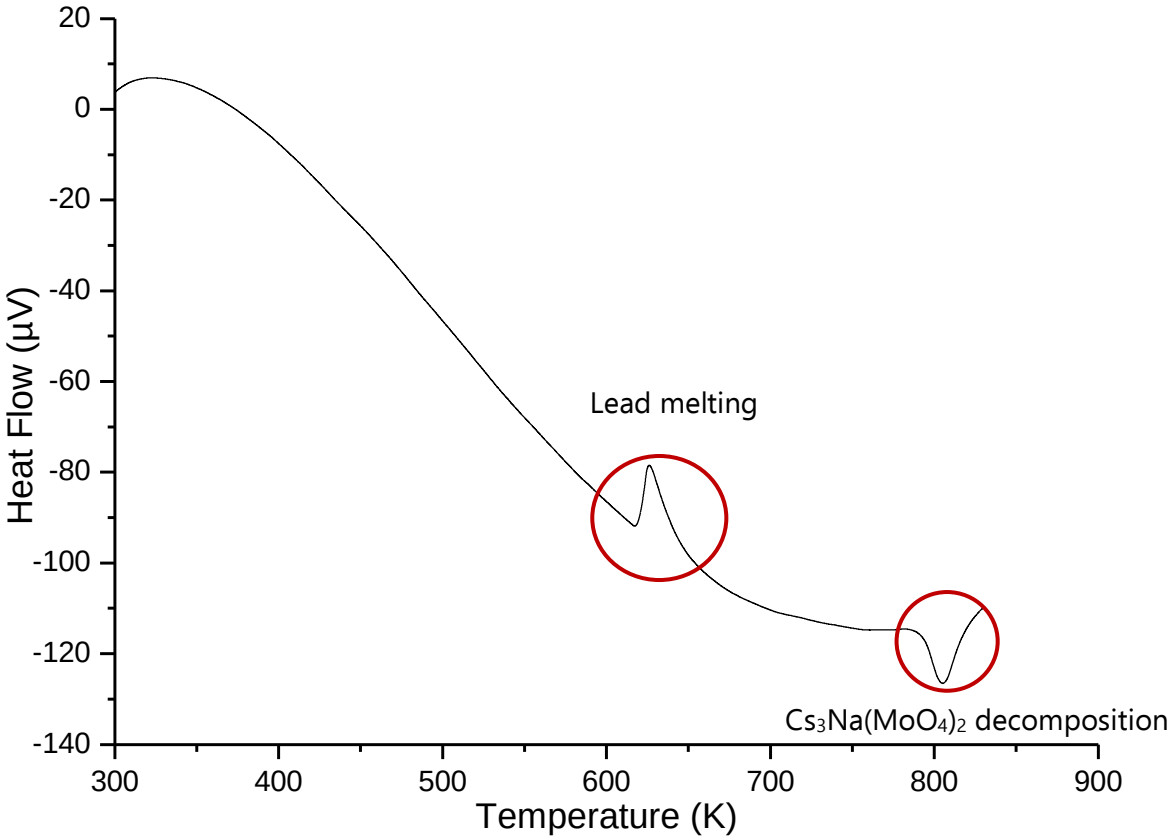

Figure 6.15: DSC measurement of $Cs_3Na(MoO_4)_2$ with a lead sample used as reference. The first peak is the melting of the lead sample in the reference crucible. The second event is the peritectic decomposition of $Cs_3Na(MoO_4)_2$.

From the data reported in **table 6.8**, one can calculate the enthalpy of the peritectic decomposition reaction of $Cs_3Na(MoO_4)_2$ using the surface of the peak of the sample and the reference. Only the first measurement cycle is reported and was used for the analysis, as in the subsequent cycles, two other phase transitions appeared (possibly associated with the phase transitions of (α-Na_2MoO_4 = β-Na_2MoO_4 and the Eutectic: { liquid = β-Na_2MoO_4 + $Cs_3Na(MoO_4)_2$}) due to an incomplete reverse transformation on cooling. This was also apparent from the decrease of the area of the peak representing the decomposition reaction.

More measurements are needed to improve the reliability of our first preliminary measurement and give an uncertainty on the reported data. Nevertheless, the melting temperature of the compound is 774 ± 5 K which is in good agreement with the results of Smith *et al.* [8] ($T_{melting}$ = 777 ± 5 K). Moreover, the experimental value for the enthalpy of the peritectic decomposition reaction, which is **39.7 kJ/mol** can be used as first approximation in the Calphad modelling of the Cs_2MoO_4-Na_2MoO_4 pseudo-binary system.

6.4.3. $CsNaMo_3O_{10}$

Following the same method as described above, the measurement of the melting temperature and the enthalpy of the observed transition of the pure sample of $CsNaMo_3O_{10}$ was performed (**Figure 6.16**). Aluminium was used as reference. Indeed, the melting temperature of aluminium was more suitable with respect to the transition temperature measured for this compound.

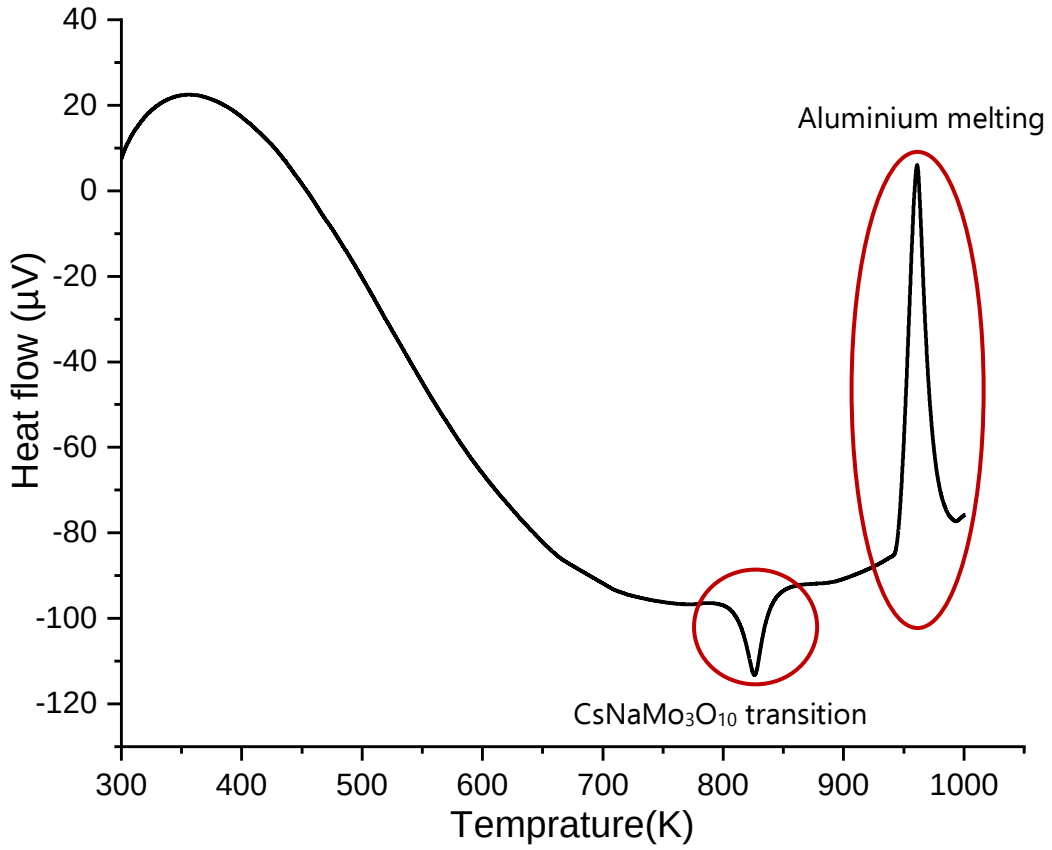

Figure 6.16: DSC measurement of $CsNaMo_3O_{10}$ with an aluminium sample used as reference. The first peak is the decomposition reaction of $CsNaMo_3O_{10}$. The second event is the melting of the aluminium sample in the reference crucible

Table 6.9: Raw data obtained after analysing the DSC measurement of $CsNaMo_3O_{10}$

Compound	m (mg)	A (µV.s)	M(g/mol)	ΔH(kJ/mol)
Al	92.5(1)	12939.8	27	10.711
$CsNaMo_3O_{10}$	72.8(1)	3522.8	603.8	82.9

As no XRD investigations could be performed after the DSC measurement or above the transition temperature, we assume here that the measured event corresponds to the decomposition reaction of $CsNaMo_3O_{10}$. However, the exact nature of the

decomposition reaction was not determined. The temperature of the decomposition reaction of $CsNaMo_3O_{10}$ obtained after analysing the DSC curves is **785 ± 5 K**.

From the data reported in **table 6.9** one can calculate the enthalpy of decomposition reaction for $CsNaMo_3O_{10}$ using the surface of the peaks for the sample and the aluminium reference. The measured transition enthalpy is **82.9 kJ/mol**. However, as for the $Cs_3Na(MoO_4)_2$ compound, only the first measurement cycle was taken into account. Indeed, the area of the peak was constantly decreasing at each new subsequent cycle for the compound (after 3 cycles the area of the peak was nearly divided by 2) whereas the one for the reference was constant. Therefore, to confirm this result and assign an uncertainty on the measured value, more thermodynamic measurements have to be performed on a fresh batch of this compound.

Even if more measurements should be performed to precisely assess the enthalpy of the decomposition reactions for both $Cs_3Na(MoO_4)_2$ and $CsNaMo_3O_{10}$, these preliminary results are useful data for the Calphad modelling of the Cs-Mo-Na-O system. Moreover, the temperature of the decomposition reaction for $CsNaMo_3O_{10}$ was assessed for the first time in this work. A post-characterisation using XRD and SEM would be extremely valuable to determine the nature of the observed transition.

6.5. Conclusion

In this chapter, structural and thermodynamic investigations of the Cs_2O-MoO_3-Na_2O system are presented.

The pseudo-binaries Cs_2O-MoO_3 and MoO_3-Na_2O are well known and have already been modelled with the Calphad method. For the Cs_2O-Na_2O system, no phase diagram data were found. However, it seems that no ternary compound exists in this system. The Cs_2MoO_4-Na_2MoO_4 pseudo-binary phase diagram was also studied by three different research groups. However, some discrepancies are found between the different studies, especially regarding the existence of the $Cs_3Na(MoO_4)_2$ compound. Thus, the pseudo-binary section has been re-investigated by DSC in the present work. A phase diagram for the Cs_2MoO_4-Na_2MoO_4 pseudo-binary system was proposed combining the two datasets coming from the literature and the newly measured data. Based on the proposed sketch of the phase diagram, a Calphad model was developed in this work as reported in Chapter 7. However, to accurately assess the co-existing phase fields, long thermal heat treatments followed by quenching tests and post-XRD characterisations should be performed.

In the literature review, two quaternary compounds were identified: $Cs_3Na(MoO_4)_2$ and $CsNaMo_3O_{10}$. The structure and thermodynamic data on the first quaternary compound

were previously measured. For $CsNaMo_3O_{10}$, the data reported are scarce. Therefore, a structural and thermodynamic investigation of this quaternary compound has been performed. The structure was refined in the *Pnma* space group like its isostructural compound $RbNaMo_3O_{10}$. The oxidation state of the molybdenum atom, which is +VI as expected from the theoretical formula, was confirmed by XANES measurements. Finally, as enough pure material was left for one DSC measurement, the temperature and transition enthalpy of the decomposition reaction of $CsNaMo_3O_{10}$ was measured. The same thermodynamic measurement was performed for $Cs_3Na(MoO_4)_2$. However, in both cases, only a single value could be determined. Therefore, the same measurement has to be repeated several times on a fresh batch to assess more precisely the enthalpies of decompositions for both quaternary compounds. Finally, thermal treatments below and above the decomposition temperature would give valuable information to identify the equilibrium reaction associated with the events observed. Nevertheless, even if the measured values are only preliminary results, they can be used as input in the Calphad modelling of the Cs-Mo-Na-O system.

REFERENCES

[1] T.N. Pham Thi, Caractérisation et modélisation du comportement thermodynamique du combustible RNR-Na sous irradiation, 2014.

[2] H.R. Hoekstra, The Cs_2MoO_4-MoO_3 system, Inorg. Nucl. Chem. Lett. 9 (1973) 1291–1301.

[3] NEA Nuclear Science Committee, Thermodynamics of Advanced Fuels - International Database (TAF-ID), https://www.oecd-nea.org/science/tafid/.

[4] R.G. Samuseva, R.M. Zharkova, V.E. Plyushchev, The Cs_2MoO_4-Na_2MoO_4 system, Russ. J. Inorg. Chem. 9 (1964) 1444.

[5] V.P. Zueva, A.N. Shabanova, T.I. Drobasheva, The Na_2MoO_4-Cs_2MoO_4-MoO_3 Ternary System, Zh Neorg Khim 3.

[6] G. Wallez, P.E. Raison, A.L. Smith, N. Clavier, N. Dacheux, High-temperature behavior of dicesium molybdate Cs_2MoO_4: Implications for fast neutron reactors, J. Solid State Chem. 215 (2014) 225–230.

[7] E.S. Zolotova, Z.A. Solodovnikova, V.N. Yudin, S.F. Solodovnikov, E.G. Khaikina, O.M. Basovich, I.V. Korolkov, I.Yu. Filatova, Phase relations in the Na_2MoO_4 –Cs_2MoO_4 and Na_2MoO_4 –Cs_2MoO_4 –$ZnMoO_4$ systems, crystal structures of $Cs_3Na(MoO_4)_2$ and $Cs_3NaZn_2(MoO_4)_4$, J. Solid State Chem. 233 (2016) 23–29.

[8] A.L. Smith, G. Kauric, L. van Eijck, K. Goubitz, N. Clavier, G. Wallez, R.J.M. Konings, Structural and thermodynamic study of $Cs_3Na(MoO_4)_2$: Margin to the safe operation of sodium cooled fast reactors, J. Solid State Chem. 269 (2019) 1–8.

[9] A.L. Smith, M.-C. Pignié, L. van Eijck, J.-C. Griveau, E. Colineau, R.J.M. Konings, Thermodynamic study of $Cs_3Na(MoO_4)_2$: Determination of the standard enthalpy of formation and standard entropy at 298.15 K, J. Chem. Thermodyn. 120 (2018) 205–216.

[10] A. Förster, H.U. Kreusler, J. Fuchs, Die kristallinen Phasen der Alkalitrimolybdate / The Crystallinic Phases of the Alkali Trimolybdates, Z. Für Naturforschung B. 40 (1985) 1139–1148.

[11] O. Beneš, R.J.M. Konings, S. Wurzer, M. Sierig, A. Dockendorf, A DSC study of the $NaNO_3$–KNO_3 system using an innovative encapsulation technique, Thermochim. Acta. 509 (2010) 62–66.

[12] W.J. Boettinger, U.R. Kattner, K.-W. Moon, J.H. Perepezko, CHAPTER FIVE - DTA AND HEAT-FLUX DSC MEASUREMENTS OF ALLOY MELTING AND FREEZING, in: J.-C. Zhao (Ed.), Methods Phase Diagr. Determ., Elsevier Science Ltd, Oxford, 2007: pp. 151–221.

[13] Shannon-Prewitt Effective Ionic Radius - Part 3 | The Elements Handbook at KnowledgeDoor, http://www.knowledgedoor.com/2/elements_handbook/shannon-prewitt_effective_ionic_radius_part_3.html.

[14] E. Epifano, A. Volfi, M. Abbink, H. Nieuwland, L. van Eijck, G. Wallez, D. Banerjee, P.M. Martin, A.L. Smith, Investigation of the $Cs_2(Mo,Te)O_4$ Solid Solution and Implications on the Joint Oxyde-Gaine System in Fast Neutron Reactors, Inorg. Chem. 59 (2020) 10172–10184.

[15] T. Sugawara, K. Jin, Enthalpy and heat capacity of Na_2MoO_4 and $CaMoO_4$, Thermochim. Acta. 669 (2018) 185–193.

Chapter 7:
Thermodynamic modelling

In this Chapter, the Gibbs energy models for the different phases are first presented. Then, the optimization procedure and the results on the thermodynamic modelling of the Ba-Na and Cs_2MoO_4-Na_2MoO_4 systems are discussed. Moreover, the modification of the Mo-O system model published by Corcoran *et al* [1] required for the assessment of the Cs_2MoO_4-Na_2MoO_4 system is also reported.

7.1. Gibbs energy models

The Thermo-Calc software was used for the assessment of the thermodynamic parameters [2].

The Compound Energy Formalism (CEF) [3] is the general model to describe many different kinds of solid, liquid and gas phases. In this formalism, the phases are described using sublattices corresponding to crystallographic sites on which elements or species (cations, anions, vacancies, molecules) are introduced. In the following section, the Gibbs energy models are described only for the phases existing in the Ba-Na, Mo-O and Cs_2MoO_4-Na_2MoO_4 systems.

7.1.1 Pure elements

The Gibbs energy functions ${}^{\circ}G_i^{\varphi}(T)$ of the pure elements i at temperature T, in the physical state φ are expressed as:

$${}^{\circ}G_i^{\varphi}(T) - {}^{\circ}H_i^{SER}(298.15\ K) = a + b.T + c.T.lnT + \sum_n d_n T^n \qquad (7.1)$$

where n is an integer (typical values of n are 2, 3, -1,...). The reference state is H_i^{SER}, the enthalpy of the stable state of i at 298.15 K and 10^5 Pa. In the present work, the Gibbs energy functions assessed by Dinsdale [4] were used for the pure elements.

7.1.2 Substitutional solutions

For the binary solid solutions with a single sublattice (A,B), the Gibbs energy $G^{\varphi}(T)$ is expressed as the sum of three terms:

$$G_m^{\varphi} - \sum_{i=A,B} x_i^{\varphi}\ {}^{\circ}H_i^{SER}(298.15\ K) = {}^{ref}G^{\varphi} + {}^{id}G^{\varphi} + {}^{ex}G^{\varphi} \qquad (7.2)$$

with

$${}^{ref}G^{\varphi} = \sum_{i=A,B} x_i^{\varphi}\ ({}^{\circ}G_i^{\varphi}(T) - {}^{\circ}H_i^{SER}(298.15\ K)) \qquad (7.3)$$

$${}^{id}G^{\varphi} = RT \sum_{i=A,B} x_i^{\varphi}\ lnx_i^{\varphi} \qquad (7.4)$$

$${}^{ex}G^{\varphi} = x_A^{\varphi} x_B^{\varphi} \sum_n L_{A,B}^n (x_A^{\varphi} - x_B^{\varphi})^n \qquad (7.5)$$

x_i^{φ} is the mole fraction of the element i in the phase φ.

${}^{ref}G^{\varphi}$ is the reference term which is the sum of the Gibbs energies of the pure elements in the phase φ.

${}^{id}G^{\varphi}$ is the ideal solution term corresponding to the configurational entropy term for the mixing of A and B.

${}^{ex}G^{\varphi}(T)$ is the excess Gibbs energy term expressed using the Redlich-Kister model reported in Redlisch and Kister [5] which $L_{A,B}^{n}$, the interaction parameter between the A and B elements can have a linear temperature dependence.

7.1.3 Stoichiometric compounds

The molar Gibbs energy function for the stoichiometric compounds is similar as for the pure elements:

$$^{\circ}G_m^{\varphi}(T) - \sum_i x_i^{\varphi}\, {}^{\circ}H_i^{SER}(298.15\ K) = a + b.T + c.T.lnT + \sum_n d_n T^n \qquad (7.6)$$

with x_i^{φ} representing the molar fraction of the element i in the compound φ.

When no heat capacity data is available on the compound, the Kopp-Neumann law is used and the Gibbs energy is expressed as:

$$^{\circ}G_m^{\varphi}(T) - \sum_i x_i^{\varphi}\, {}^{\circ}H_i^{SER}(298.15\ K) = a + b.T + \sum_n x_i^{\varphi}\ ({}^{\circ}G_i^{\varphi}\ (T) - {}^{\circ}H_i^{SER}(298.15\ K)) \quad (7.7)$$

where $^{\circ}G_i^{\varphi}(T)$ are the Gibbs energies of the pure elements. a and b are then the enthalpy and entropy of formation, respectively.

7.1.4 Non-stoichiometric solid compounds

The non-stoichiometric compounds exhibiting a composition range are generally modelled using several sublattices on which a single or several species are introduced.

In the present work, the species are either chemical elements or cations and/or anions (O^{2-}) for oxide phases.

As an example, for a phase with the formula $(A,B)_{\alpha}(C,D)_{\beta}$, the Gibbs energy is expressed as the sum of three terms:

$$^{\circ}G_m^{\varphi}(T) - \sum_i x_i^{\varphi}\, ^{\circ}H_i^{SER}(298.15\ K) = {}^{ref}G^{\varphi}(T) + {}^{id}G^{\varphi}(T) + {}^{ex}G^{\varphi}(T) \quad (7.8)$$

with

$$^{ref}G^{\varphi}(T) = y_A\ y_C\ ^{\circ}G_{A:C} + y_A\ y_D\ ^{\circ}G_{A:D} + y_B\ y_C\ ^{\circ}G_{B:C} + y_B\ y_D\ ^{\circ}G_{B:D} \quad (7.9)$$

where $^{\circ}G_{A:C}$, $^{\circ}G_{A:D}$, $^{\circ}G_{B:C}$, and $^{\circ}G_{B:D}$ are the Gibbs energies of the compounds $A_\alpha C_\beta$, $A_\alpha D_\beta$, $B_\alpha C_\beta$ and $B_\alpha D_\beta$, respectively.

The ideal Gibbs energy term is defined as:

$$^{id}G^{\varphi} = RT\left[\alpha\left(y_A\ lny_A\ + y_B\ lny_B\ \right) + \beta\ (y_C\ lny_C\ + y_D\ lny_D\ )\right] \quad (7.10)$$

Finally, interaction terms between (A and B) on the first sublattice and (C and D) on the second sublattice can be added to describe the excess Gibbs energy as follows:

$$^{ex}G^{\varphi} = \sum_{i=(C,D)} y_A\ y_B\ L^{\mathrm{n}}_{(A,B)(i)} + \sum_{i=(A,B)} y_C\ y_D\ L^{n}_{(i)(C,D)} \quad (7.11)$$

where y_i is the site fraction of the species i in either on the first or second sublattice.

7.1.5 Liquid

To describe the variation of the thermodynamic properties of a liquid from a metallic state to a liquid with a tendency for ionization (here, an oxide liquid), the partially ionic two sublattice model [6] is used in the present work to be consistent with the TAF-ID database [7,8]. The examples of the Ba-Na system (fully metallic), the Mo-O system (metal-oxide system) and the Cs_2MoO_4-Na_2MoO_4 system (fully oxide) are presented in the next section.

In this model, the first sublattice contains the cations ($C_i^{\nu_C}$) and the second one the anions ($A_j^{\nu_A}$), neutral species (B_k) and charged vacancies (Va^{Q-}):

$$(C_i^{\nu_i})_P\,(A_j^{\nu_j}\ ,\ B_k,\ Va^{Q-})_Q \quad (7.12)$$

where P and Q are the site numbers of the first and second sublattices defined as:

$$P = \sum_j \nu_j\, y_{Aj} + Q\ y_{Va} \quad (7.13)$$

$$Q = \sum_i \nu_i\, y_{Ci} \quad (7.14)$$

with ν_i, ν_j, the charges of the cations and anions, respectively. y_{Ci}, y_{Aj}, y_{Va} are the site fractions of the cations, anions and charged vacancies, respectively . The sum of the site fractions on each sublattice is unity.

In this model, the introduction of hypothetical vacancies Va^{Q-} with the charge Q- which varies with the composition allows maintaining the electroneutrality of the liquid phase.

The Gibbs energy of the liquid phase is expressed as:

$$G^{liq} = {}^{ref}G^{liq} + {}^{id}G^{liq} + {}^{ex}G^{liq} \tag{7.15}$$

$${}^{ref}G^{liq} = \sum_C \sum_A y_C y_A \, {}^\circ G^{liq}_{(C)(A)} + Q\, y_{Va} \sum_C y_C \, {}^\circ G^{liq}_C + Q \sum_B y_B \, {}^\circ G^{liq}_B \tag{7.16}$$

$${}^{id}G^{liq} = RT\left[P \sum_C y_C \ln y_C + Q\left(\sum_A y_A \ln y_A + y_{Va} \ln y_{Va} + \sum_B y_B \ln y_B \right)\right] \tag{7.17}$$

$$\begin{aligned} {}^{ex}G^{liq} = & \sum_{C_1}\sum_{C_2}\sum_A y_{C_1} y_{C_2} y_A L^{liq}_{(C_1,C_2)(A)} + \sum_{C_1}\sum_{C_2} y_{C_1} y_{C_2} y_{Va}^2 L^{liq}_{(C_1,C_2)(Va)} \\ & + \sum_C \sum_{A_1}\sum_{A_2} y_C y_{A_1} y_{A_2} L^{liq}_{(C)(A_1,A_2)} + \sum_C \sum_A y_C y_A y_{Va} L^{liq}_{(C)(A,Va)} \\ & + \sum_C \sum_A \sum_B y_C y_A y_B L^{liq}_{(C)(A,B)} + \sum_C \sum_B y_C y_B y_{Va} L^{liq}_{(C)(Va,B)} + \sum_{B_1}\sum_{B_2} y_{B_1} y_{B_2} L^{liq}_{(B_1,B_2)} \end{aligned} \tag{7.18}$$

In the reference term (Equation (7.15)), ${}^\circ G^{liq}_{(C)(A)}$ is the Gibbs energy of $(\nu_C + \nu_A)$ moles of liquid (C)ν_A(A)ν_C, ${}^\circ G^{liq}_C$ the Gibbs energy for the pure liquid element C and ${}^\circ G^{liq}_B$ the Gibbs energy of the liquid phase for the neutral species B.

The ideal term in Equation (7.17) corresponds to the random configurational entropy on each sublattice. In the excess term (Equation 7.18), the L parameters represent the interactions between the different species in each sublattice. The comas separate species interacting in the same sublattice.

7.1.6 Gas

The gas is described as an ideal mixture of the gaseous species.

The Gibbs energy is expressed as follows:

$$G^{gas} = \sum_i y_i \left[{}^\circ G^{gas}_i - \sum_j b_{ij} H^{SER}_j + RT \ln y_i \right] + RT \ln\left(\frac{p}{p_0} \right) \tag{7.20}$$

where y_i are the constituent fractions of the species *i*. b_{ij} is the number of atoms *j* in the species *i*. The standard pressure p_0 is 10^5 Pa. The partial pressure of species *i* p_i is related to the constituent fraction by: $p_i = y_i\, p$ where p is the total pressure.

The Gibbs energy functions ${}^\circ G^{gas}_i$ of the gaseous species (for one formula) come from the SGTE Substance Database Version 2.

7.2. Optimisation procedure and results

The optimisation procedure of the variables entering the Gibbs energy functions of the phases was performed using the Thermo-Calc software [9] For each system, the experimental data selected for the assessments are listed and the fitted parameters are given. Finally, a comparison with the experimental data is presented.

7.2.1 The Ba-Na system

The first study of the Ba-Na system was reported by Kanda *et al.* [10]. Thermal analysis, Differential Thermal Analysis (DTA) and X-ray diffraction techniques were used.

The authors reported the existence of the two compounds Na_4Ba and NaBa, based on the XRD results after thermal treatment in the different phase fields. Nevertheless, the structure and composition of both compounds were not assessed in this work. Indeed, only the X-ray powder reflections without intensities of the supposed compounds were reported.

Moreover, a solubility of sodium into the NaBa phase was found showing that this phase exhibits a wide composition range. Finally, the authors reported a peritectoid decomposition of Na_4Ba and an incongruent melting of NaBa as reported in **figure 7.1**.

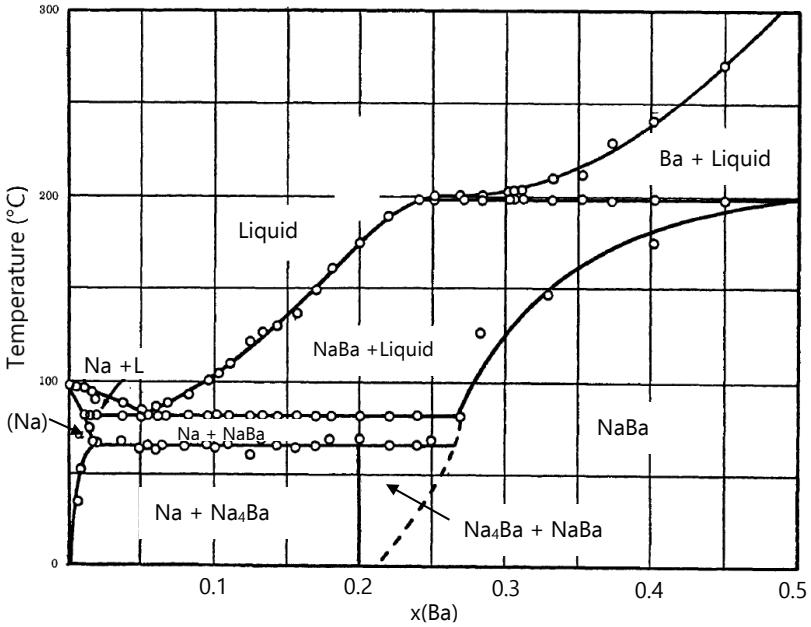

Figure 7.1: Phase diagram data reported by Kanda *et al.* [10] on the Ba-Na system

Addison *et al.* [11] reinvestigated the Ba-Na system by electrical resistivity measurements (**figure 7.2**). Nevertheless, the phases involved in the detected transitions were not characterised. As shown in **figure 7.2,** the reported phase diagram is different from the one proposed by Kanda *et al.* [10]. Moreover, the results of

Addison *et al.* [11] are not consistent with a large sodium solubility in the NaBa compound as reported by Kanda *et al.* [10].

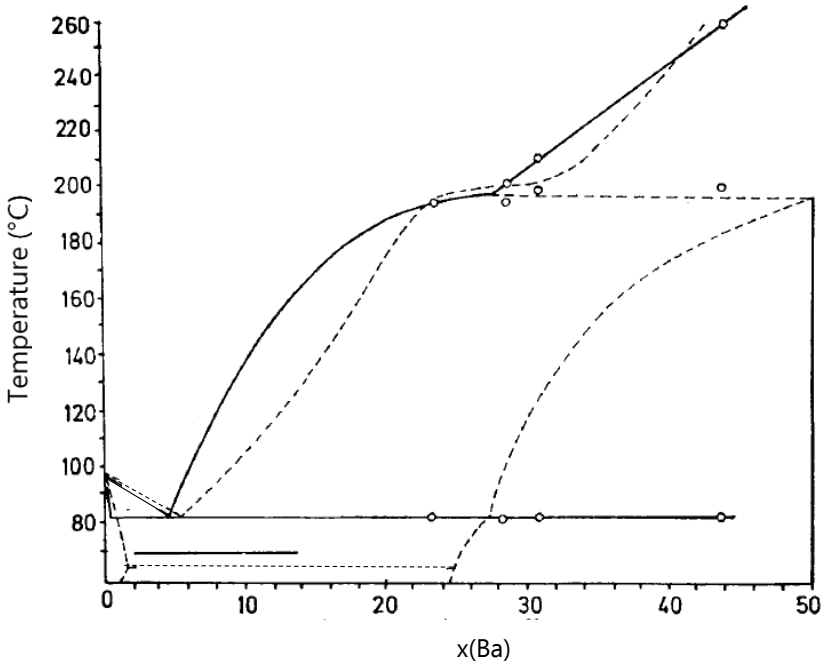

Figure 7.2: Phase diagram data reported by Addison *et al.* [11] on the Ba-Na system. The dotted lines correspond to the phase boundaries proposed by Kanda *et al* [10].

Based on the review of the data reported by Kanda *et al.* [10] and Addison *et al.* [11], Pelton [12] proposed the phase diagram in **figure 7.3**. Pelton selected the data of Addison *et al.* [11] for the liquidus in the 10-50 at.% Ba region, due to the higher accuracy of the electrical resistivity results. Nevertheless, the solubility of sodium in the NaBa phase reported in the work of Kanda *et al* [10] was considered with a large uncertainty (dotted line).

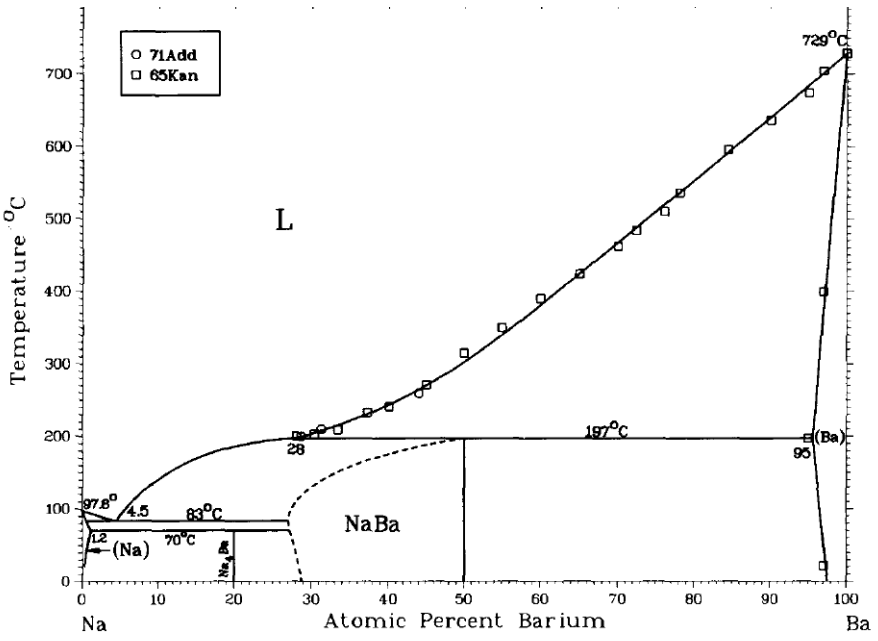

Figure 7.3: Na-Ba phase diagram reported by Pelton [12]

In the recent reinvestigation of the intermetallic compounds existing in the Ba-Na system by Snyder and Simon [13,14], all binary compounds reported in the literature were thoroughly investigated. Only NaBa and Na_2Ba compounds were observed and the structure refined by single crystal X-ray diffraction.

Moreover, the Na_4Ba compound reported in the works of Kanda et al [10], Addison et al [11] and Pelton [12] was finally reattributed to Na_2Ba as the reported XRD pattern by Kanda *et al.* [10] was matching with the Na_2Ba structure. This phase crystallises as a Laves phase in space group $P6_3/mmc$ [13].

The NaBa compound was refined in cubic symmetry in space group $Fd\bar{3}m$ and no sodium solubility into the NaBa structure was observed [14].

In the present assessment of the Ba-Na system, the phase diagram data of Kanda *et al.* [10] and Addison *et al.* [11] are used. Nevertheless, in the 10-50 at. % Ba region, the data of Addison *et al.* [11] are selected due to the high sensitivity of the electrical resistivity measurements. Moreover, no sodium solubility was introduced in NaBa, considered as a stoichiometric compound. Finally, the Na_4Ba mentioned in the studies of Kanda *et al.* [10] and Addison *et al.* [11] was reattributed to Na_2Ba with the Laves structure after the structural characterisation of Snyder and Simon [13].

The thermodynamic parameters of the phases are reported in **table 7.1**.

Table 7.1: Assessed parameters for the Ba-Na system

Phase	Parameters (J.mol^{-1})	Reference
Liquid $(Na^+,Ba^{2+})(Va^{Q-})$	${}^\circ G^{\mathrm{Liq}}_{Ba^{2+}:Va^{Q-}}$ - ${}^\circ H^{SER}_{Ba}$ = ${}^\circ G^{\mathrm{Liq}}_{Ba}$	SGTE [4]
	${}^\circ G^{\mathrm{Liq}}_{Na^+:Va^{Q-}}$ - ${}^\circ H^{SER}_{Na}$ = ${}^\circ G^{\mathrm{Liq}}_{Na}$	SGTE [4]
BCC phase (Ba,Na)(Va)	${}^\circ G^{BCC}_{Ba}$ - ${}^\circ H^{SER}_{Ba}$ = ${}^\circ G^{SER}_{Ba}$	SGTE [4]
	${}^\circ G^{BCC}_{Na}$ - ${}^\circ H^{SER}_{Na}$ = ${}^\circ G^{SER}_{Na}$	SGTE [4]
	$L^{0,\mathrm{BCC}}_{Na,Ba}$ = -8964.7 + 47.0287 ·T	This work
	$L^{1,\mathrm{BCC}}_{Na,Ba}$ = +3913.3 - 17.6479 ·T	This work
NaBa $(Na)_1(Ba)_1$	$G_{Na:Ba}$ = ${}^\circ G^{SER}_{Ba}$ + ${}^\circ G^{SER}_{Na}$ -10450 +17.3216 ·T	This work
Na_2Ba $(Na)_2(Ba)$	$G^{\mathrm{C14\_Laves}}_{Na:Ba}$ = ${}^\circ G^{SER}_{Ba}$ +2 ${}^\circ G^{SER}_{Na}$ -24013.8 + 57.1370 ·T	This work

The calculated phase diagram is compared with the experimental data in **figure 7.4 (a)** with a focus on the Na-NaBa region in **figure 7.4(b)**. At high barium content, a good agreement is obtained between the calculated phase diagram and the experimental solidus and liquidus data of Kanda *et al.* [10]. Nevertheless, for x(Ba)<0.3, the inflexion point in the liquidus curve reported by Kanda *et al.* [10] is not reproduced by our calculations. In this region, the calculated phase diagram is in good agreement with

the data of Addison *et al.* [11]. However, it is worth noting that the shape of the liquidus reported by Kanda *et al.* [10] is extremely peculiar.

The present model is the first assessment of the Ba-Na system, which was the only missing binary sub-system for the binary systems (Na-fission products).

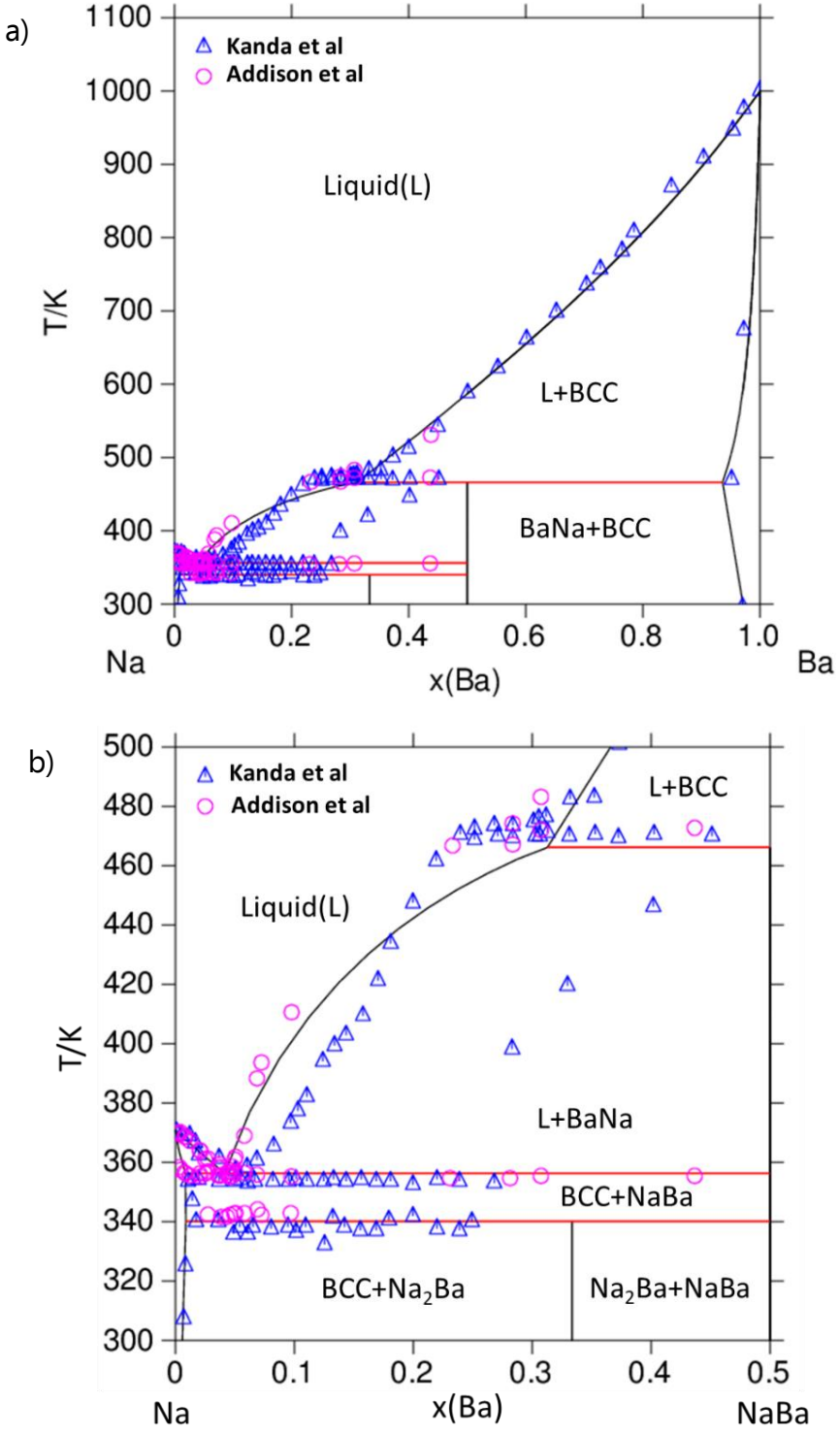

Figure 7.4: a) Calculated Ba-Na phase diagram at 1 bar and comparison with the experimental data reported by △ Kanda *et al.* [10] and ○ Addison *et al.* [11]. In b) the calculated Na-NaBa section is represented

7.2.2 The Mo-O system

The Calphad model of Corcoran *et al.* [1] is considered in the TAF-ID database.

Nevertheless, using this model, the calculated diagrams for the Na_2O-MoO_3, Cs_2O-MoO_3 and BaO-MoO_3 pseudo-binary systems exhibit a small miscibility gap in the liquid phase very close to the MoO_3 end-member, as shown in **figure 7.5** for the Cs_2O-MoO_3 system.

In the work of Corcoran *et al.* [1], the liquid phase was modelled using the sublattice model $(Mo^{4+})_P(MoO_4^{2-},O^{2-},Va,MoO_3,O)_Q$. The MoO_4^{2-} species was introduced in the second sublattice to describe the melting of the ternary compounds Na_2MoO_4, Cs_2MoO_4 and $BaMoO_4$ described by the end-members $(Na^+)_2(MoO_4^{2-})_1$, $(Cs^+)_2(MoO_4^{2-})_1$ and $(Ba^{2+})_1(MoO_4^{2-})_1$, respectively.

The origin of the miscibility gap formation in the liquid state was attributed to the Gibbs energy parameter for the $(Mo^{4+})_2(MoO_4^{2-})_4$ end-member (**see table 7.2**). The very large value for this parameter makes this MoO_4^{2-} species much unstable in the Mo-O binary system. On the contrary, this species is very stable in the ternary systems where the ternary compounds form. Thus, we found out that the very large difference in the concentration of this species between the Mo-O binary and ternary systems causes the miscibility gap formation.

To solve this problem, the parameters of the liquid phase in the Mo-O system have been slightly modified. The new parameters are listed in **table 7.2**. The most important parameter $G^{\mathrm{Liq}}_{Mo^{4+}:MoO_4^{2-}}$ was fixed to a lower positive value $(6\ G^{\mathrm{Liq}}_{MoO_3} - 2\ {}^{\circ}G^{\mathrm{SER}}_{O_2} + 195000)$ instead of $(6\ G^{\mathrm{Liq}}_{MoO_3} - 2\ {}^{\circ}G^{\mathrm{SER}}_{O_2} + 1000000)$ in [1].

This change prevented a too large difference in the stability of the MoO_4^{2-} species between the binary and ternary systems. Other parameters were slightly modified to maintain a good agreement between the calculated and experimental phase diagram data.

The calculated Mo-O phase diagram is presented in **figure 7.5** with a comparison to the experimental data. A good agreement is obtained in the Mo-MoO_2 region where only a few experimental data are available.

A zoom is presented in **figure 7.5 b)** in the composition range 0.73< x(O) <0.76. The calculations reproduce also very well the phase equilibria in this region.

The Cs_2O-MoO_3 and Na_2O-MoO_3 diagrams calculated with this modified model are shown in **figure 7.6** and **7.7**. Thanks to the new parameters of the liquid phase in Mo-O, without any other change of the parameters, the unexpected miscibility gap in the region close to MoO_3 was successfully suppressed.

Table 7.2: Modified parameters for the liquid phase of the Mo-O system

Phase	Parameters (J.mol^{-1})	Phase
Liquid $(Mo^{4+})_P(MoO_4^{2-},O^{2-},Va,MoO_3,O)_Q$	$G^{Liq}_{Mo^{4+}:O^{2-}} = 2\,(^{\circ}G^{Liq}_{Mo} + 2.\,^{\circ}G^{Liq}_{O})$	Corcoran *et al.* [1]
	$G^{Liq}_{Mo^{4+}:MoO_4^{2-}} = 6\,G^{Liq}_{MoO_3} - 2\,^{\circ}G^{SER}_{O_2} + 195000$	This work
	$G^{Liq}_{Mo^{4+}:Va} = {}^{\circ}G^{Liq}_{Mo}$	SGTE [4]
	$G^{Liq}_{MoO_3} = +48443\text{-}45.05*T+G(MoO_3)$	This work
	$G^{Liq}_{O} = {}^{\circ}G^{Liq}_{O}$	SGTE [4]
	$L^{0}_{MoO_3,O} = +20000$	This work

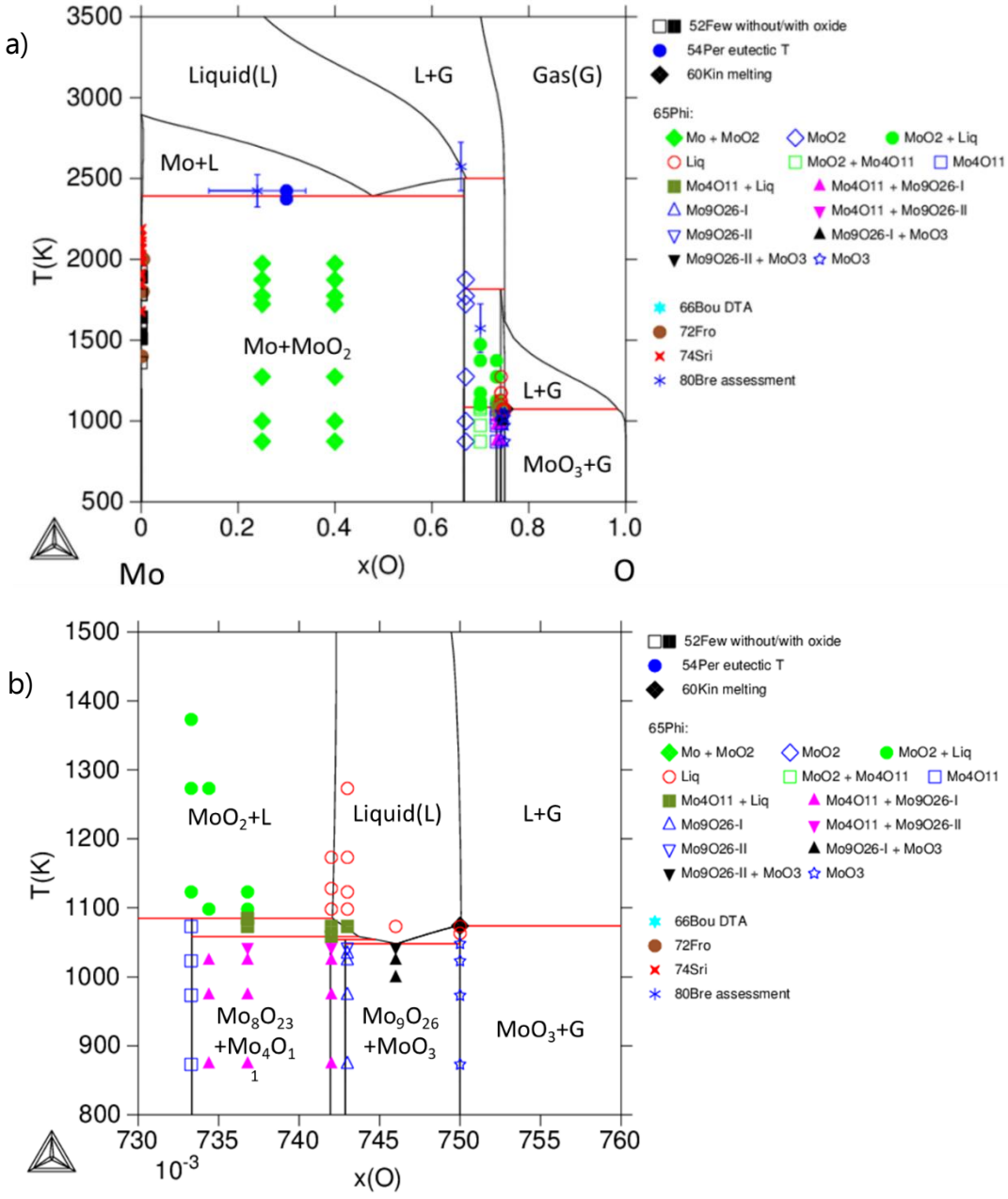

Figure 7.5: a) Calculated Mo-O phase diagram with the modified Mo-O database. In b) a focus on the section 0.73<x(O)<0.76 and 800 < T< 1500K

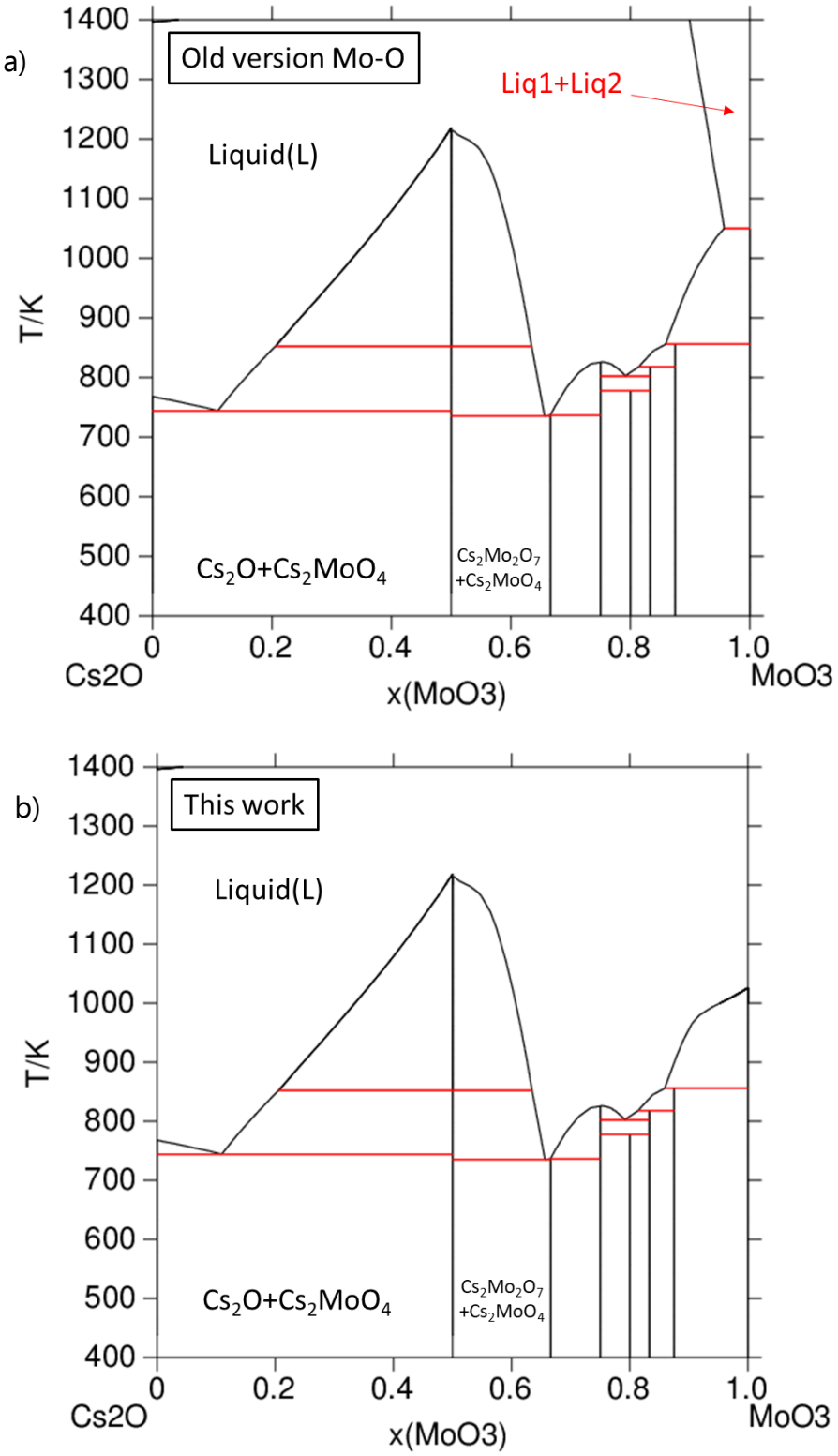

Figure 7.6: a) Calculated Cs_2O-MoO_3 phase diagram with the Mo-O parameters reported by Corcoran et al. where a miscibility gap is clearly identified in red by Liq1+Liq2. In b) the calculated Cs_2O-MoO_3 phase diagram with the Mo-O database modified in this work is represented.

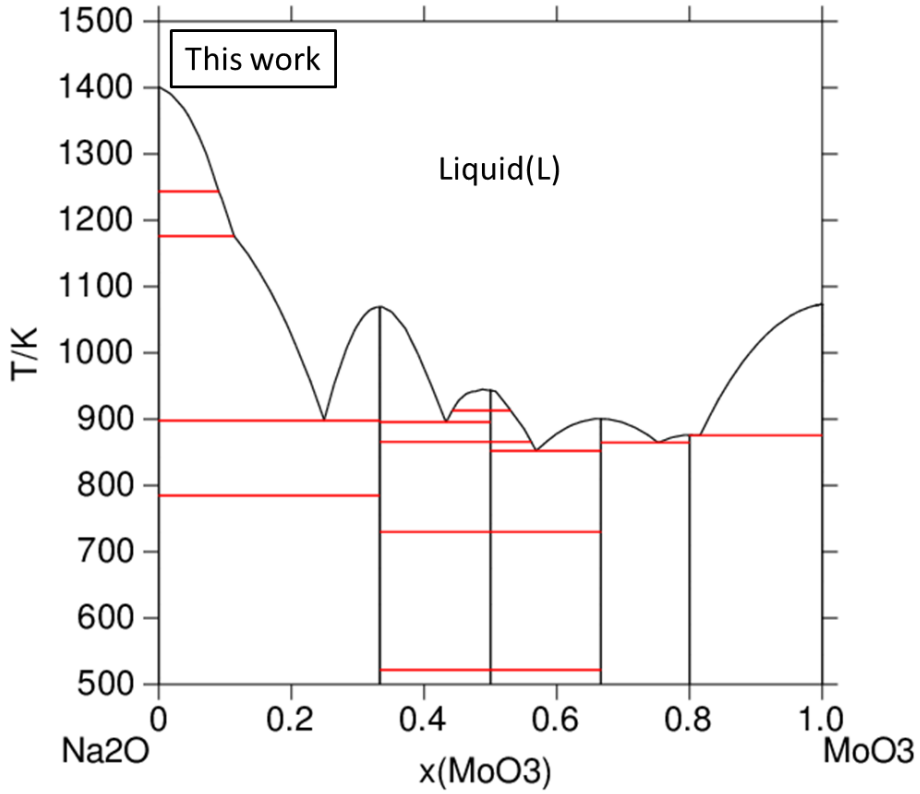

Figure 7.7: Calculated Na_2O-MoO_3 phase diagram at $PO_2=10^{-6}$ bar with the modified Mo-O database

This modified database on Mo-O was used to develop the model on the Cs-Mo-Na-O system.

The thermodynamic modelling of the Cs_2MoO_4-Na_2MoO_4 system is presented in the next section.

7.2.3. The Cs_2MoO_4-Na_2MoO_4 pseudo binary system

As described in Chapter 6, the thermodynamic properties of Cs_2MoO_4 and Na_2MoO_4 are known and Calphad models were developed for the Cs_2MoO_4-MoO_3 and Na_2O-MoO_3 sections. Therefore, the thermodynamic parameters for Cs_2MoO_4 and Na_2MoO_4 are taken from these works.

For the Cs_2MoO_4-Na_2MoO_4 section, the phase diagram data of Samuseva *et al.* [15], Zolotova *et al.* [16] and the phase diagram data measured in this work (see Chapter 6, section 6.2.1.) are considered.

The solubility of cesium into Na_2MoO_4 found by Samuseva *et al.* [15] is not considered in the modelling as no solubility was reported by Zolotova *et al.* [16] nor observed in the present experimental work.

At low temperature, the calculated allotropic transition α-Na_2MoO_4 → α'-Na_2MoO_4 at 514 K was not observed experimentally in the section Cs_2MoO_4-Na_2MoO_4. It could be

explained by the fact that it was already challenging to detect it on a pure sample of Na_2MoO_4 and the low value of the enthalpy of the phase transition (2961 J/mol).

Zolotova *et al.* [16] reported the existence of the quaternary compound $Cs_3NaMo_2O_8$ ($x(Na_2MoO_4) = 0.25$) characterised by XRD after thermal treatment. No noticeable interaction between Na_2MoO_4 and Cs_2MoO_4 was detected below 523 K. A phase transition at 663 K has been detected which was attributed to a minor unclear structural change in the structure of the compound.

In the investigation of the $Cs_3NaMO_2O_8$ by Smith *et al.* [17], the compound was synthesised at 723 K in a stainless steel container under argon. After cooling down to room temperature, the compound $Cs_3NaMo_2O_8$ was obtained as a single phase whose structure was thoroughly characterised. Smith *et al.* [17] did not observe any allotropic phase transition for the compound. Moreover, from the thermodynamic measurements, it was deduced that the compound is not stable at room temperature in agreement with the study of Zolotova *et al.* [16].

Therefore, in this work, the phase transition reported by Zolotova *et al.* [16] at 663 K was attributed to the temperature of formation of the $Cs_3NaMo_2O_8$, which is assumed irreversible as the compound has been obtained pure at room temperature by Smith *et al.* [17]. Indeed, the formation reaction on mixtures of Na_2MoO_4-Cs_2MoO_4 would be observed whereas it would not on $Cs_3NaMo_2O_8$ batch.

Moreover, the enthalpy of the peritectic decomposition was measured in the present work (Chapter 6). All these data were used to assess the Gibbs energy of the $Cs_3NaMo_2O_8$ compound.

The sodium solubility in o-Cs_2MoO_4 and h-Cs_2MoO_4 suggested by Samuseva *et al* [15], Zolotova *et al.* [16] and the data measured in this work (see Chapter 6, section 6.2.1) was also considered in the present modelling.

Zolotova *et al.* [16] also reported the existence of a very small miscibility gap in the liquid state. However, this miscibility gap has never been evidenced so it is not taken into account in the present work. Instead, an eutectic reaction equilibrium {Liquid = $Cs_3NaMo_2O_8$ + β-Na_2MoO_4} is assumed to exist in agreement with the works of Samuseva *et al*. [15] and Zueva *et al*. [18].

The parameters assessed for the liquid, the $(Cs,Na)_2(Mo)O_4$ oxide and the quaternary compound $Cs_3NaMo_2O_8$ are listed in **table 7.3**.

The calculated phase diagram is presented in **figure 7.8** and compared to the experimental data of Samuseva *et al* [15], Zolotova *et al.* [16] and the one reported in this work Chapter 6, section 6.2.1)

Table 7.3: Assessed parameters for the Cs_2MoO_4-Na_2MoO_4 system

Phase	Parameters (J.mol^{-1})	Reference
Liquid $(Cs^+, Na^+)_P(MoO_4^{2-})_Q$	$G^{Liq}_{Cs^+:MoO_4^{2-}} = G_{Cs_2MoO_4}$ +36400-31.5 * T	TAF-ID [7]
	$G^{Liq}_{Na^+:MoO_4^{2-}} = -1509762.65 + 650.522858 * T + 106629.667 - 586.502955 * T - 43.108388 * T * Ln(T) - 0.078693083 * T^2 + 3.7652355.10^{-6} * T^3 + 200011.21 * T^{-1}$	Bordier [19]
	$L^0_{Cs^+,Na^+:MoO_4^{2-}} = -5000$	This work
o-$(Cs,Na)_2MoO_4$	$G_{Cs:Mo:O} = G_{Cs_2MoO_4}$ $G_{Cs_2MoO_4}$ = -1550000 + 446.5 * T −95.9182 * T * Ln(T) − 0.0941112 * T^2 +1.1719.10^{-5} * T^3 + 47736 * T^{-1} $G_{Na:Mo:O} = G_{Na_2MoO_4}$ +10000 $L^0_{Cs,Na:Mo:O} = +38000$	This work
h-$(Cs,Na)_2MoO_4$	$G_{Cs:Mo:O} = G_{Cs_2MoO_4}$ +4600-5.4*T $G_{Na:Mo:O} = G_{Na_2MoO_4}$ +10000 $L^0_{Cs,Na:Mo:O} = +29000 - 5 * T$	This work
$Cs_3NaMo_2O_8$ $(Cs)_3(Na)_1(Mo)_2(O)_8$	$G_{Cs:Na:Mo:O}$ =+6000+52*T-9.5*T*ln(T) +1.5* $G_{Cs_2MoO_4}$ +0.5*$G_{Na_2MoO_4}$	This work
α-Na_2MoO_4	$G_{Na:Mo:O} = G_{Na_2MoO_4}$ $G_{Na_2MoO_4}$ =-1509762.65 + 650.522858*T -114.020329*T*ln(T)-0.0584679345*T^2 +3.54592662.10^{-6}*T^3 + 301434.612*T^{-1}	Bordier [19]
α'-Na_2MoO_4	$G_{Na:Mo:O}$ = -1512723.44+ 649.339278*T -113.75051*T*ln(T) - 0.0564448717*T^2 + 2.49064359.10^{-6}*T^3 +1499998.61*T^{-1}	Bordier [19]
β-Na_2MoO_4	$G_{Na:Mo:O}$ = -1491051.98+670.1554399*T -121.909124*T*ln(T) - 0.0485493486*T^2 + 2.10^{-6}*T^3+319488.393*T^{-1}	Bordier [19]
γ-Na_2MoO_4	$G_{Na:Mo:O}$ = -1486200.16+622.540518*T -114.997568*T*ln(T)-0.0541853163*T^2 +2.2002098.10^{-6}*T^3 +314985.929*T^{-1}	Bordier [19]
δ-Na_2MoO_4	$G_{Na:Mo:O}$ = -1484128.25+661.9268294*T -120.864165*T·ln(T)-0.0565458881*T^2 +2.79976941E-6*T^3 +307328.295*T^{-1}	Bordier [19]

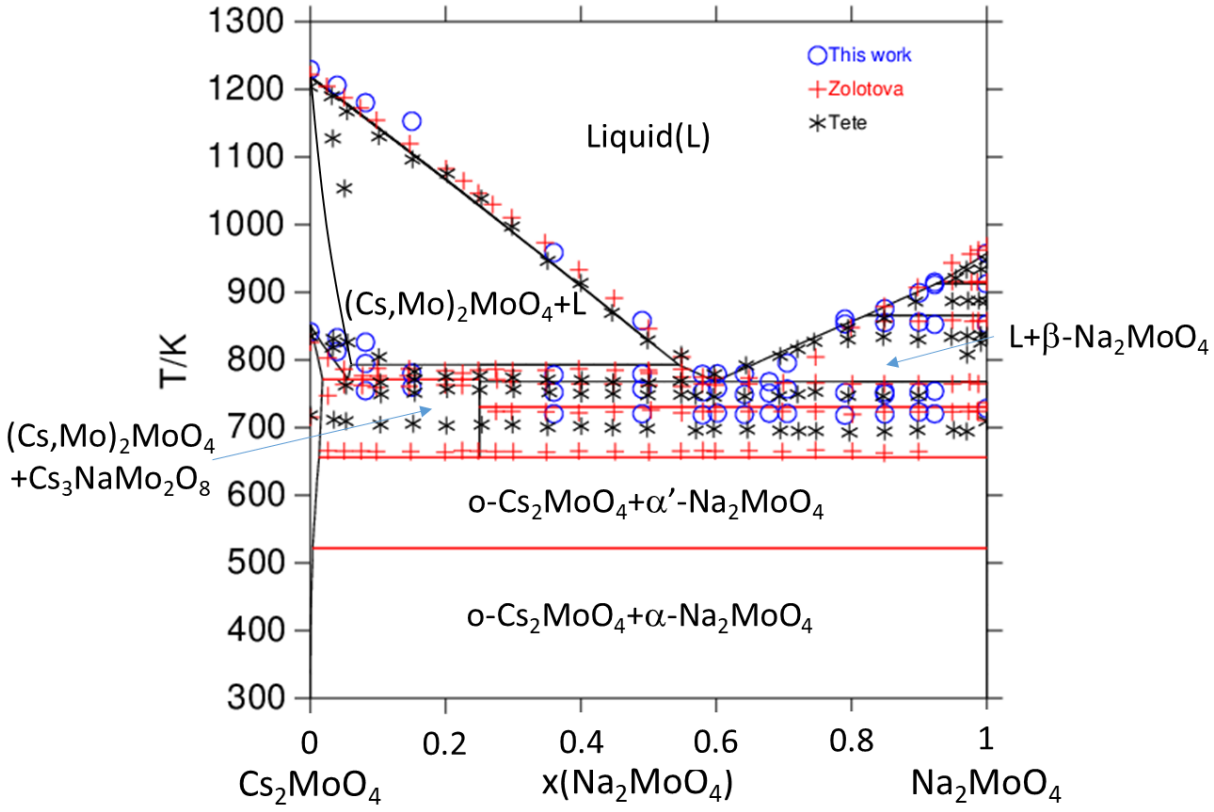

Figure 7.8: Calculated Cs_2MoO_4-Na_2MoO_4 phase diagram at $PO_2=10^{-7}$ bar

As shown in **table 7.4** and **7.5**, the calculated thermodynamic data on $Cs_3NaMo_2O_8$ are in good agreement with the experimental data within the experimental uncertainties. The enthalpy of the peritectic decomposition is also well represented by the model (**table 7.6**).

Table 7.4: Calculated and experimental thermodynamic data on the $Cs_3NaMo_2O_8$ compound.

Reaction	$\Delta_r H_m^0(298.15\ K)$ /kJ.mol^{-1}	$\Delta_r G_m^0(298.15\ K)$ /kJ.mol^{-1}	Reference
3 Cs(cr) +Na(cr) + 2 Mo(cr) + 4 O_2(g)= $Cs_3NaMo_2O_8$ (cr)	-2998.6 ± 2.9	-2784.7 ± 3.2	Smith *et al.* [17]
	-2995.5	-3133.0	This work
3/2 Cs_2O(cr) + 1/2Na_2O(cr) + 2 MoO_3(cr) = $Cs_3NaMo_2O_8$ (cr)	-780.6 ± 5.9	-796.7 ± 6.3	Smith *et al.* [17]
	779.8	-794.1	This work
3/2 Cs_2MoO_4(cr) + 1/2Na_2MoO_4(cr) = $Cs_3NaMo_2O_8$ (cr)	6.8 ± 3.7	2.3 ± 4.2	Smith *et al.* [17]
	6.4	4.7	This work

Table 7.5: Comparison between the thermodynamic data of $Cs_3NaMo_2O_8$ reported by Smith *et al.* [17] and the calculated ones with the Calphad model

Thermodynamic values of $Cs_3NaMo_2O_8$	Smith *et al.* [17]	This work
$C_{p,m}^0(298.15\ K)$ /kJ.mol^{-1}	296.3 ± 3.3	296.7
$S_m^0(298.15\ K)$ /J.K^{-1}.mol^{-1}	467.2 ± 6.8	461.0

Table 7.6: Comparison between the enthalpy of the peritectic decomposition of $Cs_3NaMo_2O_8$ measured in Chapter 6 and the calculated with the Calphad model

Peritectic decomposition reaction	H_{exp}/kJ.mol^{-1}	H_{calc}/kJ.mol^{-1}	Ref
$Cs_3NaMo_2O_8$ = Liquid + Cs_2MoO_4	39.7	33.2	This work

The calculated invariant reactions are in very good agreement with the experimental data of Zolotova *et al* [16] and of the present work.

The calculated solubility of sodium in o-Cs_2MoO_4 and h-Cs_2MoO_4 is underestimated by our model compared to the few experimental data. However, new measurements are required to better characterise this region of the phase diagram.

Finally, the calculated liquidus data and the eutectic reaction {Liquid = $Cs_3NaMo_2O_8$ + β-Na_2MoO_4} are in good agreement with the measured phase transitions.

7.3. Conclusion

The thermodynamic models of the Ba-Na and Cs_2MoO_4-Na_2MoO_4 systems were developed for the first time. A very good agreement with the available experimental data was obtained.

Nevertheless, for the Cs_2MoO_4-Na_2MoO_4 system, complementary studies using thermal treatments and XRD characterisation, above and under the $Cs_3NaMo_2O_8$ supposed formation temperature, in the miscibility gap region suggested by Zolotova *et al.* and in the Cs_2MoO_4 rich corner would be useful to improve the present model.

For the Ba-Na system, measurements or calculations of the thermodynamic properties of the compounds Na_2Ba and NaBa would also be very useful to improve the model.

The problem of the formation of an unexpected miscibility gap in the Mo-O system was fixed by modifying the parameters of the liquid phase. This is very important as Mo-O is a key binary sub-system to model the high order Ba-Cs-Mo-Na-O systems.

These models together with those published in the literature (see Chapter 2) were introduced in a database file which constitutes the starting point for the development of a database on the Na-fission product systems.

In a next step, the Ba-Mo-Na-O quaternary system could be assessed as all the binary sub-systems are now modelled.

REFERENCES

[1] E.C. Corcoran, J.-L. Flèche, N. Dupin, B. Sundman, C. Guéneau, Thermodynamic investigations of the uranium-molybdenum-oxygen system by a coupling of density functional theory and CALPHAD methodologies, Calphad. 63 (2018) 196–211.

[2] B. Sundman, B. Jansson, J.-O. Andersson, The Thermo-Calc databank system, Calphad. 9 (1985) 153–190. https://doi.org/10.1016/0364-5916(85)90021-5.

[3] B. Sundman, J. Ågren, A regular solution model for phases with several components and sublattices, suitable for computer applications, J. Phys. Chem. Solids. 42 (1981) 297–301.

[4] A.T. Dinsdale, SGTE data for pure elements, Calphad. 15 (1991) 317–425.

[5] O. Redlich, A.T. Kister, Algebraic Representation of Thermodynamic Properties and the Classification of Solutions, Ind. Eng. Chem. 40 (1948) 345–348. https://doi.org/10.1021/ie50458a036.

[6] M. Hillert, B. Jansson, B. Sundman, J. Gren, A two-sublattice model for molten solutions with different tendency for ionization, Metall. Trans. A, 6.

[7] NEA Nuclear Science Committee, Thermodynamics of Advanced Fuels - International Database (TAF-ID), https://www.oecd-nea.org/science/tafid/.

[8] C. Guéneau, N. Dupin, B. Sundman, C. Martial, J.-C. Dumas, S. Gossé, S. Chatain, F.D. Bruycker, D. Manara, R.J.M. Konings, Thermodynamic modelling of advanced oxide and carbide nuclear fuels: Description of the U–Pu–O–C systems, J. Nucl. Mater. 419 (2011).

[9] Thermo-Calc Software - Computational Materials Engineering. https://www.thermocalc.com/ (accessed September 18, 2020).

[10] F.A. Kanda, R.M. Stevens, D.V. Keller, The Barium-Sodium Equilibrium System1, J. Phys. Chem. 69 (1965) 3867–3872.

[11] C.C. Addison, G.K. Creffield, P. Hubberstey, R.J. Pulham, The sodium–barium phase diagram, J. Chem. Soc. Inorg. Phys. Theor. (1971) 2688–2691.

[12] A.D. Pelton, The Ba- Na (Barium-Sodium) system, Bull. Alloy Phase Diagr. 6 (1985) 26–29.

[13] G.J. Snyder, A. Simon, The New Laves Phase Na_2Ba, Z. Für Naturforschung B. 49 (1994) 189–192. https://doi.org/10.1515/znb-1994-0206.

[14] G.J. Snyder, A. Simon, Dalton communications. The crystal structure of NaBa, an interpenetrating network of sodium tetrahedra and barium octahedra, J. Chem. Soc. Dalton Trans. (1994) 1159. https://doi.org/10.1039/dt9940001159.

[15] R.G. Samuseva, R.M. Zharkova, V.E. Plyushchev, The Cs_2MoO_4-Na_2MoO_4 system, Russ. J. Inorg. Chem. 9 (1964) 1444.

[16] E.S. Zolotova, Z.A. Solodovnikova, V.N. Yudin, S.F. Solodovnikov, E.G. Khaikina, O.M. Basovich, I.V. Korolkov, I.Yu. Filatova, Phase relations in the Na_2MoO_4–Cs_2MoO_4 and Na_2MoO_4–Cs_2MoO_4–$ZnMoO_4$ systems, crystal structures of $Cs_3Na(MoO_4)_2$ and $Cs_3NaZn_2(MoO_4)_4$, J. Solid State Chem. 233 (2016) 23–29.

[17] A.L. Smith, M.-C. Pignié, L. van Eijck, J.-C. Griveau, E. Colineau, R.J.M. Konings, Thermodynamic study of $Cs_3Na(MoO_4)_2$: Determination of the standard enthalpy of formation and standard entropy at 298.15 K, J. Chem. Thermodyn. 120 (2018) 205–216.

[18] V.P. Zueva, A.N. Shabanova, T.I. Drobasheva, The Na_2MoO_4-Cs_2MoO_4-MoO_3 Ternary System, Zh Neorg Khim. 3.

[19] S. Bordier, Modélisation thermodynamique des phases insolubles dans les verres nucléaires. Application à la vitrification du molybdène et des produits de fission platinoïdes. 235.

Chapter 8:
General conclusion and perspectives

Among the Generation IV systems, the Sodium cooled Fast Reactor is one of the most advanced technology. To optimise the design regarding the safety issues, research on the behaviour under severe accident is ongoing at CEA.

In terms of chemical interaction, two of the main risks are:

- the reaction between solid / molten fuel and sodium;
- the reaction between fission products and sodium.

In chapter 1, after a description of the irradiated fuel under normal conditions, the different scenarii of severe accident were reviewed. It showed that under severe accidental conditions, the composition and temperature ranges are very wide. Indeed, numerous elements have to be studied from 3000°C (above the fuel melting temperature) to room temperature, as the phases forming during the cooling stage are also important to predict for waste managing in the post-accidental stage.

The extensive experimental campaigns CABRI and SCARABEE have contributed to a better understanding of the core degradation mechanisms occurring during the different scenarii of a severe accident. However, no data was found on the composition of the phases, which formed during the chemical interaction between the fuel / fission products and sodium in these experiments.

Moreover, to model core degradation under severe accident, the SIMMER mechanistic code is used. This computational tool considers simultaneously flow dynamics, melt fragmentation, heat transfer, boiling and vaporisation. Currently the chemical interaction between the fuel / fission products and sodium is not considered in these models. A further coupling of the SIMMER code with a Gibbs energy minimizer (like Open Calphad) and a thermodynamic database would improve the description of the chemical properties of the solid, liquid, gas phases in the SIMMER code.

Therefore, there is a need to develop a Calphad thermodynamic database to describe the interaction between the fuel / fission products and sodium dedicated to severe accident studies for the SFR reactor.

The aim of this work is to start the development of a database on the interaction between the fuel / fission products and sodium.

In chapter 1, two chemical systems were selected:

- The Na-O-Pu-U system, mandatory to describe the MOX / sodium interaction;
- The Ba-Cs-I-Mo-Na-O-Te system containing the most volatile elements and the major components of the JOG layer.

To fix the priorities on the experiments and modelling that should be performed on these systems, the review of the literature data on both systems was presented in chapter 2.

In the Na-O-Pu-U system, the Na-O-U sub-system was thoroughly investigated. Most of the compounds were precisely characterised (structure and thermodynamic data) except the $Na_3U^VO_4$ where some uncertainties are remaining. In the Na-O-Pu ternary and Na-O-Pu-U quaternary systems, the structure and composition range of the phases are still subject of controversy and no thermodynamic data exist.

In the quaternary system, only the Na_3MO_4 phase was investigated as it is the main product forming under operating conditions in case of ingress of sodium into the fuel pin. However for other phases, only a few structural data were reported with only one Pu/(U+Pu) ratio.

Moreover, Calphad models are available on the U-Pu-O and Na-O-U systems whereas no model exists on the Na-O-Pu system.

The review on the interaction between the fission products and sodium showed that iodine and tellurium might react with the sodium in the primary cooling system to form NaI and compounds in the Na-Te or the Na-O-Te systems.

Concerning the (Ba-Cs)-Mo-O system, several compounds were observed in the MOX fuel under irradiation such as $BaMoO_3$ or Cs_2MoO_4 and $BaMoO_4$ in the JOG layer. These phases could be in contact with sodium in case of severe accident. Quaternary compounds in both Ba-Mo-Na-O and Cs-Mo-Na-O systems were reported to exist in the literature. However, thermodynamic data are missing to develop Calphad models.

For all the binary sub-systems, a Calphad model was developed except for the Ba-Na system.

Among the ternaries containing fission products, only a few ternary systems were modelled (Na-Mo-O, Cs-Mo-O, Ba-Mo-O ..). and many ternary systems are not yet assessed.

From the review of the data on both systems, the experimental investigation of the Na-O-Pu-U, Ba-Mo-Na-O and Cs-Mo-Na-O systems was chosen.

This work was finally splitted into three contributions performed in different laboratories. The first year was dedicated to the experimental study of the BaO-MoO_3-Na_2O and Cs_2O-MoO_3-Na_2O systems in TU Delft (chapter 5 and 6). The Na-O-Pu-U system was investigated in JRC Karlsruhe during the second year (chapter 4). Finally, the modelling of three systems (Ba-Na, reassessment of Mo-O, Cs_2MoO_4-Na_2MoO_4) was performed in CEA Saclay during the third year (chapter 7).

In the study of the Na-O-Pu-U system (chapter 4), for the first time, nanosized MOX fuel particles were prepared using the newly method developed at the JRC-Karlsruhe. In this technique, the decomposition of the mixed oxalate at low temperature is performed under an atmosphere of hot compressed water (95-250 °C) and not thermally (500-800° C) as in the usual method used to produce mixed oxides with high

Pu/(U+Pu) ratios. Precursors with Pu/(U+Pu) ratio of 0.06, 0.12, 0.29 and 0.46 as well as pure UO_2 and PuO_2 were prepared.

These powders were then mixed with NaOH or Na_2CO_3. Then the samples were heated at 800°C or 850°C under argon or air to synthesise the different phases Na_2MO_3, Na_3MO_4, Na_4MO_5, Na_2MO_4 and $Na_2M_2O_7$ reported in the Na-O-Pu-U system.

All the samples were characterised by X-ray diffraction. When a single phase was obtained, HR-XANES, and on some samples 1-D and 2-D ^{23}Na-NMR spectroscopy measurements were also performed.

For a better understanding of the structural evolution of the sodium urano plutonates, the structure of two Pu end-members was first studied.

The structure of $Na_2Pu^{IV}O_3$, which was subject of controversy, was precisely determined thanks to the use of both XRD and ^{23}Na-NMR analyses.

For the Na_4PuO_5 compound, the XRD measurements were in agreement with the data reported in the literature. However, this compound was characterised for the first time with HR-XANES technique and the plutonium was found mainly as Pu^{V} with possibly small amounts of Pu^{VI} instead of pure Pu^{VI} as expected from the theoretical structure. Nevertheless, complementary local structure measurements are required to find the charge compensation mechanism.

In the Na-O-Pu-U system, under argon at 800°C, the Na_4MO_5 phase with a tetragonal structure isostructural to $Na_4U^{VI}O_5$ and $Na_4Pu^{VI}O_5$ was obtained for low Pu contents. However, two different charge compensation mechanisms were identified when Pu^{IV} and U^{VI} were observed in the samples:

- The first mechanism involves the introduction of oxygen vacancies leading to the formula $Na_4U^{VI}Pu^{IV}O_{5-x}$. Only the composition with Pu/(U+Pu)=0.06 was found as one single phase. Therefore, we can conclude that the solubility of plutonium in this structure is higher than Pu/(U+Pu)>0.06;

- The second mechanism was observed when sodium was introduced in excess. Sodium is then inserted on the actinide site leading to the formula $Na_4(U^{VI}_{1-x},Pu^{IV}_{x},Na_{2x})O_5$. The composition with Pu/(U+Pu)=0.12 was found as one single phase. Therefore, the solubility of plutonium in this structure is higher than Pu/(U+Pu)>0.12.

Both phases were found in equilibrium with either a cubic phase with a lattice parameter close to $Pu^{IV}O_2$ or with the Na_2MO_3 phase with lattice parameters lower than the end-member $Na_2Pu^{IV}O_3$. Only one sample contained the three phases Na_4MO_5, Na_2MO_3 and PuO_2 phases.

At 1000°C, the lattice parameters of the tetragonal phase Na_4MO_5 do not vary with the Pu content and the plutonium was found as Pu^V. However, the structure was not further investigated in this work.

Under oxidising atmosphere, two phases were obtained:

- The Na_2MO_4 phase which was synthesised as a single phase for the Pu/(U+Pu)=0.06 ratio. The plutonium was found in +VI oxidation state in the plutonyl structure PuO_2^{2+}. As the uranium atom is also in the uranyl structure, uranium and plutonium were considered sharing the same crystallographic site;

- The $Na_2M_2O_7$ phase which was synthesised pure for the Pu/(U+Pu)=0.12 ratio. In this phase, the plutonium is probably under Pu^{IV} oxidation state. Nevertheless, the mixture of Pu^{IV} and Pu^{VI} cannot be excluded.

When obtained as pure phases, a thorough characterisation of sodium urano plutonates Na_2MO_4, $Na_2M_2O_7$, Na_4MO_5 Na_2MO_3 was performed in this work with a systematic determination of the oxidation states of the actinides with HR-XANES techniques. In some cases, ^{23}Na-NMR analyses were also used for the first time to characterise sodium urano plutonate compounds.

Thanks to these data, peculiar charge compensation mechanisms were proposed for some phases. Therefore, these compounds present a complex structure due to the large number of oxidation states for uranium and plutonium cations and to the possible non stoichiometry in oxygen and sodium.

Moreover, data on the plutonium solubility in the phases Na_2MO_4, $Na_2M_2O_7$ and Na_4MO_5 were determined. The results obtained under argon were used to propose phase equilibria on a "tentative" isothermal section of the Na_2O-PuO_2-UO_3 system at 800°C.

In the attempt to synthesise the Na_3MO_4 phase, the Na_4MO_5 phase was always obtained. Therefore, the cubic Na_3MO_4 phase observed in the interaction studies between MOX fuel and sodium under operating temperature is probably a metastable phase.

It is the first time that the structure of the phases in the Na-O-Pu-U system were investigated as a function of the Pu content in the MOX. The data on Na-O-Pu and Na-O-Pu-U will be used as a starting point to build a thermodynamic database on the Na-O-Pu and Na-O-Pu-U systems. Then, the database could be further used to performed thermodynamic calculations on the interaction between MOX fuel and sodium in a very wide range of composition and temperature. Complementary studies are proposed in the perspectives.

To develop a thermodynamic modelling on the interaction between sodium and fission products, the BaO-MoO_3-Na_2O and Cs_2O-MoO_3-Na_2O systems were studied experimentally.

In the BaO-MoO_3-Na_2O system, the structure of the quaternary compound $Ba_2NaMoO_{5.5}$ was thoroughly investigated with neutron diffraction, X-ray Absorption Spectroscopy and Raman spectroscopy techniques. Thanks to these measurements, the existence of oxygen vacancies was highlighted and the peculiar structure of the molybdenum octahedra was assessed for the first time in this compound. Finally, the standard enthalpy of formation of the $Ba_2NaMoO_{5.5}$ was measured with solution calorimetry. This thermodynamic data is a key input data for the further modelling of the Ba-Mo-Na-O system.

In the Cs_2O-MoO_3-Na_2O system, phase transition temperatures were measured by DSC on the Cs_2MoO_4-Na_2MoO_4 pseudo-binary system. This re-investigation of the phase diagram showed that no solubility of cesium into Na_2MoO_4 exists. The temperatures of the invariant reactions and the data on the solubility of sodium into Cs_2MoO_4 were consistent with previous studies reported in the literature. The enthalpy of the peritectic decomposition of the quaternary $Cs_3Na(MoO_4)_2$ compound was also measured. This data was extremely useful in the optimisation of the Calphad model as reported in Chapter 7. However, the measurement should be repeated several times to assess its reproducibility and determine its uncertainty.

The structure of the second compound $CsNaMo_3O_{10}$ was also determined by XRD and XANES techniques and the enthalpy of its decomposition reaction was measured by DSC.

Concerning the thermodynamic modelling of the sodium-fission product systems, as mentioned in Chapter 2, models on many binary systems exist except for Ba-Na.

Therefore this binary system was modelled in the present work. The experimental phase diagram data published in the literature were first reviewed. A good agreement was obtained between the calculations and the selected experimental data. But as no thermodynamic data exist on this system, the present modelling remains quite uncertain.

The Mo-O system is a key binary sub-system involved in the Cs-Mo-O, Na-Mo-O, Ba-Mo-O ternary systems. In this work, the parameters of the liquid phase (mainly the Gibbs energy term for the MoO42- species)) in the published model by Corcoran et al were reassessed to suppress an unexpected miscibility gap in the liquid phase found out in the MoO_3 rich region of the Cs-Mo-O, Na-Mo-O, Ba-Mo-O ternary systems.

Finally, the Cs_2MoO_4-Na_2MoO_4 section was modelled using the experimental data reported in the literature and measured in this work. A good agreement was obtained

with the selected phase diagram data. The sodium solubility in Cs_2MoO_4 was described. The quaternary $Cs_3Na(MoO_4)_2$ compound was found to be stable only at high temperature consistently with the published thermodynamic data, well reproduced by our model.

Using these models together with those published in the literature (chapter 2), a database was started to be developed on the Na-(Cs,I,Te,Ba,Mo,O) system.

The scope of the present work is broad due to the large number of chemical elements which are involved in the interaction between the irradiated MOX fuel and sodium. On the basis of the results we obtained, we propose the following perspectives for the continuation of the present work:

For the Na-O-Pu-U system:

- Ab-initio calculations to calculate thermodynamic data on the sodium plutonate phases of the Na-O-Pu system;
- The thermodynamic modelling of the Na-O-Pu system using Calphad;
- The synthesis, thorough characterization of the Na-O-U-Pu phases with low sodium content (Na_2O:MO_2) ratio (1:1) and (1.5:1);
- The measurement of the decomposition temperature of the pure phases by DTA;
- The measurement of the thermodynamic properties of the pure phases using calorimetry;
- XAS analyses at the U and Pu L_3-edge of the one phase samples to study the local structure around the actinide.
- Thermal treatments under controlled oxygen partial pressure;
- The thermodynamic modelling of the Na-O-Pu-U system using Calphad.
- Interaction tests between MOX fuel and liquid sodium at 600°C ; preliminary tests were performed in the present work. However, the results are not presented as the products formed during the test could not be collected and analysed.

For the fission product systems:

- Ab-initio calculations on the compounds in the Ba-Na system to determine thermodynamic data;
- In the Cs_2MoO_4-Na_2MoO_4 system, long thermal treatments, XRD, neutron diffraction to better assess the phase fields of the phase diagram.

For the Na-fission product systems, as the list of elements to consider is very large, it would be interesting to perform interaction tests between either fission product phases (Cs_2MoO_4, $BaMoO_4$ ….) or irradiated MOX fuel and liquid sodium. This would enable to identify the phases which would form and then prioritize the list of fission products to further consider in the future experiments and modelling.

Appendices

Appendix A: Experimental techniques

The devices and principles of the main characterisation techniques used in this work are briefly described in this appendix.

A.1. X-ray and neutron diffraction techniques

All synthesised samples were first characterized using powder X-ray Diffraction to identify the phases formed and their structure. High-temperature X-ray diffraction and neutron diffraction were also performed on some samples.

A.1.1. Principle of the method

A crystalline material is made of repeating structures called lattice that can also be described by repeating planes in all directions. These planes are characterised by their Miller indices (h,k,l) and a distance d_{hkl} between the different planes. When exposed to X-rays, these planes scatter the incoming X-ray beam and the reflected beam interfere constructively only if the incident angle θ satisfies Bragg's law:

$$2d_{hkl}sin\theta = \mathrm{n}\,\lambda$$

where n is an integer and λ the wavelength used for the measurement.
If the Bragg's law is not respected, the interaction will be destructive and no intensity will be measured.
A XRD pattern represents the evolution of the incident angle as a function of the intensity of the reflected X-ray beam collected.
The position of the activated reflexions (position where intensity has been recorded) is directly related to the structure of the compound and can be used to determine the symmetry, space group and lattice parameter of the analysed compound. Finally, the intensity of each individual reflection is proportional to the square of the structure factor, F_{hkl}which depends on the atom type and their atomic position in the structure.

$$F_{hkl} = \sum_j f_j e^{2i\pi(hx_j+ky_j+lz_j)} e^{-B_j\frac{sin^2\theta}{\lambda^2}}$$ (Equation A.1)

where h, k and l are the Miller indices for a given reflexion, f_j, B_j x_j, y_j and z_j are the scattering factor, the thermal displacement and the three atomic coordinates of the j atom respectively.

A.1.2. Room Temperature X-Ray Diffraction (XRD)

X-ray diffraction analyses at room temperature performed at JRC-Karlsruhe (Chapter 4) were collected on a Bruker D8 diffractometer mounted in a Bragg–Brentano configuration with a curved Ge (1,1,1) monochromator and a ceramic copper tube (40 kV, 40 mA) and supplied with a LinxEye position sensitive detector. The data were collected by step scanning in the angle range 10° ≤2θ≤ 120° with a step size of 0.008° (2θ); total measuring time was about 8 h.

X-ray diffraction measurements at room temperature performed at TU Delft (Chapter 5 & Chapter 6) were collected using a PANalytical X'Pert PRO X-ray diffractometer mounted in the Bragg-Brentano configuration with a Cu anode (Cu-$K_{\alpha 1}$, λ=1.541 Å, Cu-$K_{\alpha 2}$, λ=1.544 Å) (0.4 mm x 12 mm line focus, 45 kV, 40 mA) and a real time multi strip (RTMS) detector (X'Celerator). Diffraction patterns were obtained by step scanning in step sizes of 0.008° (2θ) in the angle range 10° ≤2θ≤ 120° with an integration time of about 8h.

A.1.3. High Temperature X-Ray Diffraction (HT-XRD)

The thermal expansion of $Ba_2NaMoO_{5.5}$ was investigated by HT-XRD using a Bruker D8 X-ray diffractometer mounted with a curved Ge monochromator (111), a copper ceramic X-ray tube (40 kV, 40 mA), a Linx Eye position sensitive detector, and equipped with an Anton Paar HTK 2000 chamber. Measurements were conducted in 600 mbar helium atmosphere from room temperature up to 1223 K, with 100 K heating steps. The temperature, measured with a thermocouple, was previously calibrated using the thermal expansion data of MgO [1]. The uncertainty on the temperature is estimated to be 20 K at 1223 K.

A.1.4. Neutron diffraction

The neutron diffraction technique was used as complementary analysis as the atomic position of light atoms can be precisely refined whereas with the XRD technique, only the heavy atoms are visible. Indeed, X-rays are diffracted by the electronic density surrounding the nucleus, which is directly related to its atomic number whereas neutrons are diffracted by the atomic nuclei. Therefore, atoms with low atomic number can be observed on the neutron diffraction patterns, which is particularly adapted for the investigation of oxygen vacancies.
Neutron data were collected at the Hoger Onderwijs Reactor at TU Delft [2] at the PEARL beamline. The sample was encapsulated under argon atmosphere in a vanadium cylindrical can (50 mm high, 6 mm inner diameter) closed with a viton o-ring. The data were collected at room temperature, at a fixed wavelength λ = 1.667 Å for 6 hours over the range 11° ≤2θ≤ 158°.

A.1.5. Data analysis

For both XRD and neutron data collected at JRC-Karlsruhe and TU Delft, the Rietveld method implemented in the Fullprof2k [3] suite software was used for the structural analyses. However, when the atomic position of the atoms were not determined (Chapter 4), the Le Bail method was used. This method is an adaptation of the Rietveld method giving a good approximation of the lattice parameters when the precise structure of a compound is not known [4].

A.2. X-Ray Absorption Spectroscopy

X-ray Absorption Spectroscopy techniques used in this work are described hereafter. This technique is suitable to study the oxidation state and local structure of materials, especially radioactive elements as only few sample amounts are needed for the measurements.

A.2.1. Principle of the method

XAS technique is based on the photoelectric effect, which is the main interaction between matter and X-rays. The X-rays are absorbed by the material and the absorption coefficient of the material analysed is measured with the Beer's law:

$$I = I_0 e^{-\mu(E)h}$$ (Equation A.2)

where I is the transmitted beam through the sample, I_0 is the incident X-ray beam produced by the synchrotron source, E the energy of the incident beam, $\mu(E)$ the absorption coefficient of the sample and h its thickness.

Generally, the $\mu(E)$ absorption coefficient decreases smoothly, however, when the incident energy equals the binding energy of a core electron (K, L or M shell) of an element in the analysed sample, a sharp increase called "absorption edge" happens.
The absorption of X-rays at this precise energy induces the ejection of the electron from the core to empty valence levels and continuum. This can be for example 1s orbitals corresponding to the K shell, 2s, $2p_{1/2}$ or $2p_{3/2}$ orbitals corresponding to L_1, L_2 and L_3 shells or $3d_{3/2}$, $3d_{5/2}$ corresponding to M_4 and M_5 shells.

The representation of the absorption coefficient as a function of the incident energy is called the X-ray absorption spectrum. As represented in **figure A.1**, two regions can be identified:

- The X-ray Absorption Near Edge Structure (XANES) is the region going from -30 to +30 eV of the white line energy. This part is extremely sensitive to the formal oxidation state and coordination of the absorbing element.
- The Extended X-ray Absorption Fine Structure (EXAFS) is the region starting just after the end of the XANES part and extending up to 1000 eV above the edge. This region shows successive oscillations corresponding to the interaction between electrons released with high kinetic energy with first neighbouring atoms. Therefore, information on the local environment around the absorbing element are gained.

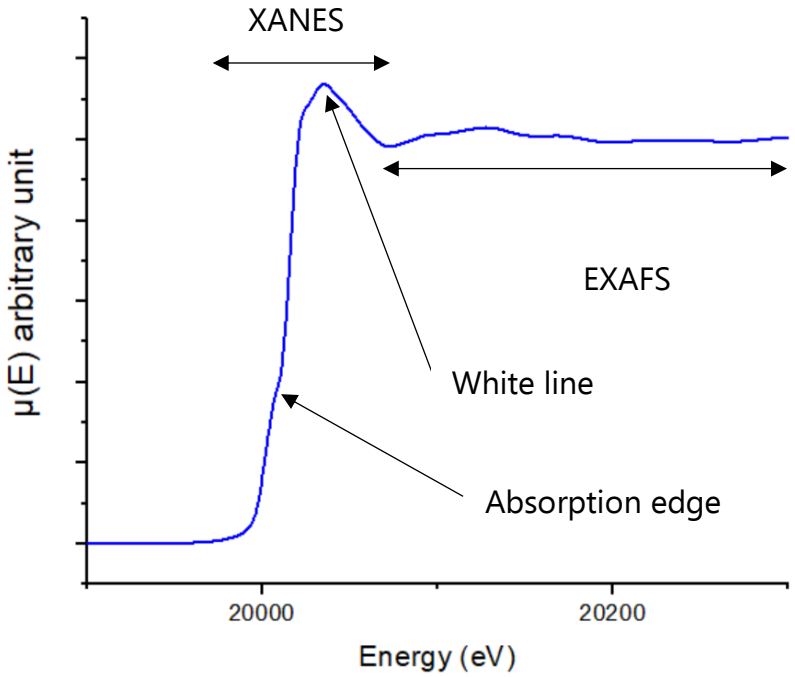

Figure A.1: Example of XAS spectrum collected in this work ($CsNaMo_3O_{10}$ spectrum chapter 6)

The modulation of the μ(E) absorption is generally best understood in terms of wave behaviour of the electrons. Therefore, the energy E dependence is usually converted to the wave number *k* of the electron:

$$k = \frac{\sqrt{2\,m\,(E-E_0)}}{\bar{h}}$$ (Equation A.3)

where *m* is the mass of an electron, *E* the energy, E_0 is the absorption edge and $\bar{h}$ the Planck constant.

The EXAFS equation describing the modulation is then expressed by:

$$\chi(k) = \sum_j \frac{N_j f_j(k) e^{-2k^2\sigma_j^2}}{kR_j^2} sin\,[2kR_j + \delta_j(k)]$$ (Equation A.4)

where *f(k)* and *δ(k)* are scattering properties of the neighbouring atoms, N is the number of neighbouring atoms, R is the distance of the neighbouring atoms and σ^2 is called the Debye-Waller factor representing the disorder in the neighbouring distances due to both thermal agitation and structural disorder.

A.2.2. Experimental setup at the BM26-DUBBLE beamline

XAS data were collected at the BM26-DUBBLE beamline of the European Synchrotron Radiation Facility (ESRF) in Grenoble (France). For the XAS measurements, around 20 mg of powdered samples were mixed with boron nitride (BN), pressed into pellets and

encapsulated in Kapton foils. The aforementioned operations were performed inside an argon-filled glove box, where oxygen and water levels were kept below 1 ppm. The storage ring operating conditions were 6.0 GeV and 170-200 mA. A double crystal monochromater mounted with a Si(111) crystal coupled to collimating and focusing Pt coated mirrors was used. Rejection of higher harmonics was achieved by three Si mirrors at an angle of 2 mrad relative to the incident beam.

XANES and EXAFS spectra were collected at room temperature, in transmission mode at the Mo K-edge. A step size of 1 eV was used in the edge region. The energy E_0 of the edge absorption threshold position was taken at the inflection point of the spectrum by using the first node of the second derivative. The position of the pre-peak in the edge was selected from the first node of the first derivative. Several acquisitions were performed on the same sample and averaged to improve the signal-to-noise ratio. Before averaging the scans, each spectrum was aligned using the XANES spectrum of a metallic molybdenum reference foil measured before and after the sample under investigation. The ATHENA software [5] was used to normalise the spectra and extract the EXAFS signal from the raw data.

The EXAFS data were collected in this work up to 15 $Å^{-1}$, and were Fourier transformed using the Hanning window over the k-range 3.5–13.5 $Å^{-1}$ (dk = 1). Curve fitting was performed based on the standard EXAFS equation using the ARTEMIS software[5] in k, k^2 and k^3 space. Phases and amplitudes for the interatomic scattering paths were calculated with the ab initio code FEFF8.40 [6]. The shift in the threshold energy (ΔE_0) was varied as a global parameter. The amplitude factor S_0^2 was fixed for all paths to 0.9. The coordination numbers, Debye–Waller factors and interatomic distances parameters, i.e. N, σ^2 and R, respectively, were allowed to vary for each shell.

A.2.3. High energy Resolution-X-ray Absorption Near Edge Spectroscopy

XAS analyses at the L_3 edges correspond to transitions from $2p_{3/2}$ to *6d* orbitals while $M_{4,5}$ edge corresponds to transitions from *3d* to *5f* orbitals.
Since the 5f valence electrons of U and Pu participate in the chemical bonding, changes of electronic structure due to variation of oxidation states and/or atomic environments of the U and Pu atoms will be better reflected in the U/Pu $M_{4,5}$ edge HR-XANES spectra.

At the U M_4 absorption edge, the energy is ~3726 eV and for the plutonium at the Pu M_5 edge, it is ~3775 eV. Therefore, in the close range of energy, uranium and plutonium oxidation state can be measured. At the An M_4 and the M_5 edge, $3d_{3/2} \rightarrow 5f_{5/2}$ and $3d_{5/2} \rightarrow 5f_{5/2}$, $3d_{5/2} \rightarrow 5f_{7/2}$ electronic transitions take place, respectively, followed by $4f_{5/2} \rightarrow 3d_{3/2}$ (M_4) and $4f_{5/2} \rightarrow 3d_{5/2}$, $4f_{7/2} \rightarrow 3d_{5/2}$ (M_5) and emission of M_β (M_4) and M_α (M_5) characteristic fluorescence (dipole selection rule $\Delta J = 0, \pm 1$).

U M_4/Pu M_5 absorption edge HR-XANES spectroscopy technique was conducted at the ACT station of the CAT-ACT-Beamline for catalysis and actinide research of the KIT synchrotron light source facility, Karlsruhe, Germany. A detailed description of the beamline is reported by Zimina *et al.* [16] The incident beam was vertically collimated by a bare Si mirror and monochromatised by a double crystal monochromator (DCM) equipped with Si(111) crystals and focused to 500 x 500 µm onto the sample by a toroidal, double-focusing Si-mirror. The DCM was calibrated by assigning 3725.5 eV/3775.0 eV to the maximum of the most intensive absorption resonance (white line, WL) of the U M_4/Pu M_5 edge HR-XANES spectrum of the UO_2/PuO_2 reference sample. The uncertainty in the energy positions of the spectral features is estimated to be about ± 0.05 eV, corresponding to half of the energy step size.
The HR-XANES spectra were obtained by using a Johann-type multi analyser crystal X-ray emission spectrometer. The sample, crystals and a single diode VITUS silicon drift detector (KETEK, Germany) were arranged in a vertical Rowland circle geometry.

The U M_4/Pu M_5 edge HR-XANES spectra were obtained by recording the maximum of the U M_β/Pu $M_{\alpha,1}$ fluorescence line as function of the incident energy. The emission energy was selected using the 220 reflections of four spherically bent Si analyser crystals (Saint-Gobain, France) with a bending radius of 1 m, aligned at a Bragg angle of 75.36° (U M_4)/74.47° (Pu M_5). A slit with a size of 500 x 500 µm was placed in front of the sample in order to cut-off tails in the profile of the X-ray beam, leading to a slight improvement of the energy resolution. The sample, crystals and detector were enclosed in a box filled with He in order to minimise intensity losses due to scattering and absorption of photons in air. A constant He flow was maintained in order to keep an oxygen concentration of ≤ 0.1 %.
The samples were placed in a multiposition plexiglass sample holder with 8 µm thickness of the Kapton windows, thereby double containment (inner and outer) of the samples was achieved. About 100 µg of sample was mixed with 10 mg bicomponent glue and placed in the inner cells.

A.3. Solid-state magic angle spinning nuclear magnetic resonance (MAS-NMR)

NMR analyses matter -solid, liquid or gas- through the detection of their spins in the presence of a magnetic field. The spin is a quantum mechanic property that can be associated to a magnetic dipole with the magnetic moment µ defined by:

$$\mu = \gamma \frac{h}{2\pi} I \quad \text{(Equation A.5)}$$

where γ is the gyromagnetic ratio, h the Planck constant and I the nuclear spin operator.
When this dipole is submitted to a magnetic field B_0, it aligns against B_0 principal axis and start rotating at the Larmor frequency ($\nu_0 = \frac{-\gamma B_0}{2\pi}$).

For this PhD work, we studied ^{23}Na, which is a quadrupolar nucleus as it possesses a spin equal to 3/2. Thus, it has a quadrupolar moment (Q) which reacts with the electric field gradient (V) leading to a non-spherical distribution of the charges as represented in **figure A.2**. The coupling between Q and V is called the quadrupolar interaction.

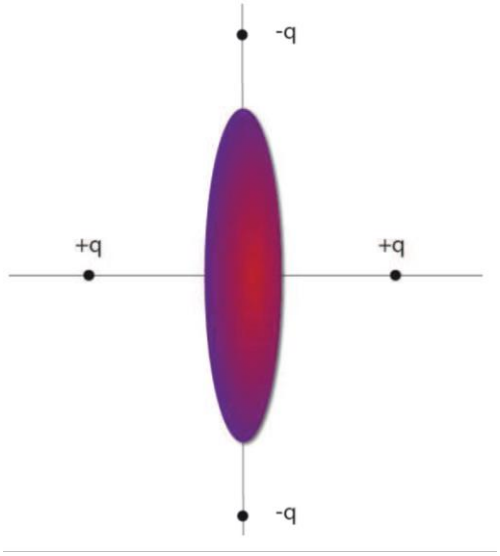

Figure A.2: from Martel PhD [7]: Ellipsoidal distribution of the nuclear electric charges: case of a quadrupolar spin. For a nucleus with a spin ½ (^{1}H, ^{29}Si) the charge distribution around the nucleus is spherical. In this example a quadrupolar nucleus with an electric charge distribution corresponding to a positif quadrupolar moment is presented.

From the analysis of the MAS NMR spectra, the peak position called the NMR shift δ, which depends on the local environment around the Na atom, and the two quadrupolar parameters can be extracted.

- η_Q represents the asymmetry parameter describing the symmetry environment around sodium
- C_Q the quadrupolar coupling constant represents the line broadening.

They are defined as:

$$\eta_Q = \frac{V_{xx}^{PAS} - V_{yy}^{PAS}}{V_{zz}^{PAS}} \text{ (Equation A.6)}$$

$$C_Q = \frac{eQV_{zz}^{PAS}}{h} \text{ (Equation A.7)}$$

With V_{xx}^{PAS}, V_{yy}^{PAS} and V_{zz}^{PAS} are the principal components of the electric field gradient tensor in the principal axis system (PAS).

Due to the radioactivity of the samples, we performed the NMR experiments using a dedicated spectrometer where the NMR probe is located in a glove box (see **figure A.3**) [8].

Figure A.3: Part of the NMR probe embedded in the dedicated radioactive glovebox. Here, we can see the sample container (rotor) inserted in the NMR probe [9].

To characterise our samples, we used a one pulse sequence. As ^{23}Na is a quadrupolar nuclei with a spin 3/2, a quantitative spectrum is obtained with a short $\pi/12$ pulse length [10]. The second sequence used is the two-dimensional multiple quantum MAS (MQ-MAS) experiment [11]. Thanks to this experiment, Na sites, which signals are overlapping when using single pulse experiment are properly differentiated.

A.4. Differential Scanning Calorimetry

3D-heat flow DSC measurements were performed using a Setaram Multi HTC module of the 96 Line calorimeter. The samples were placed in an nickel or alumina liner and encapsulated for the calorimetric measurements inside a stainless steel crucible closed with a screwed bolt to avoid vaporisation at high temperatures [12]. The temperature was monitored by a series of interconnected S-types thermocouples, and corrected on the heating ramp with a temperature calibration equation obtained from the measurement of standard materials (In, Pb, Sn, Zn, Al, Ag, Au) of well-known melting temperatures. The transition temperatures were derived on the heating ramp as the onset temperatures using tangential analysis of the recorded heat flow.

A.5. Solution Calorimetry

Solution calorimetry is an analysis technique measuring the temperature change (ΔT) produced by an interaction during mixing of two solutions or a solid and a liquid. This measured temperature change is related to the specific heat of the compound (Cp) and to the energy released (Q) by the relation

$$Q = Cp\ \Delta T \quad \text{(Equation A.8)}$$

To measure the energy release of the unknown reaction, a calibration before and after the measurement is done. A precise energy is given to the system and the temperature change is measured. Then, by comparison with the calibration values, the temperature change can be related to the energy. The energy is then used to calculate the enthalpy of reaction $\Delta_r H°_m$ as:

$$\Delta_r H°_m = Q*M/m \quad \text{(Equation A.9)}$$

with m the mass of the sample measured and M the molar mass.

The enthalpies of dissolution of $Ba_2NaMoO_{5.5}$, BaO and $Na_2Mo_2O_7$ in 2 M nitric acid solution were measured using a TA Instruments Precision Solution Calorimeter (semi-adiabatic or isoperibolic calorimeter) and TAM IV thermostat. The calorimetric unit consists of a reaction vessel and stirrer holding a glass ampoule. The experiments were performed in a thin-walled 100 mL Pyrex-glass reaction vessel equipped with a thermistor for measuring the temperature rise, and a heater for calibration during the measurement and equilibration of the initial baseline in the optimal operating range of the calorimeter before starting the experiment. The samples under study (BaO, $Na_2Mo_2O_7$, $Ba_2NaMoO_{5.5}$) were placed inside a 1 mL glass ampoule, which was sealed with bee wax. The latter operation was performed in the dry atmosphere of an argon filled glove box because of the sensitivity of the samples to air and moisture. The solid samples were dissolved into a solution of 2M HNO_3 by breaking the bottom of the glass ampoule on the sapphire breaking tip mounted at the bottom of the reaction vessel. The heat produced when breaking the ampoule is exothermic, with a value below 10 mJ, and can thus be neglected (measured values are more than 1 J >> 10 mJ). The temperature during the measurements was maintained in the oil bath with an accuracy of ± 1.10^{-4} K. Electrical calibrations were performed immediately before and after each enthalpy of reaction measurement to determine the equivalent energy of the system.

The accuracy of the measurements was verified by measuring the enthalpy of dissolution of potassium chloride (KCl, Sigma-Aldrich, 99.7%) in distilled water. The experimentally determined dissolution enthalpy of $KCl_{(cr)}$ into 1000 H_2O (molality m = 0.05551 mol.kg^{-1}), i.e. $\Delta_{diss}H°_m(1000H_2O, 298.15\ K)$ = (17.467 ± 0.011) kJ.mol^{-1} corresponds to $\Delta_{diss}H°_m(500H_2O, 298.15\ K)$ = (17.517 ± 0.011) kJ.mol^{-1} after correction to m=0.111 mol.kg^{-1}. The correction mentioned here was performed as recommended by the NBS[13]: the measured dissolution enthalpy was corrected to the molality of the certified enthalpy value m = 0.111 mol.kg^{-1} using the relationship $\Delta H°(500H_2O, 298.15\ K) = \Delta H(nH_2O, 298.15\ K) - \{\Phi L(nH_2O) - \Phi L(500H_2O)\}$. $\Delta H(nH_2O, 298.15\ K)$ is the measured dissolution enthalpy corrected to the reference temperature, and the term $\{\Phi L(nH_2O) - \Phi L(500H_2O)\}$, derived from Parker's tabulation[14] and listed by NBS[13], corrects the molality to the certified value. The uncertainty on the correction was estimated not to exceed 5 J.mol^{-1} [13].

The measured value corresponds to an enthalpy at infinite dilution of $\Delta_{diss}H°_m(\infty H_2O$, 298.15 K) = (17.174 ± 0.011) kJ.mol^{-1}, in good agreement with the NBS data[13] [15], i.e. $\Delta_{diss}H°_m(\infty H_2O$, 298.15 K) = (17.241 ± 0.018) kJ.mol^{-1}, and that in [16], i.e. $\Delta_{diss}H°_m(\infty H_2O$, 298.15 K) = 17.22 kJ.mol^{-1}.

A.6. High temperature Raman spectroscopy

High temperature Raman spectra were recorded using a Horiba Jobin-Yvon Aramis spectrometer equipped with a Linkam TS-1500 heating device. The $Ba_2NaMoO_{5.5}$ sample was placed in a platinum crucible and inserted in the furnace. A rate of 10 K/min was applied upon heating and 5 min of stabilisation time were maintained at each temperature plateau before acquisition of the spectra. The 632.8 nm line of a He-Ne laser was used as excitation wavelength and focused by means of an Olympus BX41(magnification factor: 50), thus delivering about 10 mW at the sample surface. Slits and confocal hole were set to result in a 1 cm^{-1} resolution. For each spectrum, an acquisition time of 4 s was considered with an average of 4 scans. Before analysis, the apparatus was calibrated with a silicon wafer, using the first-order Si line at 520.7 cm^{-1}. Band component analysis of the different spectra was performed with the Jandel Peakfit software, using pseudo-Voigt functions with the minimum number of components. Correlation coefficients greater than 0.997 were systematically obtained.

A.7. Thermal Ionization Mass Spectroscopy

A sample of 20 mg for each composition was dissolved in nitric acid. The elemental content of uranium and plutonium was measured by Thermal Ionization Mass Spectroscopy, adding a known amount of a solution containing the element to be investigated. Certified isotope standards are used as reference materials provided from accredited institutes such as EC-JRC (Belgium) or CETAMA (France) [15].

A.8. Transmission Electron Microscopy

The MOX samples were analysed by transmission electron microscopy (TEM) using a TecnaiG2 (FEI™) 200 kV microscope equipped with a field emission gun, modified during its construction to enable the examination of radioactive samples. They were prepared by dropping suspended samples on a TEM grid and evaporating the solvent. TEM images have been recorded using a Gatan US1000 slowscan CCD camera. Electron energy loss spectroscopy (EELS) has been used to estimate the uranium to plutonium ratio of the samples.

REFERENCES

[1] D. Taylor, Thermal expansion. Binary oxides with the silica structures, Br Ceram Trans J. 83 (1984) 5–9.

[2] L. van Eijck, L. D. Cussen, G. J. Sykora, E. M. Schooneveld, N. J. Rhodes, A. A van Well, C. Pappas, Design and performance of a novel neutron powder diffractometer: PEARL at TU Delft, J Appl Crystallogr. 49 (2016) 1398–1401.

[3] J. Rodriguez-Carvajal, Recent advances in magnetic structure determination by neutron powder diffraction, Phys. B. 192 (1993) 55–69.

[4] B.H. Toby, Estimating observed structure factors without a structure, Urnisbn978-1-118-41628-0. (2019).

[5] B. Ravel, M. Newville, ATHENA, ARTEMIS, HEPHAESTUS : data analysis for X-ray absorption spectroscopy using IFEFFIT, J Synchrotron Radiat. 12 (2005) 537–541.

[6] J.J. Rehr, R.C. Albers, Theoretical approaches to x-ray absorption fine structure, Rev. Mod. Phys. 72 (2000) 621–654. https://doi.org/10.1103/RevModPhys.72.621.

[7] L. Martel, Etude de la séparation de phase dans des verres silicatés par résonance magnétique nucléaire haute résolution solide et microscopie electronique.

[8] L. Martel, J. Somers, C. Berkmann, F. Koepp, A. Rothermel, O. Pauvert, C. Selfslag, I. Farnan, A nuclear magnetic resonance spectrometer concept for hermetically sealed magic angle spinning investigations on highly toxic, radiotoxic, or air sensitive materials, Rev. Sci. Instrum. 84 (2013).

[9] L. Martel, Technique: High resolution Magic Angle Spinning Nuclear Magnetic Resonance, Pu-Handbook book 6, ISBN: 978-0-89448-201-4.

[10] D. Fenzke, D. Freude, T. Fröhlich, J. Haase, NMR intensity measurements of half-integer quadrupole nuclei, Chem. Phys. Lett. 111 (1984) 171–175.

[11] G. Wu, D. Rovnyak, R.G. Griffin, Quantitative Multiple-Quantum Magic-Angle-Spinning NMR Spectroscopy of Quadrupolar Nuclei in Solids, J. Am. Chem. Soc. 118 (1996) 9326–9332.

[12] O. Beneš, R.J.M. Konings, S. Wurzer, M. Sierig, A. Dockendorf, A DSC study of the $NaNO_3$–KNO_3 system using an innovative encapsulation technique, Thermochim. Acta. 509 (2010) 62–66.

[13] G.A. Uriano, Technical report, Natl. Bur. Stand. Certif. Stand. Ref. Mater. 1655 Potassium Chloride KClcr Solut. Calorim. Natl. Bur. Stand. 1981. (1981).

[14] V.B. Parker, Technical report, Therm. Prop. Uni-Univalent Electrolytes Natl. Stand. Ref. Data Ser. Vol 2 Natl. Bur. Stand. 1965.

[15] I. Wadsö, R.N. Goldberg, Standards in isothermal microcalorimetry (IUPAC Technical Report), Pure Appl. Chem. 73 (2001) 1625–1639.

[16] D.D. Wagman, W.H. Evans, V.B. Parker, R.H. Schumm, I. Halow, S.M. Bailey, K.L. Churney, R.L. Nuttall, J Phys Chem Ref Data 11. (1971).

Appendix B: U M_4 HR-XANES spectra of the samples Na_4MO_5-6%(n°3), Na_4MO_5-12%(n°4), Na_2MO_4-6% (n°5), $Na_2M_2O_7$-6% (n°6), $Na_2M_2O_7$-12% (n°7) and Na_2MO_3-46% (n°8) samples and the UO_{2+x} reference.

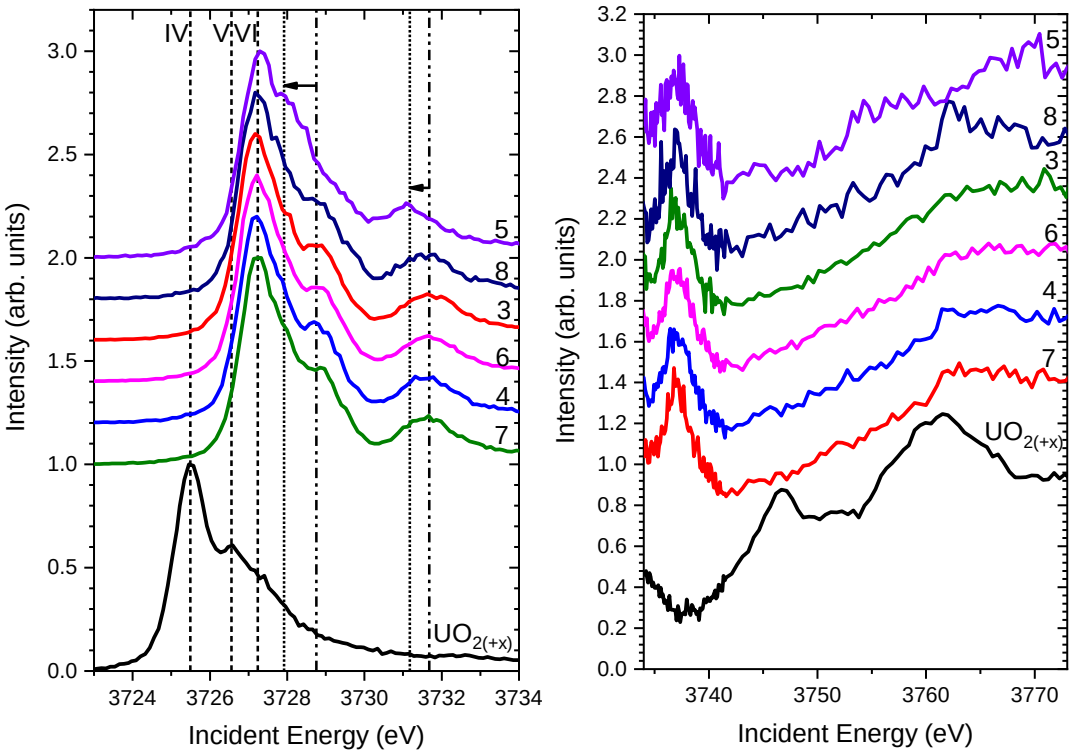

In every measured compounds, the white line corresponds to the energy of U^{VI} and the special features of the $U^{VI}O_2^{2+}$ uranyl ions with short bond length. Only the sample Na_2MO_4 presents a shift in the second local maxima discussed in Chapter 4, section 4.2.2.1.

Only in the Na_2MO_3 sample, the uranium was not expected in +VI oxidation state and this peculiarity is discussed in Chapter 4 section 4.2.2.4

Appendix C: Résumé succinct en Français

Le réacteur à neutrons rapides refroidi au sodium (RNR-Na) est à ce jour, un des concepts les plus avancés parmi les différentes technologiesétudiées pour les réacteurs de génération IV.

De nombreuses études ont été menées pour caractériser le comportement du combustible en réacteur. En particulier, des données existent sur l'interaction avec le sodium en cas de brèche dans l'aiguille combustible. Cependant, l'interaction entre le sodium et le combustible en cas d'accident grave n'est pas encore bien connue et les codes de calculs pour modéliser et simuler ces accidents ne prennent pas en compte la thermochimie et les différentes phases pouvant se former lors de l'interaction entre le combustible et le sodium. Ainsi, dans le but d'améliorer les capacités prédictives de ces codes de calculs, la description thermodynamique des interactions entre le combustible irradié et le sodium est une première approche indispensable . Pour ce faire, le développement d'une base de données décrivant les systèmes impliqués est nécessaire.

Après la revue des différents scénarii d'accident grave, deux systèmes ont été considérés. Le premier décrit l'interaction entre le combustible MOX et le sodium et est représenté par le système : Na-O-Pu-U. Le second regroupe les produits de fissions pouvant interagir avec le sodium : Ba-Cs-I-Mo-Na-O-Te.

L'interaction combustible MOX / sodium dans des conditions d'accident grave sont très différentes des conditions nominales de fonctionnement et impliquent une étude couvrant une très large gamme de température et de composition pour le système Na-O-Pu-U : de 3000°C (fusion du combustible) jusqu'à la température ambiante (après la phase de refroidissement post-accidentelle).

Pour décrire des systèmes aussi complexes, la méthode CALPHAD est la plus adaptée. Il s'agit de développer un modèle thermodynamique contenant la description des enthalpies libres des phases gaz, liquides et solides en fonction de la température, de la composition et de la pression du système. L'équilibre est alors calculé par minimisation de l'enthalpie libre du système.

Concernant l'interaction entre les produits de fission et le sodium, l'iode et le tellure pourraient se retrouver respectivement sous la forme de NaI ou de composés Na-Te ou Na-O-Te après leur relâchement dans des zones qui n'interagissent pas avec le combustible. Pour les éléments baryum et cesium, ils sont généralement associés au molybdène formant des composés ternaires comme le $BaMoO_3$, $BaMoO_4$ ou Cs_2MoO_4 dans le combustible. Lors d'un accident grave, ces composés pourraient interagir avec le sodium. De plus, dans les systèmes Ba-Mo-Na-O et Cs-Mo-Na-O des composés quaternaires ont été reportés qui pourraient se former.

Les systèmes retenus pour l'étude expérimentale sont :Na-O-U-Pu, Ba-Mo-Na-O et Cs-Mo-Na-O. Les données nécessaires à l'établissement d'un modèle thermodynamique sont :

- Les données crystallographiques sur les phases
- Les données de diagramme de phase
- Les données thermodynamiques des phases

Dans le but d'étudier expérimentalement les produits issus de l'interaction entre le sodium et le combustible MOX, des nano poudres de MOX ont été produites par décomposition de l'oxalate mixte sous pression de vapeur d'eau à basse température. Des oxydes mixtes avec des rapports Pu/(U+Pu)=0.06, 0.12, 0.29, 0.46 ont été préparés. Ces nanopoudres ont ensuite été mélangés avec des composés de sodium (NaOH ou Na_2CO_3) pour synthétiser les phases quaternaires $Na_x(U,Pu)_yO_z$. , sous argon ou sous air à 800-1000°C.

Les analyses de ces phases par DRX, RMN du sodium et HR-XANES ont permis de caractériser les différentes structures . Pour chaque échantillon contentant une seule phase (Na_2MO_4, $Na_2M_2O_7$, Na_4MO_5 Na_2MO_3 and Na_3MO_4), une détermination systématique des degrés d'oxydation de l'uranium et du plutonium a été effectuée. De plus, grâce à la combinaison de ces trois techniques d'analyse structurale, différents mécanismes de compensation de charge (soit plusieurs sites pour le sodium soit l'introduction de lacunes d'oxygène) ont été suggérés lorsque le degré d'oxydation du plutonium ne correspondait pas à la formule théorique. Enfin l'ensemble des données a été utilisé pour proposer une coupe isotherme du système Na_2O-UO_3-PuO_2.

Les systèmes BaO-MoO_3-Na_2O et Cs_2O-MoO_3-Na_2O ont ensuite été étudiés dans le but d'acquérir des données expérimentales pour développer les modèles thermodynamiques de ces systèmes quaternaires primordiaux dans l'étude de l'interaction entre le combustible irradié et le sodium.

Dans le système BaO-MoO_3-Na_2O, le composé $Ba_2NaMoO_{5.5}$ a été synthétisé. Ce composé a été caractérisé par différentes méthodes d'analyse structurale : DRX, neutron, XAS et spectroscopie Raman permettant une étude locale des octaèdres autour des atomes de molybdène et des lacunes d'oxygène. Finalement, l'enthalpie standard de formation du composé quaternaire $Ba_2NaMoO_{5.5}$ a été mesurée par calorimétrie en solution. Cette donnée thermodynamique est essentielle pour la future modélisation du système Ba-Mo-Na-O.
Dans le système Cs_2O-MoO_3-Na_2O, l'étude du pseudo-binaire Cs_2MoO_4-Na_2MoO_4 par DSC a été réalisée. Cette nouvelle étude suggère qu'aucune solubilité du cesium dans la phase Na_2MoO_4 existe en accord avec l'étude la plus récente du système. Cependant, une solubilité du sodium dans Cs_2MoO_4 a été observée en accord avec les deux précédentes études réalisées sur ce système.

Dans le système, deux composés quaternaires existent : $Cs_3Na(MoO_4)_2$ et $CsNaMo_3O_{10}$. Le premier a été étudié en détail et les données thermodynamiques ont été reportées. Pour le deuxième composé, des données DRX ont été mesurées cependant aucune étude structurale détaillée a été réalisée. Ainsi, le composé $RbNaMo_3O_{10}$ présentant la même structure a été utilisé comme structure de départ pour l'affinement des paramètres structuraux et positions atomiques dans le $CsNaMo_3O_{10}$. Finalement l'enthalpie de décomposition péritectique de $Cs_3NaMo_2O_8$ a été mesurée et s'est révélée extrêmement utile pour le développement du modèle Calphad. L'enthalpie correspondant à la décomposition de $CsNaMo_3O_{10}$ a aussi été mesurée.

Le chapitre 7 présente la modélisation Calphad de trois systèmes : Ba-Na, Mo-O (modification d'un modèle publié), Cs_2MoO_4-Na_2MoO_4. Le système Ba-Na a été modélisé à l'aide des données expérimentales de diagramme de phase de la littérature. Le système Mo-O décrit dans la littérature a été légèrement modifié pour le liquide afin d'empêcher l'apparition d'une lacune de miscibilité dans le liquide apparaissant dans les systèmes ternaires Cs-Mo-O, Na-Mo-O, Ba-Mo-O.
Finalement, le pseudo-binaire Cs_2MoO_4-Na_2MoO_4 a été modélisé, en utilisant les données :

- de diagramme de phase reportées dans la littérature et mesurées dans les chapitre 6 sur le système Cs_2MoO_4-Na_2MoO_4
- thermodynamiques du composé $Cs_3Na(MoO_4)_2$ présent sur cette coupe
- de l'enthalpie de décomposition péritectique de $Cs_3Na(MoO_4)_2$

Ce travail a permis de démarrer l'étude sur l'interaction entre le combustible MOX, les produits de fission et le sodium dans le contexte des accidents graves. La revue a permis de sélectionner les systèmes chimiques prioritaires à étudier. Les données expérimentales obtenues sur ces systèmes ont permis d'améliorer les connaissances sur ces systèmes, très complexes et de commencer à construire une base de données thermodynamiques. Il s'agit d'un outil prometteur pour améliorer les données physico-chimiques des différentes phases solides, liquides et gaz à introduire dans les codes accidents graves. Cette meilleure prise en compte de la chimie dans ces codes devrait permettre de mieux modéliser et simuler les différentes étapes de l'accident.

université PARIS-SACLAY

ECOLE DOCTORALE N°571
Sciences chimiques : molécules, matériaux, instrumentation et biosystèmes (2MIB)

Titre : Contribution à l'étude de l'interaction chimique entre le combustible MOX et le sodium pour la sûreté des Réacteurs à Neutrons Rapides à caloporteur au sodium (RNR)

Mots clés : RNR-Na, accident graves, combustible MOX, sodium, produits de fission, thermodynamique

Résumé : Dans le cas d'un accident grave dans un réacteur refroidi au sodium, des interactions entre le combustible irradié et le sodium pourraient se produire à très haute température. Pour pouvoir prédire la dégradation des aiguilles combustibles et les phases produites en tenant compte de tous les systèmes présents dans le combustible irradié, une étude des systèmes Na-PF-Pu-U-O avec PF= Ba, Cs, I, Mo, Te est primordiale. Pour un système avec de nombreux éléments à étudier sur une large échelle de température et de composition, la méthode Calphad est particulièrement adaptée. Celle-ci permet de prédire les phases formées en fonction de la température, pression et composition du système. Les composés dans le système Na-O-Pu-U ont été synthétisé par synthèse solide avec quatre ratios Pu/(U+Pu) différents dans les nanoparticules de MOX utilisés comme précurseurs. Les structures obtenues ont été caractérisés par DRX, ^{23}Na-RMN et HR-XANES. Le degré d'oxydation des échantillons a systématiquement été déterminé pour le plutonium et l'uranium et des mécanismes de compensations de charge avec insertion de sodium ou de lacunes d'oxygène ont été suggéré lorsque le dégré d'oxydation du plutonium mesuré était différent du théorique. Les structures des composés quaternaires dans les systèmes Ba-Mo-Na-O et Cs-Mo-Na-O ont ensuite ont été étudiés par DRX, diffraction neutronique, DRX-HT, spectroscopie Raman-HT, XAS. L'enthalpie standard de formation et l'enthalpie de décomposition ont aussi été déterminées. Finalement, la section Cs_2MoO_4-Na_2MoO_4 a été ré-étudiée par DSC et un model Calphad pour ce système a été developpé.

Title : Contribution to the investigation of the chemical interaction between sodium and irradiated MOX fuel for the safety of Sodium-cooled Fast Reactors

Keywords : SFR, severe accident, MOX fuel, sodium, fission products, thermodynamic

Abstract : In case of a severe accident in Sodium-cooled Fast Reactors, interactions between partly molten fuel and sodium could happen at high temperature. Therefore, to predict the degradation evolution of fuel pins and phase formation in the different systems existing in the irradiated fuel, a thorough study of the Na-FP-Pu-U-O with FP= Ba, Cs, I, Mo, Te has to be performed. For such multicomponent system and large temperature and composition range, the Calphad method is a suitable way for developing a thermodynamic database to predict the phase formation depending on the temperature, pressure and composition of the system. Compositions with four Pu/(U+Pu) ratio in the Na-O-Pu-U system were synthesised by solid state synthesis method using nanoparticules of MOX fuel and characterised by XRD, ^{23}Na-NMR and HR-XANES techniques. The oxidation state of plutonium and uranium in the different structures was systematiquely investigated. When the measured oxidation state of actinides was different from the theoretical one, charge compensation mechanisms were suggested either by adding sodium in the structure or oxygen vacancies. Then, the structure of quaternary compounds in the Ba-Mo-Na-O and Cs-Mo-Na-O systems were also investigated by several structural techniques (XRD, neutron diffraction, HT-XRD, HT-Raman spectroscopy, XAS). Thermodynamic properties such as standard enthalpy of formation or enthalpy of decomposition were also determined. Finally, the Cs_2MoO_4-Na_2MoO_4 pseudo-binary section was re-investigated experimentally by DSC and a Calphad model for this system was developed.

Université Paris-Saclay
Espace Technologique / Immeuble Discovery
Route de l'Orme aux Merisiers RD 128 / 91190 Saint-Aubin, France